Recognition of Nonideal Iris Images Using Shape Guided Approach and Game Theory

Kaushik Roy

A Thesis

in

The Department of

Computer Science and Software Engineering

Presented in Partial Fulfillment of the Requirements

for the Degree of Doctor of Philosophy (Computer Science) at

Concordia University

Montreal, Quebec, Canada

April, 2011

Concordia University

School of Graduate Studies

This is to certify that the thesis prepared

By: **Kaushik Roy**

Entitled: **Recognition of Nonideal Iris Images Using Shape Guided Approach and Game Theory**

and submitted in the partial fulfillment of the requirements for the degree of

Doctor of Philosophy (Computer Science)

complies with the regulations of the University and meets the accepted standards with respect to originality and quality.

Signed by the final examining committee:

_____ Chair
Dr. Wahid S. Ghaly

_____ Examiner
Dr. Tonis Kasvand

_____ Examiner
Dr. Sudhir P. Mudur

_____ Examiner
Dr. Abdessamad Ben Hamza

_____ External Examiner
Dr. Patrick S. P. Wang

_____ Supervisor
Dr. Prabir Bhattacharya

_____ Supervisor
Dr. Ching Y. Suen

Approved by _____
Chair of Department or Graduate Program Director

_____ _____
Dr. Robin Drew, Dean, Faculty of Engineering and Computer Science

Abstract

Recognition of Nonideal Iris Images Using Shape Guided Approach and Game Theory

Kaushik Roy, Ph.D.
Concordia University, 2011

Most state-of-the-art iris recognition algorithms claim to perform with a very high recognition accuracy in a strictly controlled environment. However, their recognition accuracies significantly decrease when the acquired images are affected by different noise factors including motion blur, camera diffusion, head movement, gaze direction, camera angle, reflections, contrast, luminosity, eyelid and eyelash occlusions, and problems due to contraction and dilation. The main objective of this thesis is to develop a nonideal iris recognition system by using active contour methods, Genetic Algorithms (GAs), shape guided model, Adaptive Asymmetrical Support Vector Machines (AASVMs) and Game Theory (GT). In this thesis, the proposed iris recognition method is divided into two phases: (1) cooperative iris recognition, and (2) noncooperative iris recognition.

While most state-of-the-art iris recognition algorithms have focused on the preprocessing of iris images, recently, important new directions have been identified in iris biometrics research. These include optimal feature selection and iris pattern classification. In the first phase, we propose an iris recognition scheme based on GAs and asymmetrical SVMs. Instead of using the whole iris region, we

elicit the iris information between the collarette and the pupil boundary to suppress the effects of eyelid and eyelash occlusions and to minimize the matching error.

In the second phase, we process the nonideal iris images that are captured in unconstrained situations and those affected by several nonideal factors. The proposed noncooperative iris recognition method is further divided into three approaches.

In the first approach of the second phase, we apply active contour-based curve evolution approaches to segment the inner/outer boundaries accurately from the nonideal iris images. The proposed active contour-based approaches show a reasonable performance when the iris/sclera boundary is separated by a blurred boundary. In the second approach, we describe a new iris segmentation scheme using GT to elicit iris/pupil boundary from a nonideal iris image. We apply a parallel game-theoretic decision making procedure by modifying Chakraborty and Duncan's algorithm to form a unified approach, which is robust to noise and poor localization and less affected by weak iris/sclera boundary. Finally, to further improve the segmentation performance, we propose a variational model to localize the iris region belonging to the given shape space using active contour method, a geometric shape prior and the Mumford-Shah functional.

The verification and identification performance of the proposed scheme is validated using four challenging nonideal iris datasets, namely, the ICE 2005, the UBIRIS Version 1, the CASIA Version 3 Interval, and the WVU Nonideal, plus the non-homogeneous combined dataset. We have conducted several sets of experiments

and finally, the proposed approach has achieved a Genuine Accept Rate (GAR) of 97.34% on the combined dataset at the fixed False Accept Rate (FAR) of 0.001% with an Equal Error Rate (EER) of 0.81%. The highest Correct Recognition Rate (CRR) obtained by the proposed iris recognition system is 97.39%.

Acknowledgements

I would like to express my sincere gratitude and profound indebtedness to my doctoral thesis advisors Dr. Prabir Bhattacharya and Dr. Ching Y. Suen for their guidance, encouragement, constructive suggestions, and support during the span of this research. I am grateful to them for providing me the freedom and motivation to explore new areas of research and new ideas. Without their help, it would not have been possible to complete this research work. I would also like to thank them for spending so many hours with me in correcting and improving the writing of the thesis. The useful suggestions provided by committee members are also greatly appreciated.

I want to acknowledge the financial support provided by Concordia University and NSERC, Canada, which was crucial for completing this research.

I am grateful to Dr. Chunming Li of Vanderbilt University Institute of Imaging Science, Nashville, Tennessee, USA and Dr. Xavier Bresson of University of California, Los Angeles, USA for their active contour source codes.

My grateful thanks go to all the members in the Centre for Pattern Recognition and Machine Intelligence (CENPARMI). Special thanks go to our Lab administrator, Nicola Nobile, for his excellent technical support and to our secretary, Marleah Blom, who cheers up every student in CENPARMI. I also wish to thank Shira Katz for her extreme patience in proofreading my thesis.

I am also grateful to all of my graduate colleagues at Computer Vision and Image Analysis (CVIA) lab in particular Dr. Emad Attari and Mahdi Yektaii. They influenced me a lot in this research.

I would also like to thank my wife, Tithi Goswami, for her love, continuous moral support, inspiration, thoughtful comments and friendly cooperation in every moment. It is beyond words to express my appreciation to the happiness brought to me by my daughter, Aratrika Roy.

Finally, I would like to express my gratefulness to my parents, brother, and in laws for their patience, love and constant encouragement.

Dedications

My Father, Dr. Kanailal Ray

My Mother, Kalpana Ray

And

My Wife, Tithi Goswami

Table of Contents

List of Figures

List of Tables

List of Acronyms

AASVM : Adaptive Asymmetrical Support Vector Machine

ASM : Active Shape Model

BLPOC : Band Limited Phase Only Correlation

CHT : Canny edge detection and Hough Transform

CRR : Correct Recognition Rate

CSA : Contribution-Selection Algorithm

DBWT : Daubechies Wavelet Transform

DCT : Discrete Cosine Transform

DFT : Discrete Fourier Transform

DLS : Direct Least Square

EE : Equal Error

EER : Equal Error Rate

FA : False Accept

FAR : False Accept Rate

FFBP : Feed-Forward neural network by using the Backpropagation

FFLM : Feed-Forward neural network by using the Levenberg-Marquardt

FPC : Fourier Phase Code

FR : False Reject

FRR : False Reject Rate

FV : Feature Vector

GA : Genetic Algorithm

GAC : Geodesic Active Contour

GAR : Genuine Accept Rate

GP : Genetic Program

GT : Game Theory

HD : Hamming Distance

HDD : Hausdorff Distance

ICA: : Independent Component Analysis

IDO : Integro-Differential Operator

IRIS : Iris Recognition Immigration System

k-NN : k-Nearest Neighbor

LDA : Linear Discriminant Analysis

LOO : Leave-One-Out

LOOCV : Leave-One-Out Cross-Validation

LS : Level Set

MAP : Maximum Posteriori Probability

MCSA : Modified Contribution-Selection Algorithm

MSA : Multi-Perturbation Shapley Analysis

NE : Nash Equilibrium

NIR : Near Infra-Red

OBD : Optimal Brain Damage

OWPT : Optical Wavelet Packet Transform

PCA : Principal Component Analysis

PDF : Partial Differential Equation

PHDD : Partial Hausdorff Distance

RAC : Region-based Active Contour

RBF : Radian Basis Function

RE : Recognition Error

ROC : Receiver Operator Characteristics

RR : Recognition Rate

SDF : Signed Distance Function

SGA : Shape Guided Approach

SIFT : Scale Invariant Feature Transform

SSS : Small-Sample-Sizes

SV : Support Vector

SVM : Support Vector Machine

SVM-RFE : Support Vector Machine-Recursive Feature Elimination

SVD : Singular Value Decomposition

VLS : Variational Level Set

VW : Visible Wavelength

Chapter 1

Introduction

In this introductory chapter, the research topic, namely, "Recognition of Nonideal Iris Images Using Shape Guided Approach and Game Theory", is presented. We begin with a description of the motivations (Section 1.1) behind this research endeavor. The proposed methods are then briefly introduced (Section 1.2) and the main contributions of this thesis are listed in Section 1.3. Finally, we conclude with an outline of this thesis in Section 1.4.

1.1 Motivations

With the increasing demands of automated personal identification, biometric-based authentication has been receiving extensive attention over the last decade. The main purpose of biometrics is to identify an individual based on physiological and behavioral attributes such as palmprints, fingerprints, irises, retina, hand geometry, faces, vein patterns, ears, key stroke patterns, gait, etc. [1-3]. Biometric-based identification systems have many advantages over the traditional authentication techniques that are based on what you know or what you possess [4-6]. Among all the biometric techniques, iris recognition has been considered as the most reliable

and accurate method for identity authentication. Iris recognition has become an active research topic in the area of pattern recognition because of its promising application values in personal identification [2]. Iris recognition has been deployed in various critical application areas, including homeland security, border control, web-based services, national ID cards, rapid processing of passengers, restricted access to privileged information, missing child identification, and welfare distribution [2]. The iris of a human eye is the annular part that is located between the black pupil and the white sclera and it contains many discriminative minute parts (e.g., furrows, rings, crypts, freckles, coronas, etc.). These rich details of the iris, denoted as textures, are unique to each person and to each eye and remain stable over a lifetime, which make the iris particularly useful for person authentication [1]. Furthermore, an iris image is typically acquired in a noncontact imagery setup, which is of great importance in real-time applications [3]. Therefore, from the above discussion, it is clear that the iris-based recognition, which is the main focus of this dissertation, provides an extremely reliable and accurate solution for personal identification.

Although most state-of-the-art iris recognition algorithms are focused on the preprocessing of iris images, recently, there have been important new directions identified in iris biometrics research [3]. These include optimal feature selection and iris pattern classification. In the first phase of the research work, we focus on improving the iris recognition performance based on the best iris feature subset selection using Genetic Algorithms (GAs) and the accurate classification of iris patterns using asymmetrical Support Vector Machines (SVMs). Most current iris

recognition algorithms claim to perform with a very high recognition accuracy in a strictly constrained situation, where the iris images are acquired in a sophisticated imagery setup. Under inflexible image acquiring constraints, it is possible to capture high quality images and attain an impressive accuracy with very low error rates. However, most state-of-the-art iris recognition algorithms fail to perform in a noncooperative environment, where the probability of acquiring nonideal iris images is very high. In an uncontrolled environment, images are captured in a flexible imagery setup and are affected from motion blur, camera diffusion, head rotation, gaze direction, camera angles, reflections, poor contrast, luminosity, occlusions, and pupil dilation. The nonidealities contained in iris images affect the iris segmentation performance considerably, and consequently degrade the overall recognition accuracy. Moreover, researchers often found that, the iris and pupil boundaries are of arbitrary shapes, and therefore, can lead to segmentation errors, if fitted with some presumed simple shapes. Therefore, it is important to compensate for such nonideal factors to augment the iris recognition accuracy. However, it still remains a challenging issue to deal with the nonideal iris images that are affected severely by several noise factors. Addressing the above problems, in the second phase of our research work, we propose iris recognition methods that can process the nonideal iris images by using active contours, GAs, Game Theory (GT), Shape Guided Approaches (SGAs) and Adaptive Asymmetrical SVMs (AASVMs). In the following section, we discuss the main steps of the proposed approaches.

1.2 Proposed Approaches: The Main Steps

We illustrate our proposed iris recognition method into two phases. In the first phase, we propose a cooperative iris recognition method based on GAs and asymmetrical SVMs. This method is not specially designed for the degraded iris images that are captured in a noncooperative environment. However, in the second phase, we process and recognize the nonideal iris images that have been acquired in an unconstrained situation and are affected severely by different noise factors.

In the first phase, we mainly focus on improving the iris recognition performance based on iris feature selection and pattern classification. We apply the morphological operations, Canny edge detection and circular Hough transform to detect the iris and pupil boundaries. To alleviate the effects of eyelid and eyelash occlusions, we extract the iris information from the pupillary region. Eyelids are detected using parabolic curves and eyelashes are isolated using 1D log Gabor filters and variance of intensity. A local intensity-based histogram equalization technique is deployed to enhance the contrast of the normalized image. The log Gabor filters are used to extract the distinctive iris features, and a GA-based scheme with a new fitness function is applied to select the most important iris features without losing recognition accuracy. The traditional SVMs are modified into asymmetrical SVMs to handle [7]: (1) the highly unbalanced sample proportion between two classes, and 2) the different types of misclassification error that lead to different misclassification losses. Furthermore, the parameter values of SVMs are optimized

in order to improve the generalization performance. A block diagram of the proposed scheme is shown in Fig. 1.1.

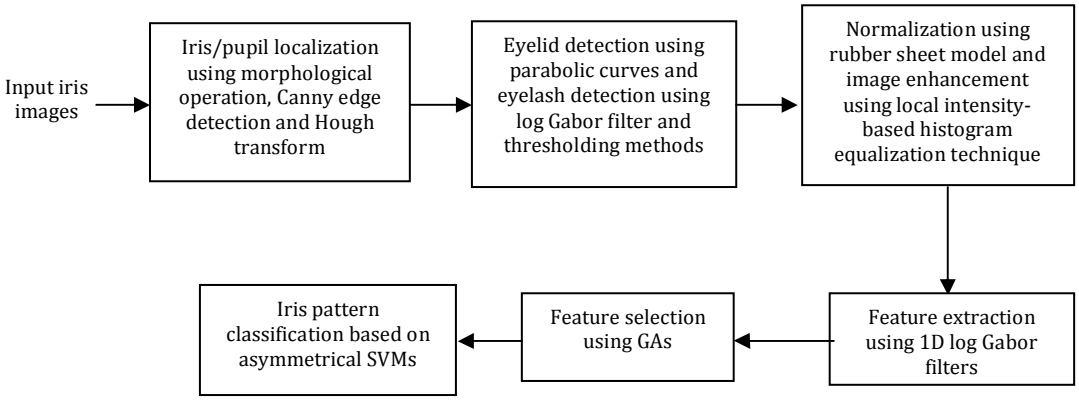

Fig. 1.1 Block diagram of the proposed iris recognition system (first phase).

In the second phase, we improve the iris recognition performance based on accurate segmentation, feature selection and matching. The iris recognition algorithm applied in the first phase may not perform well in an unconstrained situation where the possibility of capturing degraded iris images is very high due to gaze deviation, reflections, poor focus, blurring and occlusions by eyelashes, eyelids, glasses, and hair. In the second phase, we propose three iris recognition approaches that are effective for processing the nonideal iris images: 1) active contour-based methods, 2) GT-based method, and 3) SGA. In the first approach of the second phase, an elliptical fitting technique is used first to approximate the iris/pupil boundary. Then, we apply three active contour-based adaptive localization methods that aim at compensating various nonideal factors contained in the iris images. To get the optimal estimation of the inner boundary from a nonideal iris image, we first apply a Level Set (LS)-based active contour scheme with the edge stopping function [8]. The

active contour-based curve evolution scheme is employed again using the regularized Mumford-Shah segmentation model with an energy minimization algorithm to detect the outer boundary [8-10]. While the proposed iris segmentation scheme based on active contours exhibits an encouraging performance in detecting the inner/outer boundary, it requires a huge computational time due to the expensive curve evolution approach. Therefore, a Variational Level Set (VLS)-based curve evolution scheme is deployed, which uses a significantly longer time step to numerically and accurately solve the evolution Partial Differential Equation (PDF) for the segmentation of a nonideal iris image [11]. The applied LS method in the variational formulation speeds up the curve evolution process drastically. However, the proposed VLS method may not detect the outer boundary accurately when the iris/sclera region is separated by a relatively blurred boundary. Furthermore, the intensity inhomogeneity is another source of noise that can be found in most of the nonideal iris images due to reflections, motion blur, luminosity, etc. Thus, finally, a Region-based Active Contour (RAC) model is deployed to segment the nonideal iris images with intensity inhomogeneity [12]. Then, we apply the Daubechies Wavelet Transform (DBWT) to extract the textural features from the normalized iris images. GAs are deployed again to select the subset of informative texture features by combining the valuable outcomes from the multiple feature selection criteria without compromising the recognition accuracy. To speed up the matching process and to control the misclassification errors, we apply a combined approach called the 'AASVMs' [7, 13]. Fig. 1.2 demonstrates this approach.

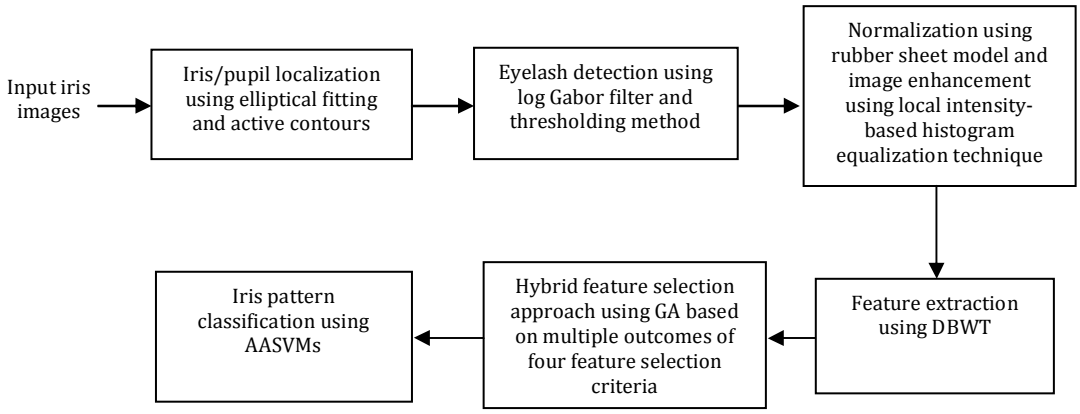

Fig. 1.2 Block diagram of the proposed iris recognition system (second phase-1st approach).

The region-based segmentation methods perform better against different noise factors and are less affected by the blurred boundaries. However, these schemes suffer from poor localization and over-segmentation. The boundary-based segmentation approaches, on the other hand, exhibit a better localization performance and demonstrate better results against the shape variations. However, the boundary finding methods are highly sensitive to noise since they depend on gradient values regarding boundary points. Therefore, in the second approach of the second phase, we apply a parallel game-theoretic decision making procedure by modifying Chakraborty and Duncan's algorithm [14, 15], which integrates: (1) the region-based segmentation and gradient-based boundary finding methods, and (2) fuses the complementary strengths of each of these individual methods. In this approach, we deploy the elliptical fitting technique again to approximate the pupil boundary and centre values, prior to applying the GT-based method. Moreover, in order to improve the quality of the iris image, we apply a two-step image enhancement technique based on the local intensity-based histogram equalization

and 2D Wiener filter. A simple Hausdorff Distance (HDD) is used for iris template matching. Fig. 1.3 demonstrates this approach.

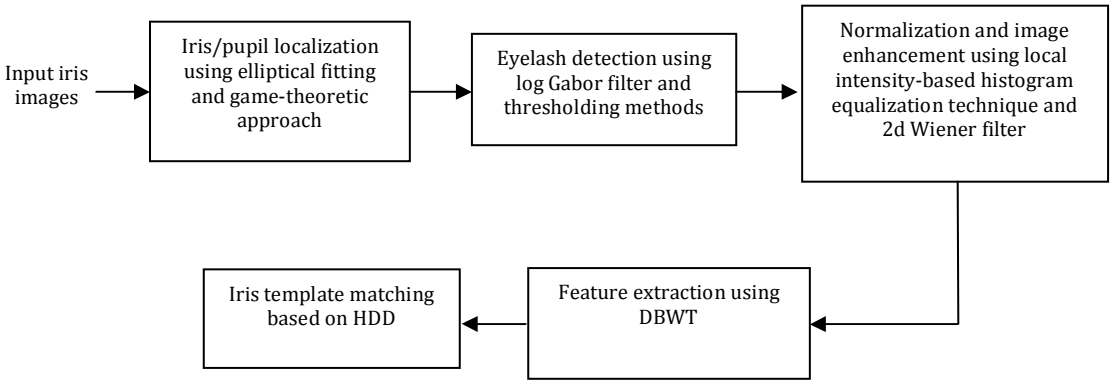

Fig. 1.3 Block diagram of the proposed iris recognition system (second phase-2nd approach).

The game-theoretic method proposed above may not handle the eyelid occlusion problems properly and fail to detect the limbic boundary in the presence of severe noise. Therefore, in the third approach of second phase, for outer boundary detection, we integrate the shape prior information of the iris region to be segmented with the gradient-based and region-based data. In this approach, a variational model is applied to localize the iris region belonging to a given shape space by using the active contour method, a geometric shape prior and the Mumford–Shah functional [16]. This variational model is robust against noise, poor localization, shape variation and weak iris/sclera boundaries. The inner boundary is estimated by using the elliptical fitting method. The extracted iris boundaries are not exactly circular and may be in any kind of shapes. Therefore, to solve this size irregularity, a simple boundary point connection method is deployed. Furthermore, we apply the Modified Contribution-Selection Algorithm (MCSA) for iris feature

ranking based on the Multi-Perturbation Shapley Analysis (MSA), a framework which relies on game theory to estimate the effectiveness of the features iteratively and select them accordingly, using either forward selection or backward elimination schemes [17]. Fig. 1.4 shows the block diagram of this approach.

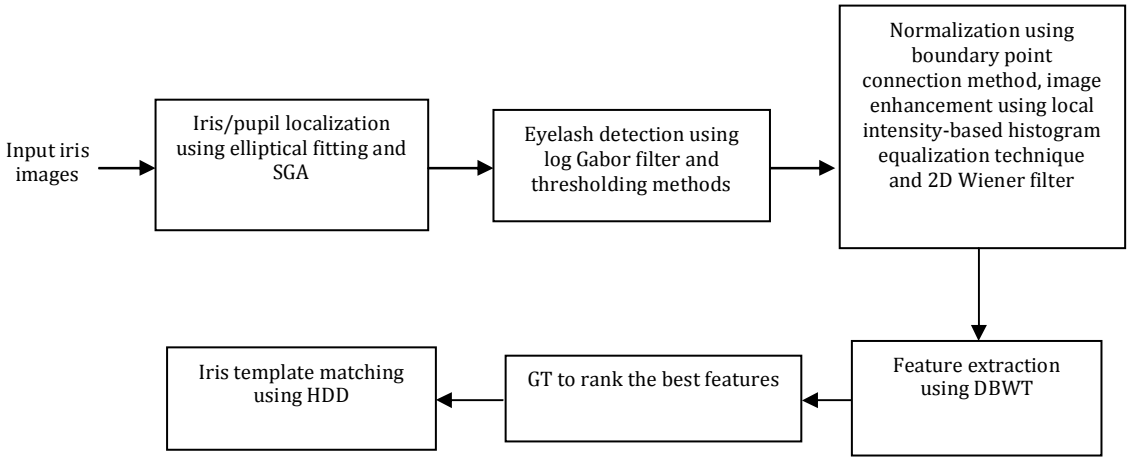

Fig. 1.4 Block diagram of the proposed iris recognition system (second phase-3rd approach).

1.3 Thesis Contributions

In this thesis, different methods have been proposed in order to enhance the performance of an iris recognition system. The new challenges in the domain of noncooperative iris recognition are consequently addressed. The six major contributions of this thesis are listed below.

1. To localize the iris/pupil boundaries accurately, we have applied three active contour-based iris segmentation schemes that account for different nonidealities presented in the iris images. First, we applied a LS-based curve evolution scheme using the edge stopping function to isolate the inner boundary from a nonideal

iris image, and employ the curve evolution approach using the regularized Mumford-Shah segmentation model with an energy minimization algorithm to detect the outer boundary. Second, to speed up the active contour-based curve propagation process, we employ a VLS-method, which utilizes a significantly larger time step to numerically solve the evolution PDF. Finally, we deployed a RAC model in variational formulation to segment the nonideal iris images with intensity inhomogeneity.

2. GAs have been deployed to select the important texture features by combining the valuable outcomes from the multiple feature selection criteria without compromising the recognition accuracy. Here, a new fitness function has been deployed to reduce the False Accept Rate (FAR) and False Reject Rate (FRR) along with the feature dimension and matching error.
3. To speed up the iris matching process and to handle different misclassification errors, we have applied a combined classification scheme denoted as AASVMs.
4. A GT-based segmentation scheme is proposed, to localize the inner and outer boundaries from nonideal iris images. A parallel game-theoretic decision making procedure has been applied by modifying Chakraborty and Duncan's algorithm, which integrates the region-based segmentation and gradient-based boundary finding methods, and combines the complementary strengths of each of these individual methods. This unified approach is robust to different noise factors and poor localization, and is less affected by weak iris/sclera boundaries.
5. To further improve the localization performance, a variational model has been applied to localize the iris region belonging to given shape space using the active

contour method, a geometric shape prior and the Mumford–Shah functional. This variational model is robust against severe eyelid occlusions.

6. An iris feature ranking method based on GT has been deployed to estimate the effectiveness of the features iteratively and select them accordingly, using either forward selection or backward elimination approaches. This iris feature ranking method further enhances the iris recognition performance.

In subsequent chapters, we will describe each of these contributions in a greater detail.

1.4 Thesis Outline

This thesis is organized as follows:

In Chapter 2, we introduce the fundamental concepts of biometrics. Then, we provide an overview of the iris recognition methods. We also discuss the noncooperative iris recognition methods and different nonideal factors that affect the overall recognition performance.

In Chapter 3, we focus on the optimal feature selection and iris pattern classification methods. We describe a segmentation scheme based on the morphological operation, the Canny edge detection and the Hough transform along with the eyelash/eyelid detection methods. We describe the normalization scheme and illustrate a feature extraction method using 1D log-Gabor filters. The GA-based feature ranking method is then introduced and an iris pattern matching technique using asymmetrical SVMs is presented. This chapter also demonstrates the experimental validation of the proposed method.

Chapter 4 describes the three active contour-based segmentation schemes that can deal with the nonideal iris images. A hybrid feature ranking method based on GA is discussed and an iris pattern classification process using AASVMs is also described. We also provide the experimental results to show the effectiveness of our proposed system.

In Chapter 5, we describe an iris segmentation scheme, which fuses the region and gradient data using GT, for improving the performance of localization routine. The performance of the proposed segmentation scheme is also evaluated.

Chapter 6 mainly focuses on iris segmentation and feature ranking methods. A shape guided model is presented and applied to further improve the localization performance. A new normalization approach is also described. An iris feature ranking method based on GT is also introduced. We provide the experimental results to demonstrate the performance of the proposed method.

Finally, Chapter 7 concludes this thesis.

Chapter 2

The Iris as a Biometric

This chapter introduces the fundamental concepts of biometrics and the practical considerations for the utilization of the iris as a biometric. First, we briefly discuss the basics of biometrics in Section 2.1. Then, we provide a general idea on iris recognition in Section 2.2. We describe the unique structure of an iris pattern, discuss the strengths and weaknesses of the iris as a biometric, discuss the iris recognition system errors and various application areas of iris recognition, and provide an overview of a typical iris recognition system. Finally, we discuss the nonideal iris recognition, which is the main focus of this research, and different noise factors that can degrade the iris recognition accuracy in Section 2.3.

2.1 Biometrics: A Brief Introduction

Nowadays, reliable and accurate identity authentication has become necessary for many security-related applications, such as accessing privileged information, border control, national ID cards, rapid processing of passengers in airports, homeless person tracking, missing person identification, etc. The increasing needs of web-based services, such as online banking and the decentralized customer services have

resulted in the rapid development of consistent identity management systems that can accommodate a large number of individuals [18]. Recognizing an individual has been a primary interest at the core of our society for many activities where ensuring the identity and authenticity of an individual is a prerequisite. Biometric-based authentication has been receiving extensive attention over the last decade with the proliferating need for automated personal identification [3]. The term *biometrics authentication* or simply *biometrics* indicates the identification of an individual based on his or her distinctive attributes. More specifically, biometrics can be defined as the science of identifying or verifying the identity of an individual based on the physiological, chemical or behavioral characteristics of the person [4, 18].

The main task of an authentication system is to determine or verify the individual's identity. The identity authentication may be required for many other reasons. However, the major purpose, in most applications, is to prevent imposters from accessing the restricted information. The conventional methods of identification mechanisms, such as knowledge-based (e. g., passwords) and token-based (e. g., ID cards) may be lost, forged, misplaced, forgotten or compromised. Biometrics authentication provides an accurate and reliable solution to identify or verify an individual by utilizing fully automated or semi-automated techniques based on biological attributes [18, 19]. Biometric-based authentication systems are expected to perform better than the conventional identification methods because they depend on *who you are* rather than on *what you possess*, such as an ID card, or *what you remember*, such as a password. Therefore, many traditional identification schemes based on passwords and ID cards may be replaced by the biometric-based

methods, thereby strengthening the security levels. An effective authentication should be robust enough to various malicious attacks including client, host and Trojan horse attacks, eavesdropping, repudiation, denial of service, etc., which are currently very common to the various password and token-based authentication schemes [18]. A reliable and accurate authentication against such security threats is possible by incorporating appropriate biometric traits related to a particular application. Biometric-based schemes also exhibit several advantages including negative recognition and non-repudiation over the traditional password or token-based approaches [18]. Negative recognition is the process that ensures that a specific individual is certainly enrolled in the system although the individual might refuse it. This is particularly very important in welfare distribution where multiple benefits might be claimed by an imposter under different names. Non-repudiation is an approach in which the system ensures that a certain facility that is accessed by an individual cannot be denied when using it in future. This is also important when a person using a certain computer resource claims later on that an imposter must have accessed it under a fallacious identification.

In a typical biometric identification (or verification) system, first, the biometrics data is acquired, distinctive features are extracted, a template is formed based on those extracted features, and then, a comparison of this template is made with a database of such templates associated with various identities. In the 'verification' approach, the claimed identity of an individual is compared between the extracted biometric measurements of that individual and the stored template linked with an identity to determine whether the claim is true or false. The 'identification'

approach, on the other hand, is based only on extracted biometric measurements. The system compares such extracted measurements of an individual to the entire database of enrolled individuals instead of just comparing a single record associated with some identifier [4]. Biometric-based authentication systems utilize various kinds of physiological and behavioral attributes (see Fig. 2.1) including the iris, face, retina, hand geometry, fingerprint, palmprint, signature, gait, keystroke pattern, mouse movement behavior, voice pattern, ear, hand vein, odor or the DNA information to identify an individual [18]. Among all the biometric traits, the iris has been regarded as one of the most reliable and accurate biometric modalities due its

Face Ear Hand geometry Iris

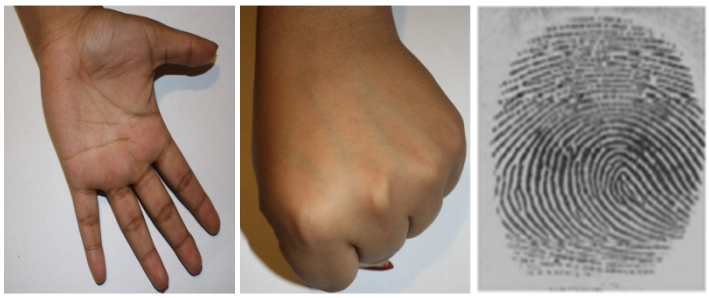

Palmprint Vein pattern Fingerprint

(a)

Gait Keystroke pattern Signature

(b)

Fig. 2.1 Examples of different biometric traits: (a) physical traits, and (b) behavioral traits.

inherent properties, i.e., stability in a lifetime, selectivity and reliability. The richness of texture details in iris images, such as freckles, coronas, crypts, furrows, etc., and the stability of an iris pattern throughout a person's lifetime make it the most consistent biometric trait for person authentication. In the next section, we will discuss the iris biometrics in detail, which has been exploited as a research topic with recognition in this research endeavor.

2.2 Iris Recognition: An Overview

Iris recognition is, perhaps, the most robust biometrics method for person authentication. It has been deployed successfully in many large-scale biometric-based identity management systems where the accurate authentication of a person's identity is a critical issue. Examples of such large-scale systems include: border management systems, accessing the networked computer resources, boarding a commercial flight, accessing the home appliances remotely, gaining access to nuclear facilities, performing a bank transaction, etc [20, 21]. Several crucial factors

of iris biometrics include rich and unique textures, noninvasiveness, stability of iris pattern throughout the person‘s lifetime, public acceptance, availability of user friendly capturing devices. These factors have attracted the researchers to work in this evolving field over the past decade. The human iris, an annular part between the pupil and the white sclera (see Fig. 2.2), has an extraordinary structure and

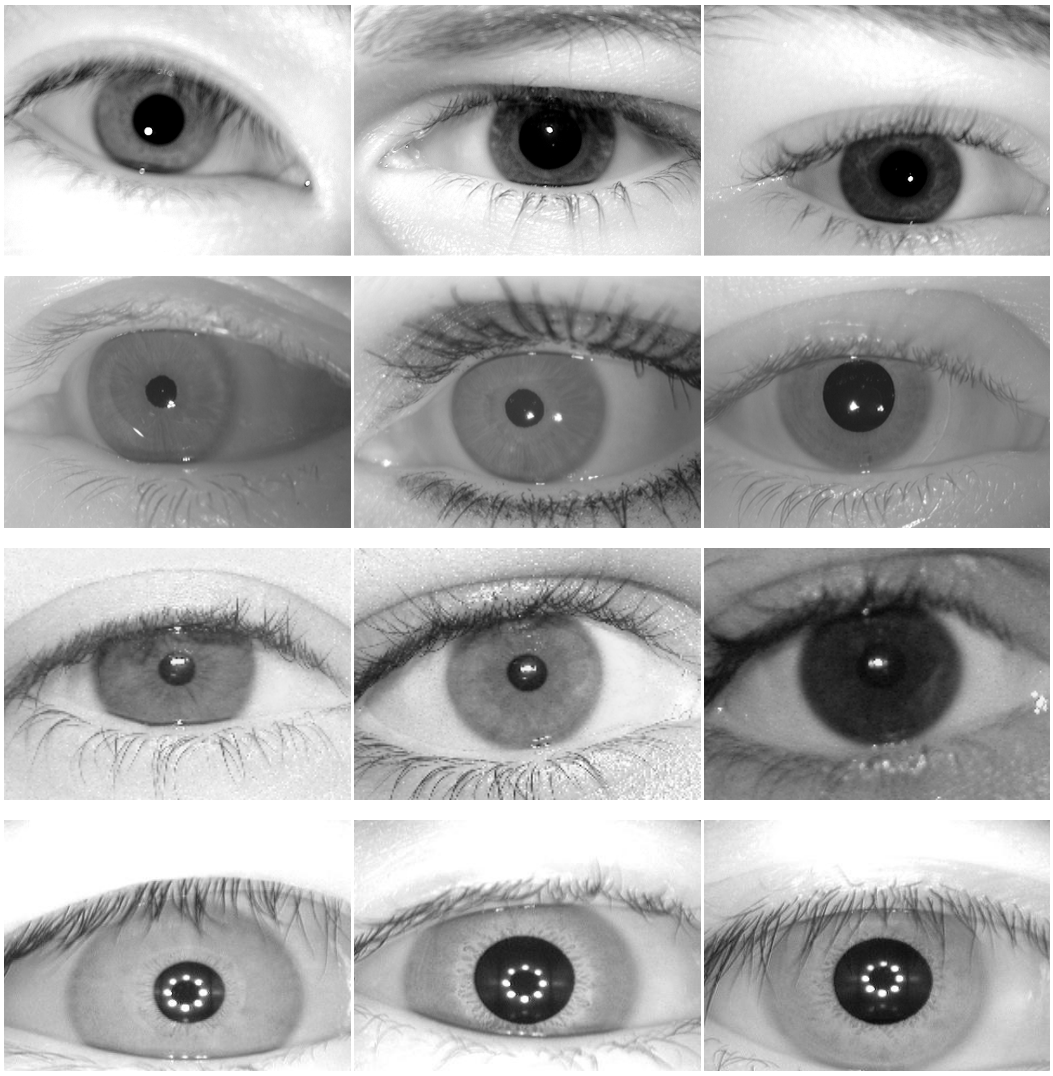

Fig. 2.2 Samples of iris images.

provides many interlacing minute characteristics such as freckles, coronas, stripes, and the pupillary area, which are unique to each subject [22]. The iris is an internal organ of the body that is readily visible from the outside and it controls the amount of light that enters the eye through the pupil, by using the dilator and sphincter muscles to control the pupil size [19, 20]. An elastic fibrous tissue that makes up the iris structure gives it a very complex and unique texture pattern. This texture pattern is independent of the genetic structure of an individual and is generated by chaotic processes [20]. The human iris begins to form in the third month of gestation and the structure is completed by the eighth month, even though the color and pigmentation continue to build throughout the first year of birth [19, 20]. After that, the structure of the iris remains stable throughout a person's life, except for direct physical damage or changes caused by eye surgery [20]. This makes the usage of an iris pattern to be as unique as the fingerprint, however, a further advantage is that it is an internal organ and is less susceptible to damages over a person's lifetime. In Fig. 2.3, we can see the anatomy of a human eye, and Fig. 2.4 shows the iris anatomy. The iris anatomy is more relevant to the proposed iris recognition methodologies. Thus, we briefly discuss the key visible features, as annoted in Fig. 2.4 [21], below.

Medial canthus: The angle between the upper and lower eyelids near the centre of the face.

Sclera: The white region of an eye image.

Pupil: The darkest part of an eye image.

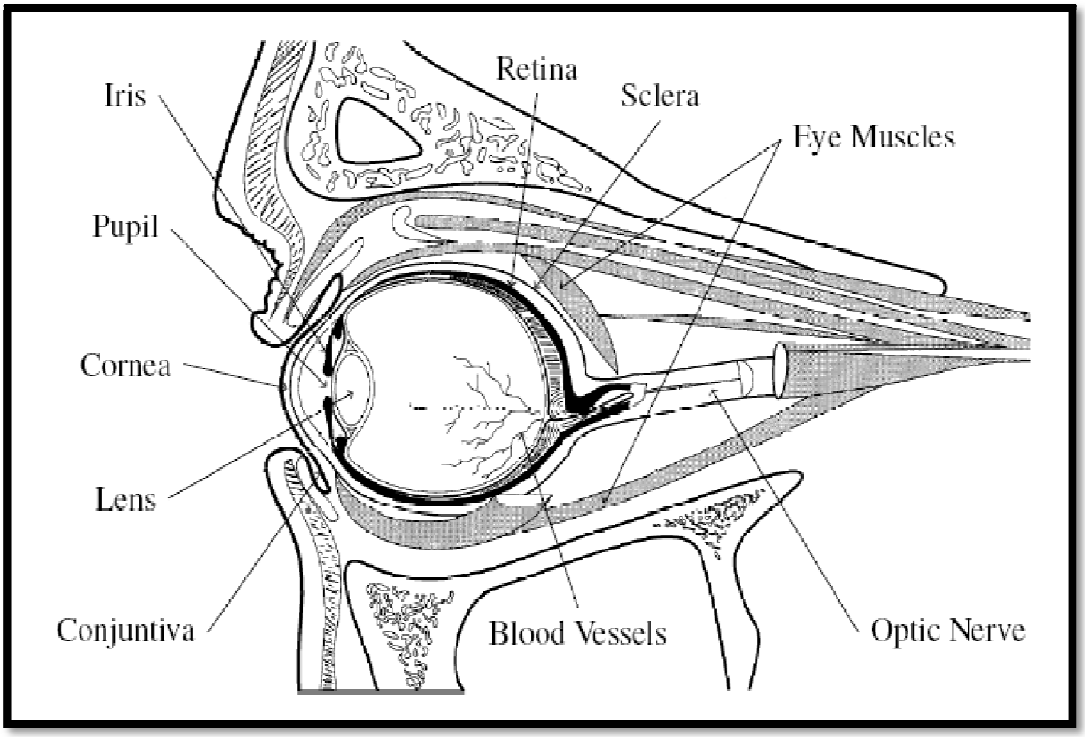

Fig. 2.3 Eye anatomy (adapted from [23, 24]).

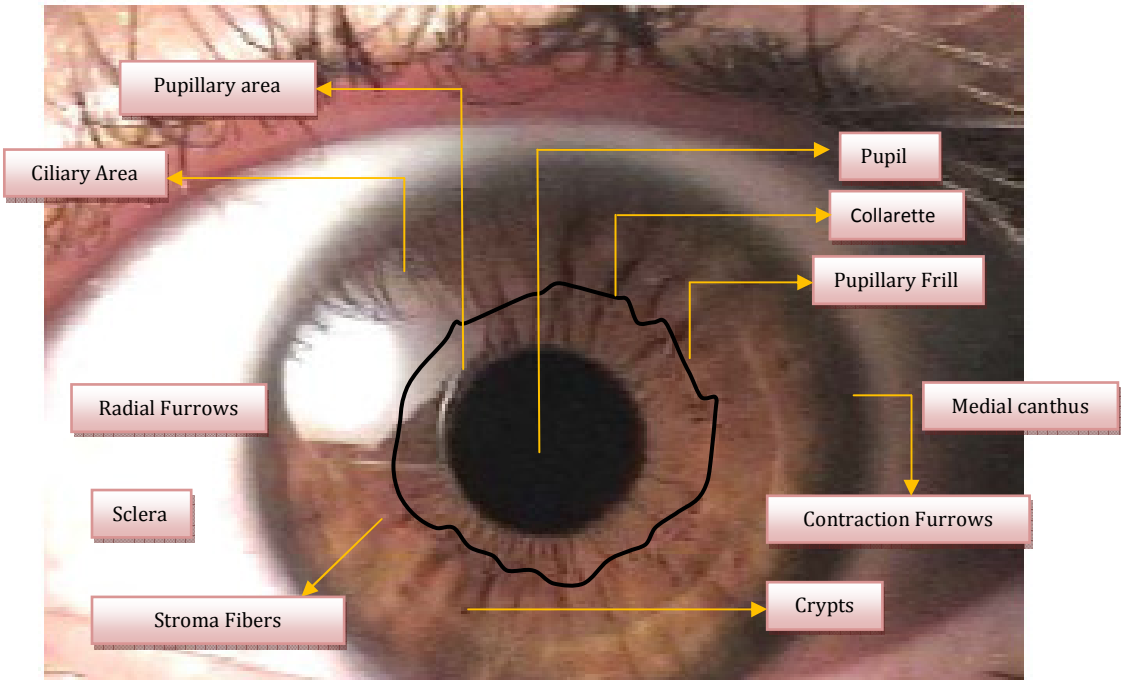

Fig. 2.4 Iris anatomy (adapted partially from [21]).

Pupillary Area: The inner part of the iris whose edges form the contour of the pupil. This is the region of sphincter muscles that close the pupil residing in this zone.

Ciliary Area: The iris region from the pupillary area to the ciliary body. This is the region of dilator muscles that open the pupil residing in this zone.

Stroma Fibers: The pigmented fibro vascular tissue that constructs most of the visible iris region.

Crypts and Furrows: The two types of inconsistencies that are usually found in the distribution of stroma fibers.

Collarette: The region that divides the pupillary area from the ciliary area.

Next, we discuss the typical iris recognition system (Section 2.2.1), iris recognition system errors (Section 2.2.2), strengths and weaknesses of the iris as a biometric (Section 2.2.3), and also describe the various application areas of iris biometrics (Section 2.2.4).

2.2.1 A Typical Iris Recognition System

Fig 2.5a shows a diagram of a typical iris recognition system. It has three major building blocks [20]:

- Iris Image Acquisition: Image acquisition is considered as the most critical step for the development of an iris recognition system since all the subsequent stages depend highly on the image quality. A specifically designed sensor is used to capture the sequence of iris images. An iris image capturing device considers the

following three key factors [19]: 1) the lighting of the system, 2) the position of the system, and 3) the physical capture system.

- Iris Liveness Detection: In order to avoid the forgery and the illegal usage of iris biometric features, the detection of iris liveness ensures that the captured input image sequence comes from a live subject instead of an iris picture, a video

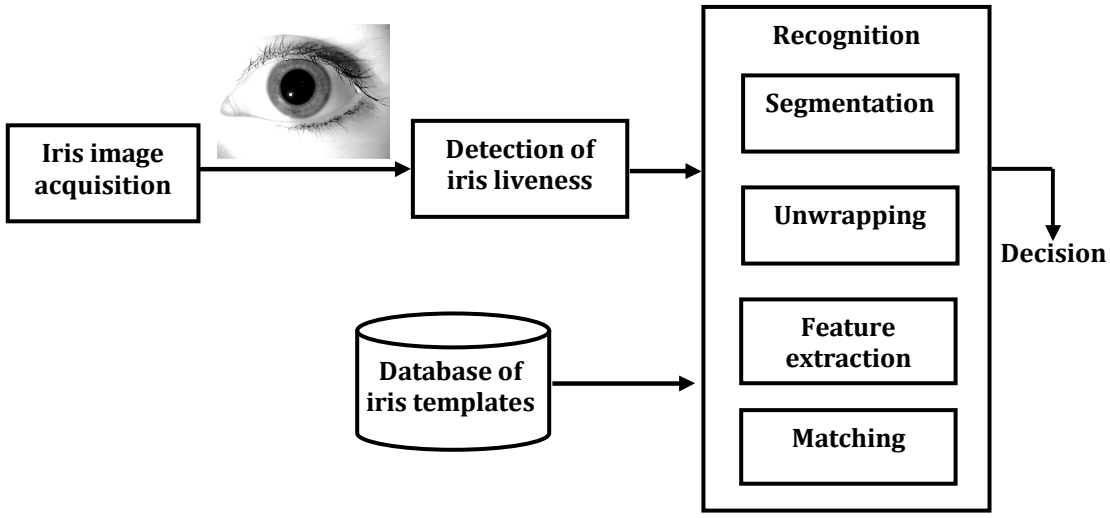

(a)

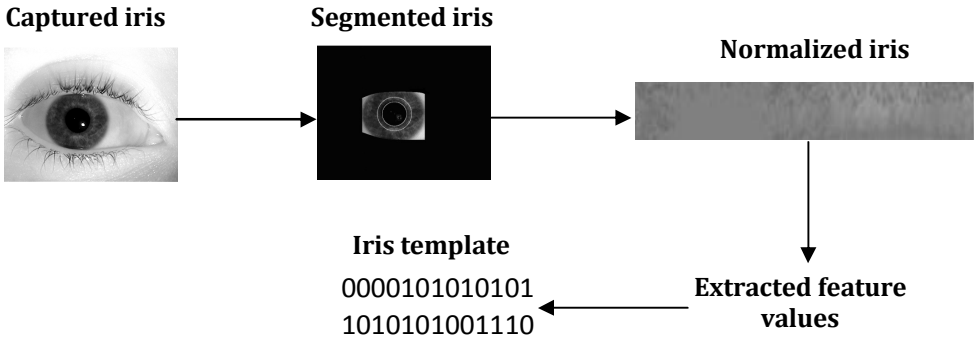

(b)

Fig. 2.5 Iris Recognition: (a) stages of a typical iris recognition system, and (b) recognition stage in greater detail.

sequence, a glass eye, and other artifacts. The utilization of the optical and physiological characteristics of the live eye is considered as the most important aspects for the assurance of the liveness of the input iris image sequence.

- Recognition: The accuracy of the iris recognition system depends on this module. This module can be further subdivided into four main phases: segmentation, normalization or unwrapping, feature Extraction, and matching. In the first phase, the iris region is segmented from the captured eye image. Secondly, the segmented iris region is unwrapped in order to avoid the size inconsistencies. Thirdly, the most discriminating features are extracted from the unwrapped image and finally, the extracted features are used for matching with the iris templates already stored in the database.

2.2.2 Iris Recognition System Errors

The following terminologies are vastly used to estimate the errors of an iris recognition system [20]:

- False Accept (FA): Accepting an imposter as an authorized subject. The probability at which the false accept errors occur is called the False Accept Rate (FAR).
- False Reject (FR): Rejecting an authorized subject incorrectly. The probability at which the false reject errors occur is denoted as the False Reject Rate (FRR).

- Equal Error (EE): When the FA and FR are equal, the error is referred to as Equal Error (ER) and the probability at which FAR=FRR, is called the Equal Error Rate (EER).

Generally, the verification performance of an iris recognition system can be demonstrated by using the Receiver Operator Characteristics (ROC) curve. If the functions *FAR (t)* and *FRR (t)* provide the error rates when the recognition decision is made at a threshold *t*, then the ROC curve is used to plot the error rates against each other [20], where:

$$ROC(t) = (FAR(t), FRR(t)) \tag{2.1}$$

The FAR and FRR are mapped as a function of *t*:

$$ROC(t) = (FAR(t), FRR(t)) \rightarrow \begin{cases} (1,0) & when \quad t \rightarrow -\infty \\ (0,1) & when \quad t \rightarrow \infty \end{cases} \tag{2.2}$$

which implies that if the *t* is high, then the FRR is high and the FAR is low and conversely when *t* is low, the FAR is high and the FRR is low.

2.2.3 Strengths and Weaknesses of the Iris as a Biometric

Among all of the biometric traits, the iris has been considered as the most accurate and reliable. However, it has some intrinsic pitfalls that cannot be ignored. The major strengths and weaknesses of the iris as a biometric are discussed respectively in Sections 2.2.3.1 and 2.2.3.2 [20].

2.2.3.1 Strengths of Iris Biometrics

- The iris patterns have small intra-class variability.
- The iris is well protected and an internal organ of the eye. It contains a high degree of randomness [25].

- The iris is externally visible and the iris image acquisition is possible from a distance [25].
- The iris pattern remains stable throughout the lifetime of a person and it is assumed that each individual has a unique iris pattern [19].
- It is possible to encode the iris pattern and the recognition system's decidability is tractable.
- No evidence of genetic influence has been found in the structure of the iris. Therefore, the iris structures in both eyes of the same person are different and those of identical twins are also different [19].
- Iris recognition systems incur extremely low maintenance costs and offer seamless interoperability between different hardware vendors, and this technology also has the ability to work well with other applications.

2.2.3.2 Weaknesses of Iris Biometrics

- It is difficult to capture the iris image since the size of the iris is very small (its approximate diameter is 1 cm). A specialized camera with an extensive apparatus setup is needed to acquire the iris images.
- The iris could be partially occluded by lower and upper eyelids, and obscured by eyelashes, reflections, and lenses [19, 25).
- As the size of the pupil changes, non-elastic deformation is another drawback [19, 25].

2.2.4 Applications of Iris Recognition

Fig. 2.6 shows various applications where iris recognition systems have been deployed. We can categorize these application areas into three main groups [18]:

- Commercial applications including accessing secured information on the internet, credit card authentication, performing online transactions, e-commerce, mobile and wireless-based devices, controlling the physical access to a secured location, distance learning, and managing medical records.
- Forensic applications including criminal investigations, corpse identification, and parenthood determination [18].
- Government applications that include a driver's license, homeland security, welfare distribution, border management, e-passports, social security, and national ID card.

2.3 Nonideal Iris Recognition: A New Challenge

Most current iris recognition algorithms are very effective in a cooperative environment, with an inflexible image capturing setup and they exhibit a very high recognition accuracy. However, their performance is greatly affected when the iris images are captured in an unconstrained situation and are partially occluded by eyelids, eyelashes, and shadows. The iris image can also be affected by specular reflections when an individual wears glasses. Moreover, the inner and outer boundaries of the iris may not maintain any particular shapes and therefore, the segmentation performance will be decreased if those boundaries are not accurately detected and modeled using a more flexible and generalized segmentation method.

(a) (b) (c)

(d) (e) (f)

Fig. 2.6 Iris recognition systems have been deployed in various applications [25] (images were extracted from the home page of Dr. John Daugman who is a Professor of Computer Vision and Pattern Recognition, University of Cambridge, UK: http://www.cl.cam.ac.uk/~jgd1000/): (a) Iris Recognition Immigration System ("IRIS") at several UK airport terminals, (b) controlling access to the premises, (c) child project, (d) enrolment of frequent flyers at Schiphol Airport, Netherlands, (e) the check-in procedure for passengers at Narita Airport, Japan, and (f) the United Nations High Commission for refugees is administrating cash grants to refugees returning into Afghanistan from surrounding countries at the Pakistan-Afghanistan border.

Other challenges include defocusing, motion blur, poor contrast, lighting reflections, oversaturation, camera diffusion, head rotation, gaze direction, camera angle, pupil dilation, etc. Thus, the nonideal conditions contained in iris images can affect the iris segmentation performance considerably, and may consequently influence the overall recognition accuracy. Therefore, it is desirable to design an accurate and robust iris recognition method that can cope with such noise factors and thereby increase the iris recognition accuracy. Several nonideal factors are described in the following subsection.

2.3.1 Nonideal Factors That Degrade the Iris Recognition Performance

In this subsection, we detect and discuss several nonideal factors that can substantially degrade the overall iris recognition performance. The most common noise factors usually arise in a less constrained imaging environment, where the images are acquired at a distance, or on the move, or under varying lighting conditions or under less user cooperation. The nonideal factors that may affect the matching accuracy include eyelid and eyelash occlusions, motion blur, specular reflections, lighting reflections, off angle gazes, poor focus, low image contrast, partially captured iris images, fully and partially closed eyes, arbitrary shaped iris/pupil boundary, etc. Nine common noise factors are discussed below in greater detail.

(1) Eyelid Occlusions: The upper eyelid and lower eyelid may occlude the significant portion of the iris, especially in its extreme vertical position (See Fig. 2.7).

Fig. 2.7 Iris region is occluded by upper and lower eyelids.

The eyelid occlusion can also occur in the lower portions of the normalized iris images.

(2) Eyelash Occlusions: Eyelashes are divided into two types, namely: The separable eyelashes and the multiple eyelashes [26]. Separable eyelashes are isolated in the eye image (See Fig. 2.8), and multiple eyelashes are bunched together and overlapping in the eye image (See Fig. 2.9).

(3) Specular Reflections: This type of reflection may occur within the iris region and may corrupt the significant portion of the iris pattern, the pupil and the cornea. The specular reflections are usually caused by imaging under natural light (See Fig. 2.10). Since a large portion of the population wears spectacles, this may cause too much specular reflection which results in the failure of automatic segmentation and/or recognition.

(4) Lighting Reflections: This type of reflection may occur due to artificial light sources that are close to the subject, and also under natural lighting conditions. These reflections are highly heterogeneous in nature as they can appear with a

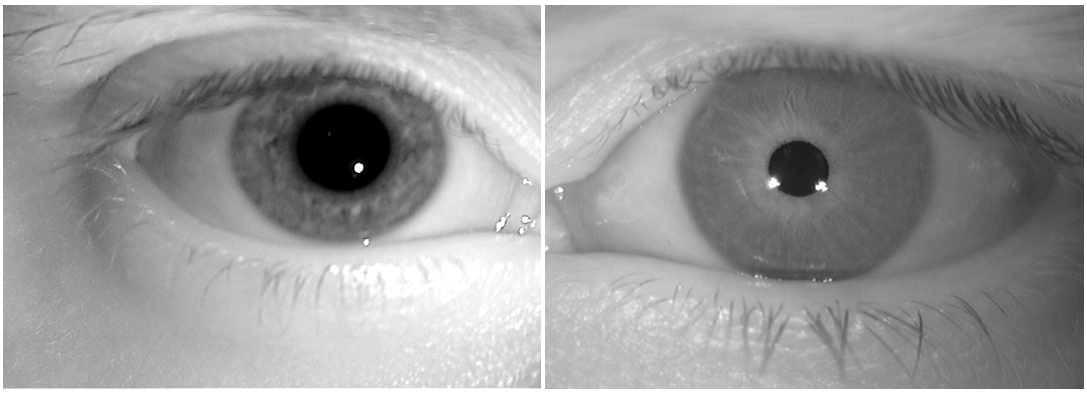

Fig. 2.8 Iris region is occluded by separable eyelashes.

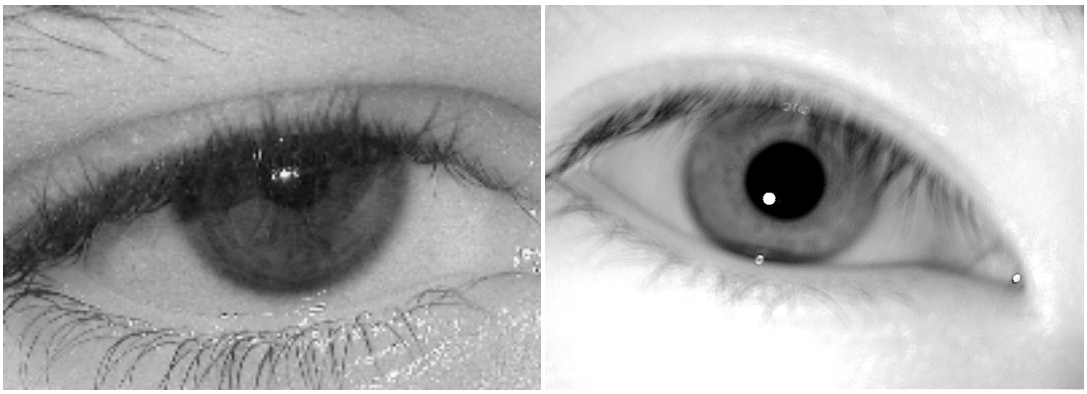

Fig. 2.9 Iris region is occluded by multiple eyelashes.

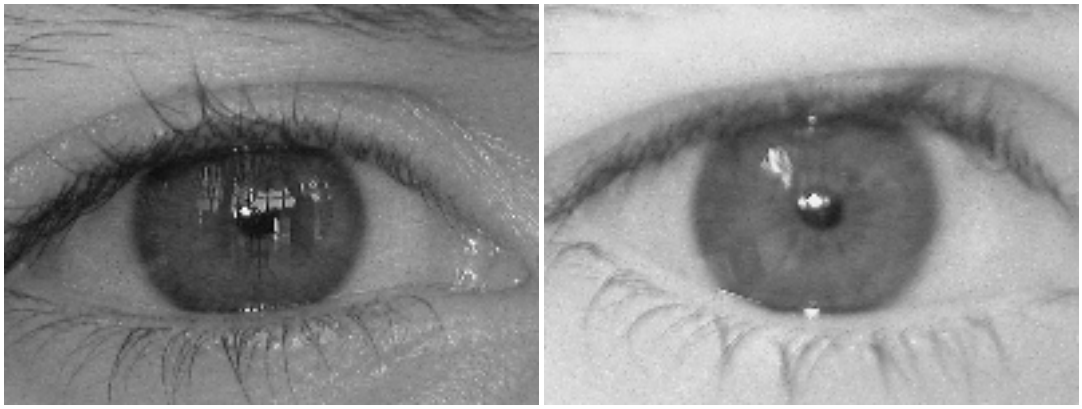

Fig. 2.10 Iris and pupil regions are occluded by specular reflections.

broad range of dimensions and can be located in different regions of the iris [24] (See Fig. 2.11). The occluded areas of the iris can typically have relatively higher intensity values than the areas affected by specular reflections.

(5) Poor Focus: The poor focus has been a critical issue for accurate iris segmentation. This may occur due to moving objects that may interact with the camera in the less constrained capturing setup and to the limited depth-of-field of any imaging system [24]. A small deviation in the distance between the eye and the camera position may create severe focus problems and this subsequently increases the FRR. Fig. 2.12 shows the defocused images.

(6) Completely Closed and Partially Opened Eyes: The completely closed eye is a severe noise factor that prevents any kind of recognition (See Fig. 2.13). If the eyes are partially opened, signification portions of the iris cannot be extracted due to occlusion, which further affects the segmentation performance (See Fig. 2.14).

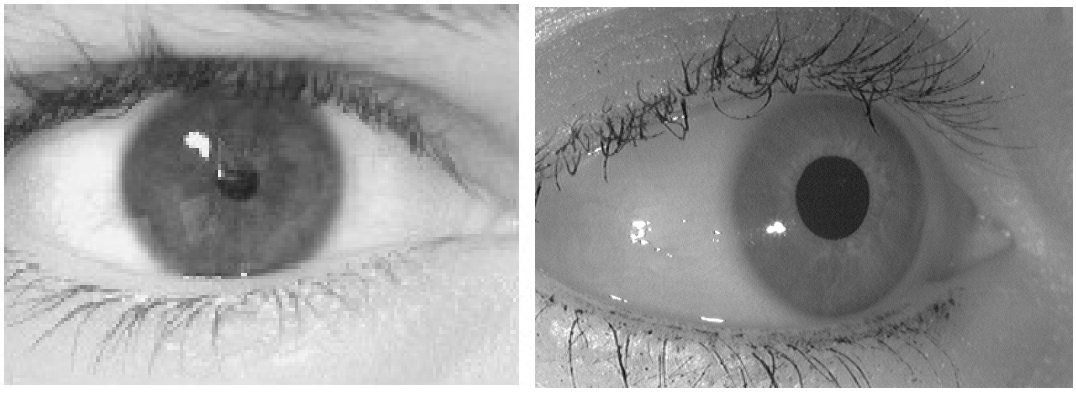

Fig. 2.11 Iris and pupil regions are occluded by lighting reflections.

Fig. 2.12 Iris images are affected by poor focus.

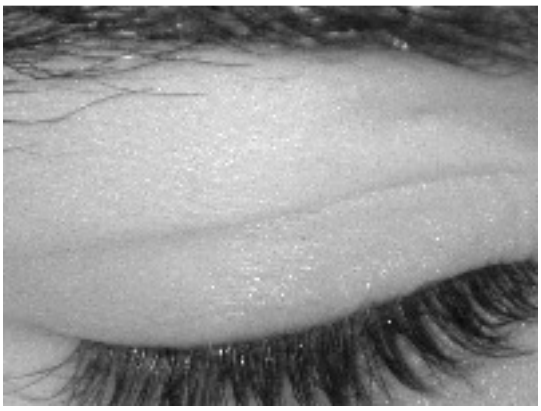

Fig. 2.13 Completely closed eye.

Fig. 2.14 Partially opened eyes.

(7) Off Angle Gaze: This type of noise usually occurs when the subject's optical axis is not aligned with camera's optical axis. The iris images with deviated gazes

may be of elliptical shapes. The projection techniques or flexible contour fitting methods can be used to deal with the off angle iris images. Fig. 2.15 shows two samples of off angle iris images.

(8) Motion Blur: The iris images captured in a noncooperative imagery setup, where the subject or camera is moving, may be affected by motion blurs. The eyelid movement is another source which significantly contributes to this type of noise [24](See Fig. 2.16).

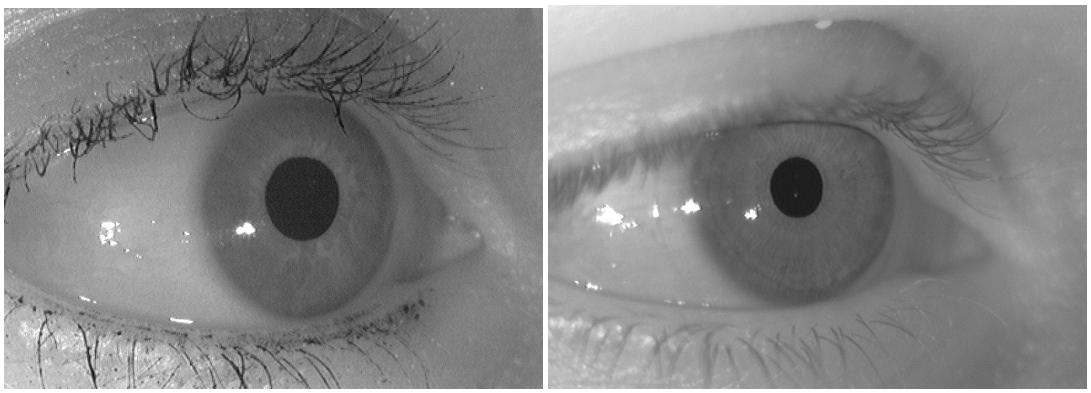

Fig. 2.15 Off angle iris images.

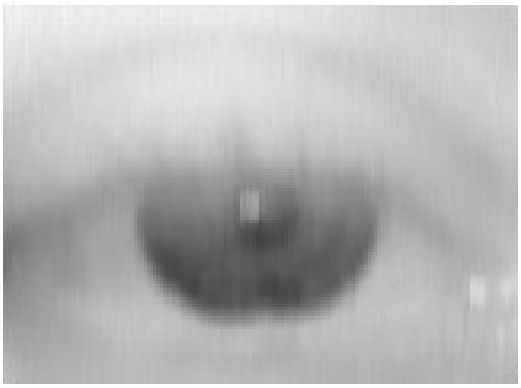

Fig. 2.16 Iris image is affected with motion blur.

(9) Nonelliptical/Noncircular Shapes of the Iris/Pupil: The pupil and limbic boundaries often have arbitrary shapes. Therefore, if these boundaries are fitted with some simple shape assumptions, then this can lead to inaccurate segmentation results.

2.4 Conclusion

In this chapter, first, we present the basic concept of the biometrics. Then, an overview of iris recognition is provided. We briefly discuss the iris anatomy, the different stages of a typical iris recognition system, the common system errors related to iris recognition, the advantages and disadvantages of the iris as a biometric, and we also highlight various application areas. Finally, we describe the nonideal iris recognition, which is the main focus of this thesis, and discuss the different noise factors that can degrade the iris recognition performance drastically.

Chapter 3

Optimal Feature Selection and Classification for Iris Recognition

In this chapter, we present our first method for iris recognition, which mainly focuses on iris feature selection and pattern classification. In Section 3.1, we briefly introduce the background of the problem. Then, in Section 3.2, we present related work around this problem. After that, in Section 3.3, we describe the preprocessing methodology, which isolates the iris/pupil boundary from the eye image. The feature extraction process is discussed in Section 3.4, and in Section 3.5, a feature selection strategy, based on GAs, is presented. Section 3.6 first introduces the iris pattern matching technique using asymmetrical SVMs. Then, the SVM parameter selection process is discussed. The experimental results are provided in Section 3.7. Finally, Section 3.8 summarizes the key points of this chapter.

3.1 Introduction

With the increasing demand for enhanced security, iris biometrics-based personal identification has become an interesting research topic in the field of pattern recognition [27-46]. While most state-of-the-art iris recognition algorithms have

focused on the preprocessing of iris images, recently, important new directions have been identified in iris biometrics research. These include optimal feature selection and iris pattern classification. In this chapter, we propose an iris recognition scheme based on GAs and asymmetrical SVMs. Instead of using the whole iris region, we elicit the iris information between the collarette and the pupil boundary to suppress the effects of eyelid and eyelash occlusions and to minimize the matching error.

The selection of the most representative feature subset from the original feature set, with a relatively high dimension, is an important issue in the field of iris recognition [43]. The iris data usually contains a huge number of textural features and comparatively a small number of samples per subject, and this makes accurate and reliable iris pattern classifications difficult [44-46]. In general, the feature selection scheme is used to select the most important features from the extracted feature sequence of a higher dimension. The traditional feature selection schemes (like *the Principal Component Analysis (PCA), Independent Component Analysis (ICA), Singular Value Decomposition (SVD),* etc.) require a sufficient number of samples per subject to select the salient feature sequence. However, it is not always realistic to accumulate a large number of samples due to some security issues. Also, the feature subset selection presents a multi-criterion optimization problem, e.g. in selecting the number of optimal features and in achieving a reasonable classification accuracy in the context of practical applications such as iris recognition. The GAs suggest a particularly attractive approach in solving this kind of problem since they are generally quite effective in a rapid global search of large, non-linear and poorly understood spaces [47, 48]. Therefore, we have applied GAs to select the optimal

feature subset from the extracted feature sequence. Our experimental results have exhibited that the proposed technique of feature selection using GAs performs reasonably well, even when the sample proportion between two classes is poorly balanced. Moreover, the proposed GA-based scheme shows an outstanding performance in the case when the iris dataset contains a high-dimensional feature set with a relatively smaller sample size.

SVMs have been used successfully in a number of classification studies due to their outstanding geometrical interpretation in discriminating one class from the other by a separating hyperplane with the maximum margin for the binary cases [49]. With SVMs, the classification accuracy can be estimated by their expected misclassification rate on the target dataset. Therefore, it is assumed that the costs for different types of misclassification error are the same. However, this assumption is not always the case in many real world situations [7]. The two cases in which the above-mentioned assumptions are not valid are described as follows: The first case is the sample ratio bias. Under some conditions, especially in the one-versus-rest condition, the sample proportion between two classes is highly unbalanced. The second case is such that the different types of misclassification error may have different costs, which can lead to different misclassification losses [7, 46, 50]. Most of the iris datasets suffer from the unavailability of sufficient iris samples per subject. Therefore, we have adopted the asymmetrical approach of SVMs by taking into account the above-mentioned issues. The proposed classification scheme with asymmetrical SVMs is well suited for different datasets (like the ICE 2005 [189] and the WVU Nonideal [192] datasets), where the number of samples per subject is not

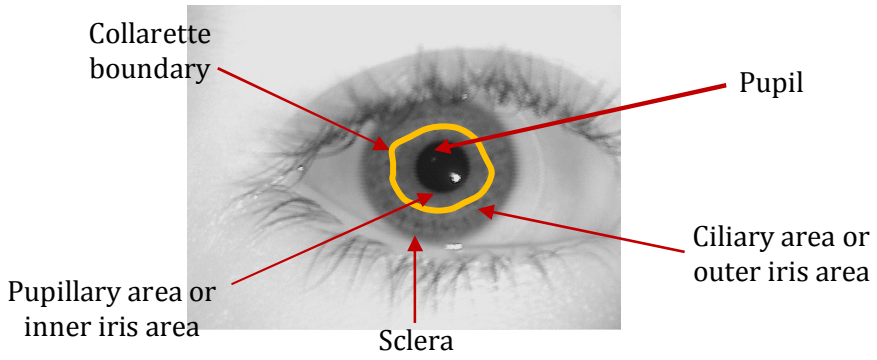

(a)

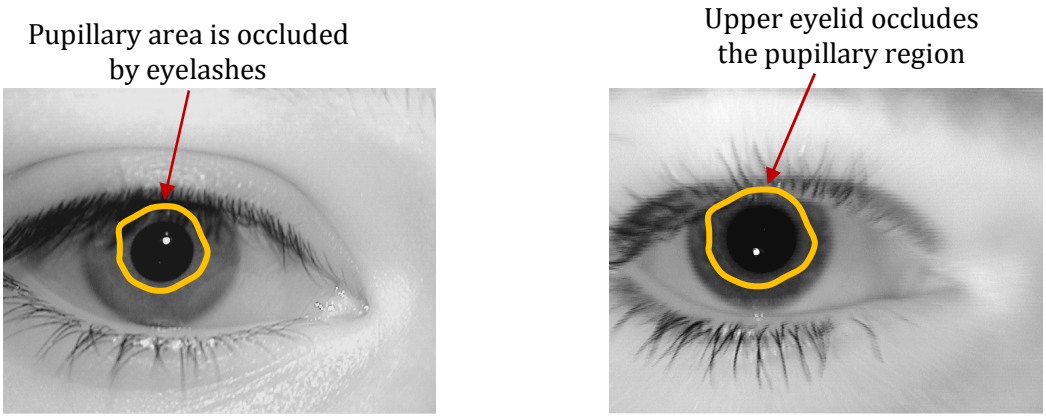

(b) (c)

Fig. 3.1 (a) Pupillary or inner iris region is indicated on a sample iris image, (b) pupillary area is occluded by eyelashes, and (c) upper eyelid occludes the pupillary region.

fixed. See Appendix A for the details about the datasets. In this chapter, we also present an iris segmentation approach based on the pupillary area, a region between the pupil and collarette boundaries (See Fig. 3.1), along with eyelid, eyelash, and noise detection techniques. We have conducted our experiments on two iris datasets, namely, the WVU Nonideal [192] and the ICE 2005 [189].

3.2 Related Work

The usage of iris patterns for personal identification began in the late 19th century; however, major investigations on iris recognition started in the last decade. Daugman [27-30] used the integrodifferential operator to segment the iris. The 2D Gabor wavelets were used for feature extraction and the Hamming Distance (HD) was used for matching. In [22], the quality of each image of an input sequence was assessed and a clear image was selected from such a sequence for further recognition. The local characteristics of the iris were captured to produce the discriminating textural features, using a bank of spatial filters whose kernels were suitable for iris recognition. Fisher's linear discriminant was used to reduce the dimensionality of the feature vector. Then, the nearest centre classifier was adopted for classification. In [31], an iris recognition approach based on characterizing key local intensity variations was proposed. The basic idea was to use the local sharp variation points to represent characteristics of the iris. Feature extraction was performed by constructing a set of 1D intensity signals to isolate the most important information from the original 2D image. A position sequence of local sharp variation points in such signals were captured as features, using a particular class of wavelets. A matching scheme based on the excusive OR operation was then adopted to measure the similarity between a pair of position sequences. Boles and Boashash [32] segmented and normalized the iris by using the edge detection and other image processing techniques. Wildes [33] localized the iris boundaries via edge detection followed by Hough transforms. In [34], the multichannel Gabor filter-based iris recognition scheme was proposed, and in [35], the circular symmetry filters were

used for iris recognition. In [37], the Discrete Cosine Transform (DCT) was used for iris feature extraction. In [38], the binary edge maps of irises were compared using the Hausdorff Distance (HDD). Sanchez-Avila and Sanchez-Reillo [39] developed an iris recognition scheme using Gabor filters and HD. In addition, they also worked in zero-crossing representation of the dyadic wavelet transform applied to two different iris signatures: one based on a single virtual circle of the iris and the other one based on an annular region. In [51], a modification to the Hough transform was made to improve the iris segmentation, and an eyelid detection technique was used, where each eyelid was modeled as two straight lines. A new matching method was implemented in [52], and its performance was evaluated on a large dataset. In [53], Masek applied circular Hough transform to detect the iris/pupil boundaries. The 1D log-Gabor filters were employed to extract the iris features and the HD was used for template matching.

While most of the existing iris literature is focused on the preprocessing of iris images [36], recently, there have been important new directions identified in iris biometric research. These include feature ranking and iris pattern classification. In [40], the matching accuracies of several iris pattern classifiers were combined by using the max and min rules. Also, most state-of-the-art iris recognition schemes exploit the complete information of the iris region. However, the iris area might be affected by pupil dilation, and occluded severely by eyelids and eyelashes. In [41], an iris segmentation method was proposed, where authors used the iris information between the collarette and the pupil boundaries. In [42], authors proposed a method for localizing the iris area between the inner boundary and the collarette

boundary. For finding the collarette boundary, histogram equalization and a high pass filter were applied to the image, after using a 1D Discrete Fourier Transform (DFT). The recognition rate was evaluated by using the SVMs. However, no eyelid detection scheme was deployed in [41, 42]. Thus, the schemes reported in [41, 42] seem to be vulnerable to the effect of severe eyelid occlusions. In our previous work [20], we also utilized the pupillary information instead of using the complete iris information. The inner boundary was detected using the simple chain code method. However, the chain code-based method fails to perform well on the underlying nonideal iris datasets.

Very few research studies have been conducted by using the SVMs and the GAs in the area of iris recognition. In [43], the basis of GAs was applied to develop a technique for the improvement of the performance of an iris recognition system. However, in [43], GAs were deployed for segmentation purposes. In [54], Gu et al. deployed the GAs to select the optimal features with respect to the objectives, namely, the coupling (the distance between iris samples of different classes) and the cohesion (the distance between iris samples in the same class) of iris classes. An iris recognition scheme was proposed in [55] based on the 2D wavelet transform for feature extraction, the direct-discriminant-linear analysis for feature reduction and the traditional SVMs for iris pattern classification. In [56], we developed an iris recognition method based on the SVMs where we used the information about the whole iris region for recognition and used the traditional SVMs for iris pattern classification. In [55, 56], the traditional SVMs, which may have failed to control the unbalanced nature of a class with respect to the other classes, were used for

classification. In [20], the asymmetrical SVMs were deployed to separate the cases of FA and FR. However, the SVMs applied in [20] failed to exhibit an acceptable performance in a poorly balanced sample space.

Addressing the above problems, we introduce a new iris-subject model based on the GAs and the asymmetrical SVMs. Furthermore, we use the information between the pupil and the collarette boundaries since the pupillary area is less affected by the eyelid and eyelash occlusions. We also employ the eyelid and eyelash detection techniques along with other noise reduction approaches for the improvement of the segmentation performance. A detailed survey of the different iris recognition algorithms can be found in [36]. Table 1 shows the comparison of several existing iris recognition schemes in strictly constrained situations.

3.3 Iris Image Preprocessing

First, we outline our preprocessing approach and then, we describe further details in the following subsections. The iris is surrounded by various non-relevant regions such as the pupil, the sclera, the eyelids, and also noise caused by the eyelashes, the eyebrows, the reflections, and the surrounding skin [22, 28, 31]. We need to remove this noise from the iris image to improve the iris recognition accuracy. To do this, we initially localize the pupil and iris regions in the eye image. Then, the inner iris area is isolated using the parameters obtained from the localized pupil. We also apply the eyelash, the eyelid and the noise reduction methods to the localized pupillary area. Finally, the deformation of the pupil variation is reduced by unwrapping the pupillary area to form a rectangular block of a fixed dimension [27].

Table 3.1: Comparison of the state-of-the-art ideal iris recognition algorithms.

Iris recognition approaches	Iris segmentation	Nature of features	Matching process	Quality evaluation
Daugman [27-29]	Integro-differential operator	Binary feature vector using 2D Gabor filters	HD	Good recognition rate and provides a faster iris/pupil detection process on ideal iris images
Wildes et al. [33]	Image intensity gradient and Hough transform	Laplacian pyramid to represent the spatial characteristics of the iris image	Normalized correlation	Matching process is time consuming, it may be suitable for identification phase, not for recognition
Boles and Boashash[32]	--	1D signature	Two dissimilarity functions: the learning and the classification	Relatively low recognition rate, high EER, faster matching process, simple 1D feature vector
Ma et al. [22]	Gray level information, Canny edge detection and Hough transform	1D real-valued feature vector using multichannel spatial filters with the length of 384	Nearest feature line	Relatively slow feature extraction process
Ma et al. [31]	Gray level information, Canny edge detection and Hough transform	1D real-valued feature vector using Dyadic wavelet with the length of 160	Weighted Euclidean distance	Local features are used for recognition
Monro et al. [37]	--	Zero crossings of 1D DCT	HD	Faster feature extraction process, higher recognition rates and lower EER
Masek [53]	Canny edge detection and Hough transform	1D log-Gabor filters	HD	Relatively lower recognition performance
Sudha et al. [38]	Canny edge detection and Hough transform	Binary edge maps of irises	Local partial HDD	Relatively higher recognition rate, faster matching scheme
Sanchez-Avila, and Sanchez-Reillo [39]	Integro-differential operator	Gabor filters and multiscale zero-crossing representation	Dissimilarity function related to zero-crossing representation of 1D signals	Good recognition rate on ideal iris dataset

Iris recognition approaches	Iris segmentation	Nature of features	Matching process	Quality evaluation
Liu et al. [51]	Modified Hough transform	2D Gabor wavelets	HD	Relatively higher recognition rate on complicated dataset, medium EER
Liu et al. [52]	Liner Hough transform	2D Gabor wavelets	HD	Relatively lower recognition rate
Feng et. al. [40]	--	--	Matching accuracies are combined using min and max rule	The classifier combination approach improves the overall performance
Proposed approach	Canny edge detection and circular Hough transform, pupillary region is considered for recognition	1D log Gabor filters	Asymmetrical SVMs	Relatively higher recognition rate with respect to nonideal iris datasets like ICE 2005 and WVU Nonideal, extra cost for feature selection

3.3.1 Iris/Pupil Localization

The iris is an annular portion of the eye that is situated between the pupil (inner boundary) and the sclera (outer boundary). In this chapter, both the inner boundary and the outer boundary of a typical iris are considered as approximate circles. However, the two circles are usually not concentric [22, 57]. We use the following approach to isolate the iris and pupil boundaries from a digital eye image:

1. First, we apply a morphological operation, namely, the opening to an input image to remove the noise.
2. The iris image is projected in the vertical and horizontal directions to approximately estimate the centre coordinates of the pupil. Generally, the pupil is darker than its surroundings; therefore, the coordinates corresponding to the

minima of the two projection profiles are considered as the centre coordinate values of the pupil:

$$X_p = \underset{x}{argmin}\left(\sum_y I(x,y)\right) \text{ and } Y_p = \underset{y}{argmin}\left(\sum_x I(x,y)\right) \quad (3.1)$$

where, *I(x, y)* is the input image and (X_p, Y_p) denotes the centre coordinates of the pupil.

3. In order to compute a more accurate estimate of the centre coordinate of the pupil, we use a simple intensity thresholding technique to binarize the iris region centred at *(Xp,Yp).* The centroid of the resulting binary region is considered as a more accurate estimate of the pupil coordinates. We can also roughly compute the radius, r_p, of the pupil from this binarized region.
4. The Canny edge detection technique is applied to a circular region centred at (X_p,Y_p) and with $r_p + 25$ [57]. Then, we deploy the circular Hough transform to detect the pupil/iris boundary.
5. In order to detect the iris/sclera boundary, we repeat step 4 with the neighborhood region replaced by an annulus band of a width, *R,* outside the pupil/iris boundary. The edge detector is adjusted to the vertical direction to minimize the influence of eyelids.
6. The specular highlight that typically appears in the pupil region is one source of edge pixels. These can be generally eliminated by removing the Canny edges at the pixels that have a high intensity value (For the ICE 2005 and WVU Nonideal datasets, these predefined values are 245 and 240, respectively). Edge pixels inside the iris region can also contribute to pushing the Hough transform result further away from the correct result. Therefore, this problem can generally be

eliminated by removing the edges of the pixels that have an intensity below some predetermined value like 32 and 36 for the ICE and WVU datasets, respectively. Figs. 3.2 (d, e, f) and 3.3 (d, e, f) show the localized pupils that have been segmented from the input iris images.

3.3.2 Isolation of Pupillary Area

The complex pattern of an iris provides many distinguishing characteristics such as arching ligaments, furrows, ridges, crypts, rings, freckles, coronas, stripes, and the pupillary area as discussed in the previous chapter [22, 31, 41, 42]. The pupillary area is one of the most important parts of the iris structure (See Fig. 3.1). This area is usually less affected by eyelids and eyelashes unless the iris is partly occluded [41, 42]. From the empirical study, it is found that the pupillary area is generally concentric with the pupil, and the radius of this area is restricted to a certain range [41]. In the cases of both the ICE and WVU iris datasets, the inner iris area is detected using the previously obtained centre and radius values of the pupil, as shown in Figs. 3.2 (g, h, i) and 3.3 (g, h, i). An experimental validation is provided in Section 3.7.1.

3.3.3 Detection of Eyelids and Eyelashes

Though the pupillary area is less affected by the eyelids and eyelashes, there might be a few cases where this region is partially occluded since it is close to the pupil. Thus, we deploy the noise reduction algorithms to suppress the effects of eyelids and eyelashes [26, 58]. The proposed eyelid and eyelash detection techniques can be summarized as follows:

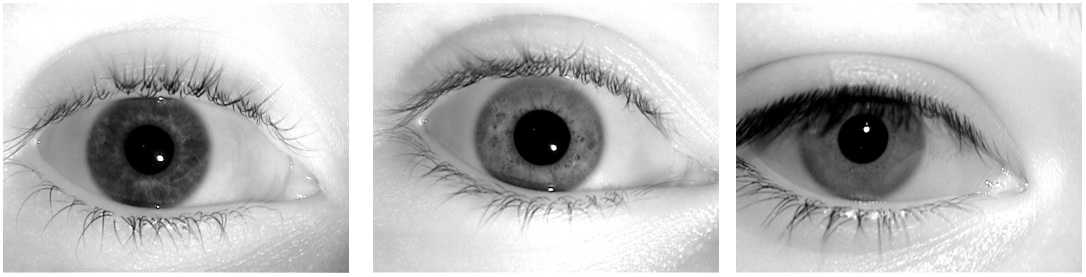

(a) (b) (c)

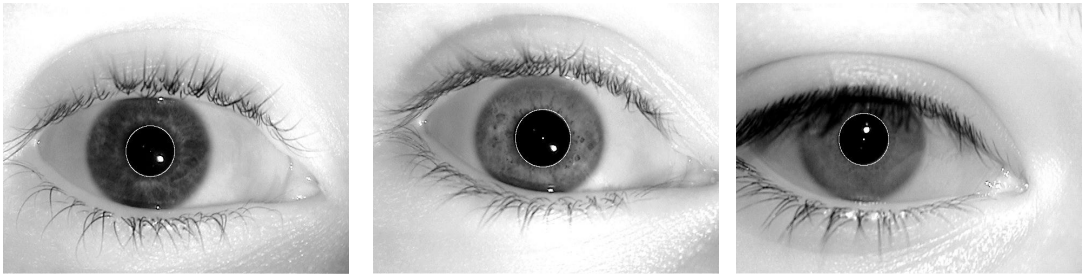

(d) (e) (f)

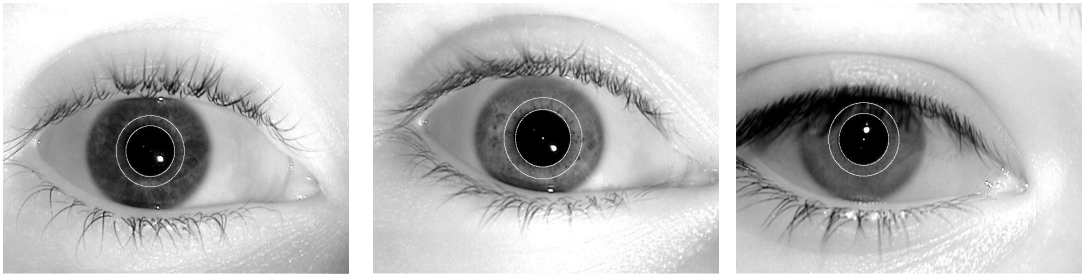

(g) (h) (i)

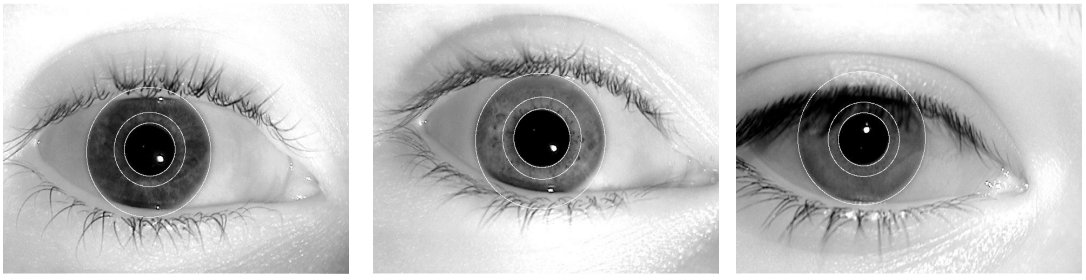

(j) (k) (l)

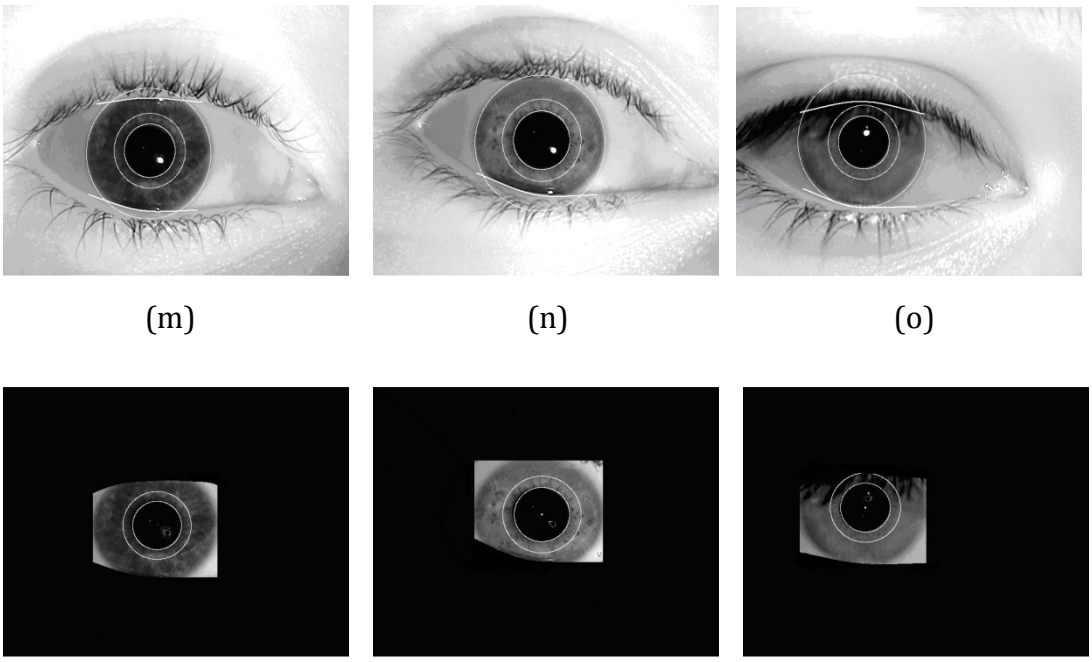

(m) (n) (o)

(p) (q) (r)

Fig. 3.2 Image preprocessing where: (a), (b), and (c) are the original iris images from the ICE 2005 dataset; (d), (e) and (f) show the corresponding localized pupil; (g), (h) and (i) represent the isolated pupillary region; (j), (k) and (l) present the localized pupillary region with the detected iris region; (m), (n), (o) reveal eyelid detection; and (p),(q), (r) show segmented images after eyelid, eyelash and reflection detection.

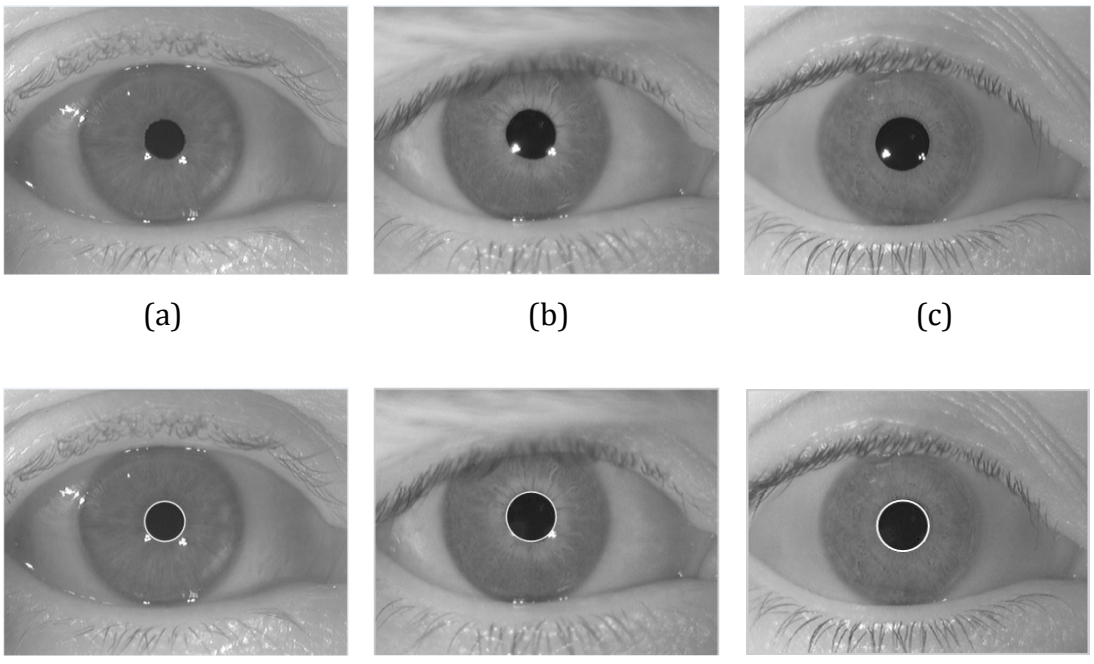

(a) (b) (c)

(d) (e) (f)

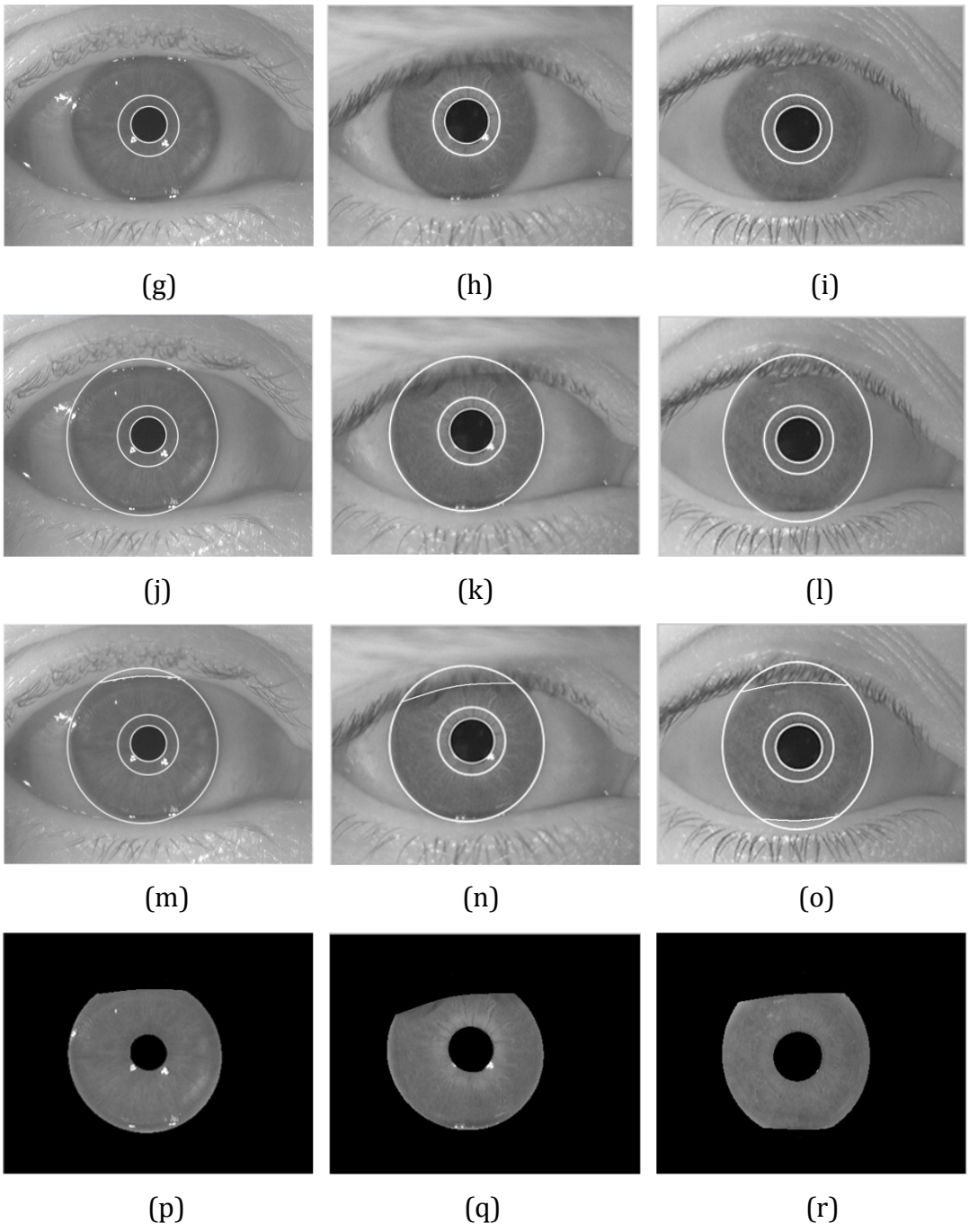

Fig. 3.3 Image preprocessing where: (a), (b), and (c) are the original iris images from the WVU Nonideal dataset; (d), (e) and (f) show the corresponding localized pupil; (g), (h) and (i) represent the isolated pupillary region; (j), (k) and (l) present the localized pupillary region with the detected iris region; (m), (n), (o) reveal eyelid detection; and (p), (q), (r) show segmented images after eyelid, eyelash and reflection detection.

1. Eyelids can be approximated as parabolic curves. Therefore, we use parabolic curves to detect the upper and the lower eyelids. Generally, the eyelids occur in the top and the lower portions of the pupil's centre. Thus, we restrict our search to those areas only. The parametric definition of a parabola is applied to construct the parabolas of different sizes and shapes. Any abrupt change in the summation of gray scale values over the shape of a parabola is estimated for various shapes and sizes of parabolas. This results in the detection of upper and lower eyelid boundaries. Figs. 3.2 (m, n, o) and 3.3 (m, n, o) show the detected eyelids.
2. There are two types of eyelashes: separable and multiple eyelashes [26]. We apply the 1D Gabor filter to detect the separable eyelashes, and the convolution of a separable eyelash with the Gaussian smoothing function results in a low output value. Thus, if a resultant point is smaller than a predefined threshold, this point belongs to an eyelash [26, 53]. Multiple eyelashes are detected by using the variance of intensity. If the values in a small window are lower than a threshold, then the centre of the window is considered as a point in an eyelash as shown in Figs. 3.2 (p, q, r) and 3.3 (p, q, r).

3.3.4 Normalization and Iris Image Enhancement

We use the rubber sheet model [27-29] to normalize or unwrap the isolated pupillary area. The centre value of the pupil is considered as the reference point. The radial vectors pass through the pupillary region [53]. We select a number of data points along each radial line that are defined as the radial resolution. The

number of radial lines passing around the region is considered as the angular resolution. A constant number of points are chosen along each radial line in order to take a constant number of radial data points, irrespective of how narrow or wide the radius is at a particular angle. The normalization approach produces a 2D array with the horizontal dimensions of the angular resolution, and the vertical dimensions of the radial resolution form the circular shaped pupillary area. In order to prevent the non-iris region data from corrupting the normalized representation, data points that occur along the pupil border or the inner iris border are discarded. Fig. 3.4 shows the unwrapping procedure. Figs. 3.4, 3.5 (a, b), and 3.6 (a, b) show the normalized images after isolation of the pupillary area from the iris images that were taken from the ICE and WVU datasets, respectively. Since the normalized iris image has a relatively low contrast and may have non-uniform intensity values due to the position of light sources, a local intensity-based histogram equalization technique is applied. This technique enhances the contrast that affects the quality of the normalized iris image, thereby increasing the subsequent recognition accuracy. Figs. 3.4, 3.5 (c, d), and 3.6 (c, d) show the effects of enhancement on the normalized iris images for the two datasets.

3.4 Extraction of Distinctive Feature Set From the Pupillary Area

In this section, we propose to apply the log polar form of 1D Gabor wavelet to elicit the textural features of iris [27, 53, 56, 59, 60]. In contrast to Gabor wavelets that are symmetric with respect to their principal axis, the 1D log polar Gabor filters show a translation of the maximum from the centre of gravity in the direction of a lower frequency and a flattening of the high frequency part. The most important

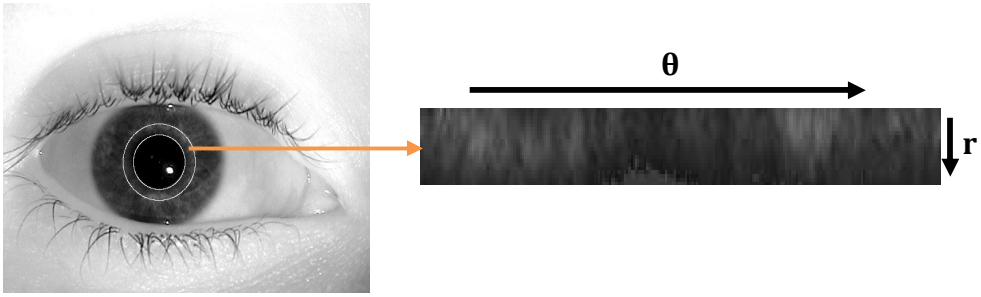

(a)

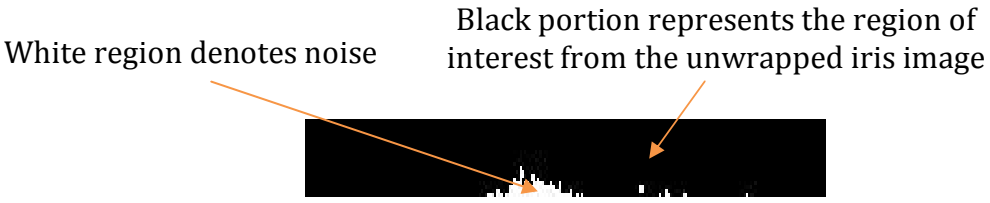

(b)

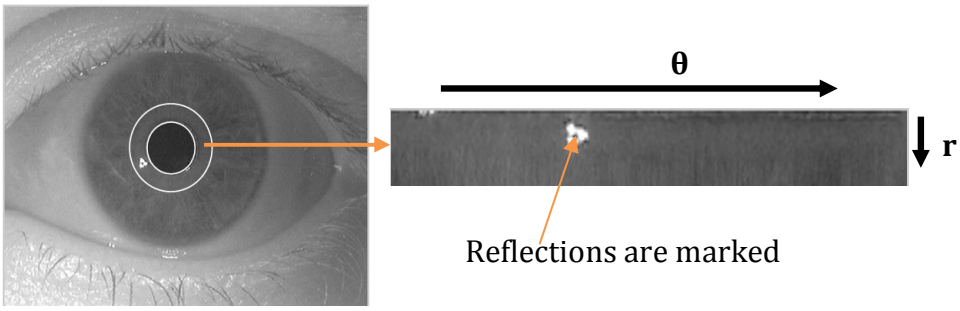

(c)

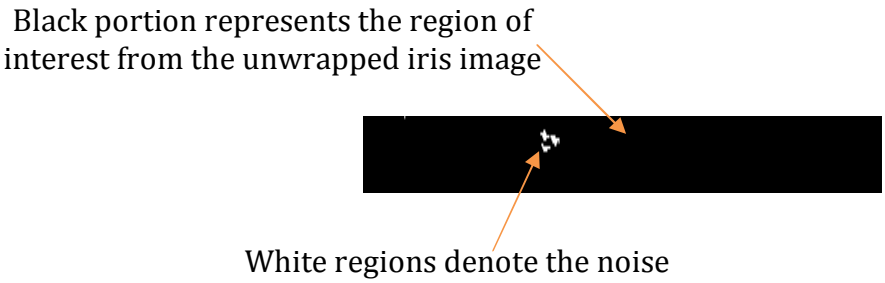

(d)

Fig. 3.4 (a) Unwrapping of the iris image from the ICE 2005 dataset; (b) noise areas are marked for the corresponding unwrapped iris image; (c) unwrapping of the iris image from WVU Nonideal dataset; and (d) noise areas are marked for the corresponding unwrapped iris image.

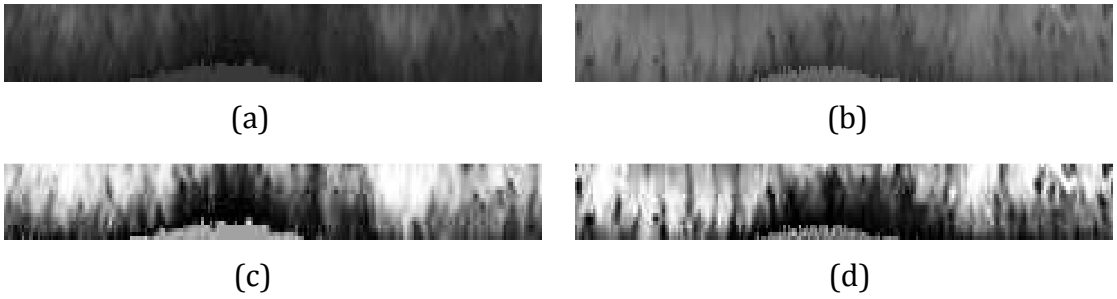

Fig. 3.5 (a, b) show the unwrapped pupillary region before the enhancement taken from the ICE 2005 dataset, and (c, d) reveal the corresponding pupillary region after enhancement.

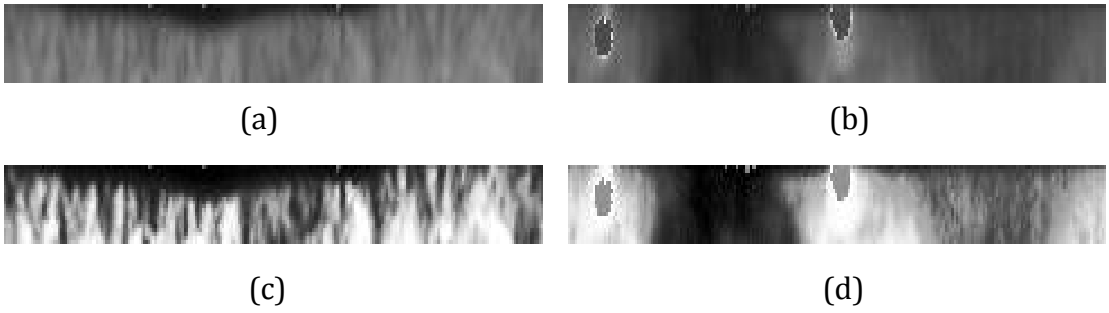

Fig. 3.6 (a, b) show the unwrapped pupillary region before the enhancement taken from the WVU Nonideal dataset, and (c, d) reveal the corresponding pupillary region after enhancement.

feature of the applied filter is that it is rotation and scale invariant. Also, the 1D log polar Gabor functions, having extended tails, should be able to encode natural images more efficiently than regular Gabor functions. They are more efficient because the regular Gabor functions would over-represent the low frequency components and under-represent the high frequency components in the encoding process. With the log-Gabor functions, more filters are obtained by multiplying the radial and the angular components, such that each even and odd symmetric pair of log-Gabor filters comprises a complex log-Gabor filter at one scale. The frequency response of a log-Gabor filter is given as:

$$G(f) = exp\left(-\left(log\left(\frac{f}{f_0}\right)\right)^2 \Big/ 2\left(\log\left(\frac{\sigma}{f_0}\right)\right)^2\right) \quad (3.2)$$

where f_0 is the centre frequency, and σ provides the bandwidth of the filter. In order to extract the discriminating features from the pupillary area, the normalized pattern is convolved with 1D log-Gabor filters [27, 53]. First, the 2D normalized pattern is isolated into a number of 1D signals. Then, these 1D signals are convolved with 1D log-Gabor filters. We consider the rows of the 2D normalized pattern as the 1D signal. Each row denotes a circular ring of the pupillary area. We use an angular direction that corresponds to the columns of the normalized pattern instead of choosing the radial one, since the maximum independence occurs in the angular direction. It is preferable to set the intensity values of the known noise areas in the normalized pattern to the average intensity level of the neighboring pixels. Thus, we can prevent the influence of noise in the output of the filtering.

3.5 Feature Selection Using Genetic Algorithms (GAs)

The iris data contains a huge number of features and a comparatively small number of samples per class, and this makes accurate and reliable classification or recognition difficult [61]. In this research effort, we propose GAs to select the prominent features based on the matching performance of asymmetrical SVMs [62]. Generally, the feature selection algorithms based on GA can be divided into two categories: the filter approach and the wrapper approach. These categories are based on whether or not the feature selection process is performed independently of the learning algorithm that is used to evaluate the feature subset. If the feature selection is accomplished independently of the learning algorithm in the feature

evaluation stage, the technique is denoted as the filter approach. The filter approach is generally computationally more effective than the wrapper approach. However, its major disadvantage is that the selected feature subset does not represent the optimal features for classification. On the other hand, the wrapper approach depends on the performance of the learning algorithm as the feature evaluation function. The wrapper approach involves substantial computational cost. However, this approach selects the optimal feature subset for classification. In this section, we have chosen to adopt the wrapper approach, since the deployed multi-class SVMs guide the GAs properly to improve the feature subset selection criteria. The GAs can search a pool of hypotheses (called *population*), which contain complex interacting parts. Each hypothesis (*individual*) of the current population is evaluated according to a specified fitness function. A new population is generated by applying genetic operations like selection, mutation and crossover. In GA-based feature selection, each individual represents a feature subset. In the genetic process, we present the choice of a representation for encoding the candidate solutions that are to be manipulated by the genetic algorithms, and each individual in the population represents a candidate solution to the feature subset selection problem. The feature pool is formed by the original features that are extracted by using the 1D log-Gabor filters. If n denotes the total number of features (available to represent the patterns to be classified), then the individual (chromosome) is represented by a binary vector of dimension, n. If a bit is a 1, it means that the corresponding feature is selected; otherwise the feature is not selected. This is the simplest and most straightforward representation scheme (See Fig. 3.7). A detailed description of GA

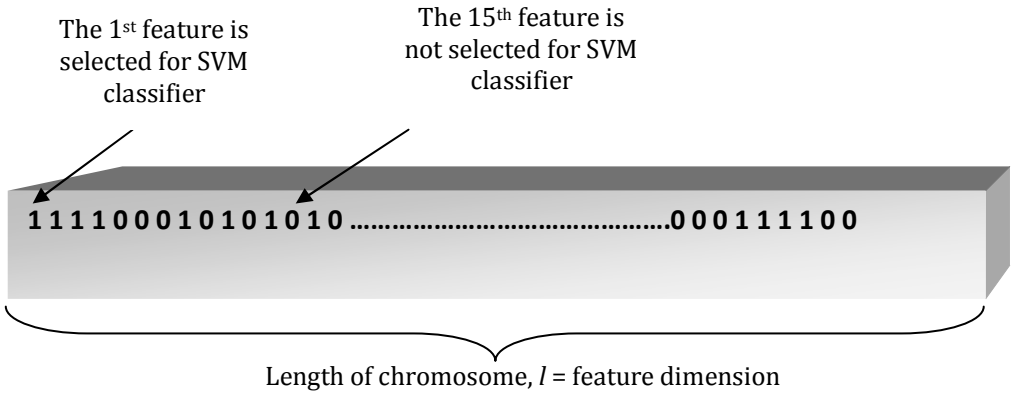

Fig. 3.7 A binary feature vector for *l*-dimension.

can be found in [62].

The proposed GAs are designed to optimize two objectives: maximize the recognition accuracy and minimize the size of the feature subset. In order to do so, we propose the following fitness function:

$$F = w*RA(x) +(1-w)*(1/FSS(x)) \quad (3.3)$$

where, x denotes the feature vector representing a selected feature subset and w is the weighting parameter between 0 and 1. The proposed fitness function contains two parts. The first part is the weighted recognition accuracy, $RA(x)$, and the second part is the weighted feature subset size, $FSS\ (x)$, of the selected feature subset represented by x. The fitness of an individual x is increased if the recognition accuracy of the x increases, and is decreased if the size of the x increases for a given w. If the value of w is reduced, it provides more penalties on the size of x. We can achieve a tradeoff between the accuracy and size of the selected feature subset by adjusting the value of w. In this effort, we use the asymmetrical SVM as an induction algorithm. We use the roulette wheel selection to probabilistically select individuals

from a population for latter breeding. The probability of selecting an individual, ind_i is estimated as:

$$P(ind_i) = F(ind_i)/\sum_{i=1}^{p} F(ind_i) \quad (3.4)$$

where, p denotes the number of individuals in the population. The probability that an individual will be selected is proportional to its own fitness and is inversely proportional to the fitness of the other competing hypotheses in the current population. Here, we use single point crossover, and each individual has a probability, $P_{n,}$ to mutate. The number of n bits is randomly selected, to be flipped in every mutation stage. The overall feature subset selection process is shown in Fig. 3.8.

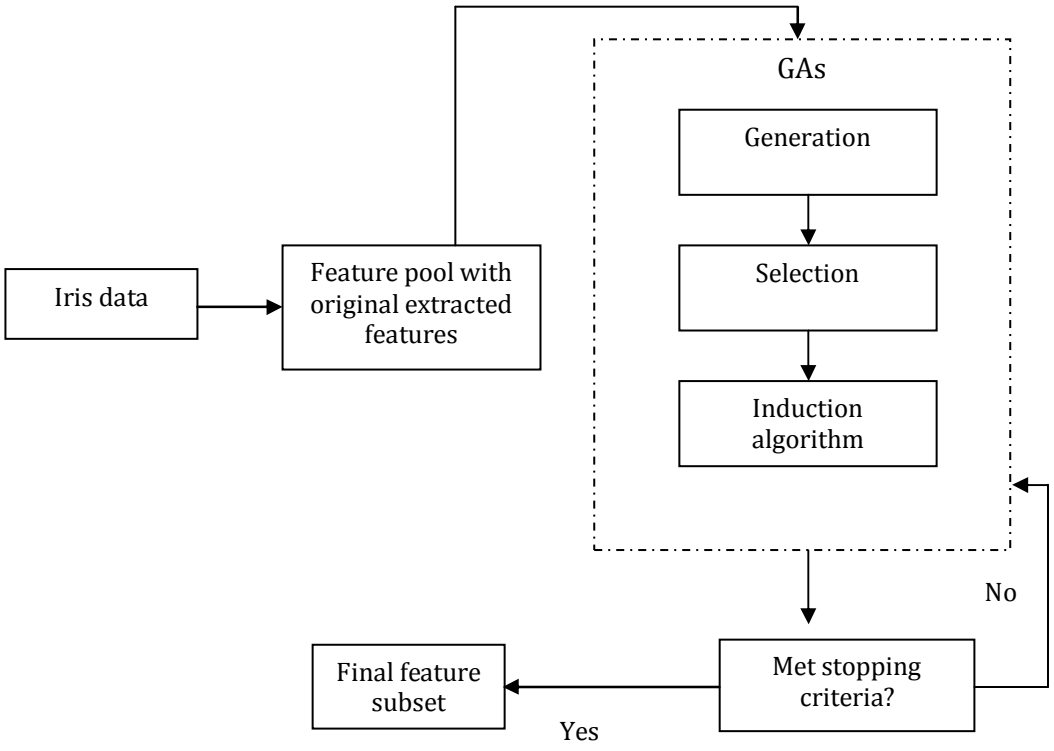

Fig. 3.8 Feature subset selection procedure with GAs.

3.6 Asymmetrical SVMs as Iris Pattern Classifiers

In this chapter, we use multi-class SVMs for iris pattern classification due to their outstanding generalization performance [49, 63, 64]. We apply the asymmetrical SVMs, to handle the issue of poorly balanced sample proportions between classes, and we briefly summarize these steps below.

1. Let us consider N sets of labeled input/output pairs $\{\boldsymbol{x_i}, y_i\,; i = 1, \dots, N\} \in X \times \{+1, -1\}$, where X is the set of input data in $\Re^D$ and y_i represents the labels. The SVM-based approach aims to obtain the largest possible margin of separation.

   The decision hyperplane can be expressed as:

$$\boldsymbol{x}.\boldsymbol{w} + b = 0 \tag{3.5}$$

2. If all the training data satisfy the constraints, then:

$$\boldsymbol{x_i}.\boldsymbol{w} + b \geq +1 \quad for\ y_i = +1, \forall i = 1, \dots, N \tag{3.6}$$

$$\boldsymbol{x_i}.\boldsymbol{w} + b \leq -1 \quad for\ y_i = -1, \forall i = 1, \dots, N \tag{3.7}$$

   and the distance between the two hyperplanes is expressed as:

$$2d = 2/\|\boldsymbol{w}\| \tag{3.8}$$

   where, the distance, d, is considered as the safety margin of the classifier.

3. Now, by combining (3.6) and (3.7) into a single constraint, we get:

$$y_i\,(\boldsymbol{x_i}.\boldsymbol{w} + b\,) \geq 1 \quad \forall i = 1, \dots, N \tag{3.9}$$

   In the training phase, the main goal is to find the Support Vectors (SVs) that maximize the margin of separation, d. Alternatively, a similar objective can be achieved if we minimize $\|\boldsymbol{w}\|^2$. Thus, the goal is to minimize $\|\boldsymbol{w}\|^2$ subject to the constraint in (3.9). We can solve it by introducing the Lagrange multipliers $\alpha_i \geq 0$ and a Lagrangian:

$$L(\boldsymbol{w}, b, \alpha) = \frac{1}{2} \|w\|^2 - \sum_{i=1}^{N} \alpha_i (y_i(\boldsymbol{x_i}.\boldsymbol{w} + b) - 1) \quad (3.10)$$

where, $L(\boldsymbol{w}, b, \alpha)$ is simultaneously minimized with respect to $\boldsymbol{w}$ and b, and is maximized with respect to α_i.

Finally, the decision boundary can be derived as follows:

$$f(\boldsymbol{x}) = \boldsymbol{w}.\boldsymbol{x} + b = \sum_{i=1}^{N} y_i \alpha_i (\boldsymbol{x}.\boldsymbol{x_i}) + b = 0 \quad (3.11)$$

4. If the data points are not separable by a linear separating hyperplane, a set of slack or relaxation variables $\{\xi = \xi_1, \dots, \xi_N\}$ is introduced with $\xi_i \geq 0$ such that (3.9) becomes:

$$y_i (\boldsymbol{x_i}.\boldsymbol{w} + b) \geq 1 - \xi_i \qquad \forall\, i = 1, \dots, N \quad (3.12)$$

The slack variables measure the deviation of the data points from the marginal hyperplane. The new objective function to be minimized becomes:

$$\frac{1}{2} \|\boldsymbol{w}\|^2 + C \sum_i \xi_i,$$

$$\text{Subject to } y_i (\boldsymbol{x_i}.\boldsymbol{w} + b) \geq 1 - \xi_i \quad (3.13)$$

where, $\sum_i \xi_i$ denotes the number of misclassifications on the training set and thus measures the empirical risk, and C is the user-defined penalty parameter that penalizes any violation of the safety margin for all the training data. Therefore, C can be used to control the tradeoff between the empirical risk and the complexity of learning.

5. In order to control the misclassification error between the positive and negative classes, we separate the empirical risk, $\sum_i \xi_i$, into two parts and assign the different penalty parameters, C^+ and C^-, corresponding to the empirical risk of positive and negative classes, respectively [7, 46]. Therefore, (3.13) becomes:

$$\frac{1}{2}\ \|\boldsymbol{w}\|^2 + \sum_i C(z_i)(\xi_i), \tag{3.14}$$

where, $C(z_i) = C^+$, if sample i is from positive class, and $C(z_i) = C^-$ if sample i is from negative class. The statistically under-presented data of a class with respect to other classes can be controlled with the variation in the value of the penalty parameter, C. Therefore, it can be inferred that the higher the $C(z_i)$, the more penalty will be required to reduce the misclassification error. Here, we consider the cost and asymmetry of samples.

6. In order to obtain a nonlinear decision boundary, we replace the inner product $(\boldsymbol{x}.\boldsymbol{x_i})$ of (3.10), with a nonlinear kernel $K(\boldsymbol{x}.\boldsymbol{x_i})$ and obtain

$$f(\boldsymbol{x}) = \sum_{i=1}^{N} y_i \alpha_i \boldsymbol{K}(\boldsymbol{x}.\boldsymbol{x_i}) + b \tag{3.15}$$

Now, in the next subsection, we discuss the SVM parameter selection process that improves the generalization performance.

3.6.1 Tuning of SVM Parameters

The optimal value of penalty parameter ratio (i. e., the ratio between C^+ and C^-) for the error term should be selected by adjusting the kernel parameters to improve the generalization performance. A careful selection of a training subset and of a validation set with a small number of classes is required. The purpose is to avoid training the SVMs with all the classes and to evaluate the performance of SVMs on the validation set due to their high computational cost when the number of classes is higher. In this section, the optimum parameter values are selected to tune the SVMs. A modified approach proposed in [65] is applied to reduce the cost of the selection procedure, as well as to adjust the parameters of the SVMs. After assigning the class labels to the training data, we divide 70% of the training data of each class

depending on the dataset used for training, and the rest of the training data is used for validation. Here, the Fisher's least square linear classifier is used with a low computational cost for each class [66]. The performance of this linear classifier is evaluated on the validation set, and the confusion matrix, **CM**, is defined as follows:

$$\mathbf{CM}=\begin{pmatrix} m_{11} & m_{12} & \dots & m_{1n} \\ m_{21} & m_{22} & \dots & m_{2n} \\ \vdots & \vdots & \ddots & \vdots \\ m_{n1} & m_{n2} & \dots & m_{nn} \end{pmatrix} \tag{3.16}$$

where, each row i corresponds to the class w_i, and each column j represents the number of classes classified to w_j. The number of misclassified iris patterns is estimated for each class as follows:

$$err_i = \sum_{j=1, j\neq i}^{n} m_{ij} \tag{3.17}$$

and then, we sort the misclassified patterns, $err_i, i = 1,2, \dots, n$ calculated from (3.16) in decreasing order, and the subscripts $i_1, i_2, \dots, i_I$ are assigned to the top I choices assuming that $I \ll N$. Next, we determine the number of classes whose patterns can be classified to the class set $\{w_{i_1}, w_{i_2}, \dots, w_{i_I}\}$ based on the following confusion matrix:

$$V = \bigcup_{k=1}^{I} \{w_j | m_{i,j} \neq 0\} \tag{3.18}$$

From the class set V, we select the training and the cross validation set to tune the ratio between the penalty parameter and the kernel parameters for the SVMs. After a careful selection of the ratio between C^+ and C^- and the kernel parameters, the whole training set with all the classes are trained.

3.7 Experimental Results, Analysis and Discussions

As mentioned earlier in Section 3.1, we have conducted the experiments on two iris

datasets, namely, the ICE 2005 [189] and WVU Nonideal [192]. The details of the datasets are given in Appendix A. Our experiments have been conducted in two stages. First, the performance of the proposed approach has been evaluated (Section 3.7.1). Second, our proposed method has been compared with three most promising ideal iris recognition algorithms and also, a comparative analysis of our method with state-of-the-art iris recognition approaches has been provided (Section 3.7.2).

In the first stage, we focus on the performance evaluation of the current approach based on the matching accuracy. We show the performance of the proposed genetic process for the selection of the optimum features and also for an augmentation of the overall system accuracy. The verification performance of the proposed approach is demonstrated using an ROC curve and EER. As mentioned in Chapter 2, the EER is the point where the FAR and the FRR are equal in value. In general, the lower the EER value, the higher the accuracy of the iris recognition system [31]. During the second stage, we carry out a series of experiments to provide a comparative analysis of our method with the existing methods with respect to recognition accuracy. We also show the average time consumption pertaining to the different parts of the proposed iris recognition system.

3.7.1 Performance Evaluation of the Proposed Method

We evaluated the success rate for the proposed method by detecting the pupil boundary. The obtained success rates were 98.60% and 97.40% for the ICE and WVU datasets, respectively. We found that a reasonable recognition accuracy was achieved when the pupillary area was isolated, by increasing the previously detected radius value of the pupil up to a certain number of pixels. A rapid drop of

matching error from 3.61% to 2.48% was observed as shown in Fig. 3.9(a), when the number of pixels was increased from 20 to 21. Therefore, we chose to increase the pupil radius up to 23 pixels because a stable matching accuracy of 97.54% was achieved in this case. In order to find an optimal value for the pupillary radius, SVMs were used for matching; however, GAs were not applied in this case. From Fig. 3.9(b), we found that if we increased the pixel values up to 26, then we obtained the highest matching accuracy of 95.39%. The experimental results show that our proposed approach fails to detect the iris/sclera boundary for a few cases; however, our method successfully isolates the iris/pupil boundary for those cases, which in turn, localizes the pupillary area correctly as demonstrated in Fig. 3.10. Fig. 3.11 shows the comparison of the feature dimension versus the recognition accuracy of SVMs compared to other matching approaches such as the HD, Feed-Forward neural network by using the Backpropagation (FFBP) rule, the Feed-Forward neural network by using the Levenberg-Marquardt rule (FFLM), the k-Nearest Neighbor (k-NN) rule. In this case, only the Radian Basis Function (RBF) kernel is considered due to its reasonable classification accuracy for the SVMs. From Fig. 3.11, we can see that with an increasing dimensionality of the feature sequence, the recognition rate also increases rapidly for all similarity measures. However, when the dimensionality of the feature sequence is increased up to 600 or higher, the recognition rate starts to level off at an encouraging rate of about 97.31% and 95.30% for the ICE and WVU datasets, respectively. Therefore, we input 600 features to the feature pool of GA for further feature selection.

In order to reduce the computational cost and to speed up the classification

process, the Fisher's least square linear classifier was used as a low-cost pre-classifier. With this classifier, a reasonable cumulative recognition accuracy can be

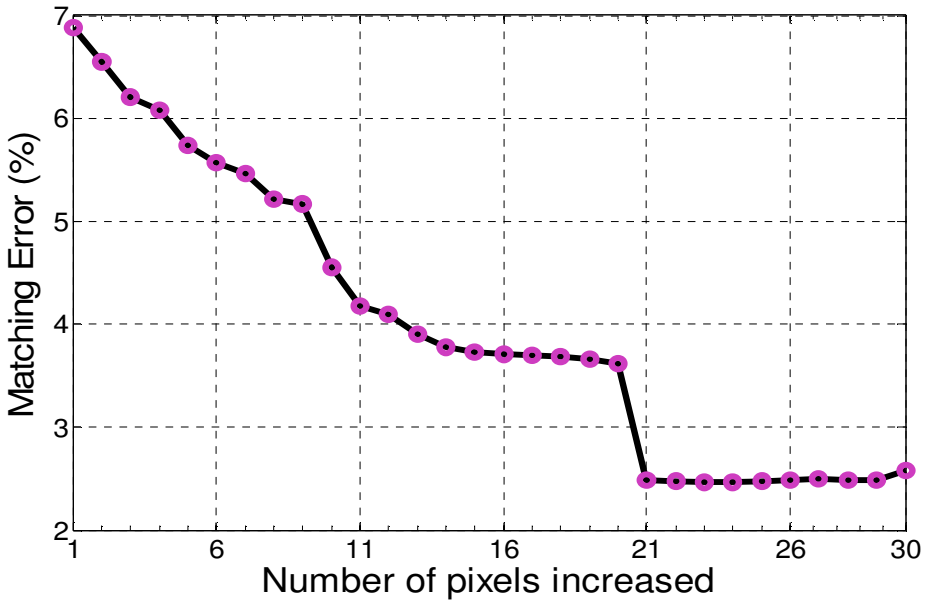

(a)

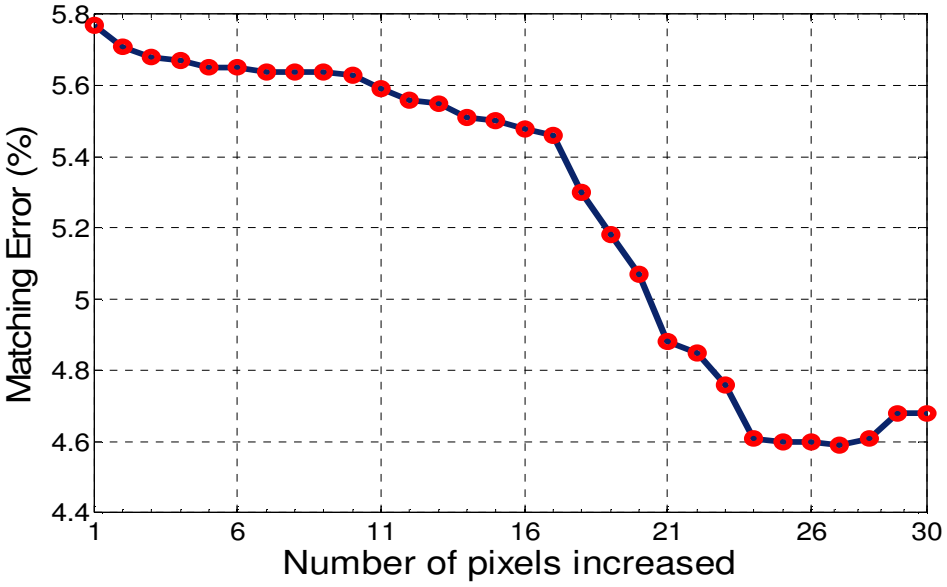

(b)

Fig. 3.9 Matching error vs. number of pixels increased on (a) ICE 2005, and (b) WVU Nonideal datasets.

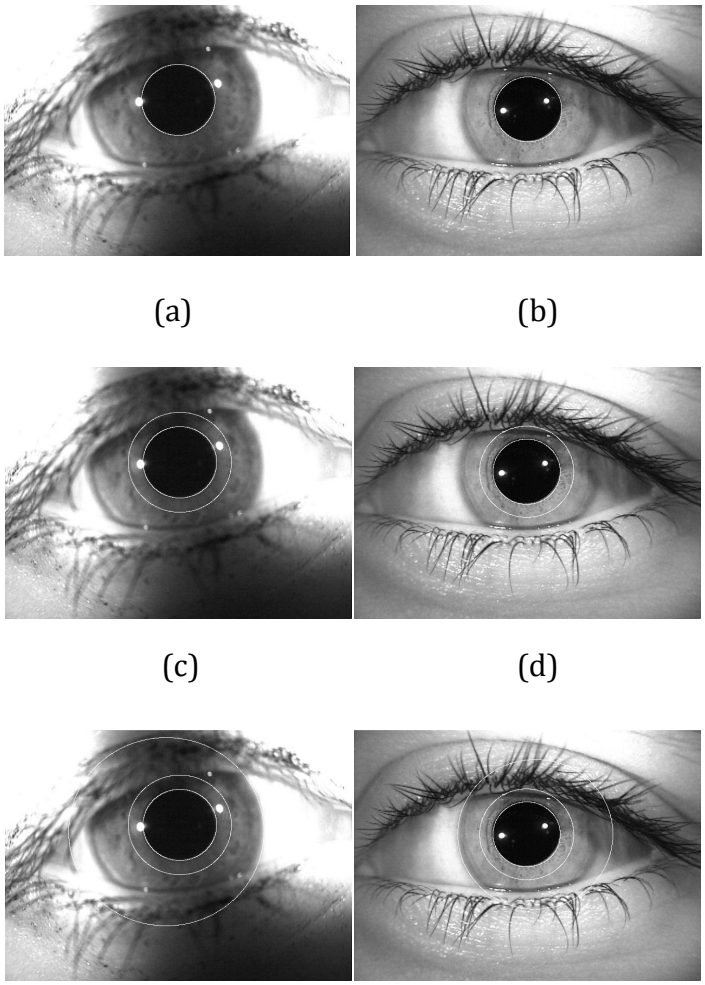

Fig. 3.10 On the WVU Nonideal dataset: (a), (b) show successful detection of iris/pupil boundary; (c), (d) provide correct localization of pupillary area; and (e), (f) show the failure of proper detection of iris/ sclera boundary.

achieved and a true class label can be given for a small number of selected candidates. For the ICE dataset, we applied the Fisher's least square linear classifier to choose ten candidates [66]. The cumulative recognition accuracy at rank 10 was 98.14%. The selected cardinal number of sets was 32 from the experimentation. This number was found by using the tuning algorithm for the SVM parameter selection (refer to Section 3.6.1). As a result, the sizes of the training and validation

sets when selecting the optimal values of the ratios between C^+ and C^-, and σ^2, were 112 (=32*5*0.7) and 48 (=32*5*0.3), respectively. When the parameter σ^2 was set at 0.6, and the ratio between C^+ and C^- was set at 18, the highest accuracy on the validation set was achieved with the RBF kernels for the ICE iris dataset. In this experiment, we considered only those classes of the ICE database that had at least five probe images for the purpose of selecting the optimal parameter values. The SVM parameters were also tuned for the WVU dataset. Here, twenty candidates were selected by using the Fisher's least square linear classifier. The cumulative recognition accuracy at rank 20 was 97.20%. The cardinal number of sets obtained for this dataset was 60. Therefore, the sizes of the training and validation sets

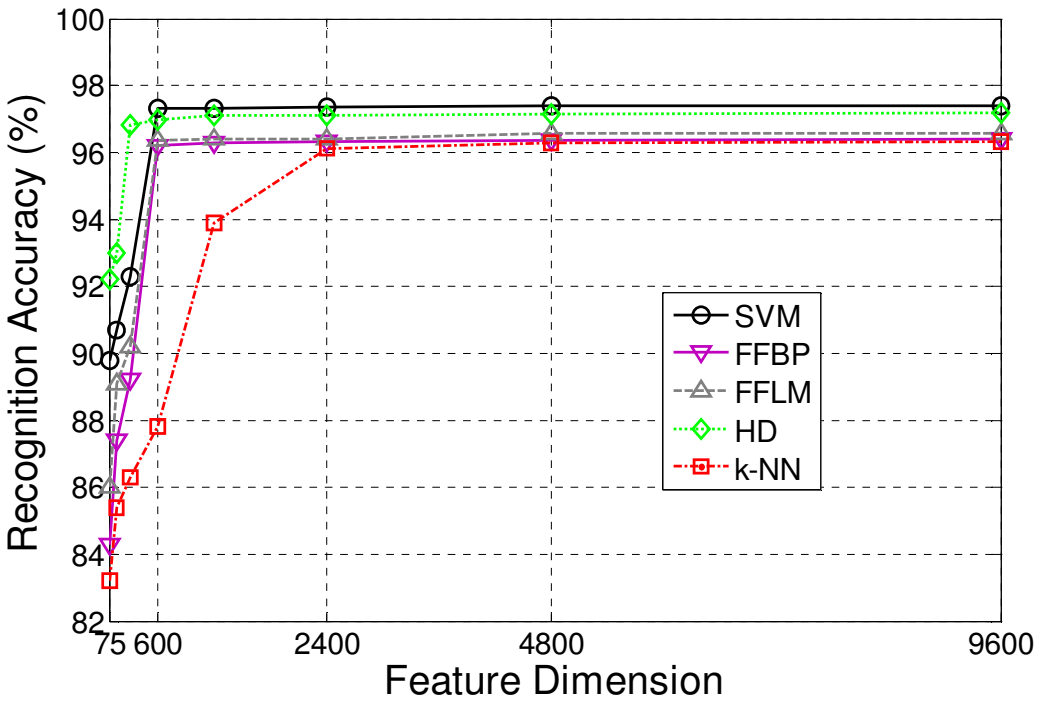

(a)

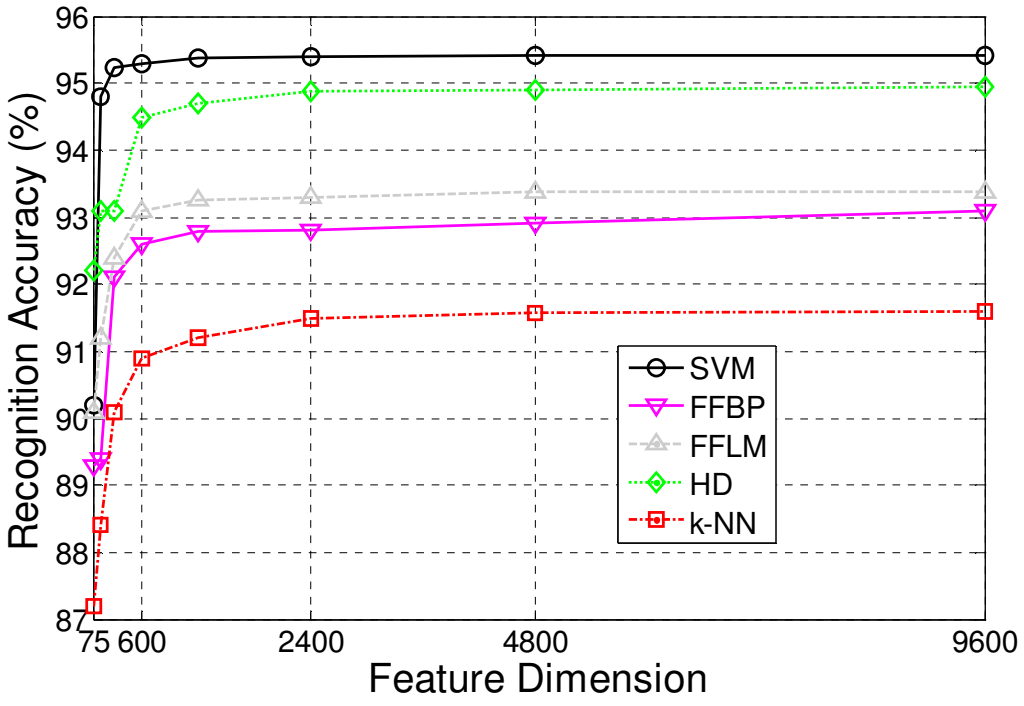

(b)

Fig. 3.11 Comparison of SVM recognition accuracy with the accuracies of FFBP, FFLM, k-NN, and HD for different feature dimensions on (a) ICE 2005, and (b) WVU Nonideal datasets.

when selecting the optimal values of the ratio between penalty parameter and σ^2 were 168 (=60*4*0.7) and 72 (=60*4*0.3), respectively. Finally, the ratio between C^+ and C^- was set at 21, and the optimal value of σ^2 remained the same as that for the ICE dataset. Table 3.2 shows the performance of different kernel functions when selecting the optimum values of SVM parameters. Since the highest classification accuracy was obtained by using the RBF kernel, this kernel was used

Table 3.2: Efficiency of the various kernel functions.

Kernel type	Classification accuracy (%) in ICE 2005 dataset	Classification accuracy (%) in WVU Nonideal dataset
Polynomial	91.1	89.2
RBF	94.3	92.4
Sigmoid	91.2	90.6

in our system for SVM-based classification. In order to evaluate the matching accuracy, we utilized the pupillary area only. For each person in the ICE database, one iris sample was used to build the template. The remaining irises from the probe image set were used for testing. From the WVU dataset, we used two iris samples for training. The remaining samples of each class were used for testing. In order to select the optimum features for the improvement of the matching accuracy, GAs were applied. GAs involved running the genetic process for several generations, as shown in Fig. 3.12, with different values of the weighting parameter, *w,* in the fitness function. In this figure, the highest matching accuracy of 97.73% was achieved at generation 200 on the ICE dataset when w = 0.90. For w = 0.95, an accuracy of 95.63% was achieved at generation 250 when the WVU dataset was used. Based on these experiments, we found that the weighting parameter, *w,* influences the

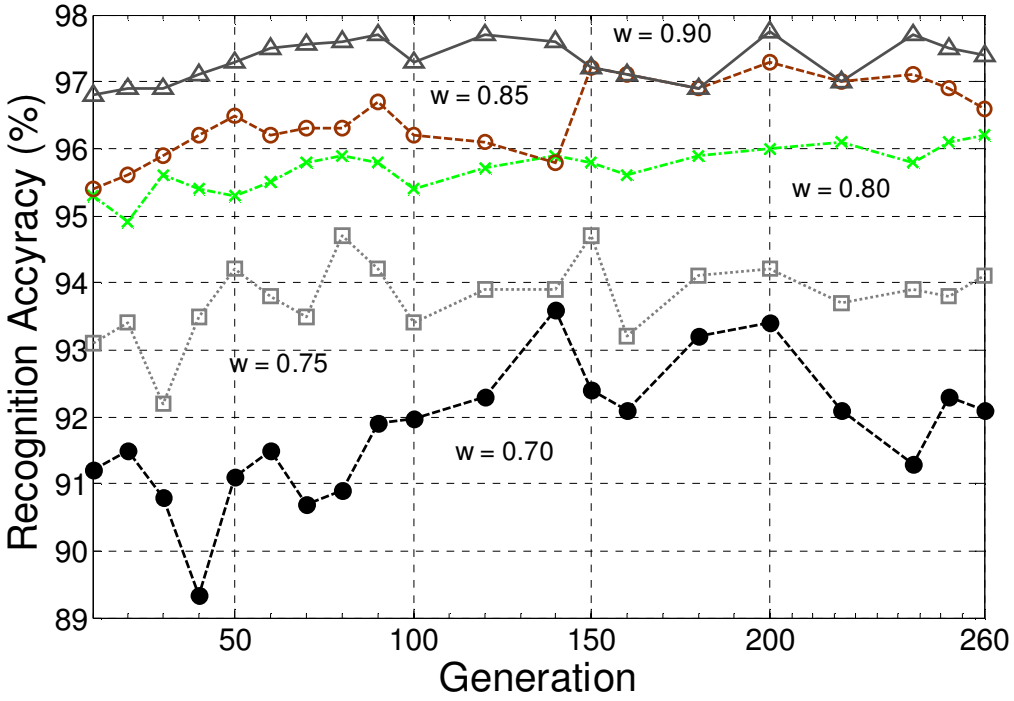

(a)

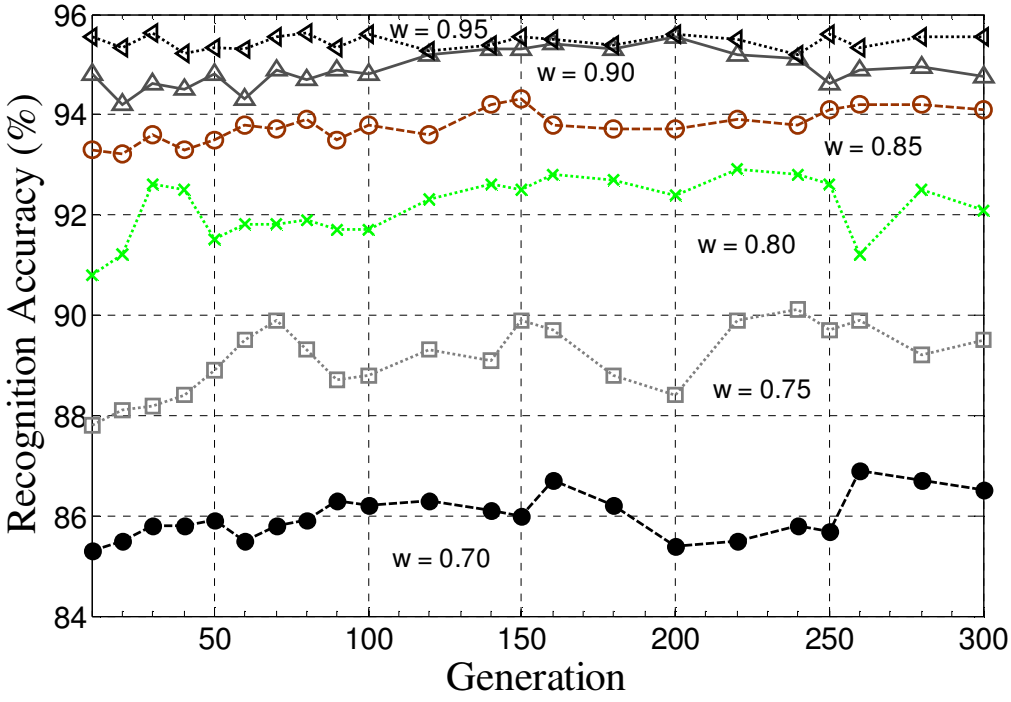

(b)

Fig. 3.12 Variation of recognition rates with several GA generations on: (a) ICE 2005, and (b) WVU Nonideal datasets, for different values of weighting parameters in the fitness function.

recognition accuracy as well as the feature subset size. As we can see in the Tables 3.3 and 3.4, and Fig. 3.12, increasing *w* affects the recognition accuracy. In general, we find that increasing the value of *w* also increases the recognition accuracy. On the other hand, reducing *w* also influences the size of the feature subsets. Smaller values of *w* impose more penalties on the size of the subsets being selected. Therefore, using smaller values of *w* leads to the selection of smaller subsets, and reducing *w* reduces the accuracy as well. However, there are a few exceptions, as shown in Tables 3.3 and 3.4. For example, in Table 3.3, GAs chose a subset of 511 features reaching the 94.10% recognition accuracy when *w* = 0.75. The recognition

accuracy of this subset is larger than the one of size 512. In Table 3.3, the highest accuracy of 97.73% is obtained when w= 0.90 and the feature subset size = 540. On the other hand, a lower recognition accuracy is achieved with a reduced feature subset of 512 when w = 0.70. Therefore, we chose a tradeoff between the accuracy and the size. Finally, since the accuracy was our major concern, we considered the case where GAs selected a subset size of 530 features and achieved a reasonable accuracy of 97.60% when w = 0.90 for the ICE dataset. Similarly, for the WVU dataset, GAs selected a subset size of 487 features with a reasonable accuracy of 95.55%, in spite of the higher accuracy of 95.63% that could be achieved for a relatively higher subset size of 510 for w = 0.95. After conducting several experiments, the arguments of GAs were set, as shown in Table 3.5.

The recognition accuracy of the proposed method, using the pupillary area is compared with that of the traditional approach, denoted as the "*previous approach*" [56] (where complete iris information between the pupil and the sclera boundary are considered for recognition). Fig. 3.13 shows the efficiency of the current approach with and without GAs in comparison with that of the previous approach. In order to show a comparative analysis, we provide the original feature set, extracted from the pupillary area of different dimensions in the feature pool of GAs. The proposed method performs relatively better with an accuracy of 97.67% on the ICE, and 95.58% on the WVU datasets. Therefore, the performance of our approach increased when the GAs were used for feature selection. The proposed approach leads to a reasonable recognition accuracy in the cases where the eyelashes and the eyelids occlude the iris so badly that the pupil is partly invisible.

Table 3.3: Recognition accuracies and their corresponding feature subset sizes for different values of the weighting parameter, *w,* experimented on the ICE 2005 dataset.

Weighting parameter, *w*	Selected feature subset size	Recognition accuracy (%)
0.70	512	93.60
	511	93.45
	504	93.10
0.75	517	94.70
	516	94.20
	511	94.10
0.80	523	96.20
	522	96.18
	520	95.90
0.85	529	97.30
	528	97.25
	526	97.10
0.90	540	97.73
	539	97.70
	530	**97.60**

For a given value of a weighting parameter, the best three accuracies and their corresponding feature sizes are shown.

Table 3.4: Recognition accuracies and their corresponding feature subset sizes for different values of the weighting parameter, *w,* experimented on the WVU Nonideal dataset.

Weighting parameter, *w*	Selected feature subset size	Recognition accuracy (%)
0.70	469	86.90
	465	86.75
	465	86.50
0.75	468	90.10
	473	90.00
	475	89.70
0.80	484	92.90
	484	92.75
	483	92.60
0.85	492	94.30
	486	94.25
	483	94.10
0.90	**487**	**95.55**
	488	95.40
	486	95.30
0.95	510	95.63
	506	95.61
	505	95.60

For a given value of a weighting parameter, the best three accuracies and their corresponding feature sizes are presented.

Table 3.5: The selected values for the arguments of GA, for ICE 2005 and WVU Nonideal datasets.

Parameters	ICE dataset	WVU dataset
Population size	244 (the scale of iris sample)	200 (the scale of iris sample)
Length of chromosome code	600 (selected dimensionality of feature sequence)	600 (selected dimensionality of feature sequence)
Crossover probability	0.61	0.65
Mutation probability	0.005	0.002
Number of generation	260	300

The performance of a verification system has been evaluated by using an ROC curve. See Fig. 3.14, which demonstrates how the Genuine Accept Rate (GAR) changes with a variation in the FAR in our previous and proposed approaches. The proposed approach achieved GARs of 97.62% and 95.53% on the ICE and WVU datasets, respectively. Based on the experiments, our approach reduces the EERs from 2.10% to 0.73% for the ICE dataset, and from 3.92% to 2.15% for the WVU dataset, both of which represent a good improvement for the proposed scheme. In Fig. 3.15(a), one can observe that when the ratio is below 18, with the increase of the ratio, the error rate is decreased, which indicates that the ill effect of sample bias is improved. When the ratio is around 18, the best performance for ICE is achieved. However, the over-tuning may reduce the accuracy. Similarly, from Fig. 3.15(b), we find that the best classification accuracy for WVU is achieved when the ratio is around 21. In reality, it is evident that the exact value of penalty parameters also affects the classifier's performance. Fig. 3.16 shows the comparison of the performance between the traditional SVMs and asymmetrical SVMs, with the exact value of the penalty parameters displayed while the ratio between C^+ and C^-

remains fixed, as previously shown in Fig. 3.15 for both of the datasets. From Figure 3.16, with the ratio between C^+ and C^-, the performance is low except in the cases when the C is small, which indicates that it is the ratio and not the exact value that influences the classifier. Therefore, asymmetrical SVMs perform relatively well when compared to the traditional SVMs. In the above experiments, we observed that decreasing the error rate by counteracting the sample bias gives a higher performance than increasing the error rate by the inherent cost-relative property of asymmetrical SVMs. Moreover, the application of asymmetrical SVMs make the authentication system more configurable, which means that the proper selection of the ratio between C^+ and C^- can influence the tradeoff between the cases of FA and FR.

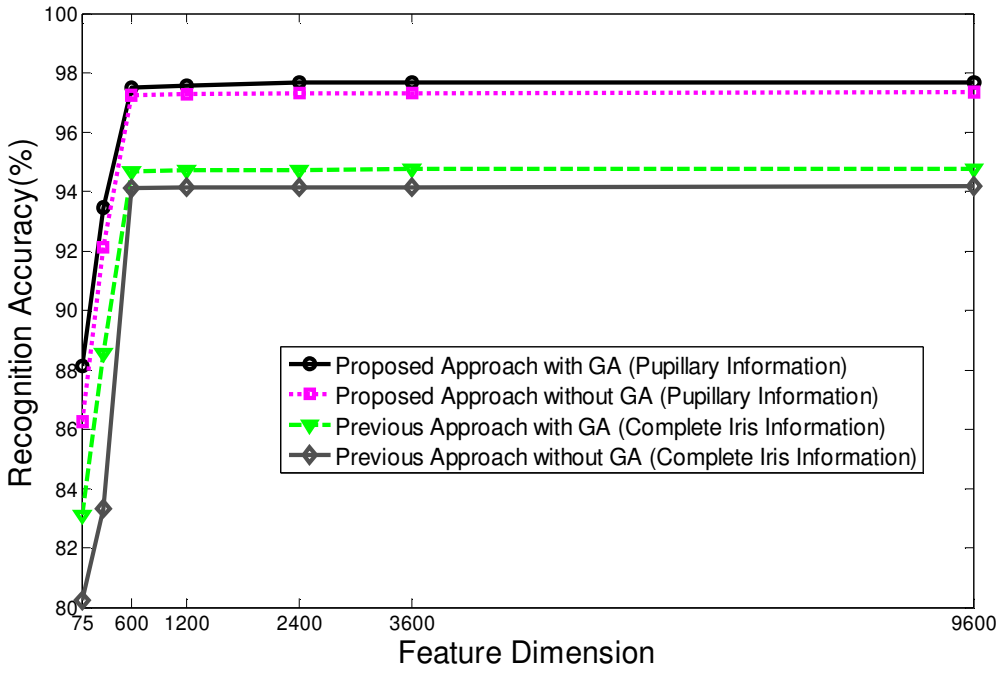

(a)

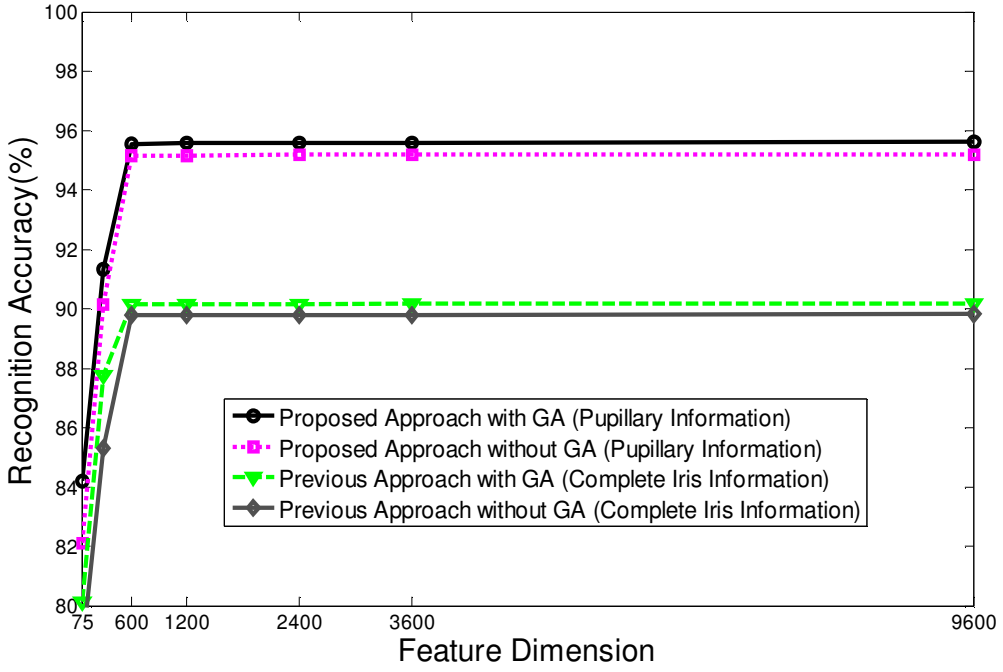

(b)

Fig. 3.13 Comparison of recognition accuracy between *previous approach* [56] and proposed approach, with and without using GAs on (a) ICE 2005 and (b) WVU Nonideal datasets.

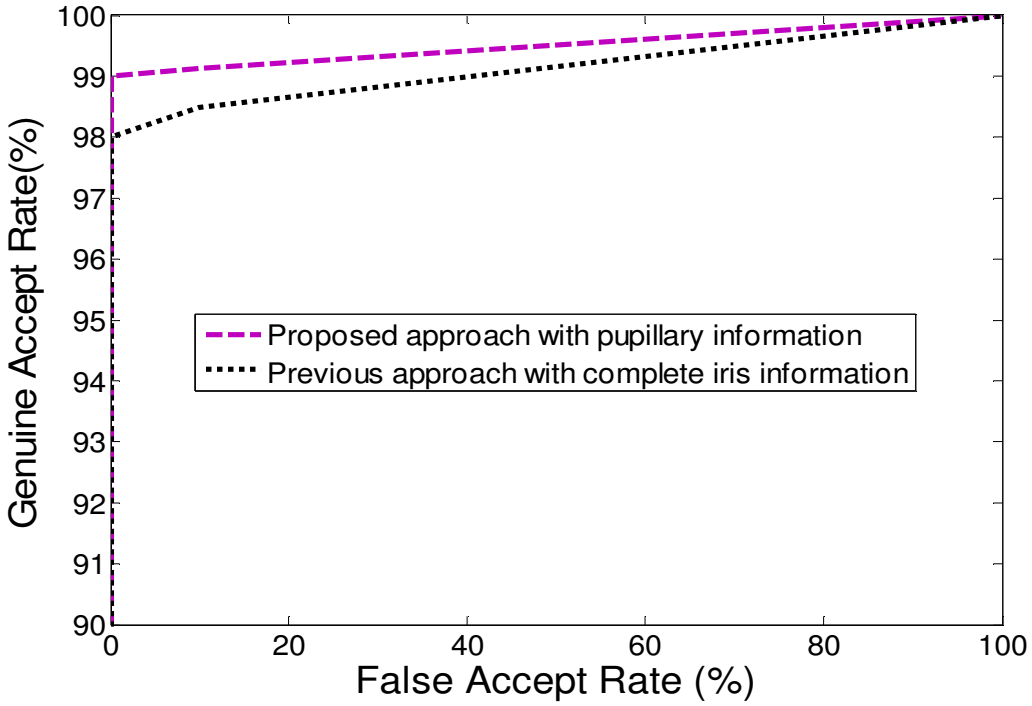

(a)

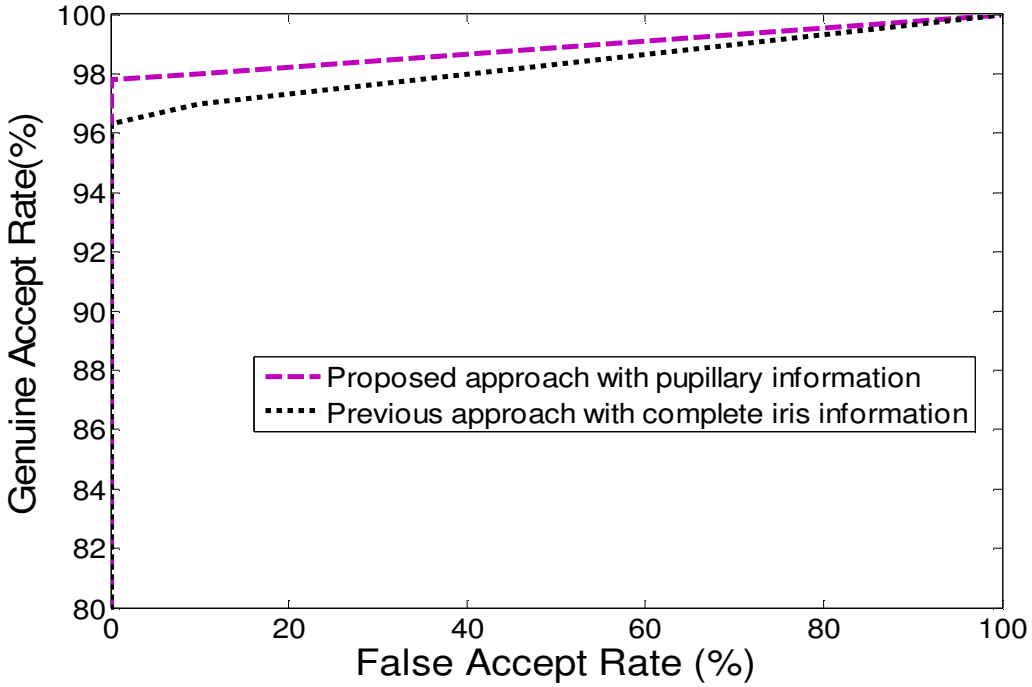

(b)

Fig. 3.14 ROC curve shows the comparison between GAR and FAR for our *previous approach* [56] and proposed approach on (a) ICE 2005, and (b) WVU Nonideal datasets.

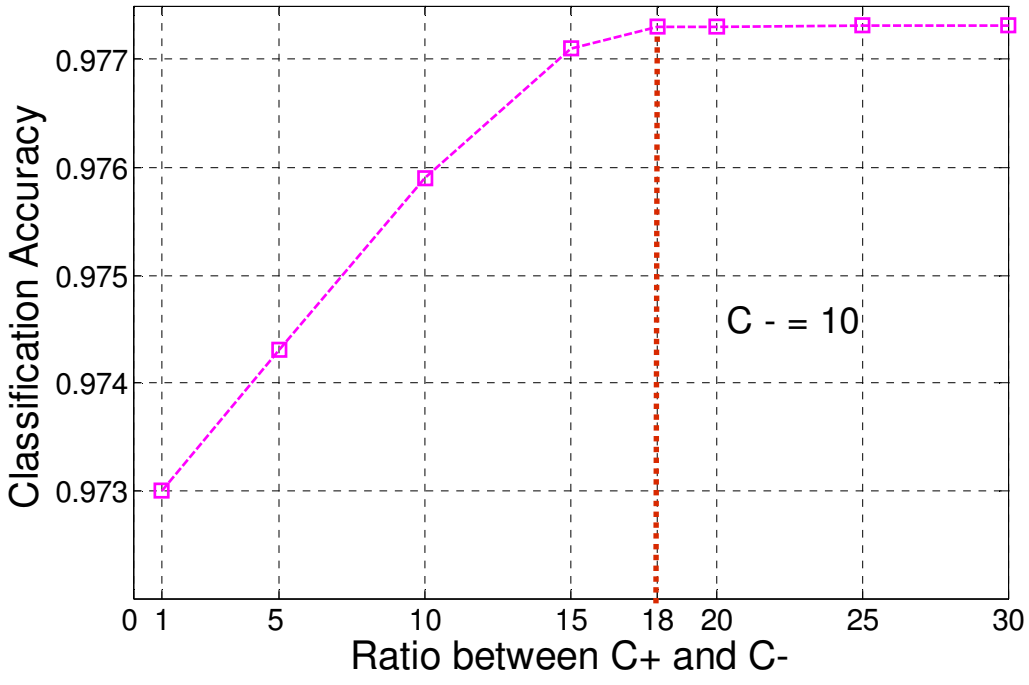

(a)

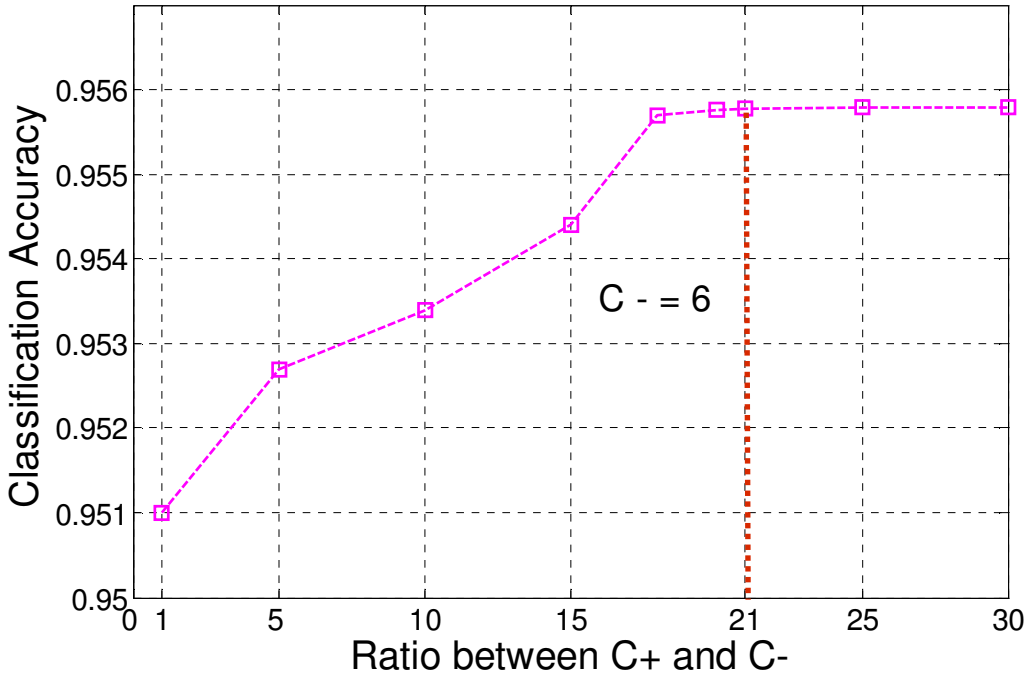

(b)

Fig. 3.15 Classifier performance vs. ratio between $\mathbf{C^+}$ and $\mathbf{C^-}$ on (a) ICE 2005, and (b) WVU Nonideal datasets.

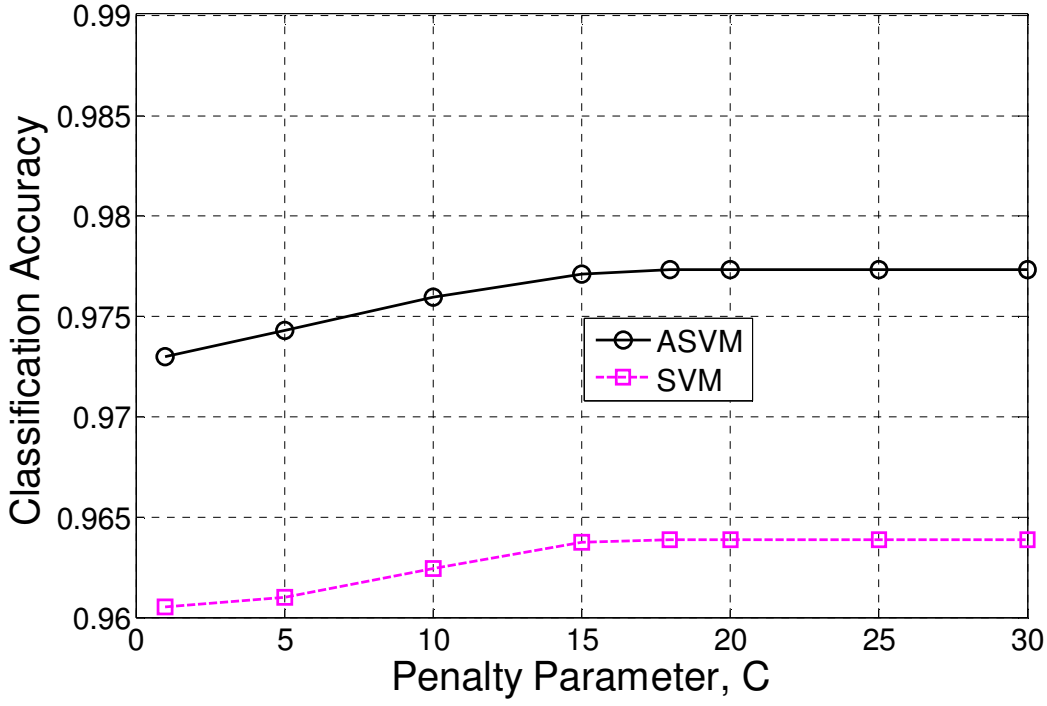

(a)

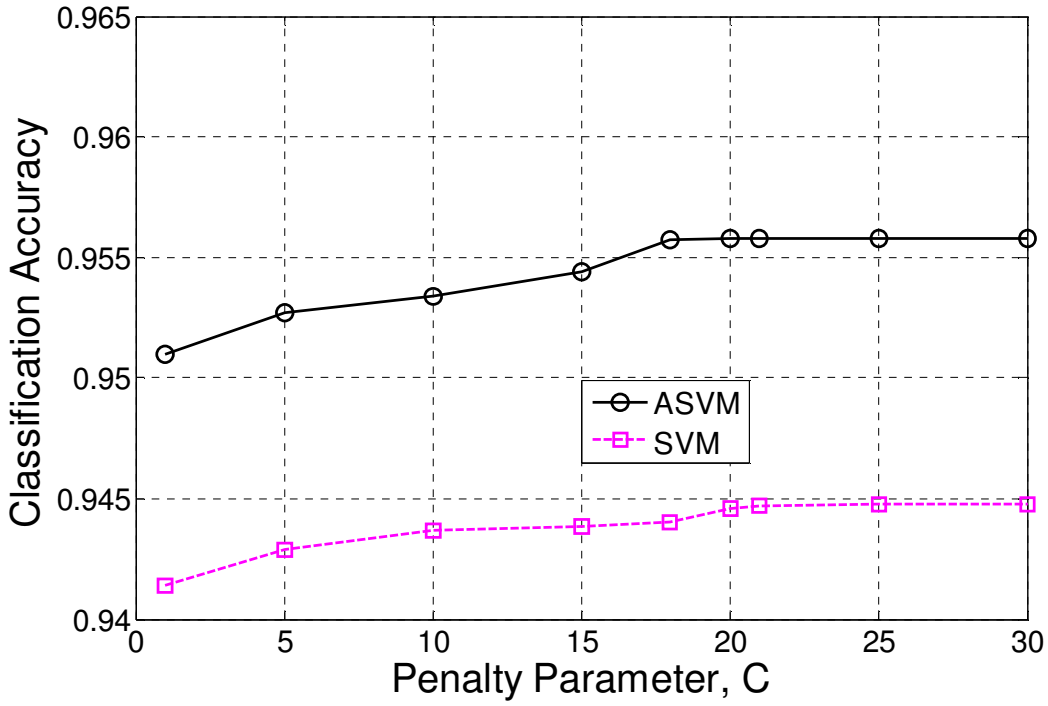

(b)

Fig. 3.16 The comparison of the performance between SVMs and asymmetrical SVMs (ASVMs) on (a) ICE 2005, and (b) WVU Nonideal datasets. The C axis denotes $\mathbf{C}^{-}$, and $\mathbf{C}^{+}$ is 18 times that of $\mathbf{C}^{-}$ for the ICE 2005 dataset and 21 times that of $\mathbf{C}^{-}$ for the WVU Nonideal dataset.

3.7.2 Comparison with State-Of-The-Art Methods

We compared the performance of the proposed algorithm with the other existing iris recognition algorithms. We implemented the well-known iris recognition algorithms proposed by Daugman [27-29] and Ma et al. [22, 31], and compared our approach with those methods on the ICE and WVU datasets. Fig. 3.17 exhibits the ROC curves that demonstrate the performance of the proposed algorithms. The ROC curves of the approaches demonstrated in [22, 27-29, 31] are also plotted for comparison, and this figure shows that the proposed algorithm achieves a higher GAR than the methods of [22, 31]. The proposed method also achieves low EERs of

0.73% on the ICE dataset. However, the approach proposed in [27-29] shows a better GAR than our algorithm on the same dataset. For the WVU dataset, the proposed algorithm achieves a better GAR than the approaches reported in [22, 27-29, 31]. The proposed method also has an EER of 2.15% on WVU dataset. The major reason for achieving a reasonable performance on the ICE and WVU datasets is that both of the datasets contain the iris images of less than ideal quality, and these images are affected by eyelid and eyelash occlusions. Thus, the effect of noise in most of the cases can be avoided, since the pupillary region is less affected by the eyelids and eyelashes. The pupillary area is detected using the centre values of the pupil, which is the darkest region of the iris and is relatively easy to isolate. It means that the proposed algorithm achieves higher discriminating capabilities than the most of the well-known state-of-the-art approaches. We provide the Correct Recognition Rates (CRRs) and time consumption of the proposed iris recognition scheme for both of the datasets. The CRR measure is defined as follows:

$$CRR = \frac{Correctly\ recognized\ user\ number}{Total\ number\ of\ users\ enrolled} \times 100 \qquad (3.19)$$

Table 3.6 shows that the method reported in [27-29] results in a reasonably better recognition rate than the performance of the proposed scheme on the ICE data set. However, the accuracy obtained by the proposed scheme is better than the other two well-known methods reported in [22, 31] and our previous method of [56]. The recognition rate on the WVU iris dataset is greater in our proposed schemes compared to that of the methods reported in [22, 27-29, 31, 56]. Table 3.6 also demonstrates a comparison of the EERs for different existing methods. This table

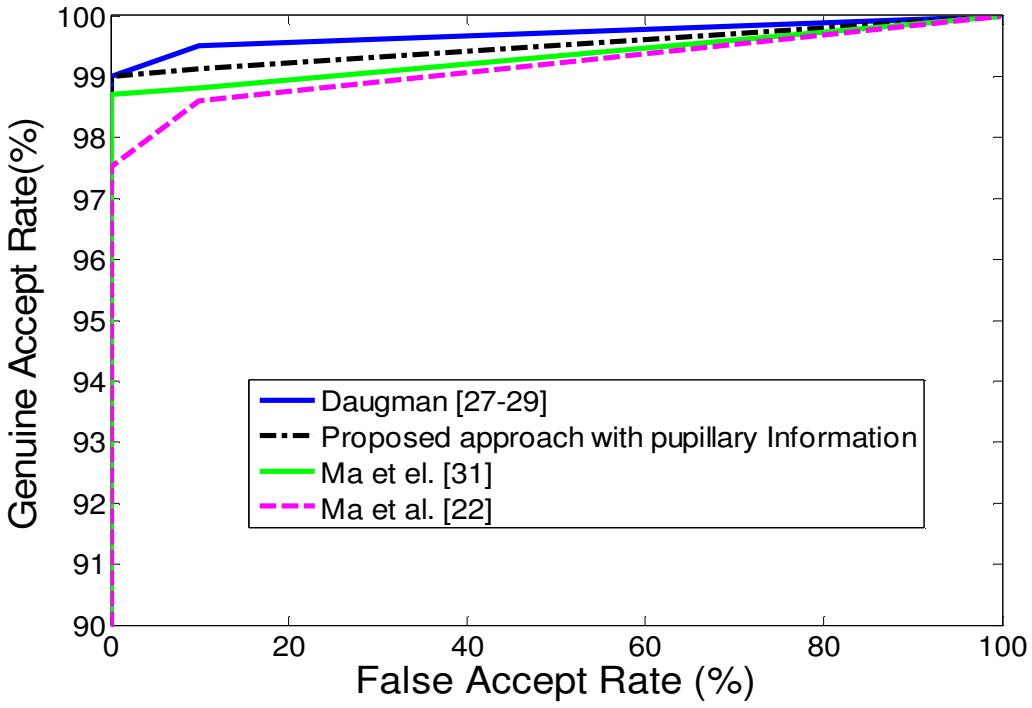

(a)

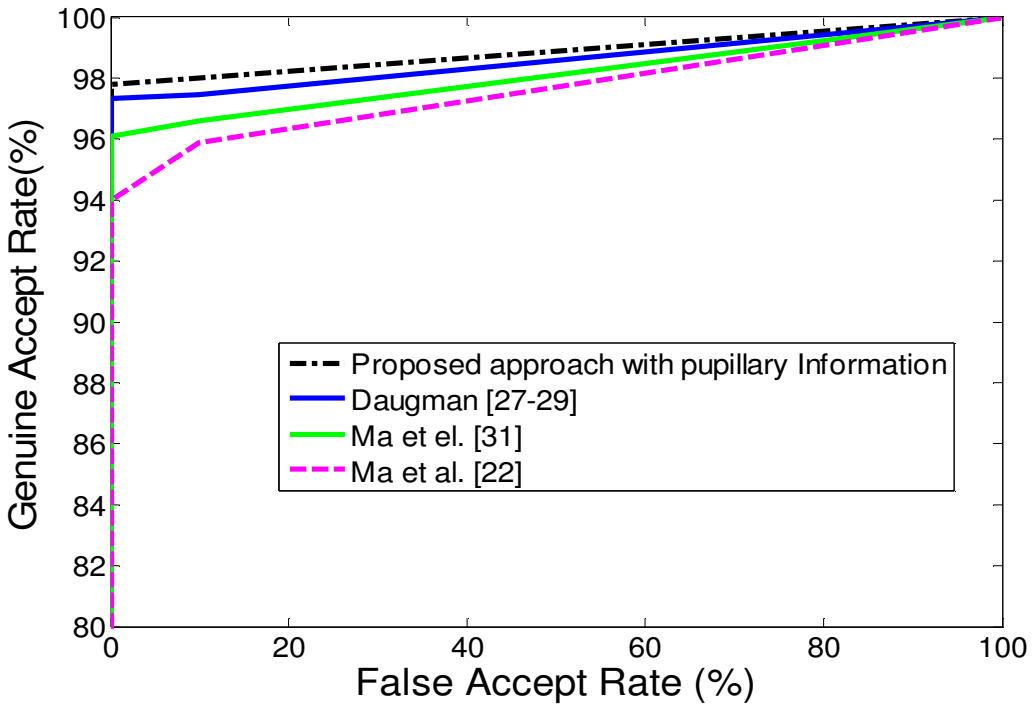

(b)

Fig. 3.17 Comparison of our proposed method with existing iris recognition schemes on the (a) ICE 2005, and (b) WVU Nonideal dataset.

Table 3.6: Comparison of CRR and EER.

Algorithm	Correct Recognition Rate (CRR) (%)		Equal Error Rate (EER) (%)	
	ICE	WVU	ICE	WVU
Daugman [27-29]	98.13	83.14	0.49	8.45
Ma et al. [31]	95.79	78.33	1.72	10.50
Ma et al. [22]	95.64	77.24	1.80	11.43
Roy et. al. [56]	94.80	90.13	2.10	3.92
Proposed*	**97.70**	**95.60**	**0.73**	**2.15**

*Two samples per class to train the Asymmetrical SVMs and the rest of the samples of each class are used for testing on all the datasets.

shows that the proposed scheme has a lower EER on the ICE dataset than the methods of [22, 31, 56] and a higher EER than the method proposed by Daugman in [27-29]. For the WVU dataset, our algorithm achieves a lower EER than the other four methods [27-29, 22, 31, 56], and therefore, the proposed algorithm shows a better performance. We conducted the above experiments on a 3.00 GHz Pentium IV PC with 2.5 GB RAM. We implemented our code in MATLAB 7.2. In order to achieve a higher recognition accuracy, the feature dimension should be small enough. In our proposed scheme, a subset of 600 original features were used for the feature pool of GAs, and the reduced dimensions of 530 and 487 features were obtained on the ICE and WVU datasets, respectively, after reasonable improvement of recognition rates. These rates were smaller than the number of features used in [27-29] and [31], where the numbers of components were 2048 and 660, respectively. However, only 200 reduced features were used in [22], a number which was much smaller than that used in the proposed method. In our proposed method, we used log-Gabor filters to capture local variations of the isolated pupillary area by comparing and quantizing the similarity between log-Gabor filters and local regions, as in the methods proposed in [22, 31]. In [22], a problem seems

to be that the use of spatial filters may fail in capturing the fine spatial changes of the iris. We overcome this possible drawback by capturing the local variations with use of log-Gabor filters, and then we use GAs to select the most discriminating feature sequence. In [41], the pupillary area was used with an eyelash detection technique for iris recognition. However, in our proposed scheme, we successfully isolated the pupillary area along with eyelash, eyelid and noise detection methods. We obtained a substantial improvement in the recognition rate and consequently overcame the problem when the pupil was badly occluded by eyelids and eyelashes. In [42], the pupillary area was utilized for iris recognition. However, no eyelash and eyelid detection methods were reported in [42]. In our proposed scheme, we deployed the eyelid and the eyelash detection methods to overcome the situation when the pupillary region is affected severely by the eyelids and the eyelashes. In [43], a basic GA was used to find a distribution of points over the iris region, leading the system to a reasonable accuracy of 99.70%, which was much higher than the accuracy of our method. However, this approach experimented on an ideal iris data set. In this chapter, we propose GAs where the main concerns are to minimize the recognition error based on the SVMs' performance on a validation dataset and to reduce the feature subset sizes. In [55], authors achieved a matching accuracy of 98.24% by using the traditional SVMs. However, their method may fail to control the unbalanced nature of sample proportions between classes and also suffer from misclassification errors. The usage of the asymmetrical SVMs proposed in this chapter can handle those issues carefully. The properly selected ratio between penalty parameters influences the trade-off between the cases of FA and FR to meet

several security requirements, depending on the various application areas, with reasonable CRRs of 97.70% and 95.60% for ICE and WVU datasets, respectively. However, a feature reduction approach based on direct discriminant analysis, other than the method proposed in this chapter with GAs, was used in [55]. Table 3.7 shows the time consumption of different parts of our proposed scheme, experimented on the ICE and WVU datasets. It shows that the iris segmentation part incurs a higher time consumption than the other parts because of the brute search strategy of the Hough transform.

Table 3.7: Comparison of average time consumption pertaining to the different parts of iris recognition system.

Methods	Iris segmentation (ms)	Normalization (ms)	Feature extraction (ms)	Matching (ms)	Total (ms)
Proposed approach (ICE dataset)	23436.0	42.6	27.8	157.7	23664.1
Proposed approach (WVU dataset)	28224.0	52.1	36.5	169.7	28482.3

3.8 Conclusion

In this chapter, an iris recognition method is proposed using an efficient iris segmentation approach based on the pupillary area localization, with the incorporation of eyelash and eyelid detection schemes. The log-Gabor filters are used to extract the discriminating features, and GAs are applied for feature subset selection. In order to increase the feasibility of the SVMs in biometric applications, the SVMs are modified into asymmetrical SVMs. The proposed iris recognition scheme using asymmetrical SVMs, GAs and pupillary area localization can be applied

to a wide range of security-related application fields. The experimental results exhibit an encouraging performance in both the accuracy and the speed in a constrained situation. In particular, a comparative study of existing methods for iris recognition is discussed. The performance evaluation and comparisons with other methods indicate that the proposed method is a viable and very efficient method for iris recognition.

Chapter 4

Towards Nonideal Iris Recognition Based on Active Contours, Genetic Algorithms and Adaptive Asymmetrical SVMs

The iris recognition algorithm discussed in the previous chapter may fail to perform well in a noncooperative environment, where the probability of acquiring nonideal iris images is very high due to gaze deviation, noise, blurring and occlusion by eyelashes, eyelids, glasses, and hair. In this thesis, the term 'nonideal' is used to account for the iris images with deviated gazes, specular reflections, blurs, variations of light, and occlusions.

In this chapter, we present iris recognition methodologies that can cope with the nonideal iris images. Section 4.1 introduces the background of the current problem. In Section 4.2, we first present a reflection detection scheme. Then, the iris/pupil localization algorithms, based on active contour models, are discussed. We also describe an unwrapping process that deals with the size inconsistencies in the localized iris regions. The distinctive feature extraction process is presented in Section 4.3. A feature selection scheme, based on GA, is proposed in Section 4.4.

Section 4.5 introduces the iris pattern matching technique using AASVMs. The performance of the proposed method is evaluated in Section 4.6 through extensive experiments. Finally, in Section 4.7, the most important findings of this investigation are summarized.

4.1 Introduction

Most current iris recognition algorithms claim to perform with a very high recognition accuracy in a strictly constrained situation, where the iris images are acquired in a sophisticated imagery setup to ensure the higher performance. Under inflexible image acquiring constraints, it is possible to capture high quality images and attain an impressive accuracy with a very low error rate. However, recognition accuracies substantially decrease when the captured images do not have enough quality, either due to focus, contrast, or brightness problems and iris obstructions or reflections [67-70]. In a strict capturing environment, individuals need to stop and look into the iris camera from a predetermined distance, and then, the images are captured. However, the iris images acquired in an unconstrained situation produce nonideal iris images with a varying image quality. If the iris regions are severely occluded by eyelids and eyelashes and the eyes are not properly opened, certain portions of the iris cannot be processed due to occlusion, which further affects the segmentation performance, and consequently, the overall recognition accuracy. Iris images may also be affected from motion blur, camera diffusion, head rotation, gaze direction, camera angles, reflections, contrast, luminosity, and problems due to contraction and dilation [67]. Daugman [27-29], Ma et el. [22, 31], Boles and

Boashash [32], Wildes et al. [33, 71] and several other researchers proposed different iris recognition methods [72-153]. While most of the literature is focused on the processing of ideal iris images, recently, there have been important new directions identified in iris biometric research. These include the processing and recognition of 'nonideal irises' and 'iris at a distance and on the move' [74]. In this chapter, we deploy the methodologies to compensate for the various nonidealities found in the iris images and to design a nonideal iris recognition scheme. We mainly focus on improving the iris recognition performance by the accurate localization of iris images, captured in a flexible imagery setup, with textural feature extraction, optimal feature subset selection and classification of iris patterns. Fig. 4.1 shows the samples of nonideal iris images.

Most state-of-the-art literature on iris biometrics is focused on the preprocessing of a frontal view iris image of an eye, which is achieved through a stop and stare

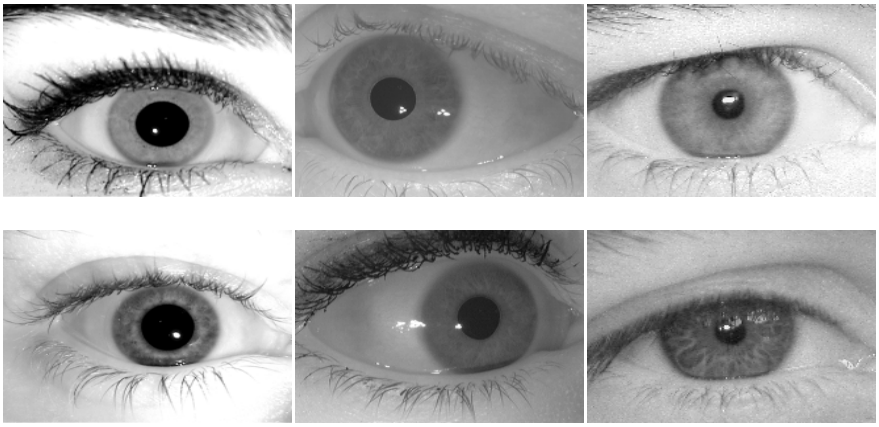

(a) (b) (c)

Fig. 4.1 Sample of nonideal iris images: (a) ICE 2005, (b) WVU Nonideal, and (c) UBIRIS Version 1.

interface, in which a user must align his/her optical axis with the camera's optical axis [67]. It is not practical to assume that a user always aligns his/her optical axis with the camera's optical axis due to the increasing security issues. For iris segmentation, most of the researchers assume that the iris is circular or elliptical. However, in the case of nonideal iris images, which are captured in an uncontrolled environment, iris may appear as noncircular or nonelliptical [67, 74]. Also, in the images where the eyes are not properly opened, highly occluded regions cannot be extracted, and thus, the segmentation performance is deteriorated [67]. As mentioned earlier, the iris images may also be affected by the following situations: the deviated gaze, non-linear deformations, pupil dilation, head rotation, motion blur, reflections, non-uniform intensity, low image contrast, camera angles and diffusion, and the presence of eyelids and eyelashes. Therefore, these factors hamper the recognition accuracy substantially. In this chapter, we propose a three-stage iris segmentation algorithm, in which, we first detect the specular reflections that usually occur inside the pupil region. In the second stage, we deploy the Direct Least Square (DLS) elliptical fitting method to approximate the pupil and iris boundaries. In the final stage, we apply the geometric active contours, i.e., the active contours implemented via the LS to localize the inner/outer boundary based on the approximation of an iris contour. The DBWT is applied to elicit the textural features from the unwrapped image, and this approach is appropriate for analyzing the signals in a multi-resolution mode.

In the field of iris biometric recognition, the iris data obtained from experiments is often high-dimensional with Small-Sample-Sizes (SSS), which results in a number of

computational and representational problems. In a secured and sophisticated biometric identification system, where the user interaction with the capturing device is kept to the minimum, the authentication system is expected to demonstrate a high level of accuracy with that limited amount of data. Therefore, the iris data obtained in a nonideal situation contains a huge number of textural features with SSS. Selecting the best features from the higher-dimensional feature space has several potential benefits, including defying the curse of dimensionality to enhance the prediction performance, reducing the measurement and storage requirements and decreasing the training and prediction times [48, 61, 62]. In this chapter, we focus on the utilization of useful information obtained from the different feature selection methods. This information is used to choose the most prominent feature subset and also to improve the matching accuracy [154]. Therefore, we propose to apply GAs to select the significant feature subset by combining the valuable outcomes from the multiple feature selection criteria. The proposed approach provides a convenient way of selecting a better feature subset based on the performance of the different feature selection schemes [154]. To evaluate the proposed scheme, the following methods are used: SVM-Recursive Feature Elimination (RFE), k-Nearest Neighbour (k-NN), T-statistics, and entropy-based methods. These methods provide the candidate features for selection of the optimal feature subset using GAs. Our experimental results exhibit an encouraging performance in a noncooperative environment, where the probability of acquiring large number of samples per iris class is very low.

The asymmetrical SVMs, discussed in chapter 3, are used to improve the performance when the sample proportion between two classes is poorly balanced and to handle the misclassification error [46, 155]. The asymmetrical SVMs also have a significant influence on the cases of FA and FR [45, 49]. Unfortunately, the asymmetrical SVMs are considerably slower in test phase, caused by the number of Support Vectors (SVs). This slowness has been a serious limitation for some real time applications like iris recognition [13, 136]. To overcome this problem, we also deploy an adaptive algorithm to select the Feature Vector (*FV*) from the SV solutions, according to the vector correlation principle and the greedy method [13, 136]. This scheme successfully overcomes the problem of the huge computation cost incurred by the large number of SVs, thereby speeding up the matching process drastically. Therefore, we combine the asymmetrical approach with the adaptive simplification of the solution for SVMs, and denote this combined approach as 'Adaptive Asymmetrical SVMs' (AASVMs). This approach is well-suited for the iris datasets such as ICE 2005, WVU Nonideal, CASIA Version 3 Interval and UBIRIS Version 1, in which the number of samples per subject is small and not fixed.

4.2 Iris/Pupil Localization Algorithm

The segmentation of the nonideal iris image is a challenging task because of the noncircular/nonelliptical shapes of the pupil and iris [85, 86]. Several researchers have proposed different techniques for segmentation [27-35, 38, 41, 42, 45, 46, 51, 52, 53, 57, 67-72, 74-78, 80-88, 91-96, 101-103, 137, 138, 140-142, 145, 146, 148-151]. As mentioned in the Chapter 3, Daugman [27-29] used the integrodifferential

operator to localize the iris/pupil boundaries. Boles and Boashash [32] applied the edge detection method and other image processing techniques to localize the iris region. Wildes et al. [33, 71] employed the binary edge map and the Hough transform to detect the iris and pupil boundaries. Ma et al. [22, 31] used the Hough transform to detect the inner and outer boundaries of the iris. In [3], Miyazawa et al. deployed a deformable iris model to detect the iris boundary. In [38, 152], authors employed the Canny edge detection and circular Hough transform to localize the iris boundaries of the noisy iris images, and the local Partial Hausdorff Distance (PHDD) was employed for comparing the binary edge maps.

Most of the current iris recognition schemes have processed the iris images that are captured on-axis. Recently, researchers have focused on the processing of nonideal iris images, which are defined as accounting for the off angle, occluded, blurred and noisy images. Previous techniques on nonideal iris recognition were not adjusted and designed specifically for the nonideal situations [68-70]. For iris segmentation, most of the researchers have assumed that the iris is circular or elliptical. However, in the case of nonideal iris images, an iris may appear as noncircular or nonelliptical. Because the inner boundary may be partially occluded by the reflections, and the outer boundary may be partially occluded by the eyelids, it is important to fit the flexible contour that can stand for such disturbances.

Several researchers have proposed different nonideal iris segmentation methods [1, 67, 74-86, 88, 91, 92, 94, 101, 102, 137, 140-149, 151]. Two approaches were proposed in [74], where the first approach compensated for the off-angle gaze direction, and the second approach used an angular deformation calibration model.

Proença [76] presented a segmentation method that could cope with the nonideal iris images. Proença [76] considered the sclera as the most easily distinguishable part of the eye in degraded images, and proposed a new type of feature that measures the proportion of the sclera in every direction. This entire process was executed in a deterministically linear time in respect to the size of the image. Thus, the segmentation procedure became suitable for real-time applications. In [77], Zhang et al. proposed a new localization algorithm based on the radial symmetry transform, in which the radial symmetry characteristic of the pupil was utilized to locate the iris. Proença and Alexandre [1] proposed an iris classification method that divided the segmented and normalized iris image into six regions. These authors [1] then compared the extracted features of each region, and combined each of the dissimilarity values through a classification rule. A nonideal iris image segmentation approach based on graph cuts was presented in [78], where both the appearance and eye geometry information were used for accurate localization. To improve the segmentation performance, the quality of iris images were enhanced using the wavelet domain with in-band de-noising method in [79]. The approach in [80] presented a fast iris segmentation method that relies on the closed nested structures of the iris anatomy and on its polar symmetry. This segmentation method was applied using the mathematical morphology for polar/radial-invariant image filtering and for circular segmentation. The morphology used shortest paths from the generalized grey-level distances. Tan et al. [138] proposed a clustering based coarse iris localization scheme to extract a rough position of the iris, as well as to identify non-iris regions such as eyelashes and eyebrows. A modified

integrodifferential constellation was then developed for the localization of pupillary and limbic boundaries. After that, a curvature model and a prediction model were learned to deal with eyelids and eyelashes, respectively.

In [142], a segmentation method that uses a coarse to fine approach to extract the iris region was deployed. In [140], authors proposed a video-based image processing approach that can help the traditional iris recognition systems to work in the nonideal situations. This scheme identified and eliminated the bad quality images from iris videos for further processing. The segmentation evaluation scheme was designed to assess the segmentation performance. The distance-based quality measure was applied to evaluate if the image has a good enough quality for recognition. Then, the segmentation evaluation score and quality score were combined to predict the recognition performance. Puhan et al. [141] proposed a segmentation scheme to localize the limbic and pupil boundaries from the noisy frontal view of iris images using the Fourier spectral density. In [143], a wavefront-coding system was applied to achieve an extended depth of field when the user cooperation is not sufficient to acquire iris images that are in focus. Hollingsworth et al. [144] observed the effect of pupil dilation on the accuracy of iris biometrics. Their experiments revealed the fact that when the degree of dilation is similar at enrollment and recognition, comparisons involving highly dilated pupils result in a worse recognition performance than comparisons involving constricted pupils. Tajbakhsh et al. [145] proposed an approach to verify the noisy irises using the modified local intensity variation method. In [146], authors applied the elliptical fitting technique to localize the iris/pupil regions along with other image processing

techniques for reflection detection, contrast enhancement, occlusion estimation and off-angle compensation. Belcher and Du [147] applied the region-based Scale Invariant Feature Transform (SIFT) to elicit the iris structure. In [148], an eyeball segmentation approach based on the Fourier spectral density was employed for the degraded iris images. Proenca and Alexandre [149] applied a clustering algorithm along with canny edge detector and circular Hough transform to separate the iris region from a nonideal iris image. In [76], the author initially detected the sclera and the iris regions. The mandatory adjacency of the sclera and the iris was then exploited to detect the noise-free iris regions. Finally, the detected iris was parameterized using the polynomial regression.

Recently, Al-Daoud [81] introduced an iris localization method based on the competitive chords. The basic idea was to create a set of chords from the left edges and the right edges of the pupil (or iris), and then find the winner chords with aligned centres. The winner chords were used to compute the correct pupil's (or iris's) centre and radius. In [82], Jeong et al. applied the AdaBoost eye detection method to compensate for the iris detection error caused by the two circular edge detection operations, and then, used a color segmentation technique for detecting obstructions by the ghosting effects of visible light. Proença and Alexandre [83, 137] analyzed the relationships between the accuracy of the iris segmentation process and the error rates of three typical iris recognition methods.

Another important consideration for accurate localization is that the inner and outer boundary models must form a closed curve [67, 75]. In this light, several researchers have proposed active contour-based iris segmentation schemes. In [75],

inner and outer boundaries were detected in terms of active contours, based on the discrete Fourier series expansions of the contour data. In [67], a curve evolution approach was proposed based on the modified Mumford-Shah segmentation model. In [84], a segmentation scheme was proposed, using a traditional active contour model and the Hough transform. The Geodesic Active Contours (GAC) were applied to segment the nonideal iris images in [85, 86]. The segmentation approaches proposed in [75, 84-86] took a long computational time as the curve evolved from the previously obtained pupil boundary to the outer boundary. Also, the parametric active contour-based iris segmentation scheme may terminate at a certain local minima such as the specular reflections, the thick radial fibres in the iris or the crypts in the ciliary region. The active contours with an edge stopping function as a halting criteria proposed in [67, 84-86] may fail to detect the outer boundary accurately, since the iris is separated from the sclera region by a relatively smooth boundary. In addressing the above problems, we propose a three-stage iris/pupil segmentation algorithm in which we first detect the specular reflections that occur inside the pupil boundary. In the second stage, we approximate the iris/pupil boundary so that the curve evolution process can start from that estimated region and can avoid any unnecessary delays during the propagation process. In the third stage, we apply three active contour-based localization schemes: LS method, VLS method, and RAC model. We first apply the LS-based curve evolution approach using the edge stopping function to detect the inner boundary [8-10, 156]. We evolve the curve (based on the LS method) again towards the outer boundary, using the energy minimization algorithm in order to detect the iris boundary [8-10, 156-

159]. Most of the current nonideal iris segmentation schemes, based on active contour model including the LS-based method proposed above, require a huge computational time due to the expensive curve evolution approach [67, 75, 84-86]. This time requirement impedes the traditional LS-based iris recognition systems, to be deployed in real-time situations. Therefore, we demonstrate the application of the VLS-based curve evolution approach to find the pupil and iris boundaries accurately [11]. The proposed segmentation scheme with the VLS approach uses a larger time step to numerically solve the evolution PDE, and thereby, this approach speeds up the curve evolution process drastically [11]. However, this method may fail to detect the outer boundary when the iris/sclera region is separated by a relatively blurred boundary. Furthermore, the intensity inhomogeneity often occurs in the nonideal iris images due to reflections, motion blur, luminosity, etc. The nonideal iris segmentation schemes based on active contour models proposed in [67, 75, 84-86] tend to rely on the intensity homogeneity in each of the regions to be segmented. Therefore, we finally apply a modified Chan-Vese [12] curve evolution scheme, which extracts the intensity information in local regions at a controllable scale. This RAC model finds the pupil and iris boundaries accurately [9, 10, 12, 156-159]. A data fitting energy is defined in terms of a contour and two fitting functions that locally approximate the image intensities on the two sides of the contour. This energy is then incorporated into a VLS formulation with a regularization term. Due to the kernel function used in the energy functional, the extracted intensity information of the local regions is deployed to guide the motion of the contour. This extracted information assists the curve evolution scheme to cope with the intensity

inhomogeneity that occurs in the same region [12]. In addition, the LS regularization term is used to ensure the accurate computation and to avoid the expensive reinitialization of the evolving curve. In the following paragraphs, we describe the three-stage iris/pupil segmentation process in detail.

According to Kong and Zhang [26], in the first stage of segmentation, we detect the strong reflection area by deploying a simple thresholding approach. A pixel, which has an intensity value higher than a certain threshold, belongs to the strong reflection area. The reflection is detected by the following inequality [26]:

$$g(x, y) > T_s \tag{4.1}$$

where $g(x, y)$ denotes the intensity of an image at the point (x, y), and T_s is the required threshold value. A weak reflection, on the other hand, is defined as a transition from a strong reflection to the iris [26]. The following statistical inequality is deployed to detect the weak reflection points [26]:

$$\mu + \gamma\sigma < g(x, y) \tag{4.2}$$

where μ and σ are the mean and standard deviation for the distribution of the intensity in the iris image $g(x, y)$, respectively, and γ is a control parameter. Any point that is around the strong reflection area and that satisfies the equation (4.2) belongs to weak reflection. A detailed description of this method can be found in [26]. Fig. 4.2 exhibits the reflection detection results. In the second stage, prior to applying the curve evolution approach, we first deploy DLS-based elliptical fitting to approximate the pupil boundary. The DLS-based elliptical fitting returns five

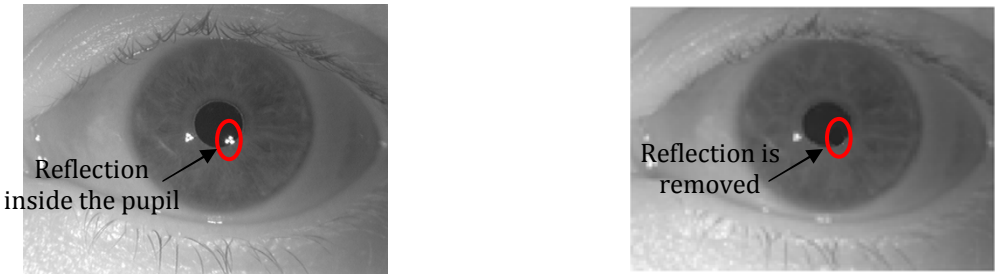

(a)

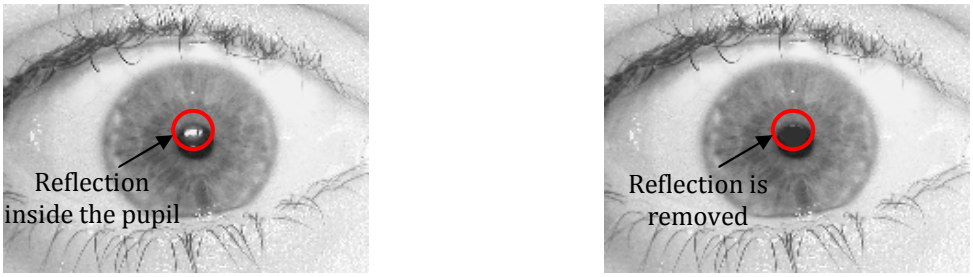

(b)

Fig. 4.2 Reflection detection on (a) a sample image of the WVU Nonideal dataset, and (b) a sample image of the UBIRIS Version 1 dataset.

parameters (p_1, p_2, r_1, r_2, φ_1): the horizontal and vertical coordinates of the pupil centre (p_1, p_2); the length of the major and minor axes (r_1, r_2); and the orientation of the ellipse φ_1. To approximate the outer boundary, we apply the DLS-based elliptical fitting again, and obtain five parameters (I_1, I_2, R_1, R_2, φ_2): the horizontal and vertical coordinates of the iris center (I_1, I_2); the length of the major and minor axes (R_1, R_2); and the orientation of the ellipse φ_2. This method, thus, provides the rough estimation of iris and pupil boundaries. Fig. 4.3 shows the approximated iris/pupil boundary. Finally, in the following subsections, we segment the iris and pupil boundaries from the eye image using three active contour models (Sections 4.2.1, 4.2.2 and 4.2.3), and then, we detect the eyelash and unwrap the localized iris region into a rectangular block of a fixed dimension (Section 4.2.4).

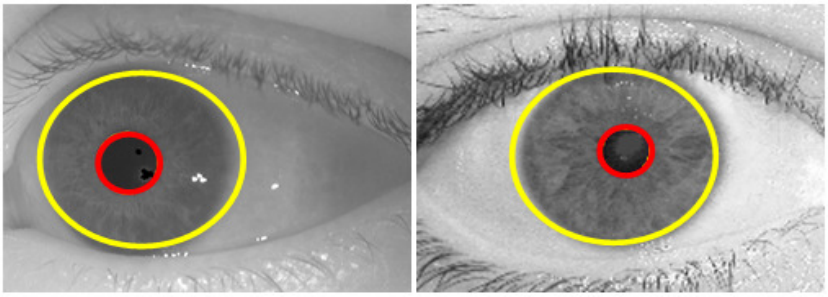

Fig. 4.3 Approximation of iris and pupil boundaries using the DLS-based elliptical fitting.

4.2.1 Localization using Level Set (LS) Method

As mentioned in the previous section, we apply the active contour models to isolate the inner and outer boundaries. A detailed description of the proposed iris/pupil segmentation algorithm, using the LS method, is given below.

4.2.1.1 Pupil Segmentation Using LS Method

In order to obtain the optimal estimate of the inner (pupil) boundary, we apply the geometric active contours. This method is based on the edge stopping function in a narrow band over the estimated inner boundary, since the pupil region is the darkest part of the eye and is separated by a relatively strong gradient from the iris region [67]. A brief discussion of the LS-based curve evolution approach is given as follows [8, 68]:

Let Ω be the image domain, and I be the 2D iris image. Let us consider the evolving curve C in Ω, as the boundary of an open subset ω of Ω. The main idea is to embed this evolving curve as the zero-LS of a higher dimensional function. We can define the following function:

$$\phi(x, y, t = 0) = \pm d \tag{4.3}$$

where d denotes the distance from (x, y) to C at time $t=0$. The plus (or minus) sign is selected if the point (x, y) is outside (or inside) the curve C. Therefore, in the curve evolution approach for pupil segmentation, we need to solve the PDE of the following form [159]:

$$\frac{\partial \phi}{\partial t} = g(I)\big(S_1|\nabla_\phi| + S_2|\nabla_\phi|\big), \phi(x, y, 0) = \phi_0(x, y) \tag{4.4}$$

where S_1 is a constant advection term that forces the curve to expand or contract uniformly based on the its sign, while S_2 depends on the curve geometry and is used to smooth out the high curvature region. The set $\{(x, y), \phi_0\,(x, y) = 0)$ defines the initial contour, and $g(I)$ is an edge stopping function that is used to halt the evolution of the curve at the inner boundary. The $g(I)$ can be defined as:

$$g(I) = \frac{1}{1+|\nabla G_\sigma(x,y) * I(x,y)|^\rho}\ , \rho \geq 1 \tag{4.5}$$

where $G_\sigma(x, y) * I(x, y)$ is the convolution of I with the Gaussian $G_\sigma(x, y) = \sigma^{-1/2} e^{-|x^2+y^2|/4\sigma}$. Now to discretize ϕ, we apply the finite differences scheme proposed in [157]. To evolve the curve, we perform the discretization and linearization of (4.4) [156, 157]:

$$\emptyset_{i,j}^{n+1} = \emptyset_{i,j}^{n} - \Delta t\big[\hat{g}(I)(\hat{s}_1|\nabla_\phi| + \hat{s}_2|\nabla_\phi|)\big] \tag{4.6}$$

where Δt is the time step, $(x_i, y_{j,})$ are the grid points for $1 \leq i, j \leq M$, and $\phi_{i,j}^n = \phi\ (x_i, y_{j,} n\delta t)$ approximates $\phi(x, y, t)$ with $n \geq 0, \phi^0 = \phi_0$. In [157], an upwind scheme is used to estimate $s_1|\nabla_\phi|$ of (4.6):

$$s_1|\nabla_{\emptyset}| =$$

$$\left[\max\left(\Delta_{-}^{x}\phi_{i,j}^{n},0\right)^2+\min\left(\Delta_{+}^{x}\phi_{i,j}^{n},0\right)^2+\max\left(\Delta_{-}^{y}\phi_{i,j}^{n},0\right)^2+\min\left(\Delta_{+}^{y}\phi_{i,j}^{n},0\right)^2\right]^{1/2} \quad (4.7)$$

and the term $s_2|\nabla_{\emptyset}|$ depends on curvature K ($K = div\left(\frac{\nabla_{\phi}}{|\nabla_{\phi}|}\right)$) and can be estimated as:

$$s_2|\nabla_{\phi}| = -\epsilon K[(^{\phi_{i+1,j}^{n}-\phi_{i-1,j}^{n}}/_{2})^2+(^{\phi_{i,j+1}^{n}-\phi_{i,j-1}^{n}}/_{2})^2] \quad (4.8)$$

where ϵ is a constant. Next, the active contour ϕ_0 is initialized to the approximated pupil boundary, and the optimal estimate of the inner boundary is measured by evolving the initial contour in a narrow band of ± 10 pixels. Fig. 4.4(b) shows segmentation of a pupil based on the algorithm mentioned above.

4.2.1.2 Iris Segmentation Using LS Method

In order to evolve the curve towards the outer boundary, we apply the Mumford-Shah segmentation model with the regularization terms [8-10]. Therefore, the main objective is to minimize the length of the curve and the area of the region inside the curve. We introduce the following energy function, E [8]:

$$E(C,c_1,c_2) =$$

$$\mu\int_{\Omega}\delta\left(\phi(x,y)\right)\left|\nabla_{\phi}(x,y)\right|dxdy+v\int_{\Omega}H\left(\phi(x,y)\right)dxdy+\lambda_1\int_{\Omega}|I(x,y)-$$

$$c_1|^2H\left(\phi(x,y)\right)dxdy+\lambda_2\int_{\Omega}|I(x,y)-c_2|^2\left(1-H\left(\phi(x,y)\right)\right)dxdy \quad (4.9)$$

where $\mu \geq 0, v \geq 0, \lambda_1 > 0, \lambda_2 > 0$ are the positive constants, C is the evolving curve, c_1, c_2 are the averages of iris image I inside and outside of C, respectively, ϕ denotes the zero LS of the Signed Distance Function (SDF) representing C as in (4.3), H is the

Heaviside function, and δ is the Dirac measure. The first and the second terms on the right-hand side of (4.9) denote the area and length at $\phi = 0$, respectively. Therefore, the main goal is to estimate the values of C, c_1, c_2 such that $E(C, c_1, c_2)$ is minimized. We parameterize the descent direction by $t \geq 0$, and deduce the Euler-Lagrange PDE from (4.9), which leads to the following active contour model:

$$\phi_t' = \delta(\phi)\left[\mu\, div\left(\nabla_\phi \Big/ |\nabla_\phi|\right) - v - \lambda_1(I - c_1)^2 + \lambda_2(I - c_2)^2\right] = 0 \quad (4.10)$$

Next, we regularize the Heaviside function H, and the Dirac measure δ as in [9]:

$$H_\epsilon\big(\phi(x,y)\big) = \frac{1}{2} + \frac{1}{\pi}\arctan\left(\frac{\phi(x,y)}{\epsilon}\right) \quad (4.11)$$

and thus,

$$\delta\big(\phi(x,y)\big) = \frac{1}{\pi}\cdot\frac{\epsilon}{\epsilon^2 + (\phi(x,y))^2} \quad (4.12)$$

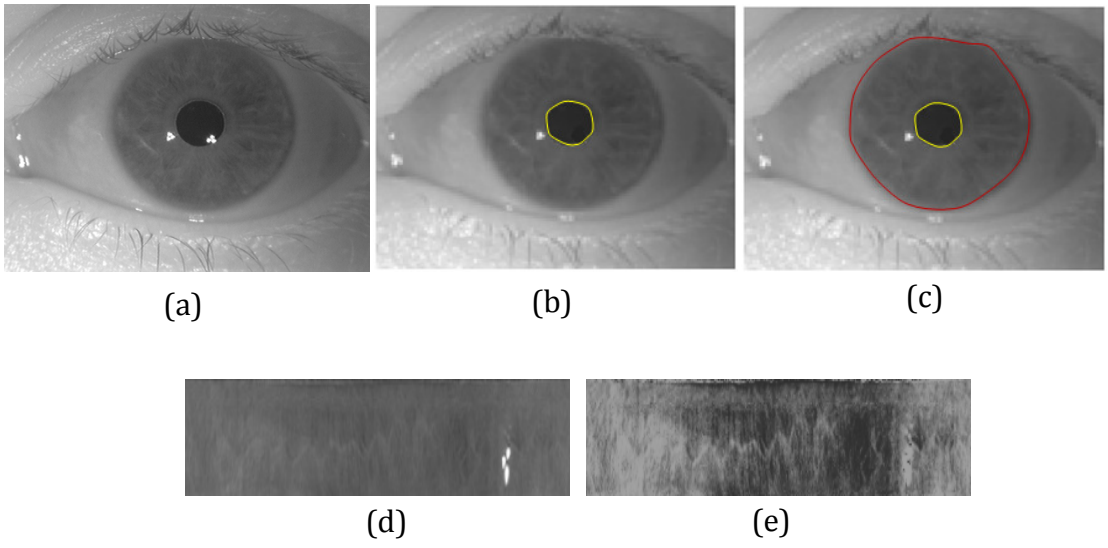

Fig. 4.4 (a) Original image from the WVU Nonideal dataset, (b) pupil detection using the LS Method, (c) iris detection using the LS Method, (d) normalized image, and (e) enhanced image.

From (4.12), we can observe that the evolution scheme has the tendency to measure the global minimizer with the applied regularizations. By discretizing and linearizing (4.10), we obtain:

$$\frac{\phi_{i,j}^{n+1}-\phi_{i,j}^{n}}{\Delta t} = \delta_{\epsilon}\left(\phi_{i,j}^{n}\right)[\mu K - v - \lambda_1\left(I_{i,j} - c_1(\phi^n)\right)^2 + \lambda_2\left(I_{i,j} - c_2(\phi^n)\right)^2] \quad (4.13)$$

Here, we use the rough estimation of the iris boundary as the initial contour ϕ, and the curve is evolved in the narrow band of ± 15 pixels to detect the exact outer boundary. Fig. 4.4 (c) shows the iris segmentation result.

4.2.2 Localization Using Variational Level Set (VLS) Method

Based on the approximation of the inner and outer boundaries using the elliptical fitting process, the curve is evolved by using the VLS method for accurate segmentation of the pupil and the iris regions [9, 11, 69]. In the following paragraphs, we briefly discuss this segmentation process by using VLS method.

In the LS formulation, the active contours, denoted by C, can be represented by the zero LS $C(t) = \{(x, y)|\phi(t, x, y) = 0\}$ of a LS function $\phi(t, x, y)$. To evolve the curve towards the inner and outer boundaries, we define the following total energy functional according to [11]:

$$\varepsilon(\phi) = \mu\rho(\phi) + \varepsilon_{g,\lambda,v}(\phi) \quad (4.14)$$

where $\varepsilon_{g,\lambda,v}(\phi)$ denotes the external energy, which depends on the image data and drives the zero LS towards the iris boundaries, and $\mu\rho(\phi)$ $(\mu > 0)$ denotes the internal energy, which penalizes the deviation of ϕ from the SDF during the evolution and is defined as:

$$\rho(\phi) = \int_{\Omega} \frac{1}{2}(|\nabla\phi| - 1)^2 dxdy \tag{4.15}$$

where Ω is the image domain. In (4.14), g denotes the edge detector function and is defined by:

$$g = \frac{1}{1+|\nabla G_{\sigma} * I|^2} \tag{4.16}$$

where G_{σ} is the Gaussian kernel with a standard deviation denoted as σ, and I denotes an iris image. We can further define the external energy term $\varepsilon_{g,\lambda,v}(\phi)$ of (4.14) as:

$$\varepsilon_{g,\lambda,v}(\phi) = \lambda L_g(\phi) + vA_g(\phi) \tag{4.17}$$

where $\lambda > 0$ and v are constants, and the terms $L_g(\phi)$ and $A_g(\phi)$ in (4.17) are respectively defined by [11]:

$$L_g(\phi) = \int_{\Omega} g\delta(\phi)|\nabla\phi| dxdy \tag{4.18}$$

and

$$A_g(\phi) = \int_{\Omega} gH(-\phi) dxdy \tag{4.19}$$

where δ is the univariate Dirac function, and H is the Heaviside function. The energy functional $L_g(\phi)$ measures the length of the zero LS curve of ϕ, and $A_g(\phi)$ is used to speed up the curve evolution. From the calculus of variations, the Gateaux derivative of the functional ε in (4.14) can be written as:

$$\frac{\partial\varepsilon}{\partial\phi} = -\mu\left[\Delta\phi - div\left(\frac{\nabla\phi}{|\nabla\phi|}\right)\right] - \lambda\delta(\phi) div\left(g\frac{\nabla\phi}{|\nabla\phi|}\right) - vg\delta(\phi) \tag{4.20}$$

where Δ is the Laplacian operator. The function ϕ that minimizes this functional satisfies the Euler-Lagrange equation $\frac{\partial\varepsilon}{\partial\phi} = 0$. Next, the desired evolution equation of the LS function is defined as:

$$\frac{\partial\phi}{\partial t} = \mu\left[\Delta\phi - div\left(\frac{\nabla\phi}{|\nabla\phi|}\right)\right] + \lambda\delta(\phi) div\left(g\frac{\nabla\phi}{|\nabla\phi|}\right) + vg\delta(\phi) \tag{4.21}$$

The second and third terms on the right-hand side of (4.21) represent the gradient flows of the energy functional and are responsible for driving the zero level-curve towards the inner/outer boundaries of the iris. The Dirac function $\delta(x)$ in (4.21) is defined by:

$$\delta_\epsilon(x) = \begin{cases} 0, & |x|>\epsilon \\ \frac{1}{2\epsilon}\left[1+\cos\left(\frac{\pi x}{\epsilon}\right)\right], & |x|\leq\epsilon \end{cases} \tag{4.22}$$

In order to estimate the exact boundary of the pupil, we initialize the active contour ϕ to the approximated pupil boundary, and evolve the curve in the narrow band of ± 10 pixels. We evolve the curve from inside the approximated inner boundary to avoid the effect of reflections that may occur just outside the pupil. Similarly, for computing the outer boundary, the active contour ϕ is initialized to the estimated iris boundary, and the optimal estimation of the iris boundary is computed by evolving the curve in a narrow band of ± 20 pixels. In this case, the curve is evolved again from inside the approximated iris boundary to reduce the effects of the eyelids and the eyelashes. Fig. 4.5 shows the iris/pupil segmentation results using the VLS method.

4.2.3 Localization Using Region-Based Active Contour (RAC) Model

In this phase of the segmentation, the curve is evolved using the modified Chan-Vese functional [9, 12, 160] for accurate segmentation of the pupil and iris regions. In the following paragraphs, we briefly discuss the segmentation process based on the

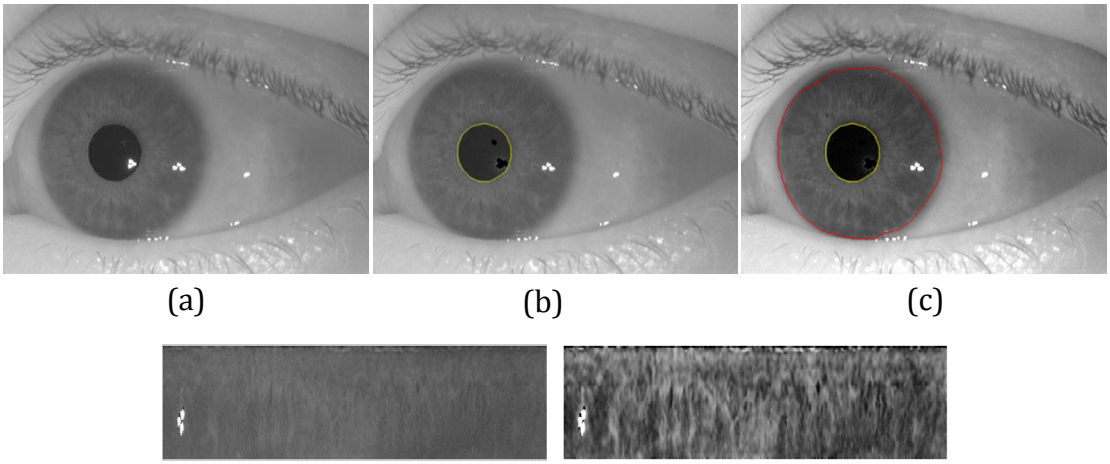

Fig. 4.5 (a) Original image from the WVU Nonideal dataset, (b) pupil detection using the VLS method, (c) iris detection using the VLS method, (d) normalized image, and (e) enhanced image.

RAC approach [9, 12]. In our proposed curve evolution method, the following energy functional is deployed:

$$F\left(\varphi, f_{1,} f_2\right) = E\left(\varphi, f_{1,} f_2\right) + \mu P(\varphi) \tag{4.23}$$

The term $E\left(\varphi, f_{1,} f_2\right)$ in (4.23) can be defined as [12]:

$$E\left(\varphi, f_{1,} f_2\right) = \sum_{i=1}^{2} \lambda_i \int \left(\int G_\sigma(x-y) |I(y) - f_i(x)|^2 N_i\left(\varphi(y)\right) dy \right) dx + \nu \int \left|\nabla H\left(\varphi(x)\right)\right| dx \tag{4.24}$$

where, the LS function φ represents the closed contour C in the image domain Ω, and this closed contour separates Ω into two regions: $\Omega_1 = outside\,(C)$ and $\Omega_2 = inside\,(C)$. The λ_i are positive constants, and the functions $f_i(x)$ are the values that approximate the image intensities outside and inside of the closed contour C. In this research effort, the LS function φ takes the positive and negative values outside and inside C, respectively. In (4.24), H is the Heaviside function and $N_1(\varphi) = H(\varphi)$,

$N_2(\varphi) = 1 - H(\varphi)$. The intensities $I(y)$ are effectively involved in the above energy term, and are in a local region centred at the point x. The size of $I(y)$ can be controlled by the Gaussian kernel function, $G_\sigma = \frac{1}{(2\pi)^{n/2}\sigma^n} e^{-|u|^2/2\sigma^2}$ with a scale parameter $\sigma > 0$. The last term $\int \left|\nabla H\left(\varphi(x)\right)\right| dx$ on the right-hand side of (4.24) computes the length of the zero-level contour of φ. The length of the zero-level contour can be equivalently defined by the integral $\int \delta(\varphi)|\nabla\varphi| dx$ with the Dirac delta function, δ. The Heaviside function H can be approximated as follows:

$$H_\epsilon(x) = \frac{1}{2}\left[1 + \frac{2}{\pi}\arctan\left(\frac{x}{\epsilon}\right)\right] \tag{4.25}$$

The derivative of H_ϵ is $\delta_\epsilon(x) = H'_\epsilon(x) = \frac{1}{\pi}\frac{\epsilon}{\epsilon^2 + x^2}$. If we replace H in (4.24) with H_ϵ, the energy functional E in (4.24) can be approximated by [12, 70]:

$$E_\epsilon\left(\varphi, f_{1,} f_2\right) = \sum_{i=1}^{2} \lambda_i \int \left(\int G_\sigma(x-y)|I(y) - f_i(x)|^2 N_i^\epsilon\left(\varphi(y)\right) dy\right) dx + \nu \int \left|\nabla \mathrm{H}_\epsilon\left(\varphi(x)\right)\right| dx \tag{4.26}$$

where $N_i^\epsilon(\varphi) = H_\epsilon(\varphi)$ and $N_i^\epsilon(\varphi) = 1 - H_\epsilon(\varphi)$.

The LS regularized term $\mu P(\varphi)$, $(\mu > 0)$ in (4.23), which is used for accurate computation and stable LS evolution, can be defined as $P(\varphi) = \int \frac{1}{2}(|\nabla\varphi(x)| - 1)^2 dx$. This regularized term measures the deviation of the function φ from an SDF. Next, we minimize the energy functional $F\left(\varphi, f_{1,} f_2\right)$ with respect to φ, using the standard gradient descent method by solving the gradient flow equation as follows:

$$\frac{\partial\varphi}{\partial t} = -\delta_\epsilon(\varphi)(\lambda_1 e_1 - \lambda_2 e_2) + \nu\delta_\epsilon(\varphi) div\left(\frac{\nabla\varphi}{|\nabla\varphi|}\right) + \mu\left(\nabla^2\varphi - div\left(\frac{\nabla\varphi}{|\nabla\varphi|}\right)\right) \tag{4.27}$$

where e_1 and e_2 are functions which can be expressed as:

$$e_i(x) = \int G_\sigma(y-x)|I(x) - f_i(y)|^2 dy\,, \quad i = 1,2 \tag{4.28}$$

The above (4.27) is the required active contour model. The term $-\delta_\epsilon(\varphi)(\lambda_1 e_1 - \lambda_2 e_2)$ is responsible for driving the active contour toward the iris/pupil boundaries. The second term $\nu\delta_\epsilon(\varphi)div\left(\frac{\nabla\varphi}{|\nabla\varphi|}\right)$ has a length shortening or smoothing impact on the zero-level contour, which is useful in maintaining the regularity of the contour. The third term $\mu\left(\nabla^2\varphi - div\left(\frac{\nabla\varphi}{|\nabla\varphi|}\right)\right)$ is denoted as a LS regularization term, which is used to maintain the regularity of the LS function. In order to estimate the exact boundary of the pupil, we initialize the active contour φ to the approximated pupil boundary, and evolve the curve in the narrow band of ± 10 pixels. We evolve the curve from inside the approximated inner boundary to avoid the effect of reflections that may appear just outside the pupil region. Similarly, for computing the outer boundary, the active contour φ is initialized to the estimated iris boundary, and the optimal estimation of the iris boundary is computed by evolving the curve in a narrow band of ± 20 pixels. In this case, we evolve the curve again from inside the approximated iris boundary to reduce the effects of the eyelid and eyelash occlusions. Fig. 4.6 (b, c) shows the segmentation results.

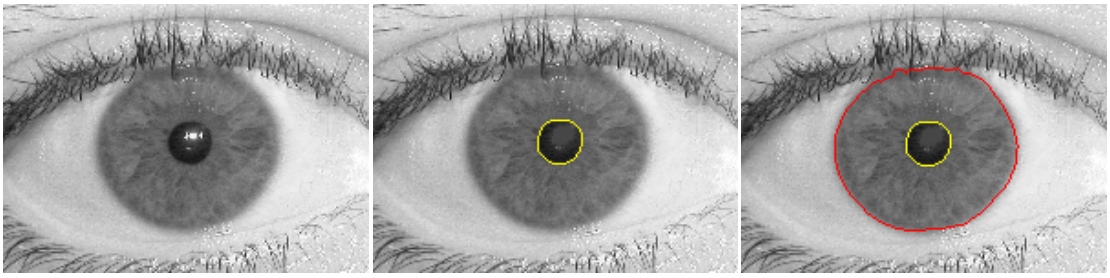

(a) (b) (c)

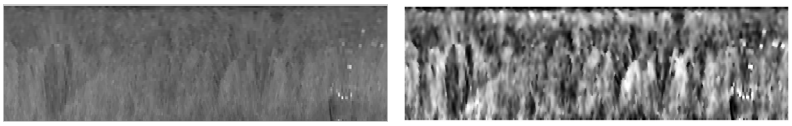

(d) (e)

Fig. 4.6 (a) Original image from the UBIRIS Version 1 dataset, (b) pupil detection using the RAC model, (c) iris detection using the RAC model, (d) normalized image, and (e) enhanced image.

4.2.4 Eyelash Detection and Unwrapping

The eyelashes may occlude the iris region and decrease the iris recognition performance. We apply eyelash detection methods described in Chapter 3. We create a binary mask based on the extracted iris contour and detected eyelashes. Since the elicited iris regions are not exactly circular and elliptical and may be of arbitrary shapes, a circle fitting strategy proposed by Shah and Ross [85] has been deployed to compensate for the size irregularities. To convert the detected iris region to a rectangular form, the radius and the corresponding centre coordinates of the iris are required to be estimated. Shah and Ross [85] considered only those points on the contour lying on the iris/sclera boundary, since the circle that fits all the points of the extracted contour may lie inside the actual iris boundary if a significant portion of the iris is occluded by eyelids. In order to approximate the radius *R,* six points at the angles of [-30°, 30°, 0°, 150°, 180°, 210°] with respect to the horizontal axis are selected from the extracted iris contour, and their average distance from the centre of the pupil is calculated. A circle fitting strategy is then adopted so that all the points on the contour are within a distance of *R±15* pixels from the centre of the pupil. Similarly, we can obtain the approximated pupil boundary. The centre values obtained through the elliptical fitting process and the

approximated radius of such a circle are used for the unwrapping process. Refer to [85] for a detailed description. Fig. 4.7 shows the approximated iris/pupil contours. Fig. 4.8 shows the segmented iris images after iris/pupil localization, eyelash detection and iris/pupil boundary approximation. To compensate for the elastic deformation in the iris texture, we unwrap the extracted (and localized) iris region into a normalized rectangular block of a fixed size 64× 512, by converting from the Cartesian coordinates to the polar ones [27-29]. If $I(x, y)$ is the localized image, then the polar representation of the form $I(r, \theta)$ can be obtained as follows:

$$r = \sqrt{(x - x_i)^2 + (y - y_i)^2}, \qquad 0 \leq r \leq r_{max} \tag{4.29}$$

$$\theta = tan^{-1}\left(\frac{y - y_i}{x - x_i}\right) \tag{4.30}$$

where r and θ are defined with respect to centre coordinates (x_i, y_i). The centre coordinate values obtained during the elliptical fitting are used as the centre points for the unwrapping procedure. Figs. 4.4 (d), 4.5 (d) and 4.6 (d) show the normalized images. Since the normalized iris image has a relatively low contrast and may have non-uniform intensity values due to the position of the light sources, a local intensity-based histogram equalization technique is applied to enhance the quality of the normalized iris image as described in the Chapter 3. In this chapter, a local cumulative histogram is applied to the image sub-block of size 10× 10 centred at the pixel to be converted. Figs. 4.4 (e), 4.5 (e), 4.6 (e), and 4.9 show the effect of enhancement on the normalized iris images. In the following section, we discuss the feature extraction process, which elicits the distinctive feature values from the normalized images.

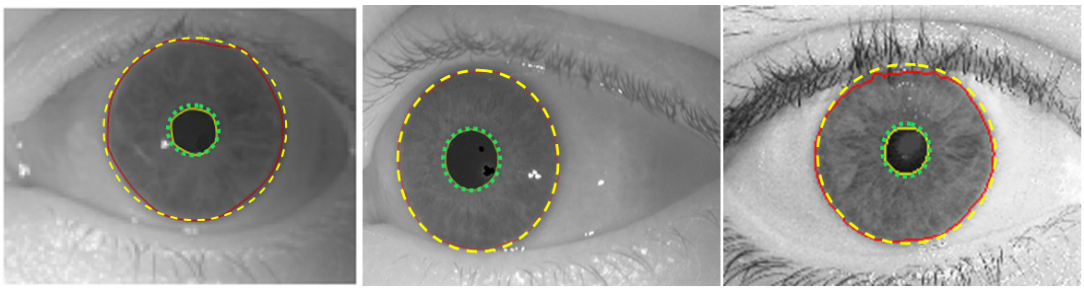

Fig. 4.7 Approximation of iris and pupil boundaries using the circle fitting strategy.

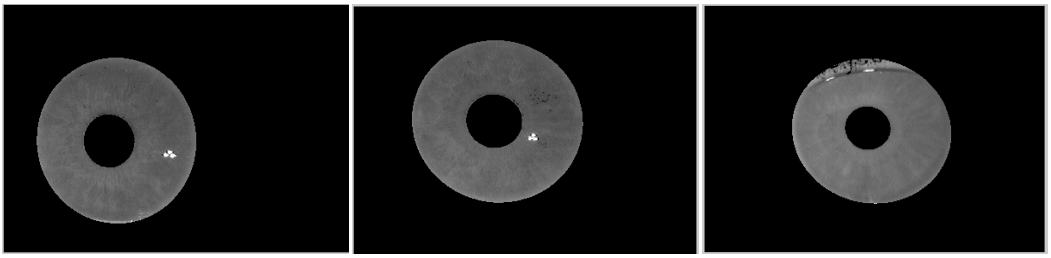

(a)

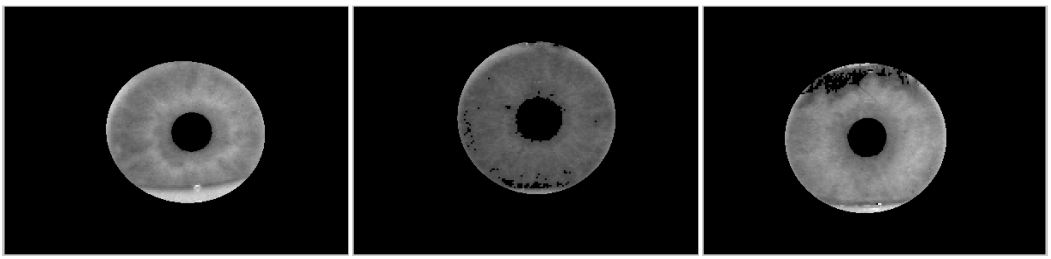

(b)

Fig. 4.8 Several samples of segmented iris images after iris/pupil localization, eyelash detection and iris/pupil boundary approximation: (a) samples of WVU Nonideal dataset; and (b) samples of UBIRIS Version 1 dataset.

4.3 Distinctive Feature Set Extraction

Different feature extraction algorithms have been proposed by several researchers to extract the most distinctive iris feature set from the iris images, including those irises that are captured in nonideal imagery setups [3, 37, 42, 100-112]. In [100], a feature extraction method based on the application of 2D-wavelet transform on the overlapped blocks of the iris texture was proposed to cope with degraded iris

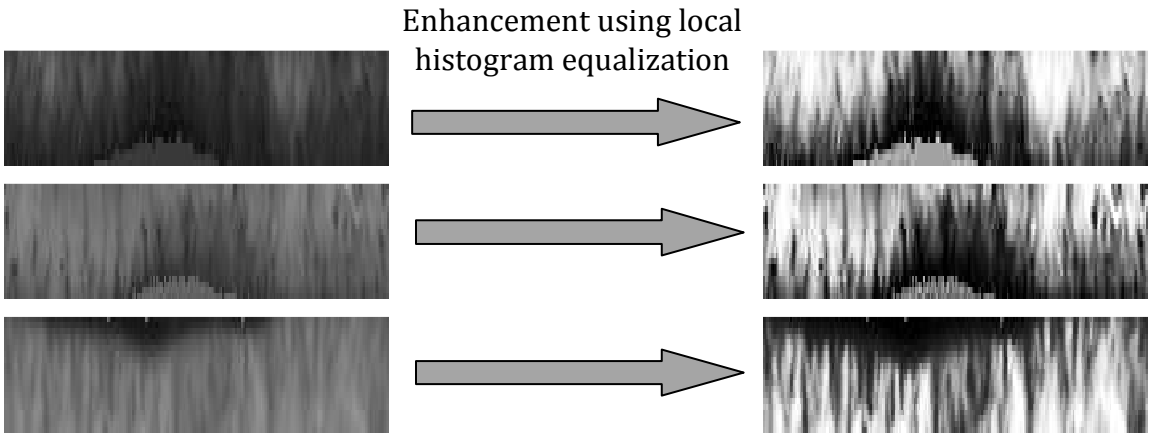

Fig. 4.9 Contrast Enhancement using local cumulative histogram equalization technique.

images. In [101, 102], a bi-orthogonal wavelet network was proposed to represent the iris features extracted from the off angle iris images. Dorairaj et al. [103] proposed an encoding technique based on the application of the global ICA to the masked iris images. In [104], an iris feature extraction scheme, based on wavelet maxima components and moment invariants, was employed. An extension of the traditional Gabor wavelet-based algorithm, which utilizes the local ordinal information extracted from original unfiltered images, was proposed in [105]. The modified log-Gabor filters were deployed in [106] to extract the iris phase features regardless of the background brightness. In [107], Cai et al. introduced an Optical Wavelet Packet Transform (OWPT) technique for the extraction of the iris features. In [108], authors embedded 2D-PCA into the 2D-Linear Discriminant Analysis (LDA) to elicit the characteristic iris features. A method for iris matching using zero crossings of 1D DCT as a means of feature extraction was proposed by Monro et al. [37]. In [109], Han et al. extracted the multi-direction and multi-scale information features from a normalized iris image by using a contourlet transform.

Sung et al. [42] applied the DBWT to the unwrapped images for textural feature extraction. Zhou and Kumar [110] exploited the orientation information of the local iris textural features using the finite Radon transform. Miyazawa et al. [3] used the phase components of 2D DFT of the given images and introduced the 2D Fourier Phase Code (FPC) to represent the iris information. Vijaya Kumar et al. [111] applied the correlation filters for feature extraction. In their method, normal variations in an iris image could be accommodated by designing a frequency-domain array that captures the consistent part of iris images while deemphasizing the varying parts. In [112], authors extracted the iris features using the oriented separable wavelet transforms (directionlets). In [161], a new iris representation method based on regional ordinal measure encoding was proposed, which provided an over-complete iris feature set for learning. Recently, Vatsa et al. [67] and several other researchers proposed different feature fusion schemes to improve the feature extraction performance [13, 113-115]. Vatsa et al. [67] applied 1D log-Gabor filters to extract the textural features and an Euler number to elicit the topological features. An SVM-based fusion strategy was then deployed to combine the textural and the topological features.

In this chapter, the DBWT is used to extract the characteristic values from the normalized (and enhanced) image block of size 64×512 pixels, and this technique is well-suited for analyzing the signals in a multi-resolution mode [162, 163]. We first divide the normalized image block into sixteen sub-images of size 32×64 and then apply the Daubechies four coefficients wavelet transform to each sub-image, as shown in Fig. 4.10. We also conducted our experiments using the Daubechies

wavelet function with eight and more coefficients. However, we did not achieve any higher performances than the wavelet function with four coefficients. Moreover, the feature extraction process using DBWT with more coefficients increases the computational cost. Fig. 4.11 shows the four-level decomposition using DBWT, and in this figure, 'L' and 'H' denote the low and high frequency components, respectively. We transform each image sub-block using the Daubechies wavelet in horizontal and vertical directions, and after applying the DBWT, divide the image into four regions: LL, HL, LH, and HH. We deploy the DBWT on the LL region again, since this portion represents the most significant iris information. After applying the DBWT repeatedly, the distinctive feature values of the further-reduced regions, such as HH_2, HH_3, and HH_4 are obtained. The values of HH_4 in each sub-block are considered as the components of the distinctive feature vector, and the region HH_4 contains the information of $2 \times 4 = 8$ data. The iris information on HH_1, HH_2, and HH_3 is also obtained by calculating the mean value of each of such regions and assigning those values to one dimension. This procedure is applied to each

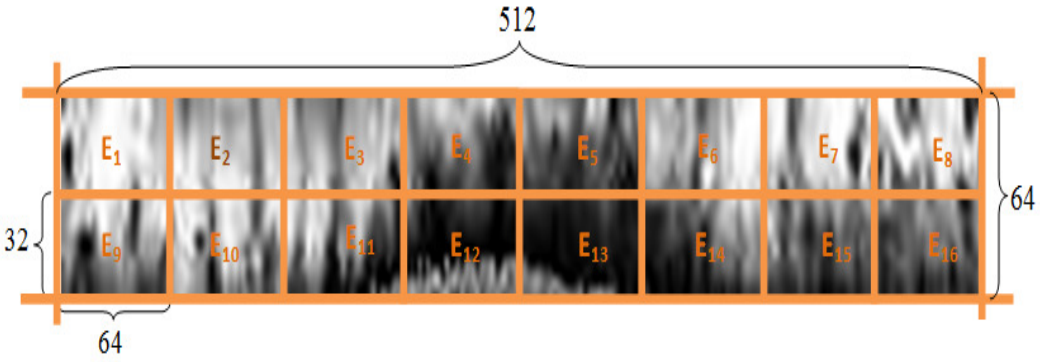

Fig. 4.10 Normalized image is divided into sixteen sub-images.

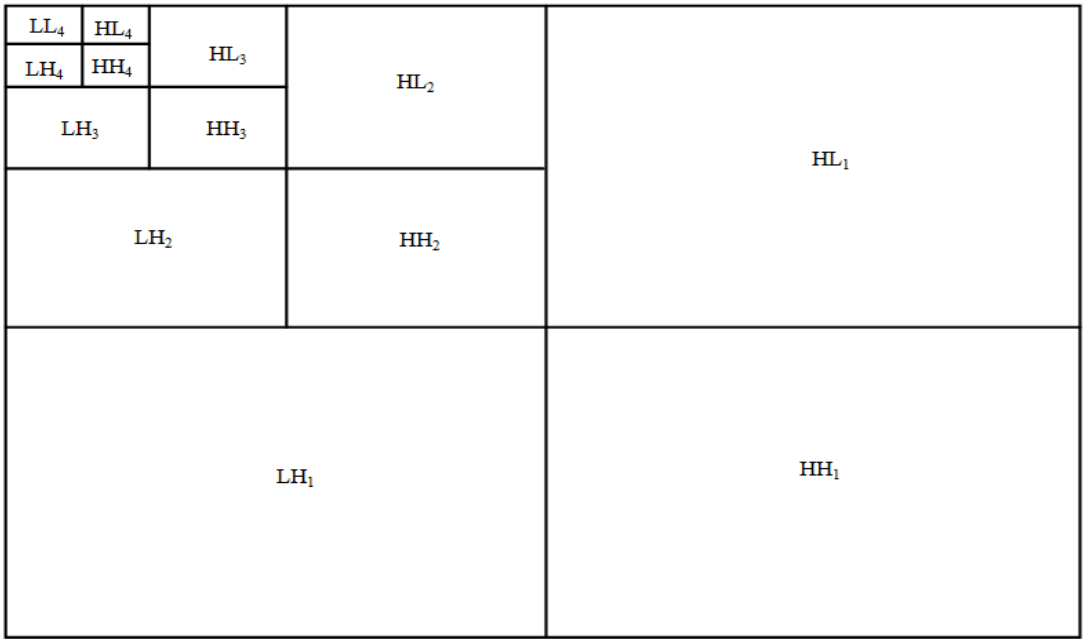

Fig. 4.11 Four-level decomposition using DBWT.

image sub-block. Therefore, the normalized image is represented by a distinctive feature set of $(2 \times 4 + 3) \times 16 = 176$ components. A hybrid feature selection scheme, discussed in the next section, is then deployed to select the most important features from the extracted feature sequence.

4.4 Feature Selection Using Genetic Algorithms (GAs)

The iris data contains a large number of textural features and a comparatively small number of samples per class, and this makes accurate and reliable classification challenging. A few research solutions have been accomplished in the area of iris feature subset selection. In [117], a sequential forward floating search was adopted to select a suitable subset of textural features. Chen et al. [118] proposed a method for selecting edge-type features for iris recognition, and the AdaBoost algorithm was then used to select a filter bank from a pile of filter candidates. The authors in [119]

applied a feature correlation evaluation approach for iris image quality measure. This approach could discriminate the artificial patterns from the natural iris patterns and could also measure the iris image quality for uncompressed images. In the proposed approach of [120], the portions of the iris with the most distinguishable changing patterns were chosen and used to measure the feature information. The combination of occlusion and dilation was used to determine the amount of iris region available, and this information was considered for the iris quality measure. Proenca and Alexandre [121] proposed a method to measure the quality of each feature in the extracted feature sequence and separated them into two sets: the noisy features and noise-free features. The similarity between these two feature sets was then measured and used to discover the identity of a specific subject. In [122, 123], authors reported that some iris bits were more consistent than others. They compared different regions of the iris to evaluate their relative consistency, and found that the middle bands of the iris were more consistent than the inner bands. Kong et al. [124] provided an analysis of IrisCode by extending the coarse phase representation to a precise phase representation and uncovering the relationship between the IrisCode and other coding methods.

While most of the traditional feature selection schemes like PCA, ICA, SVD, etc., require a sufficient number of iris samples per class, the GA-based feature reduction algorithm performs reasonably well despite the unavailability of a sufficient number of iris samples per individual. It has also been found that feature selection through GA is a very powerful tool that could be used to find a set of good classifiers [154]. Besides, it can overcome problems such as scaling and sensitivity towards the

weights. In this light, we are applying a new scheme for selecting the optimal features based on GA. Moreover, several feature selection schemes produce different results on the same data set because of the feature redundancy, interactions and correlations between features, and the biases in the selection or ranking criteria. In Chapter 3, we applied a GA-based feature selection scheme where the extracted feature sequence was directly input to GA for best feature selection. However, in this chapter, we propose GAs to select the prominent features based on the valuable outcomes of the four feature selection algorithms, namely, the Entropy-based approach, the k-NN-based method, T-statistics and the SVM-RFE approach. In order to obtain the most significant feature subset from the different feature selection algorithms, we propose a hybrid approach, as shown in Fig. 4.12. In this feature selection scheme, we adopt a GA that combines multiple feature selection criteria and finds the optimal subset of informative features. In this effort, we provide the top-ranked features, obtained from the multiple feature selection algorithms, to GA instead of using all the features from the original iris feature set. The top-ranked features form the collection of candidate features called feature pool. The selection of the feature subset from these algorithms can be subjective to their performance. In order to choose the sets of top-ranked features, we deploy four existing feature selection algorithms, two filter approaches (entropy-based, T-statistics) and two wrapper approaches (SVM-RFE, k-NN) to form the feature pool. We apply each algorithm to the extracted feature sequence and generate a ranking of those features. Given a ranking of features, we pick a number of top-ranked features from each algorithm and provide these features for the

feature pool of GA. Below, we briefly describe each of the four feature selection algorithms.

In the entropy-based method [154], the entropy is lower for orderly configurations and higher for disorderly configurations. Therefore, when an irrelevant feature is eliminated, the entropy is reduced more than that for a relevant feature. This algorithm ranks the features in descending order of the entropies after removing each feature one at a time. We can estimate the entropy measure of a data set for *N* instances as follows:

$$E = -\sum_{i=1}^{N}\sum_{j=1}^{N}\left(d_{ij} \times log d_{ij} + \left(1 - d_{ij}\right) \times log\left(1 - d_{ij}\right)\right) \qquad (4.31)$$

where, $d_{ij} = exp^{-\alpha \times ED_{ij}}$ and $\alpha = {-ln\ 0.5}/{\overline{AD}}$

Here, d_{ij} denotes the similarity between two instances, x_i and x_j, where ED_{ij} is the Euclidean distance between the two, and $\overline{AD}$ is the average distance among the instances. This approach is used for unsupervised data since no class information is required.

In [154], the SVM-RFE has been used for selecting the genes that are relevant for a cancer classification problem. We have adopted this approach to find the top-ranked iris features from the extracted features sequence. The idea is to eliminate one worst feature (i.e., the one that modifies the objective function *Obj* the least after being eliminated) at one time. This method is based on the backward sequential selection:

$$Obj = {\|w\|^2}/{2} \qquad (4.32)$$

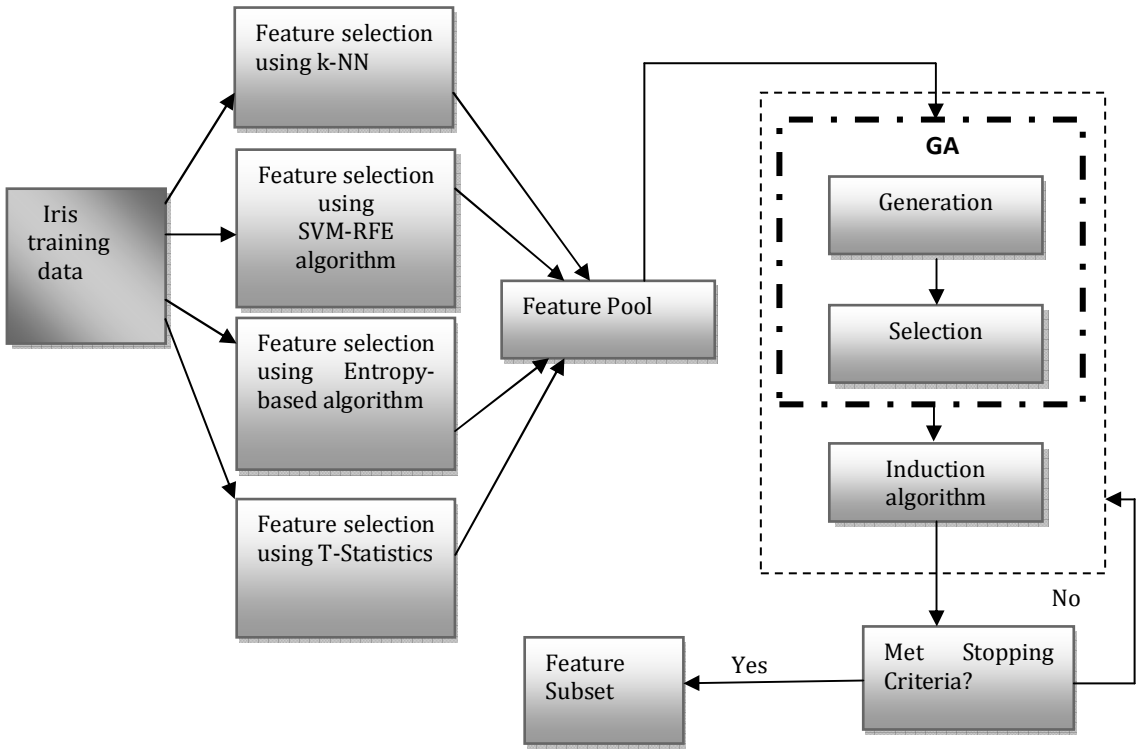

Fig. 4.12 Feature selection procedure using GAs (Hybrid approach).

$$w = \sum_{i=1}^{N_s} \alpha_i y_i x_i \tag{4.33}$$

where, N_s denotes the number of *SVs* that are defined to be the training samples with $0 < \alpha_i \leq C$; C is the penalty parameter for the error term; and x_i and y_j are the data instance and its class label, respectively. The modification of Obj is approximated by the Optimal Brain Damage (OBD) algorithm so that:

$$\Delta\, Obj\,(i) = (\Delta w_i)^2 \tag{4.34}$$

where, ${w_i}^2$ is considered as the ranking criteria. The iterative procedure of RFE is given as follows:

- The SVM is trained with training data.
- The ranking criterion is measured for all features.
- Then, the feature with smallest ranking criterion is eliminated.

- The procedure is stopped when all the features are ranked.

In the T-statistics-based feature selection approach, each sample is labeled with $\{1, -1\}$. The mean, μ_i^1 (μ_i^{-1}), and the standard deviation, δ_i^1 (δ_i^{-1}), are calculated for the samples labeled as 1 (-1) or for each feature f_i. Then a score $T(f_i)$ is obtained as follows:

$$T(f_i) = \left|\mu_i^1 - \mu_i^{-1}\right| \Big/ \sqrt{\frac{(\delta_i^1)^2}{n_1} + \frac{(\delta_i^{-1})^2}{n_{-1}}} \tag{4.35}$$

where, n_1 (n_{-1}) denotes the number of samples labelled as 1 (-1). In order to make a decision, the features with the highest scores are considered as the most distinctive features.

In k-NN-based feature selection, a direct method based on nonparametric feature-subset-selection evaluation is applied. The evaluation technique denoted as 'Leave-One-Out (LOO)' method is used. The main idea of the LOO method is given as follows:

- Design the decision rule using N-1 samples of the total N samples.
- Apply this decision rule to the one remaining sample.
- This process is repeated for all partitions of size N-1 for the design sample set and of size one for the test set.
- Estimate the probability of error by the ratio of the test samples that have been incorrectly classified to the total number of samples classified.

In the previous chapter, GAs were applied to optimize the matching accuracy and to optimize the selected feature dimension. However, in the iris biometrics

recognition systems, the number of FAs and FRs plays an important role for fighting against ongoing security threats. Most of the current iris recognition algorithms have relatively lower FARs. However, the reduction of FRRs of an iris biometrics system still remains a major challenge in further strengthening of the security. Therefore, the proposed GAs are designed to optimize four objectives: minimization of the (a) recognition error, (b) FAR, and (c) FRR, and (d) size of the selected feature subset. In order to smooth out the fitness function so that a small improvement in Genetic Program (GP) could be reflected, we propose the following fitness function based on the nature of the underlying problem:

$$\text{F}itness = W_1.(1 - RR) + W_2.FAR + W_3.FRR + W_4.\left(\frac{FeatureSize}{Total\ Number\ of\ Features}\right) \quad (4.36)$$

where, W_1, W_2, W_3 and W_4 are constant weighting parameters which reflect the relative importance between the *Recognition Rate* (RR), the *FAR,* the *FRR* and the *Feature Size*. We expect that this fitness function will increase both the efficiency and the effectiveness of the evolutionary search. It will also have a tendency to reduce the redundancy, making the programs more comprehensible. We will employ the asymmetrical SVM as an induction algorithm in the experiments to separate the cases of FA and FR [46]. As applied in Chapter 3, we will use the Roulette wheel selection method to probabilistically select the individuals from a population. In this chapter, we use the single point crossover, and each individual has a mutation probability, $P_{n,}$. We randomly select the number of *n* bits that are to be flipped in every mutation stage. Therefore, we can summarize the GA-based hybrid feature selection process as follows (See Fig. 4.12):

Step1: Input the extracted feature set obtained by DBWT to four feature selection algorithms.

Step 2: Apply each algorithm to the extracted feature set, and generate a ranking of those features.

Step 3: Given a ranking of features, pick a number of top-ranked features from each algorithm and provide these features for the feature pool of GA.

Step 4: Select the best-ranked features using the genetic process based on the proposed fitness function.

Next, the selected iris feature subset will be used for pattern matching by using adaptive asymmetrical SVMs, which are described in the following section.

4.5 Iris Pattern Matching Using Adaptive Asymmetrical SVMs

Most of the researchers have applied the HD for iris pattern matching [36]. However, recently, several researchers have proposed different iris matching techniques that can cope with the degraded iris images [125-129]. In [38, 125, 152], the modified HDD was used to compare the binary edge maps of irises. Krichen et al. [126] presented a phase-correlation-based iris matching approach in order to deal with the noisy irises. This matching system is a fusion of global and local Gabor phase-correlation schemes. In [127], authors employed the Du measure as a matching mechanism and generated a set of the most probable matches (ranks) instead of only the best match. Such authors claimed that the system works with eyes that are tilted, since this method generates 1D signatures that are rotation-invariant. In [128], authors derived a Maximum Posteriori Probability (MAP)

estimate of the parameters of the relative deformation between a pair of iris images. This estimation process can perform two things simultaneously: 1) it normalizes the iris for pattern warping, and 2) it returns a distortion-tolerant similarity metric that can be used for matching two nonlinearly deformed image patterns. To deal with the noisy iris images and to enable iris recognition on less-than-ideal images, Ziauddin et al. [129] introduced a weighted majority voting technique. This technique was applicable to any biometric authentication system using bitwise comparison of enrollment-time and verification-time biometric templates. Sung et al. [42] and Son et al. [133] employed the traditional SVMs for pattern matching. Gu et al. [54] used the non-symmetrical SVMs to separate the cases of FA and FR. In Chapter 3, we used the asymmetrical SVMs in order to control the misclassification errors. However, the asymmetrical SVMs involve huge computation time for pattern matching despite their good performance in poorly balanced sample space. In this chapter, we propose the Adaptive Asymmetrical SVMs (AASVMs) to control the poorly balanced sample proportion between classes and also to reduce the matching time of a test sample. First, we apply a new scheme to adaptively select the FV from the SV solutions [13]. Since the number of FVs is often less than that of SVs, the substitution of FV for SV greatly improves the sparsity of the solution and speeds up the matching time when testing a new sample [70]. Then, we apply the asymmetrical SVMs to satisfy several security demands and also to control the statistically under-presented data of a class with respect to other classes. Therefore, we combine the asymmetrical approach with the adaptive simplification of the

solution for SV and denote this combined approach as 'AASVMs'. We briefly state our proposed scheme below [70].

1. In order to reduce the decision time for a new sample, *FV* is selected adaptively according to the vector correlation principle and the greedy algorithm [13]. Let $(\boldsymbol{x_i}, y_i)_{1\leq i\leq l}(\boldsymbol{x_i} \in R^N, y \in R)$ be the *SV* and ψ be the nonlinear mapping function. If ψ maps the input space of the *SV* into a feature Hilbert space *HS*, we get:

$$\Psi: R^N \rightarrow HS,$$

$$\boldsymbol{x} \rightarrow \psi(\boldsymbol{x}) \tag{4.37}$$

Therefore, mapping the *SV* set in a feature space is $(\psi(\boldsymbol{x_i}), y_i)_{1\leq i\leq l}(\psi(\boldsymbol{x_i}) \in HS, y \in R)$, which lies in the subspace HS_s of the HS with the dimension up to l. The dimension of this subspace is far lower than l and equal to the number of its base vector. If *FV* approximates the *SV* accurately, testing on the original *SV* will be equal to the test on the *FV*. To simplify the notation, the mapping of $\boldsymbol{x_i}, \psi(\boldsymbol{x_i})$ is denoted as ψ_i and the selected *FVs* are noted by $\boldsymbol{x}_{F_j}$ and $\psi\left(\boldsymbol{x}_{F_j}\right) = \psi_{F_j}$ for $1 \leq j \leq P$ (P is the number of *FVs*). Let us consider the *FV* set $X_F = \{x_{F_1}, x_{F_2}, \ldots\ldots, x_{F_P}\}$, and the mapping of any vector $\boldsymbol{x}_i$ can be expressed by a linear combination of the X_F with the following form:

$$\hat{\psi}_i = \boldsymbol{\alpha}_i^T \Psi_F \tag{4.38}$$

where $\Psi_F = (\psi_{F_1}, \psi_{F_2}, \ldots\ldots\ldots, \psi_{F_P})^T$ is the matrix of the mapping *FV* and $\boldsymbol{\alpha}_i = (\alpha_{i1}, \alpha_{i2}, \ldots\ldots\ldots, \alpha_{iP})^T$ is the corresponding coefficient vector. For the given $(\boldsymbol{x_i}, y_i)_{1\leq i\leq l}$, the main objective is to find the *FV*, $X_F = \{x_{F_1}, x_{F_2}, \ldots\ldots, x_{F_P}\}$ such

that the estimated mapping $\hat{\psi}_i$ becomes as close as possible to the original mapping ψ_i:

$$\varepsilon = \sum_{\boldsymbol{x}_i \in X} \varepsilon_i = \sum_{\boldsymbol{x}_i \in X} \left(\left\| \psi_i - \hat{\psi}_i \right\|^2 \right) \tag{4.39}$$

The ε denotes the approximation error between the *FV* set and the original *SV* set. In order to select the *FV*, we need to minimize ε:

$$\underset{X_F}{min\ (\varepsilon)} = \underset{X_F}{min} \left(\sum_{\boldsymbol{x}_i \in X} \varepsilon_i \right) \tag{4.40}$$

The feature set fitness, ε_F, and the fitness of each vector, ε_{F_i}, corresponding to the given *FV* set, X_F, can be defined as follows:

$$\varepsilon_F = \frac{1}{l} \sum_{x_{i \in X}} \varepsilon_{F\,i}, \tag{4.41}$$

where

$$\varepsilon_{F_i} = \frac{\psi_i^T \psi_i (\Psi_F^T \psi_i)^T \Psi_F^T \psi_i}{\Psi_F^T \Psi_F} \tag{4.42}$$

Now, minimization of (4.40) is equivalent to minimizing the following form:

$$\underset{X_F}{\min\ (\varepsilon_F)} \tag{4.43}$$

A greedy iterative algorithm is used to select the *FV*. For selecting the first *FV*, we pick the samples that provide the minimum ε_F . In each iteration, we use (4.41) to estimate the performance of the current feature set and (4.42) is used to select the next best feature vector candidate. When we obtain the maximal fitness ε_F for the current feature set, we select it as the next feature vector. When the current fitness of feature set reaches the predefined fitness threshold, the algorithm stops. Therefore, the number of *FVs* can be controlled adaptively as long as the different approximation errors, ε_F, are set.

2. Next, we separate the empirical risk into two parts and assign the different penalty parameters corresponding to the empirical risk of positive and negative classes, as mentioned in the Chapter 3 (Section 3.6). The separation of empirical risk controls the misclassification error between the positive and negative classes.

4.6 Experimental Results and Analysis

In this section, we have conducted a set of experiments to evaluate the performance of the proposed scheme and summarized the results. The extensive experimentation has been conducted on four datasets, namely, ICE 2005 [189], CASIA Version 3 Interval [190], UBIRIS Version 1 [191], and WVU Nonideal [192]. We also conducted our experiments on the heterogeneous combined dataset. The details about the datasets are given in Appendix A. We have conducted our experiments in two stages: first, we evaluated the performance of our proposed algorithms with respect to segmentation, feature selection, and pattern matching (Section 4.6.1), and second, we compared the performance of our method with other state-of-the-art algorithms to show its effectiveness (Section 4.6.2). Extensive experiments on different nonideal iris image datasets were conducted to evaluate the performance in two modes: verification (one-to-one) and identification (one-to-many). In the verification mode, we measured the performance in terms of GAR, FAR, and EER with the assumption that a test sample would be from a specific subject. In the identification mode, we made a one-to-many search in the entire dataset for a given

test sample in order to find the highest matched template with that test sample [18]. Thus, in identification, we used the CRR measure, as defined in the Chapter 3.

4.6.1 Performance Evaluation of the Proposed Scheme

To validate the performance of the proposed algorithms, we used the four datasets mentioned above. In order to detect the strong specular reflections, we set the predetermined threshold values. For the ICE 2005, WVU Nonideal, CASIA Version 3 Interval and UBIRIS Version 1 datasets, these predefined values were set at 245, 247, 240 and 237, respectively. We selected a common set of curve evolution parameter values for the LS approaches. These selected values were applied to segment the nonideal iris images accurately. To detect the inner boundary, based on LS with the edge stopping function, the selected parameter values were set at $\Delta t = 0.05$ and $\epsilon = 0.015$. The selected parameter values that were used to find the outer boundary, using LS with the energy minimization algorithm, were set at $\mu = 0.00001, v = 0.02,\ \lambda_1 = \lambda_2 = 1, \Delta t = 0.1$ and $\epsilon = 1$. Fig 4.13 shows the segmentation results on the four datasets. This figure shows that our segmentation scheme performs well, despite the fact that the iris and the sclera regions are separated by a blurred boundary, especially in the WVU and UBIRIS datasets.

For the VLS-based segmentation scheme, we also selected a common set of curve evolution parameters to segment the nonideal iris images accurately. The selected parametric values that were applied to find the inner and outer boundaries, using the VLS algorithm were set at $\mu = 0.001, v = 2.0, \lambda = 5.0$ and time step $\tau = 4.0$. This time step was significantly larger than the one used for traditional LS methods.

Fig. 4.14 demonstrates the segmentation performance on the four underlying nonideal datasets. Our segmentation scheme performs reasonably well when the iris and the sclera regions are separated by a weak boundary. The selected parameter values to find the inner and outer boundaries, using RAC algorithm were set at $\sigma = 2.0, \lambda_1 = 0.5, \lambda_2 = 1.0, \mu = 1, v = 200.0,$ and time step $\Delta t = 0.4$. Fig. 4.15 shows the segmentation results on the four datasets. This figure shows that our segmentation scheme performs well, even if the intensity inhomogeneity occurs in the iris region.

Our proposed segmentation scheme is also robust in noisy situations. A sudden variation in the intensity level may occur in the iris image due to a noisy pixel and

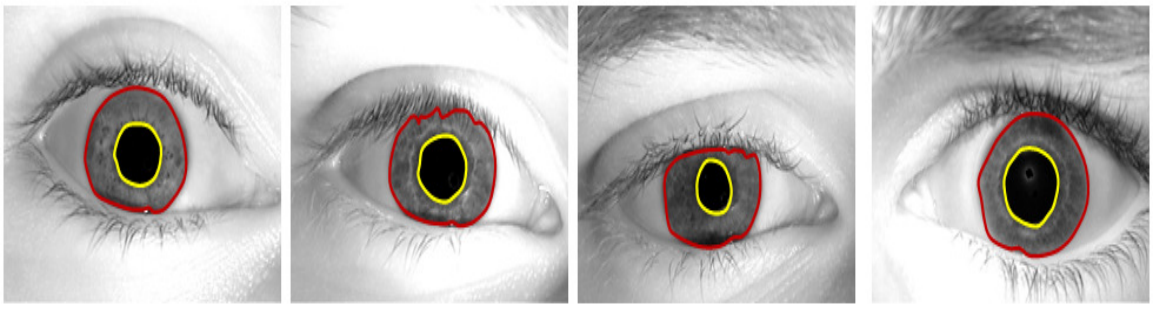

(a)

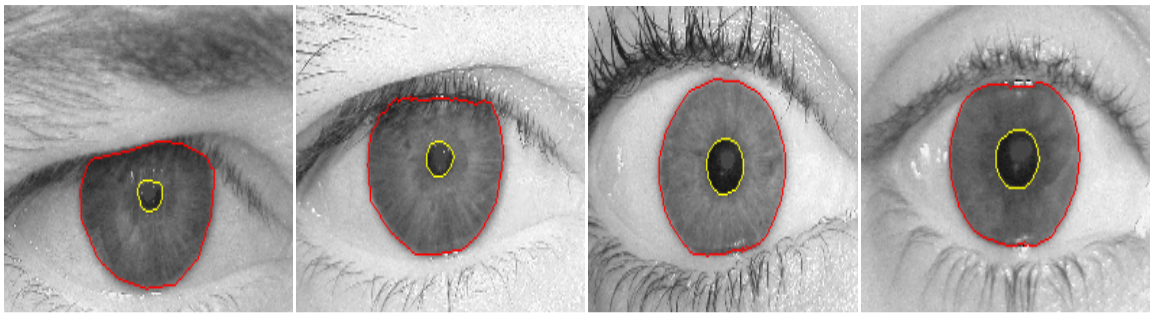

(b)

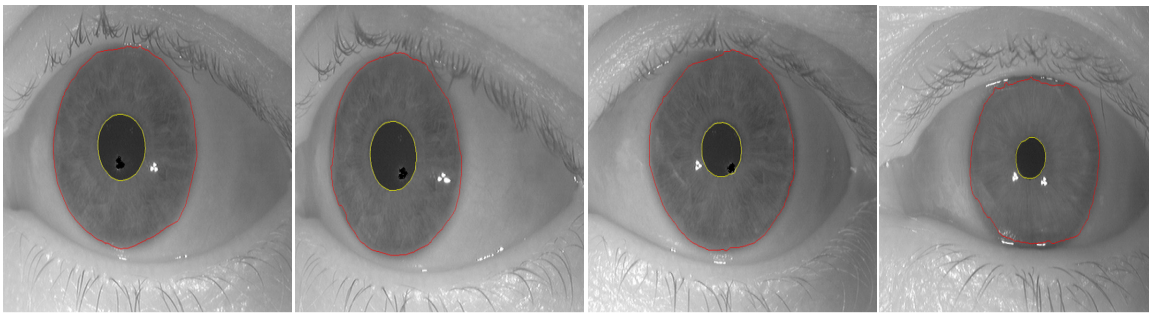

(C)

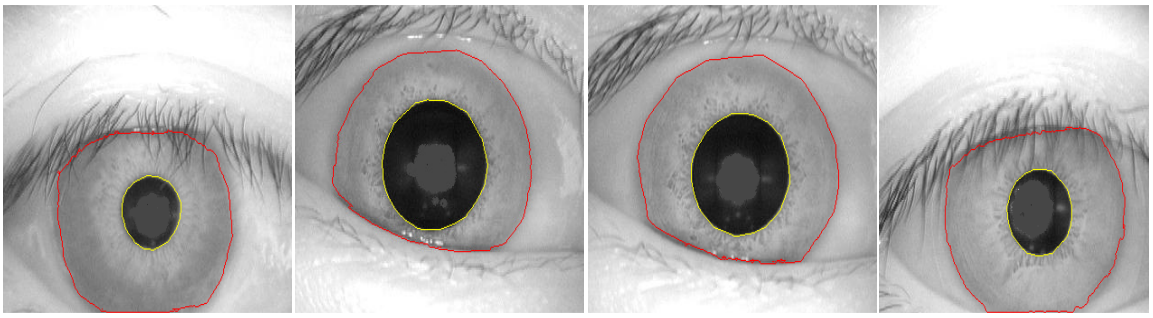

(d)

Fig. 4.13 LS-based segmentation results from the following datasets: (a) ICE 2005, (b) UBIRIS Version 1, (c) WVU Nonideal, and (d) CASIA Version 3 Interval datasets.

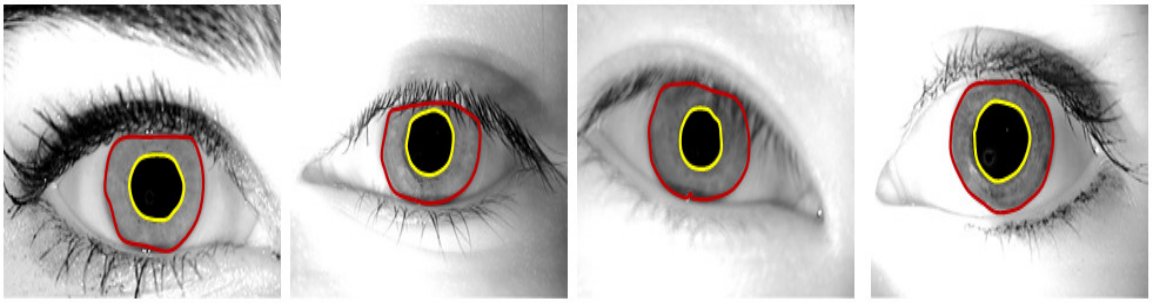

(a)

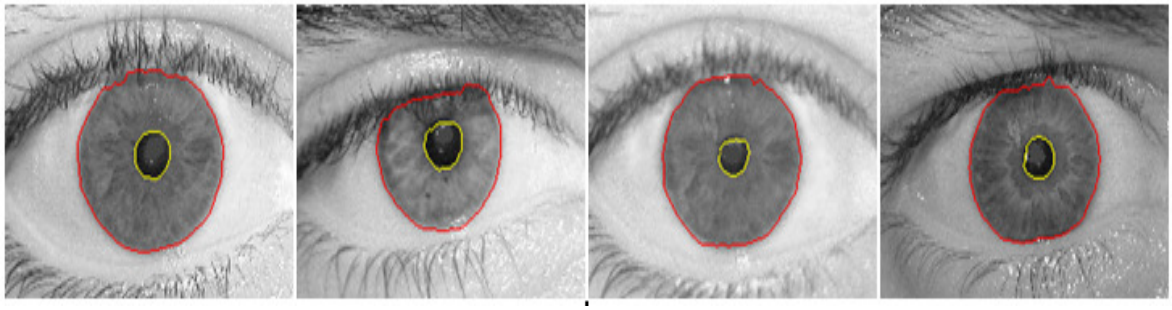

(b)

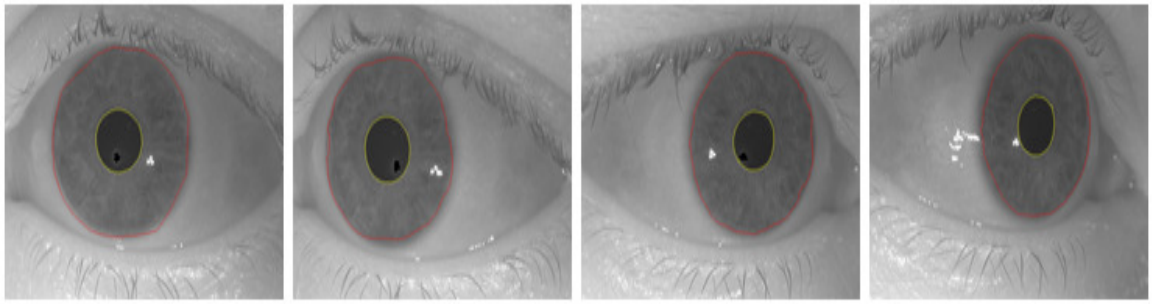

(c)

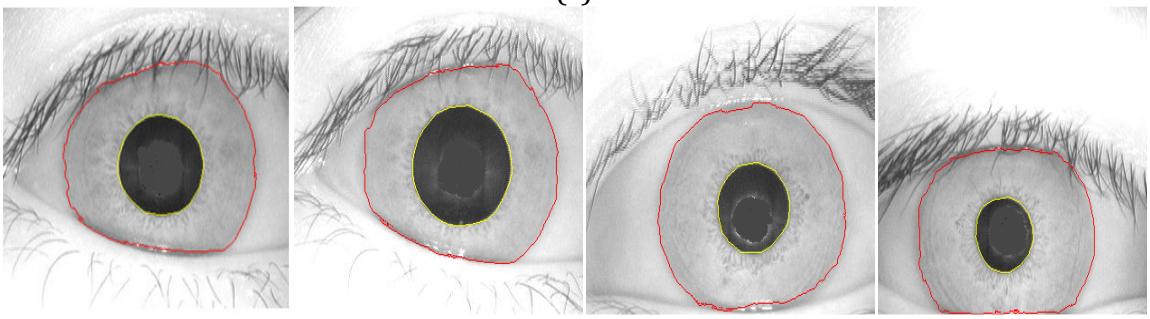

(d)

Fig. 4.14 VLS-based segmentation results from the following datasets: (a) ICE 2005, (b) UBIRIS Version 1, (c) WVU Nonideal, and (d) CASIA Version 3 Interval datasets.

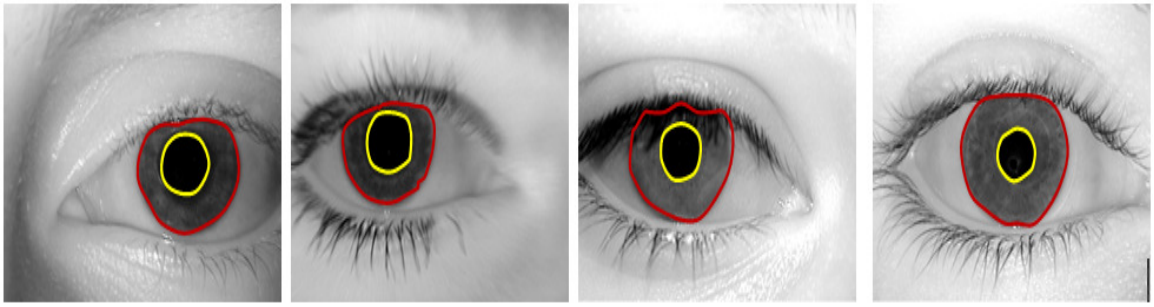

(a)

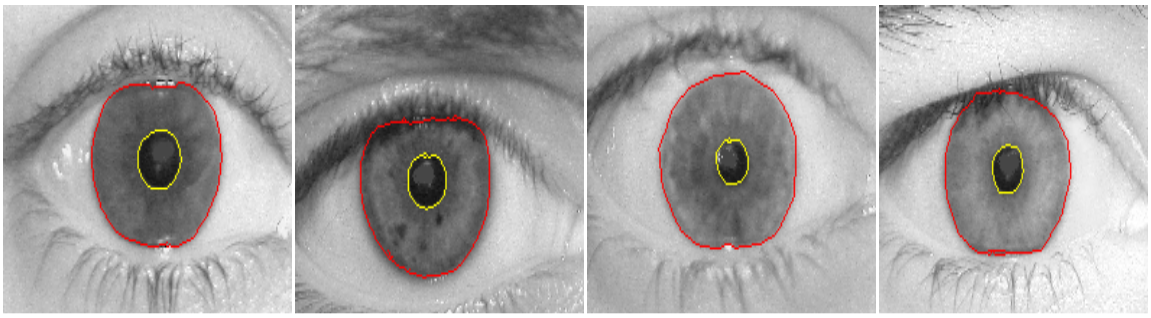

(b)

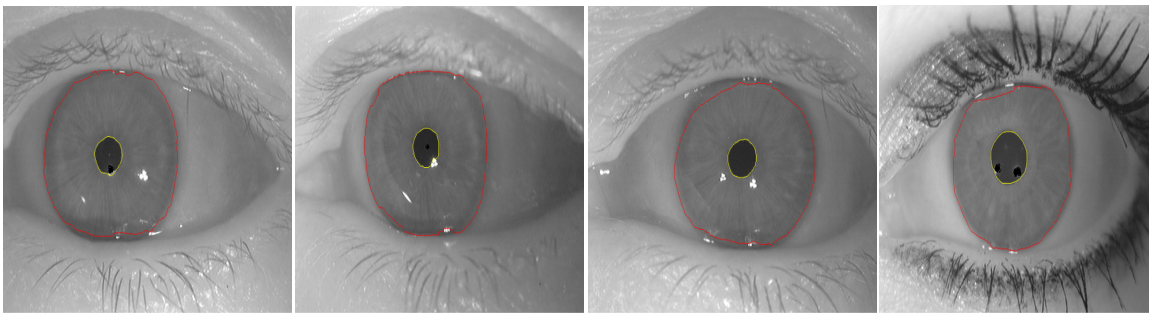

(c)

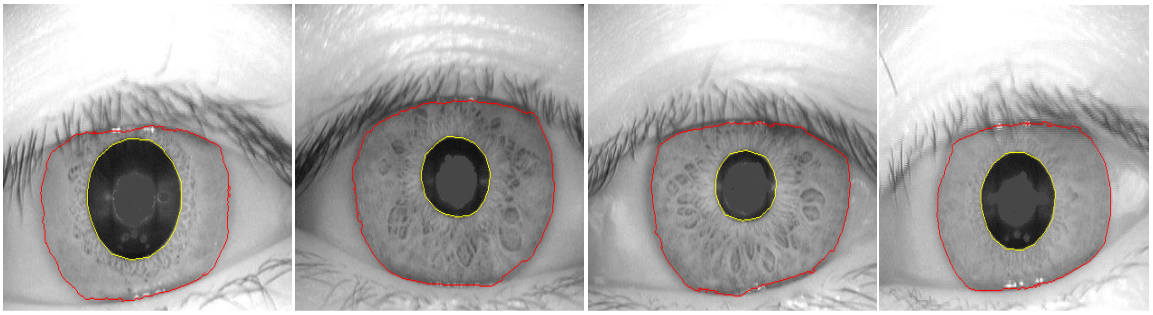

(d)

Fig. 4.15 RAC model segmentation results from the following datasets: (a) ICE 2005, (b) UBIRIS Version 1, (c) WVU Nonideal, and (d) CASIA Version 3 Interval datasets.

thus, the moving front of boundary points may stop. However, in our case, the other boundary points continue to move and, hence, the curve evolution processes, based on VLS and RAC, keep propagating towards the inner and the outer boundaries. Fig. 4.16 (b, c) shows the outputs of applying our proposed VLS scheme to an iris image with a Gaussian white noise. Fig. 4.16 (d, e, f) shows the results of applying our VLS approach to an iris image with the Poisson noise, the salt and pepper noise, and the speckle noise, respectively. One major advantage of our algorithm as compared to the methods proposed in [75, 85, 86] is that the topology preserving technique is used instead of the standard active contour-based method. Therefore, even in the noisy situations, our proposed approach can localize the inner and outer boundaries

accurately. Similarly, Fig. 4.17 shows that the localization method, based on RAC, also performs well in noisy situations. However, the proposed LS-based segmentation scheme is unable to exhibit the expected level of performance in the noisy environment, as shown in Fig. 4.18.

In order to exhibit the effectiveness of our segmentation approaches, we compared our LS, VLS and RAC schemes on all the datasets with the following approaches: Integro-Differential Operator (IDO) proposed by Daugman [27-29], the Canny edge detection and Hough Transform (CHT) based approaches applied in the Chapter 3 [46, 135, 136], and the active contour-based localization approaches demonstrated in [67] and [85, 86]. For comparison purposes, we only implemented the segmentation approaches proposed in [27-29, 67, 85, 86], and for feature extraction and matching, we applied our proposed algorithms to each of those schemes. However, we did not use the feature reduction algorithm for this purpose. The ROC curves in Fig. 4.19 show that the matching performance is improved when the geometric active contours are used for segmentation with the edge stopping function and the energy minimization algorithm. The proposed segmentation scheme shows a better performance than the active contour-based methods

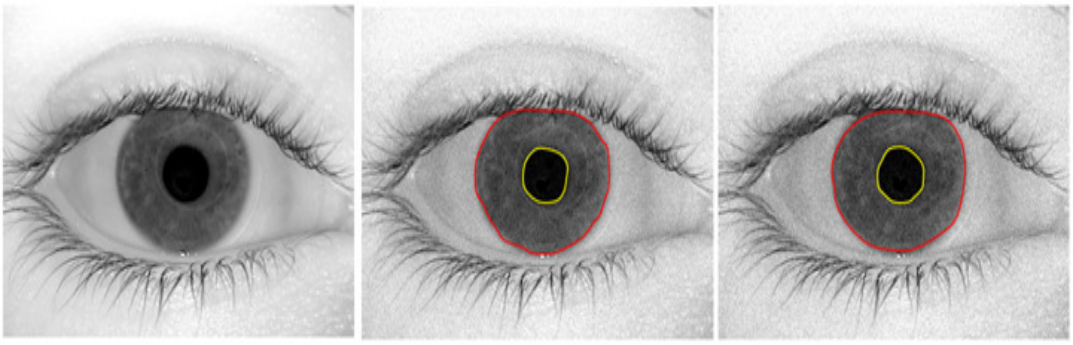

(a) (b) (c)

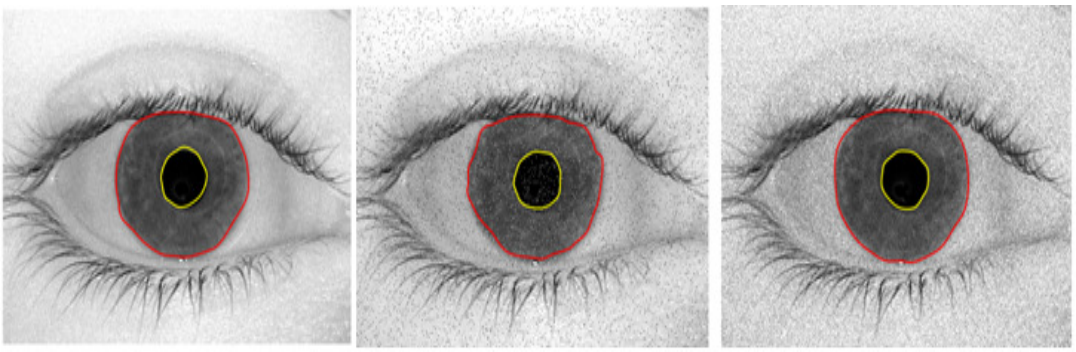

(d) (e) (f)

Fig. 4.16 Performance of our VLS algorithm in noisy situations: (a) original image after filling the white spots from the ICE 2005 dataset, (b) Gaussian white noise (mean=0 and variance = 0.005), (c) Gaussian white noise (mean=0 and variance = 0.007), (d) iris image with Poisson noise, (e) iris image with salt and pepper noise (noise density = 0.06), and (f) iris image with speckle noise which adds the multiplicative noise (mean=0 and variance = 0.07).

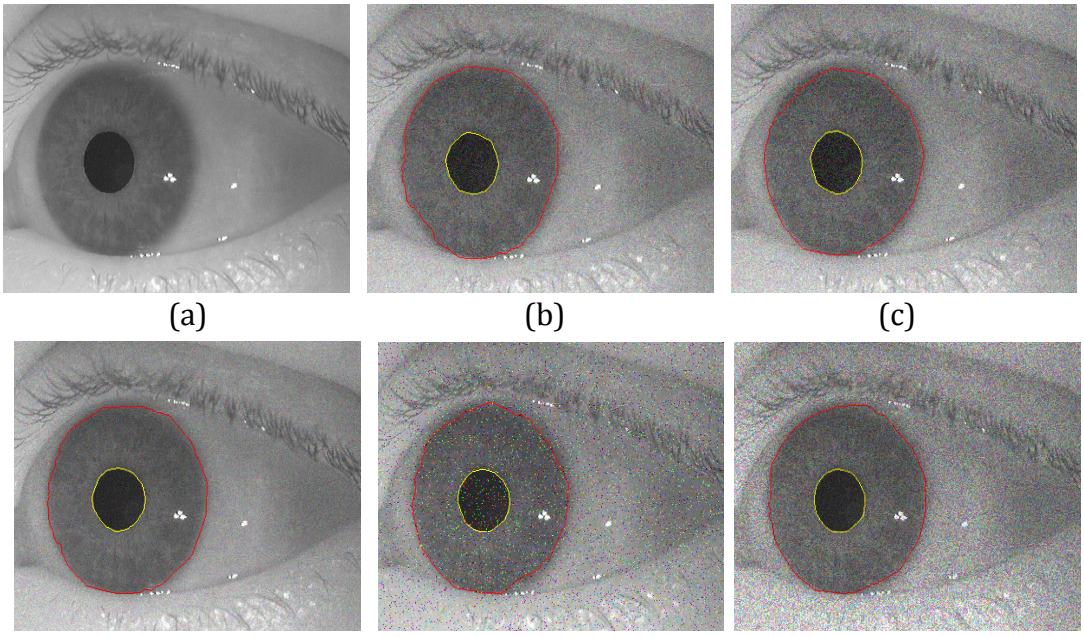

(a) (b) (c)

(d) (e) (f)

Fig. 4.17 Performance of our RAC algorithm in noisy situations: (a) original image after filling the white spots from WVU Nonideal dataset, (b) Gaussian white noise (mean=0 and variance = 0.005), (c) Gaussian white noise (mean=0 and variance = 0.007), (d) iris image with Poisson noise, (e) iris image with salt and pepper noise (noise density = 0.06), and (f) iris image with speckle noise which adds the multiplicative noise (mean=0 and variance = 0.07).

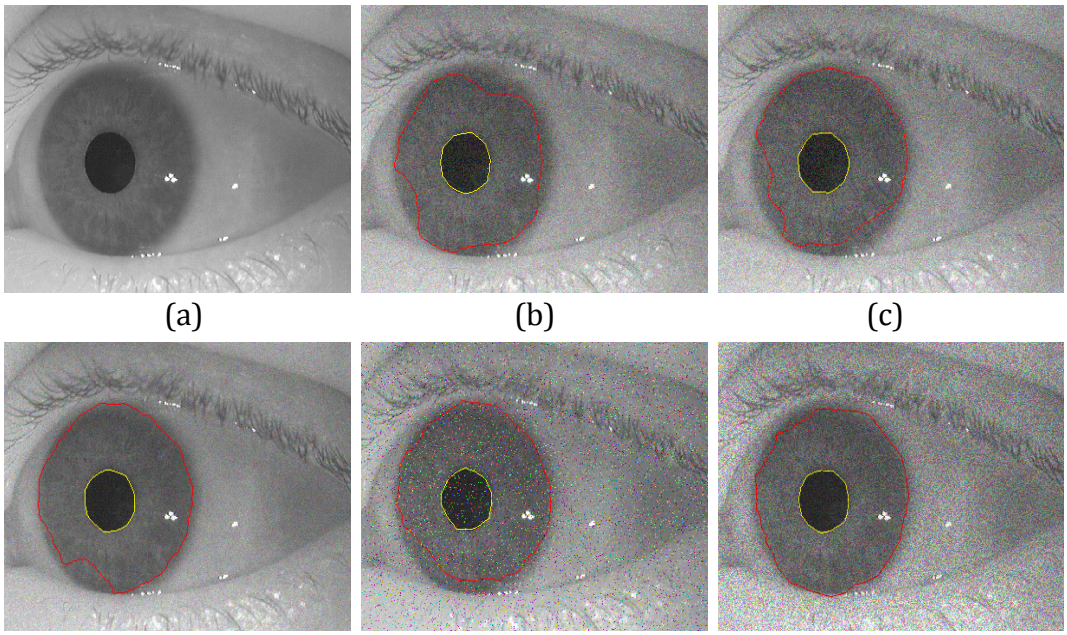

Fig. 4.18 LS algorithm failed to perform well in noisy situations: (a) original image after filling the white spots from WVU Nonideal dataset, (b) Gaussian white noise (mean=0 and variance = 0.005), (c) Gaussian white noise (mean=0 and variance = 0.007), (d) iris image with Poisson noise, (e) iris image with salt and pepper noise (noise density = 0.06), and (f) iris image with speckle noise which adds the multiplicative noise (mean=0 and variance = 0.07).

reported in [67, 85, 86], since our LS-based segmentation approach uses an energy minimization algorithm for the outer boundary detection. The energy minimization approach is suitable for the underlying iris datasets, where a large number of iris images suffer from a weak iris/sclera boundary.

The proposed segmentation scheme, using VLS, also shows a better performance than the active contour-based methods reported in [67, 85] due to the advantageous properties of variational formulation over the traditional LS methods. The external energy of the total energy functional drives the zero LS toward the iris/pupil boundaries, and on the other hand, the internal energy term penalizes the deviation

of the LS curve from the SDF during the evolution process. Another advantage of the proposed segmentation algorithm is that this technique performs well, even when the iris/sclera boundary is separated by a quite blurred boundary. Also, the proposed VLS-based algorithm speeds up the curve evolution process considerably. Fig. 4.19 also demonstrates that the matching performance is improved when the RAC model is used for segmentation with VLS formulation. Our proposed scheme with RAC shows a better performance than the traditional active contour-based methods reported by Vatsa et al. [67] and Shah and Ross [85, 86] due to the benefit of taking into account the image inhomogeneity, which often occurs in the iris region. Also, the proposed RAC algorithm speeds up the curve evolution process to a great extent, since the applied regularization term avoids the costly reinitialization process. Again, the proposed segmentation algorithm, using RAC, shows a reasonable performance when the iris/sclera boundary is separated by a weak boundary. Furthermore, the proposed LS curves are evolved over a narrowband and thus, this process reduces the overall segmentation time in all cases of the above-mentioned iris/pupil detection schemes.

With the LS method, the GAR at a fixed FAR of 0.001% was (a) 98.03% in ICE 2005, (b) 96.10% in WVU Nonideal, (c) 97.08% in UBIRIS Version 1, and (c) 97.00% in CASIA Version 1 Interval datasets. The GAR obtained for the LS method on the combined dataset, at the fixed FAR of 0.001% was 96.82%. After deploying the VLS method, the GAR at a fixed FAR of 0.001% was (a) 98.10% in ICE 2005, (b) 96.23% in WVU Nonideal, (c) 97.10% in UBIRIS Version 1, and (c) 97.08% in CASIA Version 1 Interval datasets. The GAR for the VLS method on the combined dataset at the

fixed FAR of 0.001% was 97.00%. When we employed the RAC model for iris/pupil detection, we found that the GAR at a fixed FAR of 0.001% was (a) 98.20% in ICE 2005, (b) 96.31% in WVU Nonideal, (c) 97.20% in UBIRIS Version 1, and (c) 97.14% in CASIA Version 1 Interval datasets. The GAR for the RAC method on the combined dataset at the fixed FAR of 0.001% was 97.12%. From the experimental results, we found that the RAC model exhibited a better performance than the LS-based and VLS-based methods, since the RAC model includes the intensity information for the localization purpose. However, the VLS method evolves quickly towards the inner/outer boundary as compared to the LS and RAC methods. Furthermore, Fig. 4.19 shows that the localization algorithm, using RAC, results in a drastic improvement of the segmentation performance on the WVU Nonideal dataset, which contains off-angle iris images. However, the proposed active contour-based segmentation algorithms (LS, VLS, and RAC) failed to perform on some images of the UBIRIS dataset due to the huge occlusion, as shown in Fig. 4.20. Fig. 4.21 also shows that the elliptical fitting strategy fails to detect the outer boundary accurately; however, this strategy provides an initial estimate of the inner and outer boundaries for the final segmentation when using LS approaches. Fig. 4.21 shows that the VLS-based localization process isolates the iris and pupil boundaries accurately in those corresponding cases. Therefore, we observed that the elliptical fitting process alone could not provide an optimal estimation of the iris boundary. However, the results show that the elliptical fitting technique performs reasonably well for pupil detection since the pupil is the darkest region of the iris and is easier to isolate. In Fig. 4.22, when applying the LS method, we can also see that the segmentation error

occurs on several iris images due to the poor quality of the images, the huge occlusions and the deviated gazes.

In this chapter, we use AASVMs for iris pattern classification. Table 4.1 shows the performance of different kernel functions on the combined dataset. This table demonstrate that the highest accuracy is obtained by using the RBF kernel, and thus, this kernel is used in our system for pattern matching with AASVMs. We also tune the parameter values of AASVMs to improve the generalization performance, as described in Chapter 3. In order to reduce the computational cost and to speed up the classification process, the Fisher's least square linear classifier is used again as a low-cost pre-classifier. The Fisher's least square linear classifier allows a reasonable cumulative recognition accuracy to be achieved and includes a true class label for a small number of selected candidates. The selected values for tuning the SVM parameters are given for the combined dataset in Table 4.2. The deployment of AASVMs also reduces the matching time of a test sample considerably. Table 4.3 summarizes the recognition results, and this table shows that a drastic reduction in the decision time can be achieved when the number of SVs is lower. However, the selection of the matching accuracy/testing time is a security requirement trade-off. The selected accuracy with the decision time, the simplification rate and the number of FVs are shown in the bold form in Table 4.3 for the combined dataset.

The proposed GA-based feature selection approach is used to reduce the feature dimension without compromising the recognition rate and is based on the multiple

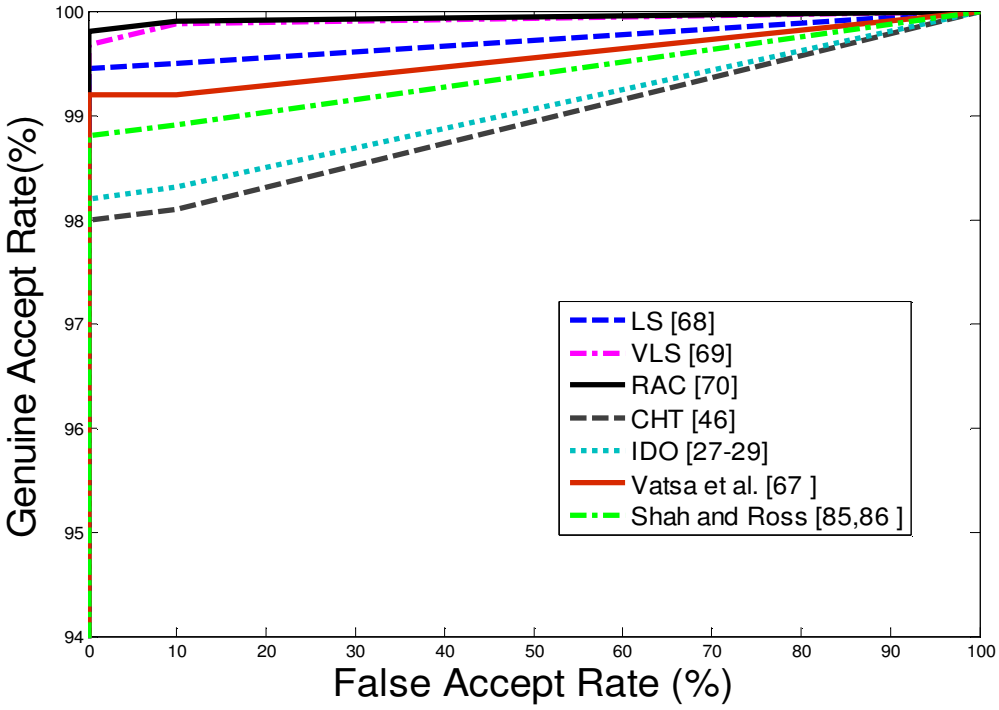
Genuine Accept Rate(%)
False Accept Rate (%)
LS [68]
VLS [69]
RAC [70]
CHT [46]
IDO [27-29]
Vatsa et al. [67]
Shah and Ross [85,86]

(a)

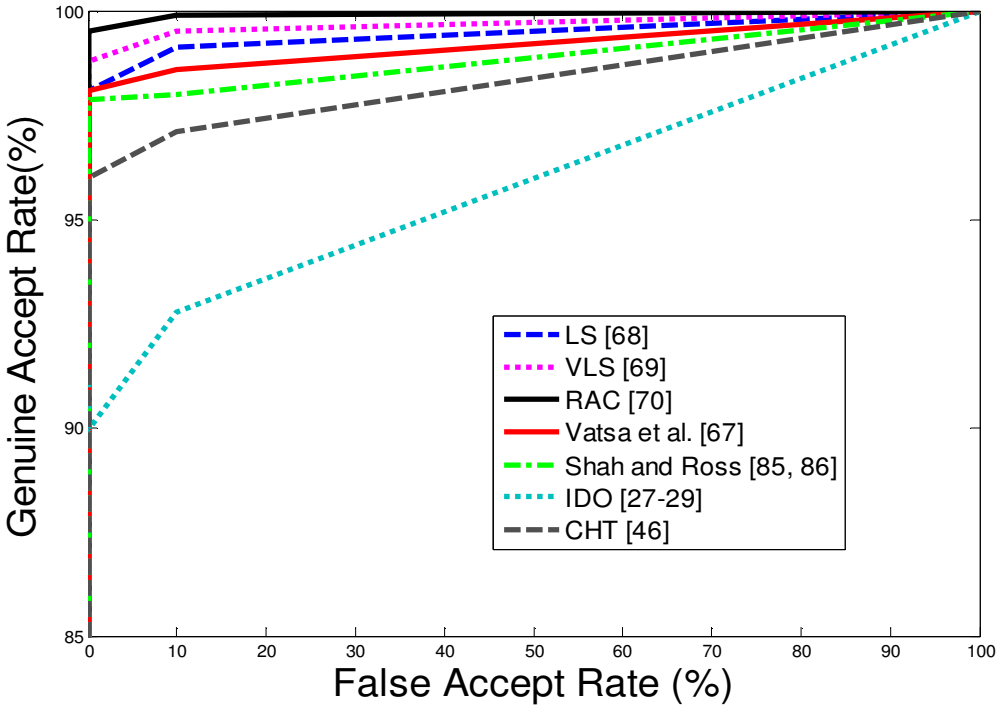
Genuine Accept Rate(%)
False Accept Rate (%)
LS [68]
VLS [69]
RAC [70]
Vatsa et al. [67]
Shah and Ross [85, 86]
IDO [27-29]
CHT [46]

(b)

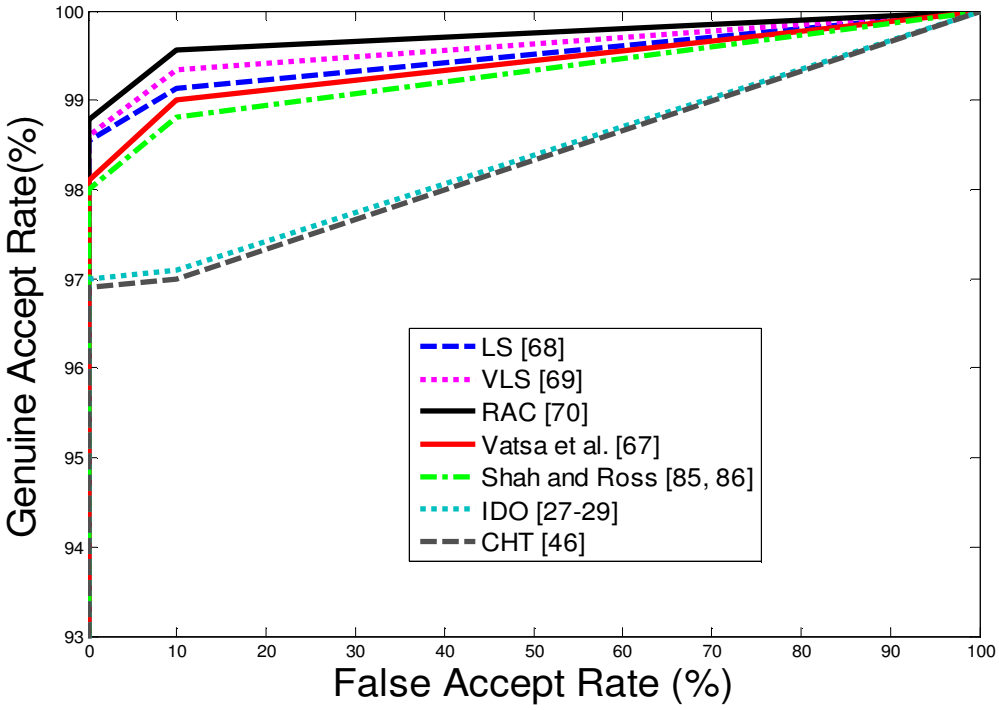
Genuine Accept Rate(%)
False Accept Rate (%)
LS [68]
VLS [69]
RAC [70]
Vatsa et al. [67]
Shah and Ross [85, 86]
IDO [27-29]
CHT [46]

(c)

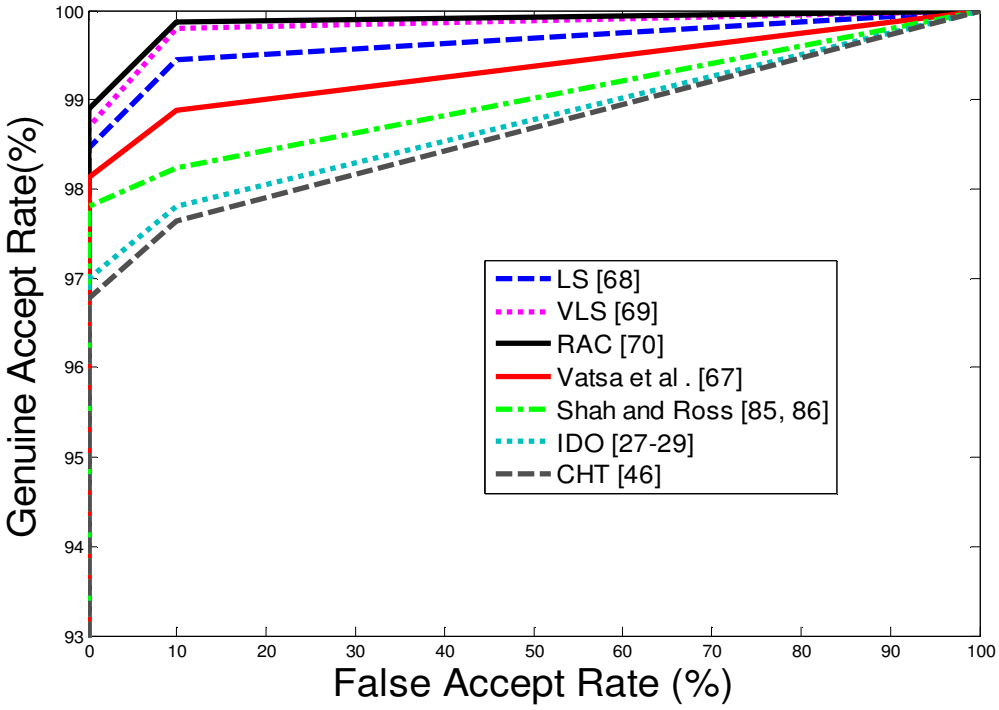
Genuine Accept Rate(%)
False Accept Rate (%)
LS [68]
VLS [69]
RAC [70]
Vatsa et al . [67]
Shah and Ross [85, 86]
IDO [27-29]
CHT [46]

(d)

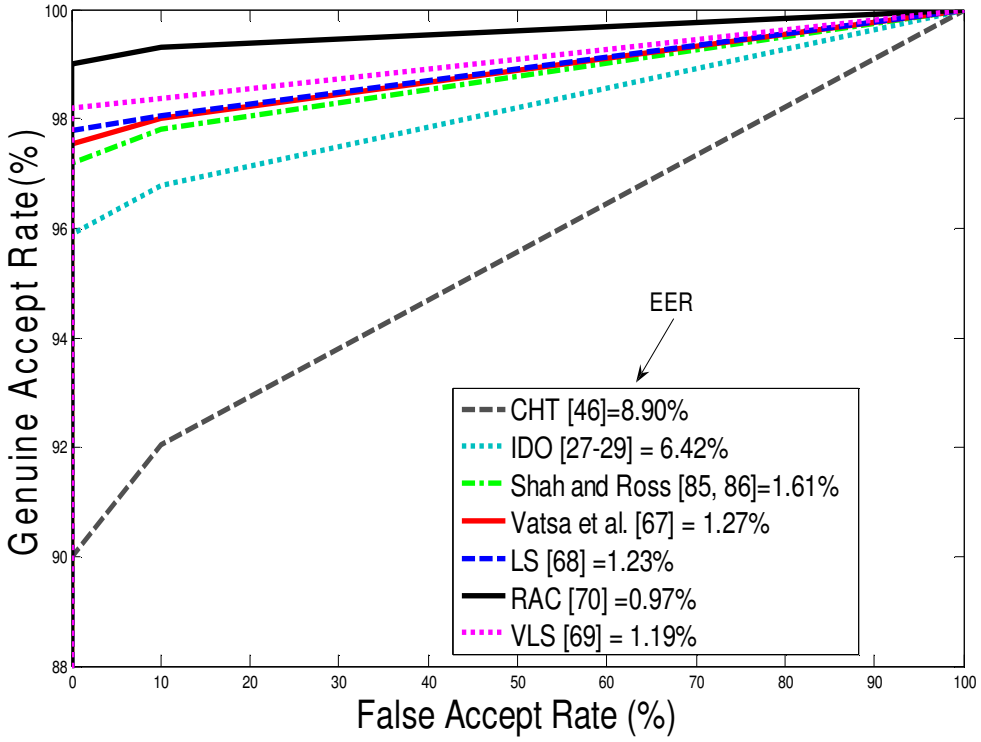

(e)

Fig. 4.19 ROC curves show the comparison of existing segmentation techniques on (a) ICE 2005, (b) WVU Nonideal, (c) CASIA Version 3 Interval, (d) UBIRIS Version 1, and (e) Combined datasets.

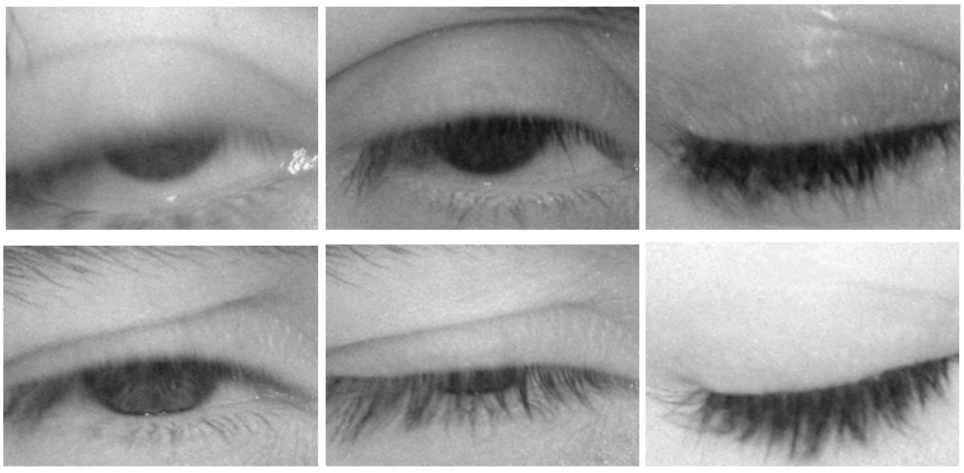

Fig. 4.20 Samples of iris images from UBIRIS Version 1 dataset, on which the proposed segmentation schemes using LS, VLS, RAC, GT and SGA fail to detect the iris/pupil boundary.

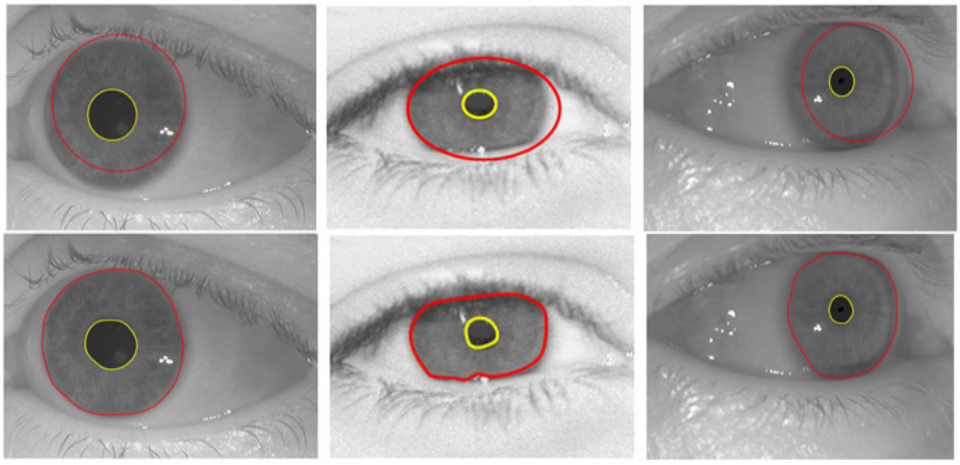

Fig. 4.21 Samples of iris images on which the DLS-based elliptical fitting approach fails to detect the outer boundary accurately (Upper row). However, our proposed VLS-based segmentation approach successfully isolates the inner and outer boundaries for the corresponding images (Lower row).

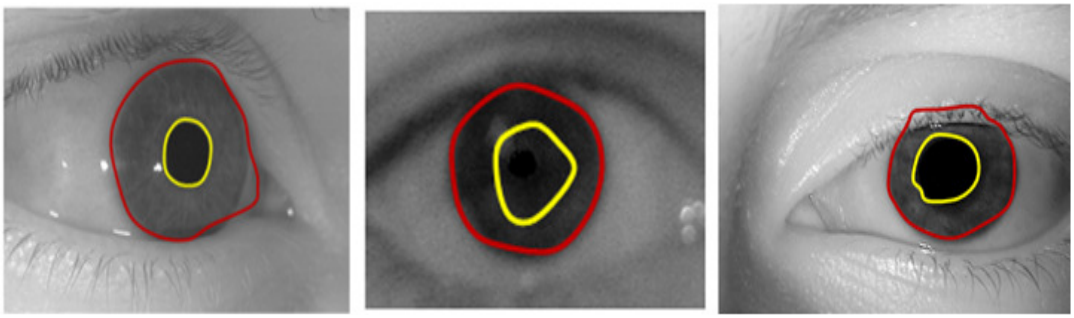

(a) (b) (c)

Fig. 4.22 Segmentation errors found on several images of (a) WVU Nonideal, (b) UBIRIS Version 1, and (c) ICE 2005 datasets, using VLS-based approach.

Table 4.1: Performance of different kernel functions on the Combined dataset.

(a) LS Method

Kernel type	Classification accuracy (%) on Combined dataset
Polynomial	92.14
RBF	94.45
Sigmoid	91.67

(b) VLS Method

Kernel type	Classification accuracy (%) on Combined dataset
Polynomial	93.45
RBF	94.81
Sigmoid	91.84

(c) RAC Method

Kernel type	Classification accuracy (%) on Combined dataset
Polynomial	93.90
RBF	95.12
Sigmoid	92.10

Table 4.2: Selected values for tuning SVM parameters on the Combined dataset.

Datasets	Cumulative recognition accuracy	Rank	Number of cardinal sets	Training size	Validation size	Ratio between C^+ and C^-	σ^2
Combined (LS)	98.10%.	70	180	378	162	20	0.65
Combined (VLS)	98.33%.	80	200	420	180	25	0.80
Combined (RAC)	98.25%	85	210	441	189	22	0.65

Table 4.3: Test results on the Combined dataset.

(a) LS Method

Algorithm	#fv/#sv	Simplification rate (%)	Testing time (ms)	Recognition rate (%)
$SVM_{Adaptive}$	90/95	5.26	150.12	96.88
	70/95	26.31	123.40	96.80
	60/95	**36.84**	**100.10**	**96.76**
	40/95	57.90	97.00	96.31
SVM	95/95	0	160.70	96.90

*** Kernel-RBF, σ^2=0.65, Ratio between penalty parameter=20**

(b) VLS Method

Algorithm	#fv/#sv	Simplification rate (%)	Testing time (ms)	Recognition rate (%)
$SVM_{Adaptive}$	90/95	5.26	155.20	97.04
	70/95	**26.31**	**128.70**	**97.00**
	55/95	42.10	110.00	96.90
	40/95	57.90	98.90	96.60
SVM	95/95	0	167.10	97.05

*** Kernel-RBF, σ^2=0.80, Ratio between penalty parameter=25**

(c) RAC Method

Algorithm	#fv/#sv	Simplification rate (%)	Testing time (ms)	Recognition rate (%)
$SVM_{Adaptive}$	90/95	5.26	152.10	97.10
	70/95	26.31	122.00	97.06
	50/95	**47.36**	**105.10**	**97.05**
	40/95	57.90	93.00	96.80
SVM	95/95	0	162.90	97.13

*** Kernel-RBF, σ^2=0.65, Ratio between penalty parameter=22**

outputs from four feature selection algorithms. Since the number of samples from most iris datasets is limited, the cross-validation procedure is commonly used to evaluate the performance of a classifier. In *k*-fold cross validation, the data is divided into *k* subsets of (approximately) equal sizes. We train the classifier k *times*, each time leaving out one of the training subsets, but using only the omitted subset to compute the classification accuracy. The Leave-One-Out Cross-Validation (LOOCV) is a special case of *k*-fold cross-validation where *k* equals the sample size. LOOCV was used for ICE dataset, and for WVU, CASIA and UBIRIS datasets, we used 2-fold cross validation to obtain the training accuracy for GAs. Fig. 4.23 shows the accuracy of the selected feature subsets, with a different number of top-ranked features from the four feature selection algorithms on four data sets. We select the first 150 top-ranked features from each algorithm for the feature pool of GAs, since most of the curves start to level-off at 150. Fig. 4.23 shows that SVM-RFE achieves a better accuracy than the other feature selection methods, using all the segmentation schemes discussed earlier. Therefore, after obtaining 150 top-ranked features from different feature reduction algorithms, we input them to the feature pool used by the GAs, as demonstrated previously in Fig. 4.12.

In order to select the optimal features for the improvement of the matching accuracy, GAs involve running the genetic process for several generations with different values of weighting parameters in the proposed fitness function, as shown in Fig. 4.24. We conducted several experiments, and selected a common set of arguments for the GAs, as reported in Table 4.4. However, the performance degraded slightly on the combined dataset for the common set of parameter values, due to the variations in image contrast, the capturing devices and also due to the differences in sample populations. The parametric values were obtained by using the existing heuristics in the genetic process plus some minor efforts in empirical searching via experiments. We ran the learning/evolutionary process for a fixed number (*max-generations*) of 60 generations, unless the GA finds a program that solves the problem perfectly (e. g., with a 100% detection rate), or if there is no increase in the fitness for 10 generations, then the evolution is terminated early. From the experiments, we found that the proposed GA-based scheme achieved the highest accuracy of: (a) 96.85% at the 40^{th} generation, with a reduced feature subset of 123 for the combined dataset using LS; (b) 97.03% at the 30^{th} generation, with a reduced feature subset of 130 for the combined dataset using VLS; and (c) 97.10% at the 15^{th} generation, with a reduced feature subset of 110 for the combined dataset using RAC. We conducted the above experiments on a 3.00 GHz Pentium IV PC with 2.5 GB RAM in a MATLAB 7.2 environment. The average time consumed in matching an iris image was: (a) 17760 ms using LS; (b) 7628 ms using VLS; and (c) 8515 ms using RAC, as exhibited in Table 4.5. The Table 4.5 shows that the LS

method involves a higher computation time than the other two segmentation approaches.

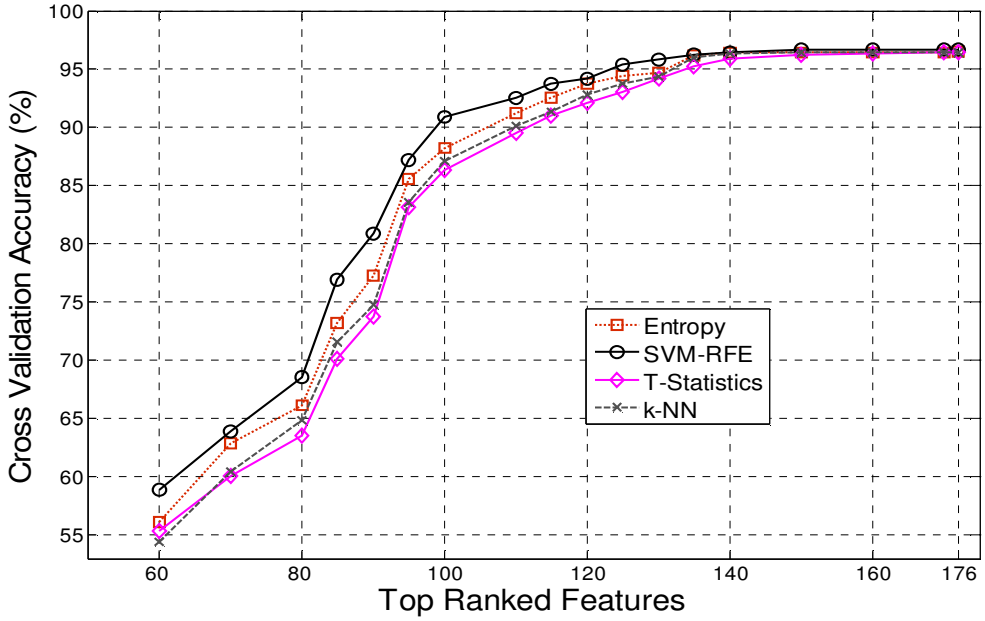

(a)

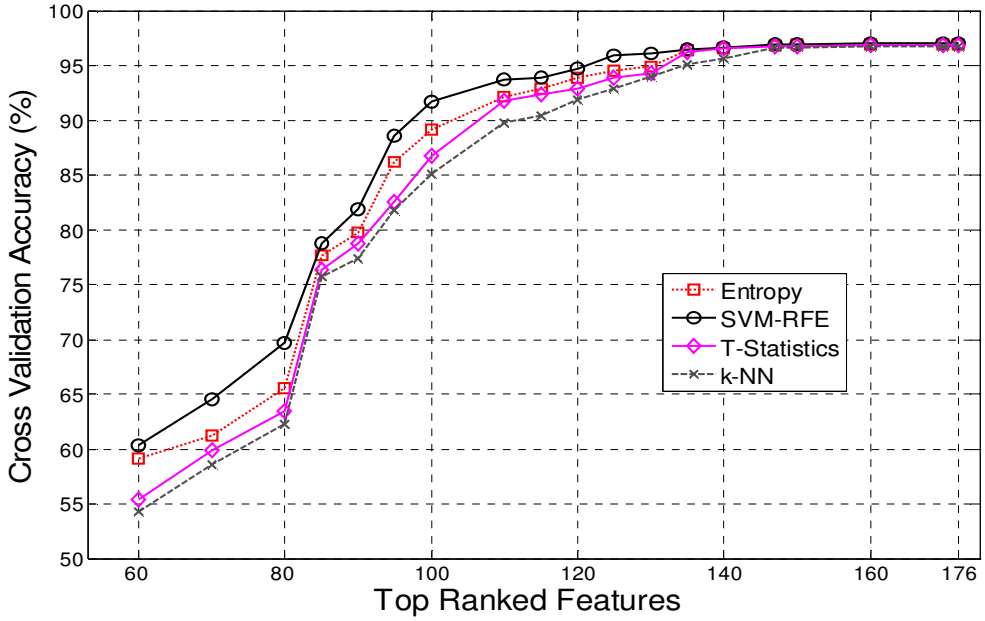

(b)

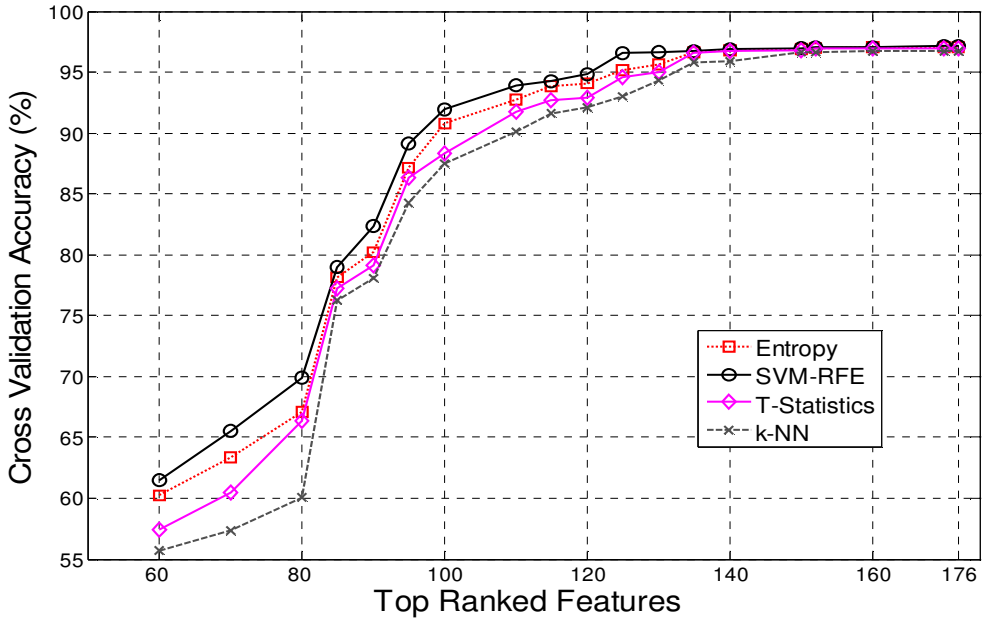

(c)

Fig. 4.23 Cross-validation accuracy vs. top-ranked features on the Combined dataset for: (a) LS, (b) VLS, and (c) RAC methods.

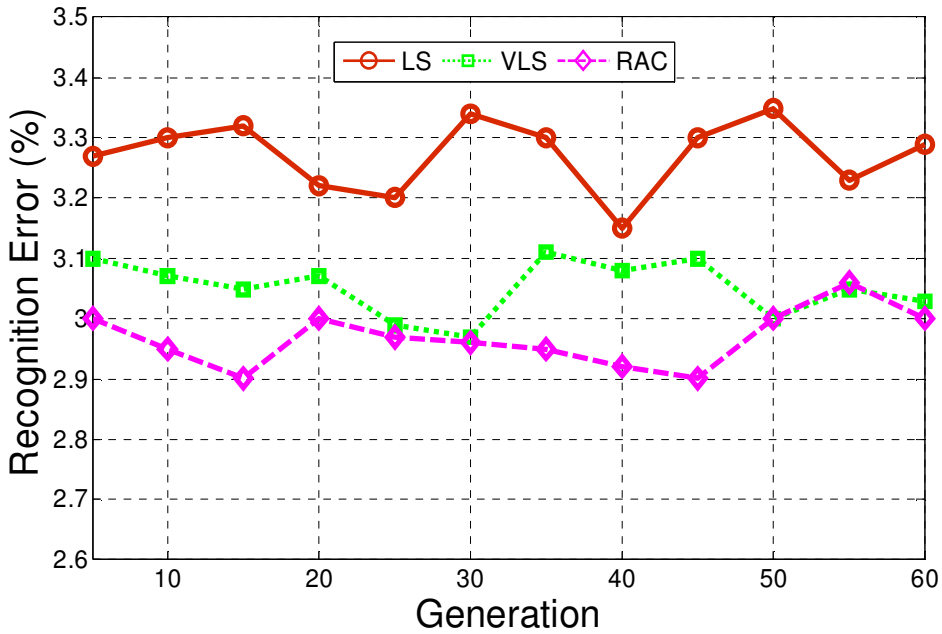

Fig. 4.24 Comparison between generation and recognition error on the Combined dataset for LS, VLS and RAC methods.

Table 4.4: Common set of arguments for GA on the Combined dataset for LS, VLS and RAC methods.

Parameters	Combined Dataset
Population Size	1081 (the scale of iris sample)
Length of Chromosome code	150 (input dimensionality of feature sequence obtained from multiple feature selection algorithms)
Crossover probability	0.60
Mutation probability	0.008
Number of generation	60 (Selected dimension of 123, 130 and 110 elements for LS, VLS and RAC methods, respectively)
Weighting Parameters	W_1= 2000, W_2 =150 W_3= 10,W_4 =1000

Table 4.5: Average time consumption of different parts of the proposed iris recognition system in LS, VLS and RAC methods.

(a) LS Method

Algorithm	Time (ms)
Iris Segmentation	17500
Unwrapping	95
Feature Extraction	65
Matching	100
Average Execution Time*	17760

*Extra cost for feature subset reduction

(b) VLS Method

Algorithm	Time (ms)
Iris Segmentation	7340
Unwrapping	95
Feature Extraction	65
Matching	128
Average Execution Time*	7628

*Extra cost for feature subset reduction

(c) RAC Method

Algorithm	Time (ms)
Iris Segmentation	8250
Unwrapping	95
Feature Extraction	65
Matching	105
Average Execution Time*	8515

*Extra cost for feature subset reduction

4.6.2 Comparison of the Proposed Methods with the State-of-the-Art Algorithms

We compared the performance of the proposed algorithm with other existing iris recognition algorithms. We implemented the well-known iris recognition algorithms proposed in [27-29] and [22, 31], and compared our approach with those methods on the combined dataset. Fig. 4.25 exhibits the ROC curves of the proposed algorithms with the curve evolution approaches on the non-homogeneous combined dataset. The ROC curves of the approaches demonstrated in [27-29, 22, 31] are also plotted for comparison, and this figure shows that the proposed algorithm achieves higher GARs as compared to the other methods for the combined dataset. This means that the proposed algorithms based on LS, VLS and RAC achieve higher discriminating capabilities than the approaches proposed in [27-29, 22, 31]. Moreover, the approaches proposed in [27-29, 22, 31] were not designed specifically for the noncooperative environments. The proposed approach, based on the LS curve evolution with an edge stopping function and an energy minimization algorithm, obtains a higher GAR of 96.86% at the fixed FAR of 0.001% on the combined dataset. This dataset contains the iris images with irregularities due to motion blur, off-angle gaze, diffusion, and other real-world problems. Similarly, VLS and RAC-based methods achieve GARs of 97.02% and 97.14% at the fixed FAR of 0.001% on the combined dataset, respectively. Therefore, the ROC curves in Fig 4.25 reveal the effectiveness of the proposed scheme in a nonideal situation. The major difficulty, which is common to any dataset, is the segmentation error. The localization approach, described in Section 4.2, works well for most of the cases and even for the iris images of deviated gazes. The DLS-based elliptical fitting provides

an initial estimate of the inner boundary, and the active contours localize the iris and pupil regions accurately. In Table 4.6 (a, b), the proposed schemes exhibited the highest CRRs for ICE, CASIA, WVU and UBIRIS datasets. For the combined dataset, we found the CRR of 96.91% using the LS method, revealing a top class performance with respect to the nonideal datasets under consideration. The EER of the proposed approach, using LS on the combined dataset was 1.20%, which was

Table 4.6: Comparison of CRR, EER and length of feature vectors.

(a) Comparison of CRR.

Algorithm	Correct Recognition Rate (CRR) (%)				
	ICE	CASIA	UBIRIS	WVU	Combined
Daugman [27-29]	98.13	95.70	97.28	83.14	93.43
Ma *et al.* [31]	95.79	95.54	95.45	78.33	92.56
Ma *et al.* [22]	95.64	94.90	95.78	77.24	91.23
Proposed LS*	**98.15**	**97.10**	**97.21**	**96.12**	**96.91**
Proposed VLS*	**98.20**	**97.13**	**97.27**	**96.25**	**97.03**
Proposed RAC*	**98.25**	**97.18**	**97.40**	**96.42**	**97.15**

*Two samples per class were used to train the AASVM and the rest of the samples of each class were used for testing for all the datasets.

(b) Comparison of EER

Algorithm	Equal Error Rate (EER) (%)				
	ICE	CASIA	UBIRIS	WVU	Combined
Daugman [27-29]	0.49	1.80	0.96	8.45	6.38
Ma *et al.* [31]	1.72	2.07	1.21	10.50	6.40
Ma *et al.* [22]	1.80	2.62	1.13	11.43	8.72
Proposed LS	**0.48**	**1.10**	**0.75**	**1.93**	**1.20**
Proposed VLS	**0.43**	**0.96**	**0.70**	**1.80**	**1.14**
Proposed RAC	**0.40**	**0.90**	**0.60**	**1.72**	**0.93**

(c) Comparison of feature vector length

Algorithm	Length of feature vectors
Daugman [27-29]	2048 bits
Ma *et al.* [31]	160 elements
Ma *et al.* [22]	384 elements
Proposed LS	**123** elements
Proposed VLS	**130** elements
Proposed RAC	**110** elements

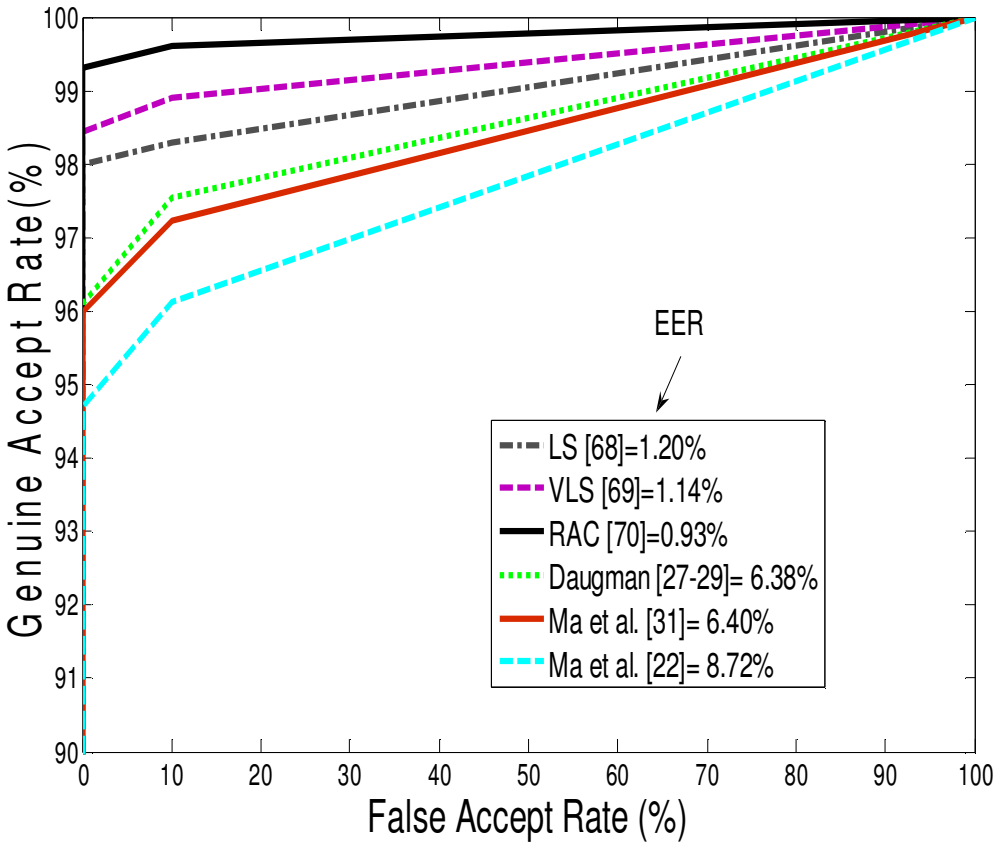

Fig. 4.25 Comparison of our proposed methods with existing iris recognition schemes on the Combined dataset.

also encouraging. We further improved the identification performance using the VLS and RAC approaches. The VLS method achieved CRR of 97.03% with the EER of

1.14%. The segmentation scheme, using RAC, reached the CRR of 97.15% with a very low EER of 0.93%. Moreover, the lengths of the feature vectors were 123, 130 and 110 using LS, VLS and RAC methods, respectively. Thus, the obtained feature lengths were much smaller than the feature vector lengths reported in literature pertaining to the other existing iris recognition algorithms. Therefore, the computational complexities were reduced without compromising the recognition rate.

4.7 Conclusion

In this chapter, we focused on three performance issues: First, the accurate localization of the iris regions from degraded eye images that may be affected by the following problems: gaze deviation, diffusion, non-linear deformation, low intensity, poor acquisition process, eyelid and eyelash occlusions and small opening of the eye. We presented a nonideal iris segmentation scheme using the LS-based curve evolution approaches with the edge stopping function and energy minimization method. Since most state-of-the-art active contour-based iris segmentation schemes require a substantial computational time, the proposed VLS method uses a significantly larger time step to solve the PDE evolution equation, and therefore, this speeds up the curve evolution process considerably. The intensity inhomogeneity often occurs in iris images and may cause considerable difficulties in iris/pupil segmentation. The proposed RAC algorithm provides a better performance than the existing nonideal iris recognition algorithms, when the iris images suffer from intensity inhomogeneity.

Second, GAs are used to find the subset of informative texture features. The proposed GA incorporates four feature selection criterions, namely, the SVM-RFE, the k-NN, the T-statistics, and the entropy-based methods to find the subset of informative texture features that can improve the analysis of iris data. The experimental results show that the proposed method is capable of finding feature subsets with better classification accuracies and/or smaller sizes than each single individual feature selection algorithm.

Third, in order to increase the feasibility of SVMs in biometric applications, the SVMs are modified to AASVMs. The adopted simplification scheme of solutions for the *SV* captures the structure of the feature space by approximating a basis of the *SV* solutions. Therefore, the statistical information of the solutions for the *SV* is preserved. Furthermore, the number of *FVs* is selected adaptively according to the task's need to control the generalization/complexity trade-off directly. We validated the proposed iris recognition scheme on the ICE 2005, the WVU Nonideal, the UBIRIS Version 1, CASIA Version 3 Interval datasets and the nonhomogeneous combined datasets, all of which resulted in encouraging performances.

Chapter 5

Enhancement of Iris Segmentation Performance Using Game Theory

This chapter presents a new iris segmentation technique that is based on Game Theory (GT). Section 5.1 discusses the motivation behind this research effort. In Section 5.2, the proposed iris segmentation method is discussed. In this section, first, we present the game theoretic localization scheme, and then, describe the unwrapping and enhancement techniques. A simple matching strategy, based on Hausdorff distance (HDD), is also introduced in this section. The experimental results on different nonideal datasets are presented in Section 5.3. Finally, in Section 5.4, some features of the proposed method are summarized with some concluding remarks.

5.1 Introduction

The exact segmentation of the iris plays perhaps the most important role in iris recognition. The main task of the segmentation routine is to localize the inner/outer boundary from the iris. Apart from the proper localization of the iris structure, the

segmentation scheme should also identify the eyelid and eyelash occlusions and detect the other noisy regions such as reflections. The localization error may result in lower recognition performance due to incorrect encoding of the textural content of the iris.

Most existing iris segmentation methods use the gradient information to locate the inner and outer boundaries of the iris [2, 3, 22, 27-33, 37, 38, 42, 45, 46, 51, 52, 55, 68, 69, 71, 74, 75, 77, 79-81, 85, 86, 124, 140, 141, 145, 146, 148, 149, 165-168]. However, the low-level boundary methods, like edge detection, are not suitable for extracting whole edges as they suffer from false and broken edges. Several researchers have applied the deformable whole boundary methods that rely on the gradient features at a subset of the spatial positions of the image [3, 68, 69, 74, 75, 85, 86]. This approach handles the discontinuities in the data effectively by imposing the global shape information and is more adaptable to changes in the topology of the object under consideration [9, 10, 156, 157, 159]. However, such a method relies on the value of the gradient regarding the boundary points and thus, suffers from noise sensitivity.

Another well known approach for segmentation is the region-based method that depends on the homogeneity of spatially localized features and other pixel statistics [67, 70, 147]. The main advantage of these schemes is that they depend directly on the gray-level image and thus, are less susceptible to noise than the other methods that use the derivative information. However, such a region-based scheme suffers from poor localization and over-segmentation. Therefore, the region-based schemes have better noise properties and are less affected by the blurred boundaries. The

boundary-based approaches, on the contrary, have a superior localization performance and perform better against the shape variation [14, 15].

From the above discussion, it is clear that a better segmentation performance can be achieved if we integrate both segmentation methods and fuse the complementary strengths of these individual schemes. Most state-of-the-art research on iris-based biometrics is focused on the preprocessing of the frontal view image of an eye's iris. In an ideal imagery setup, the iris image is captured through a stop-and-stare interface [75]. However, in many occasions, the irises are imaged in an environment where the user interaction with the capturing devices is required to be kept at a minimum due to some ongoing security issues. For iris segmentation, most researchers assume that the iris regions always maintain circular or elliptical shapes. However, in the case of nonideal iris images, which are captured in an uncontrolled environment, the iris may not maintain a particular shape [67, 74, 75, 165]. Also, in the images where the eyes are partially opened, the severely covered regions cannot be extracted, and hence, the segmentation performance is hampered. The iris images may also be affected rigorously by the following nonideal factors, as discussed in Chapter 2: deviated gazes, non-linear deformations, pupil dilations, head rotations, motion blurs, reflections, non-uniform intensities, low image contrast, camera angles and diffusion, and presence of eyelids and eyelashes. In this chapter, we use the methodologies to account for such disturbances and develop a robust nonideal iris segmentation scheme using GT, which integrates the complementary strengths of the region-based and gradient-based boundary finding methods.

5. 2 Iris Segmentation using Game Theory (GT)

Most of the state-of-the-art iris localization schemes use only the gradient or the region data for segmentation purposes [36]. Table 1 shows the comparison of existing nonideal iris segmentation algorithms. The segmentation approaches reported in [3, 67-69, 75, 84-86, 94, 142, 146] are based on the deformable boundary. These approaches produce a good fit and handle the discontinuities in contour data. However, the performance of such approaches may be deteriorated by the effects of a weak iris/sclera boundary, non-uniform intensity and low image contrast since each of these schemes uses only the boundary-based information for iris localization. The nonideal iris segmentation approaches reported in [76, 77, 79-81, 140, 141, 145-149, 167, 168] solely depend on the gradient-based information for iris/pupil detection. Furthermore, the parametric active contour-based iris segmentation scheme proposed in [75, 141] may terminate at a certain local minima such as terminating at the specular reflections, the thick radial fibers in the iris or the crypts in the ciliary region. Also, the technique reported in [75] depends on the order of the Fourier series to approximate the inner and outer boundaries of the iris. However, the order of the two boundaries may be different. Thus, selecting the order of the Fourier series is a difficult task [86]. The curve evolution approaches deployed in [68, 69, 85, 86, 169] depend on the value of the gradient for the boundary points and thus, may suffer from the noise sensitivity. Also, the region-based approaches proposed in [67, 70, 147, 170, 171] may be affected by poor localization and over segmentation. Addressing the above problems, a GT-based fusion scheme is deployed to accurately extract the iris from the

Table 5.1 Comparison of different nonideal iris segmentation algorithms.

Authors	Iris segmentation algorithms
Daugman [75]	Active contours and generalized coordinates, excluding eyelashes using statistical inference
Proenca and Alexandre [164]	Integro-differential operator
Vatsa et al. [67]	Modified Mumford-Shah functional
Miyazawa et al. [3]	Deformable iris model with 10 parameters
He et al. [166]	Pulling and pushing elastic approach to obtain the centre and radius of iris boundary, a spline-based fitting scheme to approximate noncircular iris/pupil boundary, a curve fitting strategy for eyelid detection, and a learned prediction model to detect eyelashes and shadows
Schuckers et. al. [74]	Integro-differential operator and angular deformation model
Shah and Ross [85, 86]	Geodesic Active Contours (GACs)
Puhan et al. [141, 148]	Fourier spectral density
Roy et al. [68]	LS-based method
Roy et al. [69]	VLS- based method
Roy et al. [70]	RAC model
Zhang et al. [77]	Radial symmetry transform
Abhyankar and Schuckers [79]	The wavelet domain in-band de-noising method to enhance the quality of iris images
Luengo-Oroz et al. [80]	Mathematical morphology
Al-Daoud et al. [81]	Competitive chords to detect the pupil/iris and the iris/sclera boundaries
Tajbakhsh et al. [145]	Local intensity variation method
Koh et al. [84]	Traditional active contour model and circular Hough transform
Jeong et al. [82]	Circular edge detection and AdaBoost eye detection
Pundlik et al. [168]	Graph cut-based energy minimization algorithm
Proenca [76]	Iris parameterization using polynomial regression
Zhou et al. [140]	video-based image-processing techniques to identify and eliminate the bad quality images, iris image quality assessment
Zuo and Schmid [146]	Elliptical fitting technique along with reflection detection, contrast enhancement, occlusion estimation and off-angle compensation methods
Du et al. [142]	The quality filter to remove images without an eye, a coarse-to-fine segmentation scheme to improve the overall efficiency, a DLS elliptical fitting method to model the deformed pupil and limbic boundaries, and a window gradient-based method to remove noise in the iris region
Belcher and Du [147]	Region-based SIFT approach to elicit the iris structure
Proposed approach	Game-theoretic fusion strategy that combines the complementary strengths of region-based and boundary-based methods

surrounding structures in an iterative fashion. Game theoretic methods have been used in the field of medical image analysis to segment MRI images of the heart and brain, and also to rank the best features from the extracted feature sequence of a relatively higher dimension [172]. Furthermore, GT has been used extensively in wireless network research to help researchers develop an understanding of stable operation points for networks [173]. In this chapter, the significance of GT in the context of nonideal iris segmentation is demonstrated.

We propose a three-stage iris segmentation algorithm, in which, we first apply a noise-removal scheme to reduce the effects of specular reflections. In the second stage, we estimate an initial approximation of the centre point of the pupil by using the DLS [52]-based elliptical fitting. In the third stage, we apply a parallel game-theoretic decision making procedure by modifying the algorithm designed by Chakraborty and Duncan's [14, 15]. This algorithm combines the region-based segmentation and the boundary finding methods for the optimal estimation of the inner and the outer boundaries. Furthermore, to improve the quality of the iris image, we apply a local histogram equalization technique, and to suppress the effect of noise, we deploy the 2D Wiener filter to the equalized images [174].

In the first stage of segmentation, we remove the specular reflection spots that are found inside the pupillary region (see Figs. 5.1(a) and 5.2(a)), as these white spots may cause a false inner boundary detection and may also halt the region-growing process prematurely. To remove these spots, first we complement the input iris image by taking the absolute subtraction of each pixel's intensity level from 255, and then, we fill the dark holes found in the pupillary region in the complemented iris

image. A “hole” is the set of dark pixels surrounded by light pixels that cannot be reached from the edge of the image. We adopt the connectivity of 4-pixels on the background pixels. Finally, we complement the processed image again and apply the Gaussian filter to smoothen the resulting sharp image. This process is illustrated in Figs. 5.1 and 5.2. In the second stage, we deploy a DLS-based elliptical fitting to approximate the pupil boundary as discussed in Chapter 4. The DLS-based elliptical fitting returns five parameters (p_1, p_2, r_1, r_2, φ_1): the horizontal and vertical coordinates of the pupil center (p_1, p_2), the length of the major and minor axes (r_1, r_2), and the orientation of the ellipse (φ_1). This method, thus, provides a rough estimation of the pupil boundary and the centre of the pupil.

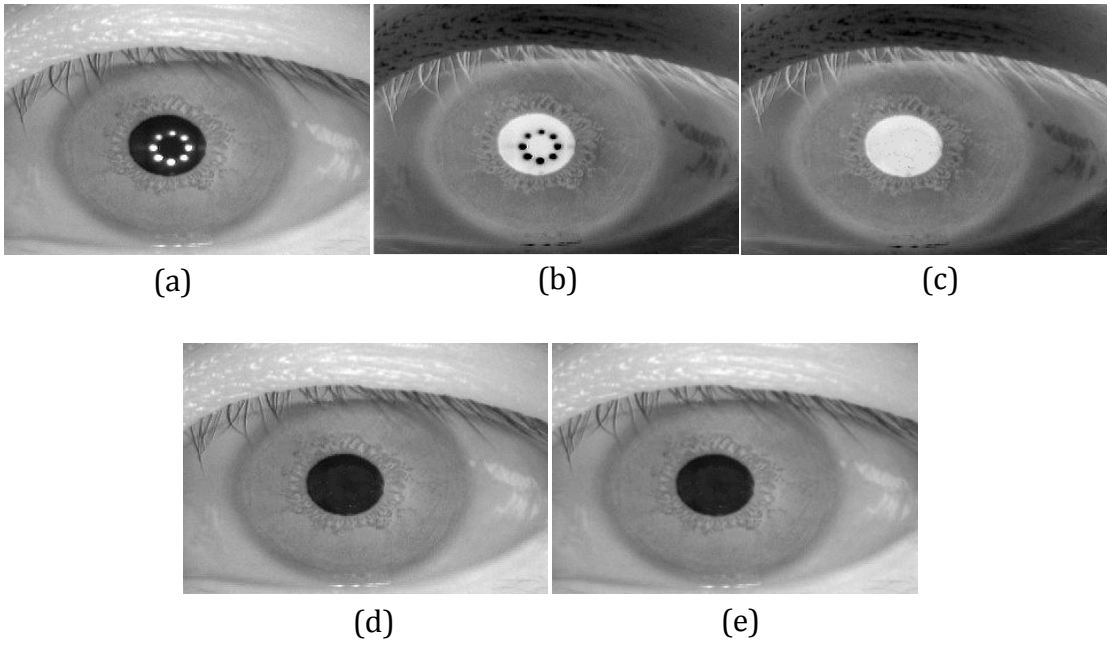

Fig. 5.1 Image preprocessing on CASIA Version 3 Interval dataset: (a) Original image; (b) complement of the image (a); (c) filling the holes; (d) complement of image (c); and (e) image after Gaussian smoothing.

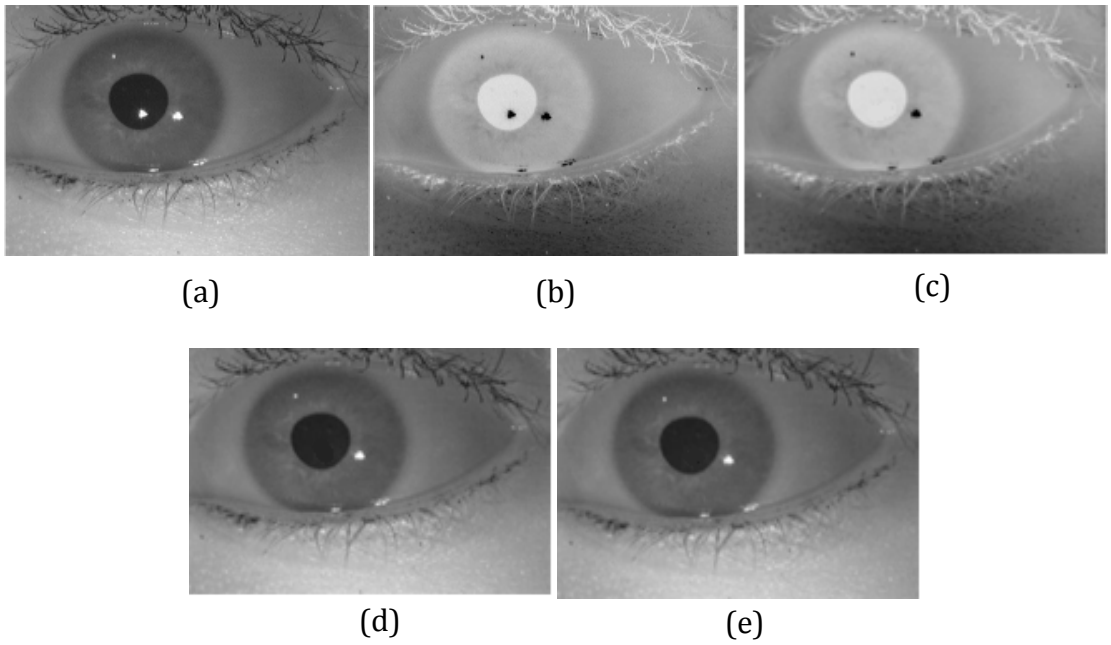

Fig. 5.2 Image preprocessing on WVU Nonideal dataset: (a) Original image; (b) complement of the image (a); (c) filling the holes; (d) complement of image (c); and (e) image after Gaussian smoothing.

In the third stage, we apply a parallel game-theoretic decision making approach that is based on a modification of Chakraborty and Duncan's method for the exact estimation of the iris/pupil boundary [14, 15]. In this effort, a fully bidirectional framework is developed for integrating the boundary finding scheme and the region-based segmentation scheme. This framework leads to a system where the two schemes can operate in parallel, such that at each step, the output of each scheme gets updated using the information from outputs of both the schemes from the previous iteration and the data itself. Thus, as the game progresses, both the schemes improve their positions through a mutual information sharing (See Fig. 5.3). It was found that the boundary-finding and the region-based segmentation by themselves were unable to provide us with all the necessary information for an

accurate segmentation; this is because, while the region-based segmentation is not likely to give us precise information regarding the iris shape and location, the boundary-finding method may not be feasible if some of the structures are not well located. Therefore, we can expect that a game-theoretic fusion of the two methods will perform better than either of the methods alone, by integrating the complementary strengths of these individual schemes.

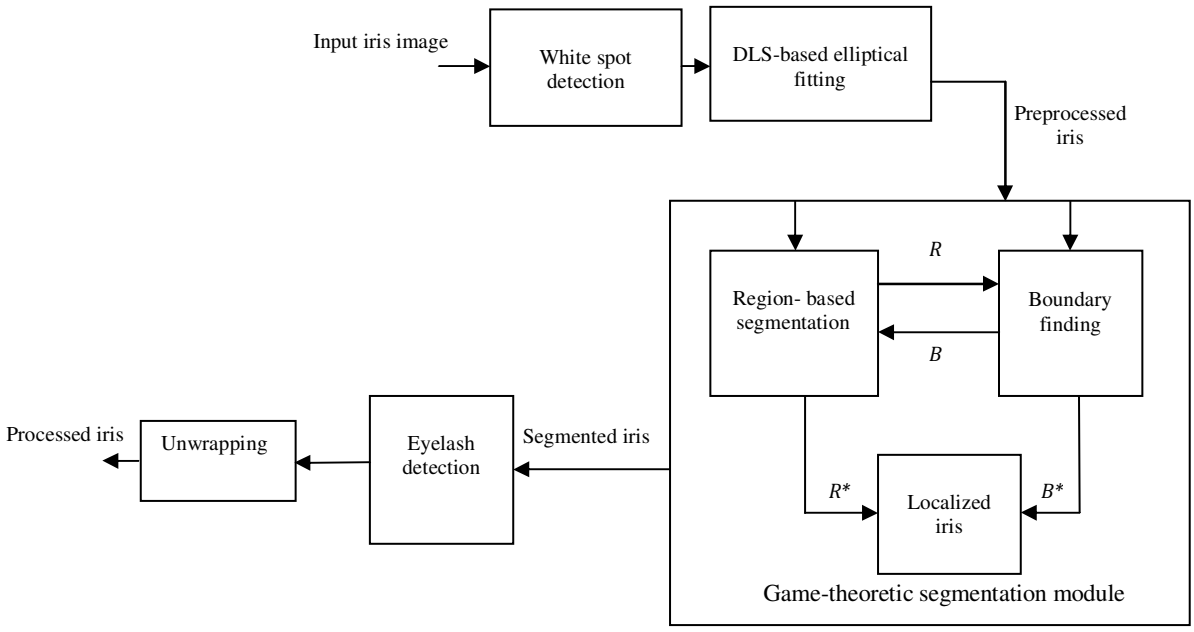

Fig. 5.3 Flow diagram of the proposed iris segmentation scheme. Game-theoretic segmentation module integrates the region-based segmentation and boundary finding methods.

The game is played out by a set of decision makers (or "players"), which in our case, corresponds to the two segmentation schemes, namely, the region-based and the gradient-based boundary finding methods [175, 176]. The iris segmentation problem can be formulated as a two-player game. If p^1 is the set of strategies of the Player 1, and p^2 is the set of strategies of the Player 2, then each player tries to

minimize the payoff function, $F^i(p^1, p^2)$. The main objective is to find the *Nash Equilibrium* (NE) of the system $(\bar{p}^1, \bar{p}^2)$, such that:

$$F^1(\bar{p}^1, \bar{p}^2) \leq F^1(p^1, \bar{p}^2), F^2(\bar{p}^1, \bar{p}^2) \leq F^2(\bar{p}^1, p^2) \tag{5.1}$$

If we move toward the NE iteratively by taking t as the time index, we can formulate the game as:

$$p_{t+1}^1 = \underset{p^1 \in P^1}{\arg min} F^1(p^1, p_t^2);\ p_{t+1}^2 = \underset{p^2 \in P^2}{\operatorname{argmin}} F^2(p_t^1, p^2) \tag{5.2}$$

Chakraborty and Duncan [14] proved that there is always existing NE solution if F^1 and F^2 are of the following form:

$$F^1(p^1, p^2) = f_1(p^1) + \alpha f_{21}(p^1, p^2) \tag{5.3}$$

$$F^2(p^1, p^2) = f_2(p^2) + \beta f_{12}(p^1, p^2) \tag{5.4}$$

where α and β are scaling constants, F^i is bounded in $p^i \in P^i$, F^i is continuously second-order differentiable in $p^i \in P^i$, and there is an existing closed neighborhood of $u^i \subseteq p^i$ such that F^i is strongly convex in u^i. Based on the above assumptions, Chakraborty and Duncan [14] provided the following theorem:

For the payoff functions $F^1(p^1, p^2)$ and $F^2(p^1, p^2)$, there exists a locally stable NE solution. For any $p^1 \in U^1 \subseteq P^1$ and $p^2 \in U^2 \subseteq P^2$, the sequence of rational choices generated by the parallel decision making process converges, and the limit point is the NE solution if α and β satisfy the following condition [14]:

$$\left\| \left[\left(\alpha^{-1} \frac{\partial^2}{\partial p^1 \partial p^1} f_1(p^1) + \frac{\partial^2}{\partial p^1 \partial p^1} f_{21}(p^1, p^2) \right)^{-1} \left(\frac{\partial^2}{\partial p^1 \partial p^2} f_{21}(p^1, p^2) \right) \right] * \left[\left(\beta^{-1} \frac{\partial^2}{\partial p^2 \partial p^2} f_2(p^2) + \frac{\partial^2}{\partial p^2 \partial p^2} f_{12}(p^1, p^2) \right)^{-1} \left(\frac{\partial^2}{\partial p^2 \partial p^2} f_{12}(p^1, p^2) \right) \right] \right\| < 1 \tag{5.5}$$

In the region-based method, the iris image is partitioned into connected regions by grouping the neighbouring pixels of similar intensity levels. The adjacent regions are then merged under some criteria involving the homogeneity or sharpness of the region boundaries. Now, if $y_{i,j}$ is the intensity of a pixel at (i,j) of the original image and $x_{i,j}$ is the intensity of a pixel at (i,j) of the segmented image, then, a common approach is to minimize an objective function of the form:

$$E = \sum_{i,j}(y_{i,j} - x_{i,j})^2 + \lambda^2(\sum_{i,j}\sum_{i_s,j_s}(x_{i,j} - x_{i_s,j_s})^2) \tag{5.6}$$

where, i_s and j_s are indices in the neighborhood of pixel $x_{i,j,}$ and λ is a constant. In the above equation, the first term on the right-hand side is a data fidelity term, and the second term on the right-hand side enforces the smoothness. Therefore, the first term tries to minimize the differences between the classification and the pixel intensity. The second term minimizes the difference between the classifications of the neighbouring pixels, essentially to minimize the region boundary. To detect the inner/outer boundary of the iris, the objective functions are described as follows:

For the region-based module (Player 1) [176]:

$$F^1(p^1, p^2) = \min_x \left[\sum_{i,j}\left(y_{i,j} - x_{i,j}\right)^2 + \lambda^2\left(\sum_{i,j}\left(x_{i,j} - x_{i-1,j}\right)^2 + \sum_{i,j}\left(x_{i,j} - x_{i,j-1}\right)^2\right)\right] + \alpha\left[\sum_{i,j\in A_{\vec{p}}}\left(x_{i,j} - u\right)^2 + \sum_{i,j\in \bar{A}_{\vec{p}}}\left(x_{i,j} - v\right)^2\right] \tag{5.7}$$

where, $y_{i,j}$ is the intensity of the original image, $x_{i,j}$ is the intensity of the segmented image given by p^1 as mentioned earlier, u is the intensity inside the contour given by p^2, and v is the intensity outside the contour given by p^2. $A_{\vec{p}}$ corresponds to the points that lie inside the contour, and $\bar{A}_{\vec{p}}$ represents those points that lie outside the

contour. The first term on the right-hand side of (5.7) minimizes the difference between the pixel intensity values and the obtained region, as well as enforces continuity. The second term tries to match the region and the contour. In the region growing approach, we select an initial seed that is a single pixel within the region of interest for the inner boundary detection. At each iteration, the neighbouring pixels are observed and the value of E is measured from (5.6). The pixels, for which the value of E is less than a predefined threshold, are accepted into the region.

The objective function of the Player 2 (i.e., the boundary finding module) is as follows [14]:

$$F^2(p^1, p^2) = \underset{\vec{p}}{argmax} \left[M_{gradient}\left(I_g, \vec{p}\right) + \beta M_{region}(I_r, \vec{p})\right] \tag{5.8}$$

where, $\vec{p}$ denotes the parameterization of the contour given by p^2, I_g is the gradient image, I_r is the region segmented image, and β is a constant. In [14], the Fourier parameterization was used to represent the evolving contour. However, the parametric active contour-based curve evolution may terminate at a certain local minima such as at the specular reflections, the thick radial fibers in the iris or the crypts in the ciliary region, and thus, is not suitable for nonideal iris boundary detection. Therefore, we apply a VLS-based active contour model to represent the contour data during the game-theoretic propagation [68] as described in Chapter 4. The proposed segmentation scheme with the VLS approach uses a larger time step to numerically solve the evolution PDE, and thereby, the curve evolution process speeds up considerably [68]. The applied VLS evolution could be developed using a simple finite difference scheme, and the LS function could be initialized as a more efficient function than the traditional SDF [11]. Also, the contours represented by

the LS may break and merge naturally during evolution, and thus, the topological changes are handled automatically [10, 157-159].

To estimate the exact boundary of the pupil, we deploy the game-theoretic segmentation algorithm mentioned above and use the centre of the pupil obtained through the DLS-based elliptical fitting process as the seed point. This pupil segmentation result is shown in Figs. 5.4 and 5.5. Similarly, for computing the exact estimate of the outer boundary, we again apply the segmentation scheme based on the GT. We select a circular region of radius *r*, which was found in the previous step, and select it just beyond the pupillary boundary so that the game-theoretic localization scheme moves towards the outer boundary from this region. This process is shown in Figs. 5.6 and 5.7.

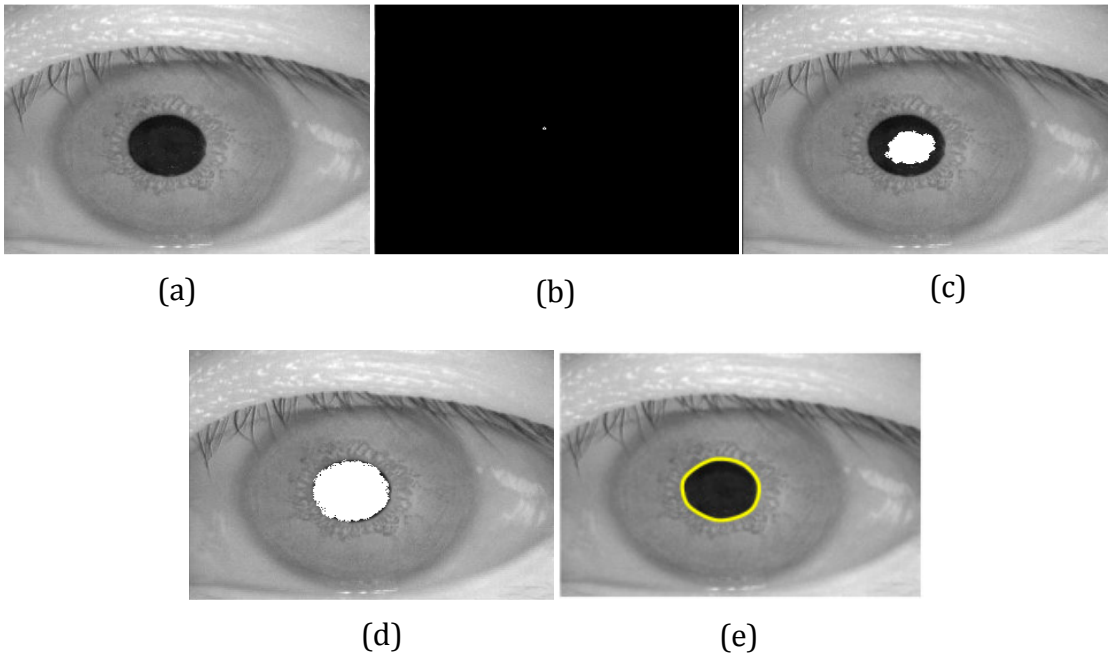

Fig. 5.4 Pupil segmentation using game-theoretic integration approach on CASIA Version 3 Interval dataset: (a) preprocessed image, (b) seed image, (c, d) game-theoretic region growing process and boundary finding method, and (e) final contour of pupil.

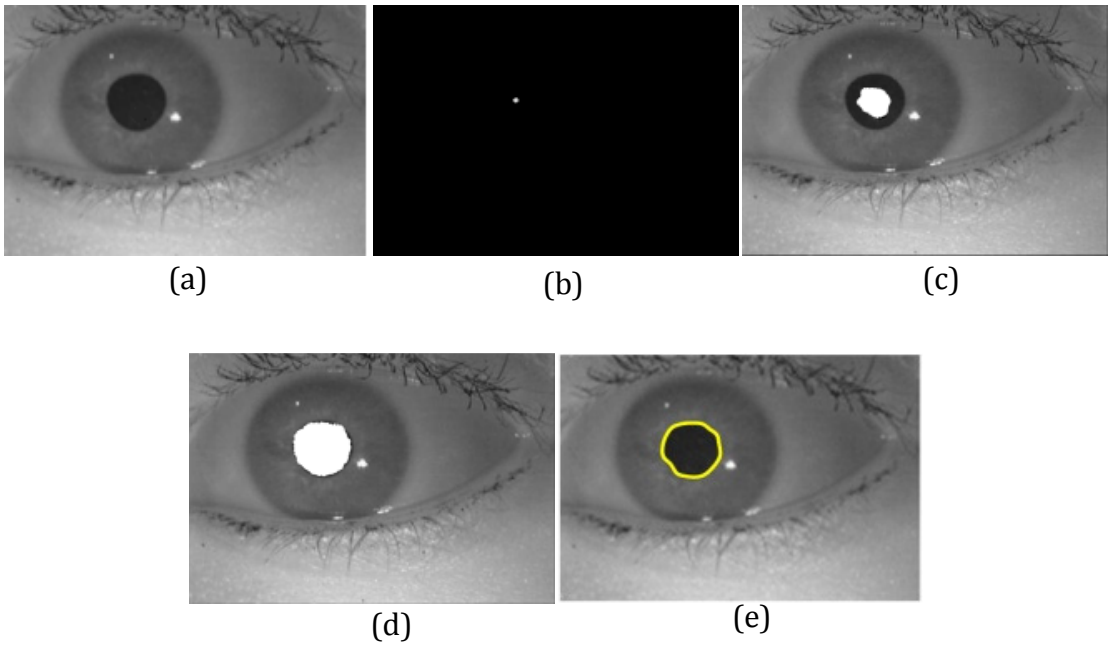

Fig. 5.5 Pupil segmentation using game-theoretic integration approach on WVU Nonideal dataset: (a) preprocessed image, (b) seed image, (c, d) game-theoretic region growing process and boundary finding method, and (e) final contour of pupil.

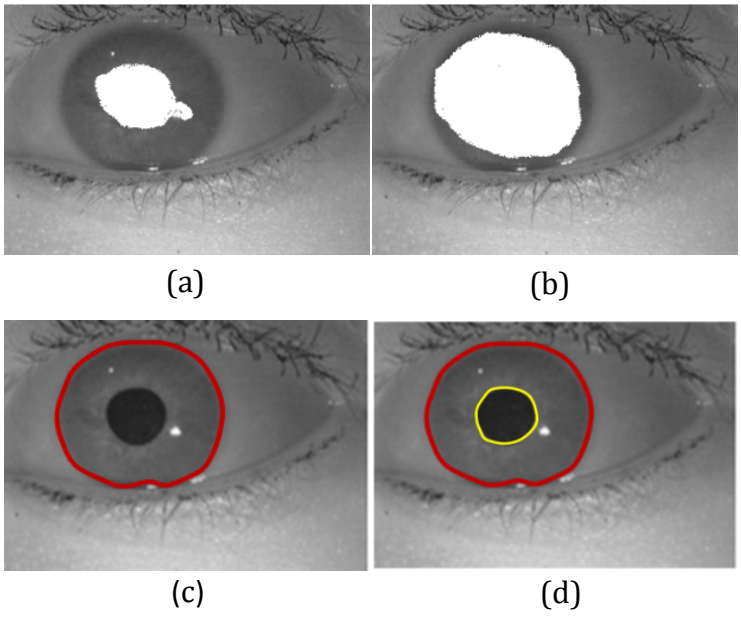

Fig. 5.6 Iris segmentation using game-theoretic integration approach on WVU Nonideal dataset: (a) iris segmentation starts just beyond the previously obtained pupil boundary, (b) game-theoretic region growing process, (c) final contour of the iris, and (d) final contours of iris and pupil.

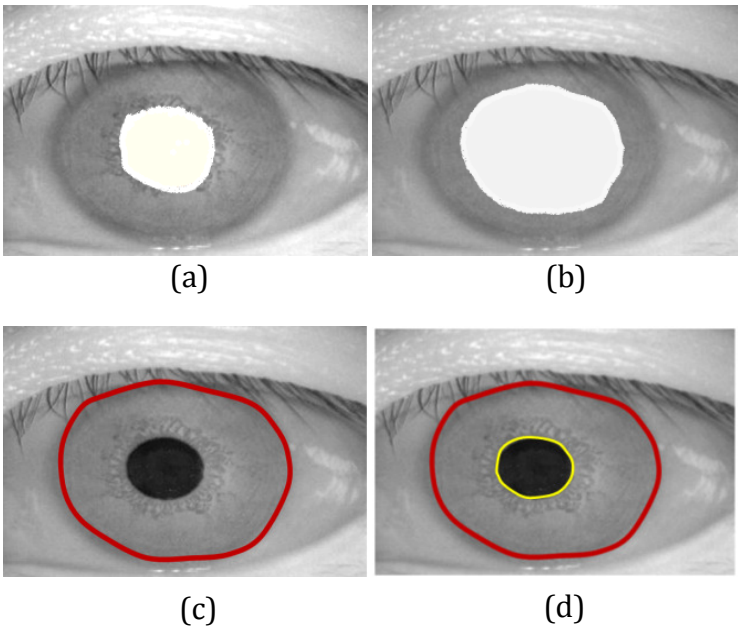

Fig. 5.7 Iris segmentation using game-theoretic integration approach on CASIA Version 3 Interval dataset: (a) iris segmentation starts just beyond the previously obtained pupil boundary, (b) game-theoretic region growing process, (c) final contour of the iris, and (d) final contours of iris and pupil.

5.2.1 Noise detection, Unwrapping and Enhancement

We deploy the eyelash detection technique as used in previous chapter [68, 70]. We use a mask based on the extracted eyelashes and iris contours. This mask is used to detect the iris region without noise. In order to compensate for the elastic deformation in the iris texture, we unwrap the extracted (and localized) iris region into a normalized rectangular block with a fixed size of 64×512, by converting from the Cartesian coordinates to the polar coordinates and using the circle fitting strategy as discussed in chapter 4. Fig. 5.8(a) indicates the estimated iris/pupil boundary, and Fig. 5.8(b) shows the unwrapped image. In order to improve the quality of the iris image, we have applied a two-step image enhancement technique [176]:

Step1: Since the normalized iris image has a relatively low contrast and may have non-uniform intensity values due to the position of the light sources, a local intensity-based histogram equalization technique is applied. This technique enhances the quality of the contrast in the normalized iris image, thereby increasing the subsequent recognition accuracy. In our method, a local cumulative histogram is applied to the image sub-block of size 10× 10, centred at the pixel to be converted.

Step 2: To reduce the effect of noise, we apply a pixel-wise adaptive 2D Wiener filter [174]. The 2D Wiener filter is a low-pass filter that is used to remove the high frequency noise. This filter emphasizes the local statistics that are estimated from a local neighborhood, η of size 3 × 3 for each pixel, and is defined by:

$$WF\ (n_1, n_2) = \ \mu + \frac{(\sigma^2 - v^2)}{\sigma^2} * (I(n_1, n_2) - \mu) \qquad (5.9)$$

where, v^2 denotes the noise variance, μ and σ^2 are the local mean and variance, and I is the gray level intensity in $n_1, n_2 \ \in \ \eta$. If the noise variance is not provided, the filter uses the average of all the local estimated variances. Figs. 5.8(c) and 5.9 also show the effects of enhancement on the normalized iris images.

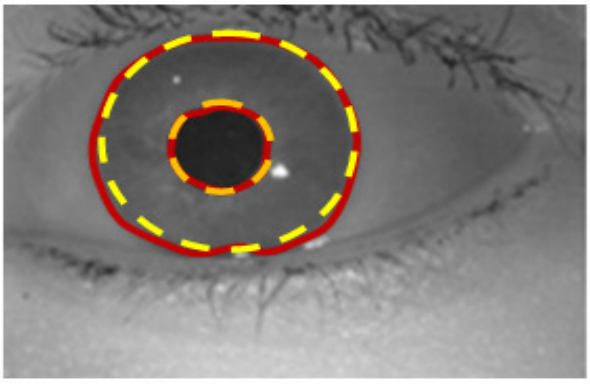

(a)

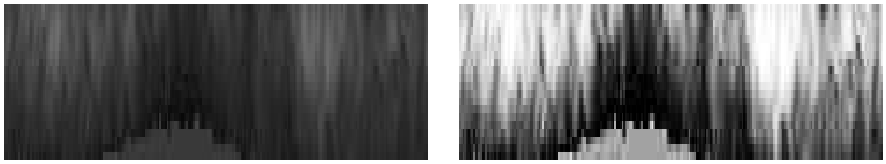

(b) (c)

Fig. 5.8 Unwrapping and Enhancement: (a) estimated iris/pupil boundary using the circle fitting strategy, (b) unwrapped iris image (c) enhanced iris image.

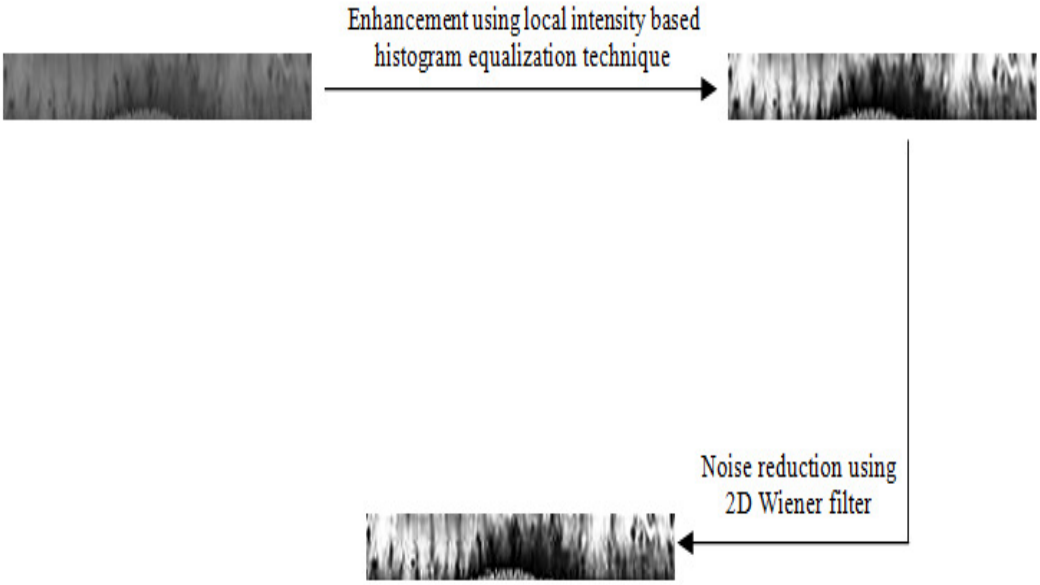

Fig. 5.9 Contrast Enhancement using local cumulative histogram equalization technique and noise reduction with 2D Wiener filter.

5.2.2 Feature Encoding and Matching

In this chapter, the DBWT has been applied to extract the characteristic values from the normalized (and enhanced) image block with a size of 64 ×512 pixels [177]. We use the simple HDD for iris template matching. The HDD is used to measure the dissimilarity between two sets of feature points. If $A = \{a_1, a_2, a_3, \ldots\ldots, a_m\}$ and $B = \{b_1, b_2, b_3, \ldots\ldots, b_n\}$ are two sets of iris features, then the *HDD* between A and B

are given by [69, 176]:

$$H\ (A,B) = max(h(A,B), h(B,A)) \tag{5.10}$$

where, h is the directed Hausdorff defined by $h\ (A,B) = \underset{a_i \in A, b_i \in B}{maxmin} \|a_i - b_i\|$ and $\|\cdot\|$ is the norm of the vector.

5.3 Results and Analysis

In this section, we evaluate the performance of the proposed scheme and report the results of a set of experiments. Our experimentation setup remains the same as that described in Chapter 4. To validate the performance of the proposed algorithms, we carried out the experiments on several datasets, namely, the ICE 2005, the UBIRIS Version 1, WVU Nonideal, the CASIA Version 3 Interval and the Combined non-homogeneous datasets (See Appendix A for the details about the datasets). We will describe the experiments in two stages: first, we will evaluate the performance of our proposed algorithms with respect to the game-theoretic segmentation scheme. Secondly, we will compare the performance of our approach with performances of the other state-of-the-art algorithms to show the effectiveness of the proposed scheme.

5.3.1 Performance Evaluation of the Proposed Scheme

For the iris segmentation, we have applied the game-theoretic integration approach, and the segmentation results are shown in Figs. 5.10 and 5.11. These figures show that our segmentation scheme performs well, despite the fact that the iris and the sclera regions are separated by a blurred boundary especially, in the UBIRIS and WVU datasets. An extensive set of experiments was conducted on all the datasets,

and the coupling coefficients, α and β were set to 0.27 when the game-theoretic integration module was used. To obtain the contour data of the inner/outer boundary during game-theoretic evolution, the selected parameter values using the VLS algorithm were set to $\mu = 0.001, v = 2.0, \lambda = 5.0$ and time step $\tau = 3.0$. Comparisons were first made between the outputs generated using the game-theoretic fusion and the corresponding outputs obtained without using the information integration. Equations (5.7) and (5.8) jointly represent the outputs of the game-theoretic fusion, where (5.7) provides the region output and (5.8) gives the boundary output under the integrated framework. For the stand-alone modules, the coupling coefficients, α and β were set to 0. It is clear that the final contour output as shown in Fig. 5.12(d), with the information fusion, is much better than the outputs of the stand-alone modules as shown in Fig. 5.12(b, c), where no information fusion is deployed.

Our proposed segmentation scheme is also robust in noisy situations. A sudden variation in the intensity level may occur in the iris image due to a noisy pixel and thus, the moving front may stop. However, in our case, the other boundary points continue to move and, hence, the curve evolution process based on game-theoretic fusion keeps propagating towards the inner and the outer boundaries. Fig. 5.13(b, c) shows the outputs of applying our proposed game-theoretic scheme to an iris image with Gaussian white noise. Fig. 5.13 (d, e, f) shows the results of applying our approach to an iris image with the Poisson noise, the salt and pepper noise, and the speckle noise, respectively. One major advantage of our algorithm as compared to the methods proposed in [85, 86] is that our algorithm uses the topology preserving

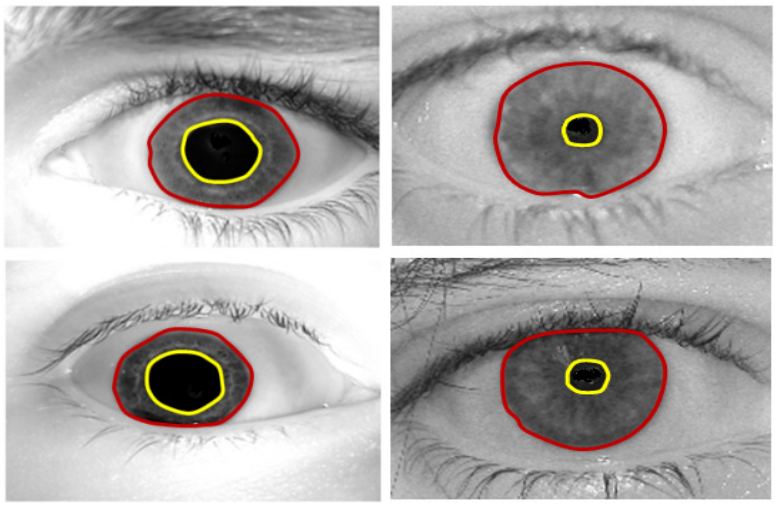

(a) (b)

Fig. 5.10 Segmentation results on datasets: (a) ICE 2005, and (b) UBIRIS Version 1.

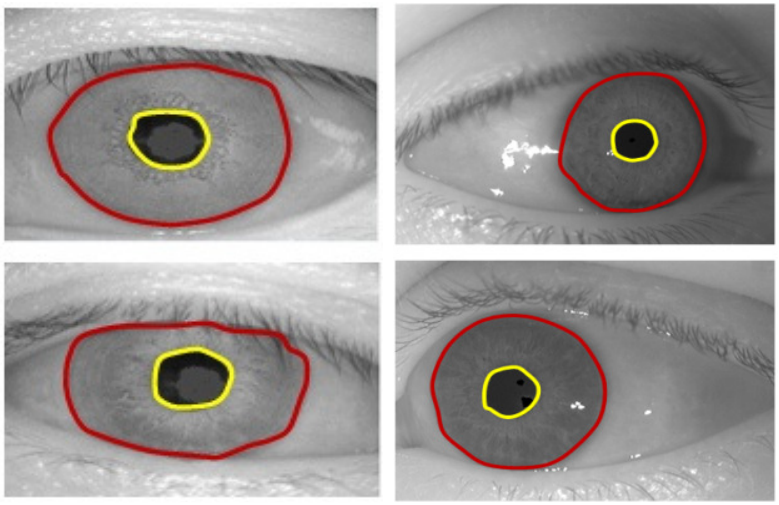

(a) (b)

Fig. 5.11 Segmentation results on datasets: (a) CASIA Version 3 Interval, and (b) WVU Nonideal.

technique instead of the standard GACs. Therefore, even in the noisy situations, our proposed approach can localize the inner and outer boundaries accurately. In order to exhibit the effectiveness of our segmentation approach, we compared our GT-

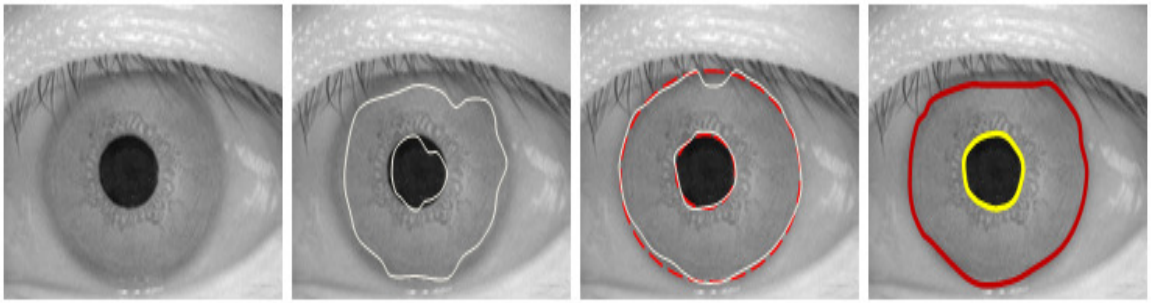

(a) (b) (c) (d)

Fig. 5.12 Effectiveness of our proposed segmentation scheme based on game-theoretic fusion on a sample iris image from CASIA Version 3 dataset: (a) original image; (b) output of the region-based approach without game-theoretic approach (only final contours are shown); (c) output of the boundary-finding approach without game-theoretic approach. The white contour denotes the final output for inner and outer boundaries; and (d) output with proposed game-theoretic integration.

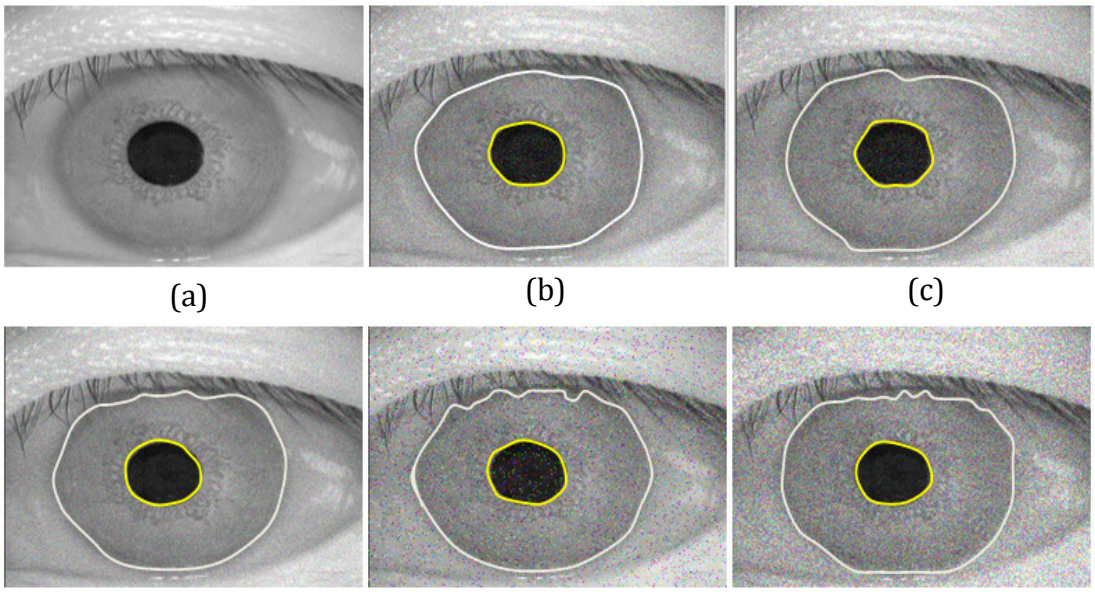

(a) (b) (c)

(d) (e) (f)

Fig. 5.13 Performance of our game-theoretic algorithm in noisy situations: (a) original image after filling the white spots from CASIA Version 3 Interval dataset, (b) image (a) with Gaussian white noise (mean=0 and variance = 0.005); (c) image (a) with Gaussian white noise (mean=0 and variance = 0.007); (d) iris image (a) with Poisson noise; (e) iris image (a) with salt and pepper noise (noise density = 0.06); and (f) iris image (a) with speckle noise which includes the multiplicative noise (mean=0 and variance = 0.07).

based approach with: the IDO proposed by Daugman [27-29]; the CHT-based approach applied in Chapter 3 [46, 136]; and the active contour-based localization approaches proposed by Vatsa et al. [67] and Shah and Ross [85, 86] for all the datasets. For comparison purposes, we only implemented the segmentation approaches proposed in [27-29, 67, 85, 86]. The ROC curves in Fig. 5.14 show that the matching performance improves when the game theoretic integration is used for segmentation. The proposed segmentation scheme shows a better performance than the active contour-based methods reported by Vatsa et al. [67] and Shah and Ross [85, 86], and the reason is that our proposed scheme uses the region-based information as well as the gradient data with the game-theoretic fusion method. Moreover, the eyelash separation and the white spot detection techniques are applied to an input image to restrain the interference from reflections, occurring inside the pupil. The DLS fitting approach provides a reasonable approximation of the inner boundary. The GAR at a fixed FAR of 0.001% is: (a) 98.21% in ICE; (b) 97.17% in CASIA; (c) 97.24% in UBIRIS; and (d) 96.40% in WVU datasets. In order to show the robustness of the game-theoretic approach, we also compare the proposed segmentation algorithm with the RAC model [70], VLS method [69] and LS-based [68] methods, as proposed in Chapter 4. Fig. 5.15 shows that our algorithm achieves the highest GAR of 97.20% on the combined dataset at the fixed FAR of 0.001%. Furthermore, we also provide the EERs of each scheme in Fig. 5.15, and our proposed segmentation scheme effectively increases the performance with the EER of 0.86%. The reason seems to be the inclusion of both the region-based and boundary-based information for segmentation whereas the schemes reported in

[27-29, 85, 86, 68] used only the gradient information, and the segmentation algorithm depicted in [67, 70, 147, 170, 171] used only the region data. Therefore, the localization algorithms of [27-29, 68, 69, 75, 85, 86] may suffer from noise sensitivity and blurred iris/sclera boundary, but on the contrary, the approaches in [67, 70, 147, 170, 171] seem to experience poor localization and over-segmentation.

The proposed GT-based segmentation algorithm failed to perform on some images of the UBIRIS dataset due to a huge occlusion as shown in Fig. 4.20. For experimental purposes, we also applied the DLS-based elliptical fitting approach to detect the outer boundary as well as the inner boundary. Fig. 5.16 exhibits that the DLS elliptical fitting strategy failed to detect the outer boundary accurately; however, the game-theoretic localization process isolated the iris and pupil boundaries accurately in those corresponding cases. Therefore, our experiments show that the elliptical fitting process alone cannot provide an optimal estimation of the iris boundary. In Fig. 5.17, we also found that segmentation errors occurred on several iris images due to a poor quality of the images, huge occlusions and the deviated gazes. We conducted the above experiments on a 3.00 GHz Pentium IV PC with 2.5 GB RAM in a MATLAB 7.2 environment. The average time consumption of matching an iris image was 11593 ms as exhibited in Table 5.2.

5.3.2 Comparison with the Other State-of-the-Art Algorithms

We compared the performance of the proposed algorithm with three well-known iris recognition algorithms proposed by Daugman [27-29] and Ma et al. [22, 31] on

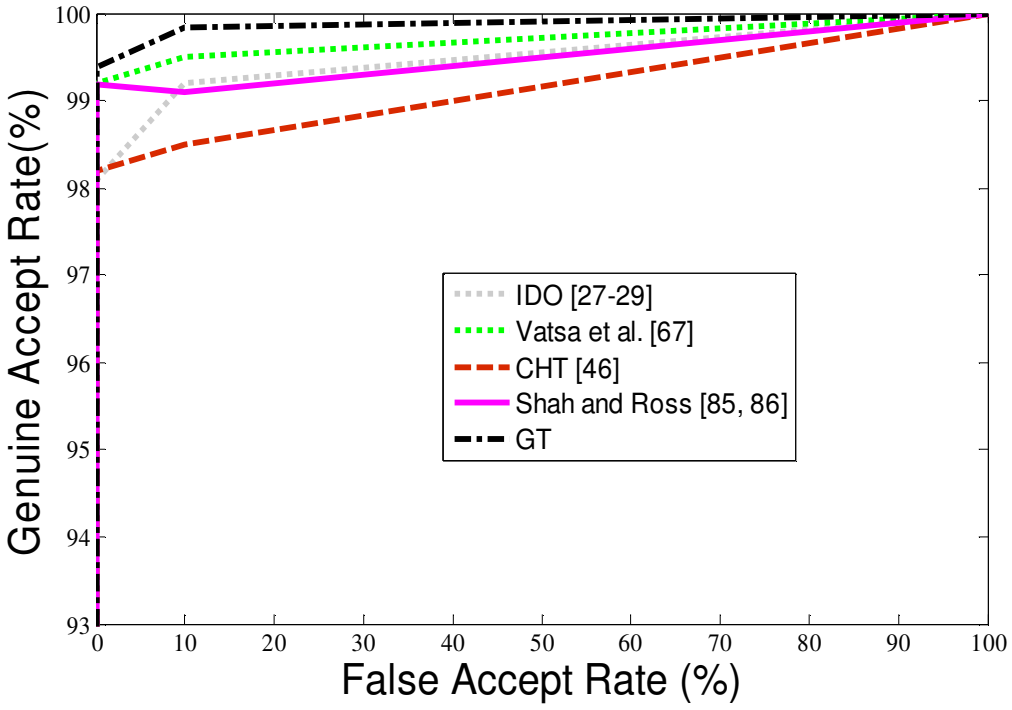
Genuine Accept Rate(%)
False Accept Rate (%)
IDO [27-29]
Vatsa et al. [67]
CHT [46]
Shah and Ross [85, 86]
GT

(a)

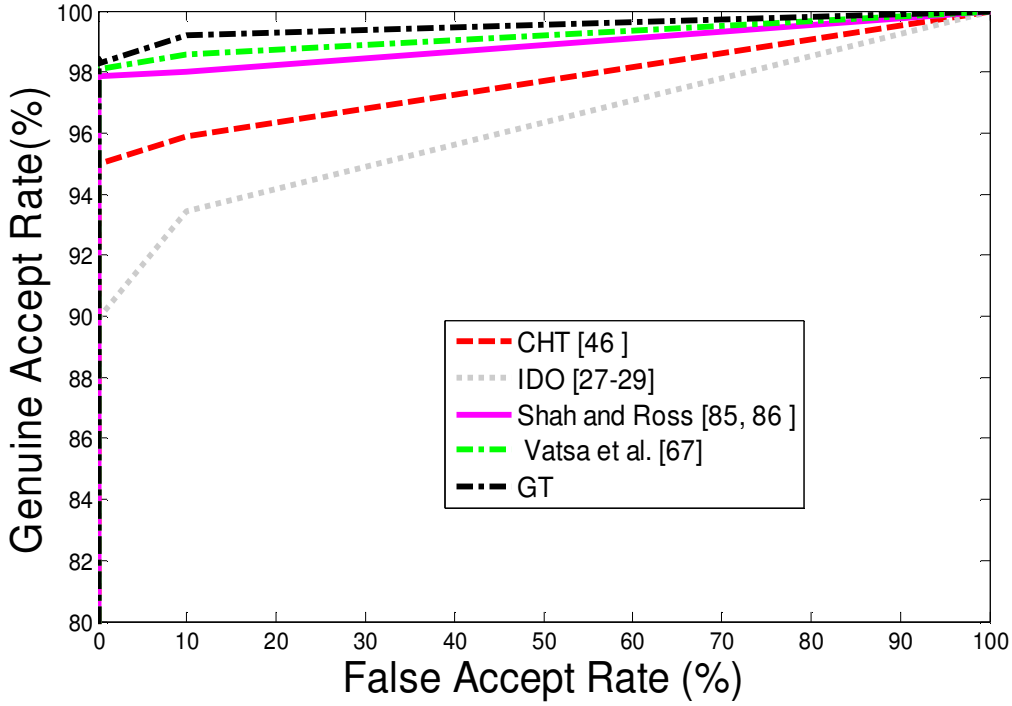
Genuine Accept Rate(%)
False Accept Rate (%)
CHT [46]
IDO [27-29]
Shah and Ross [85, 86]
Vatsa et al. [67]
GT

(b)

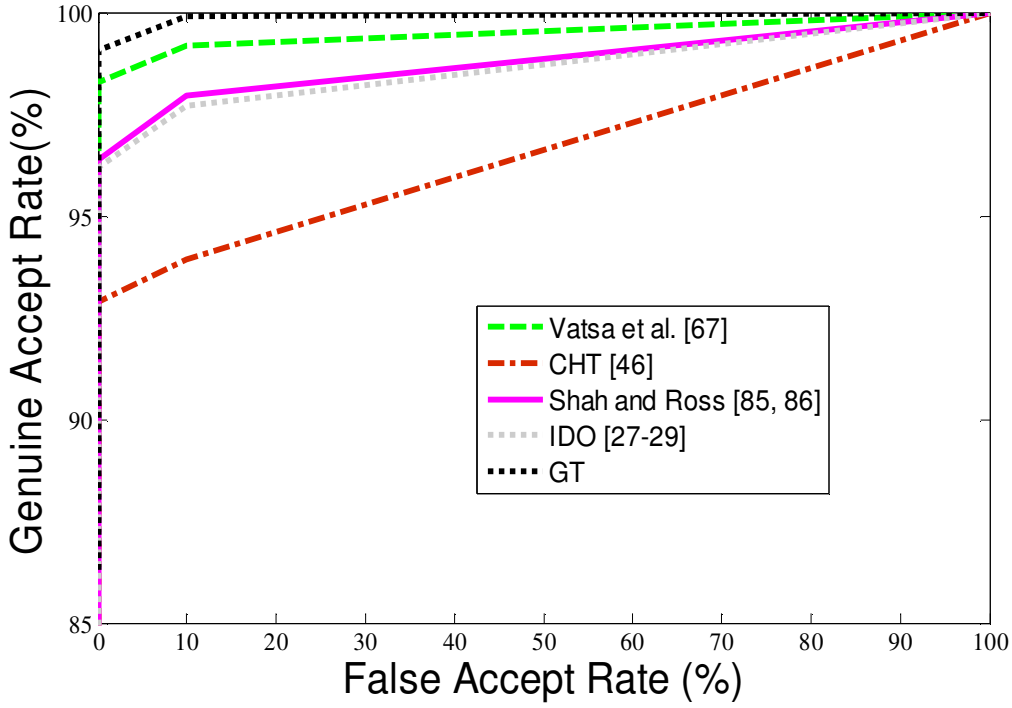

(c)

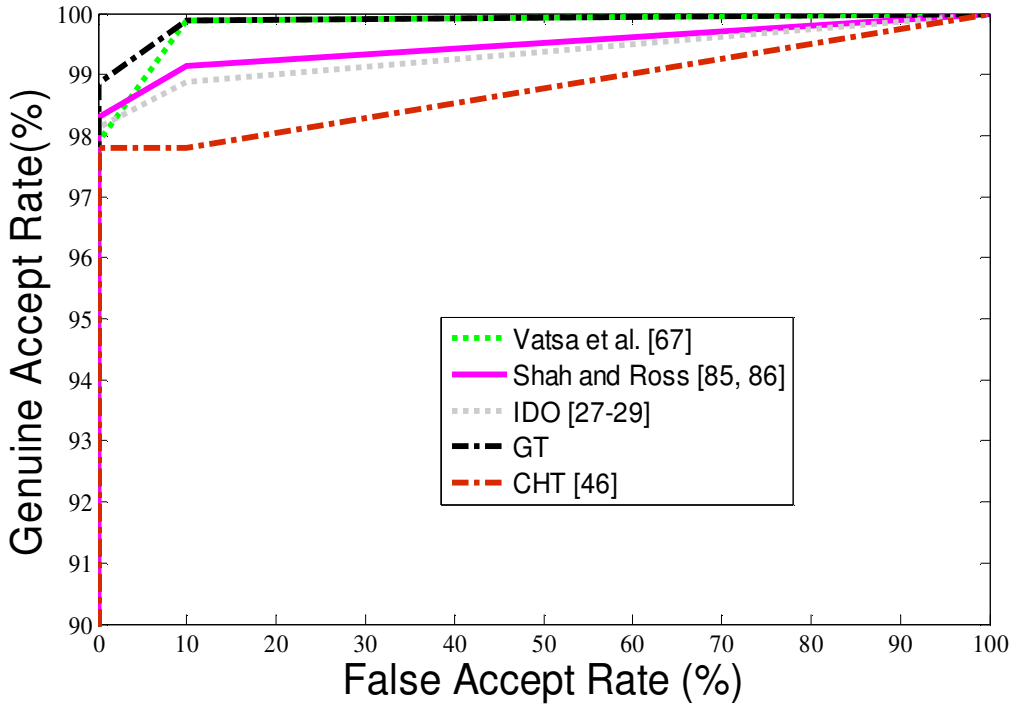

(d)

Fig. 5.14 ROC curves show the comparison of our algorithm with existing segmentation techniques on: (a) ICE 2005, (b) WVU Nonideal, (c) CASIA Version 3 Interval, and (d) UBIRIS Version 1 datasets.

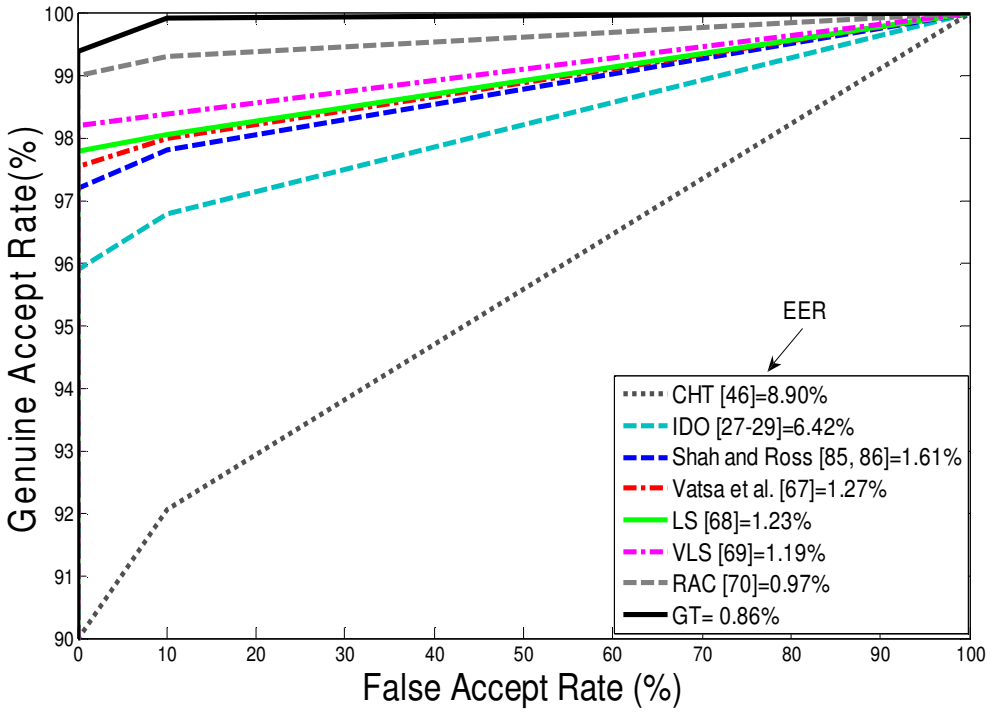

Fig. 5.15 ROC curves show the comparison of our algorithm with the existing segmentation techniques on the Combined dataset.

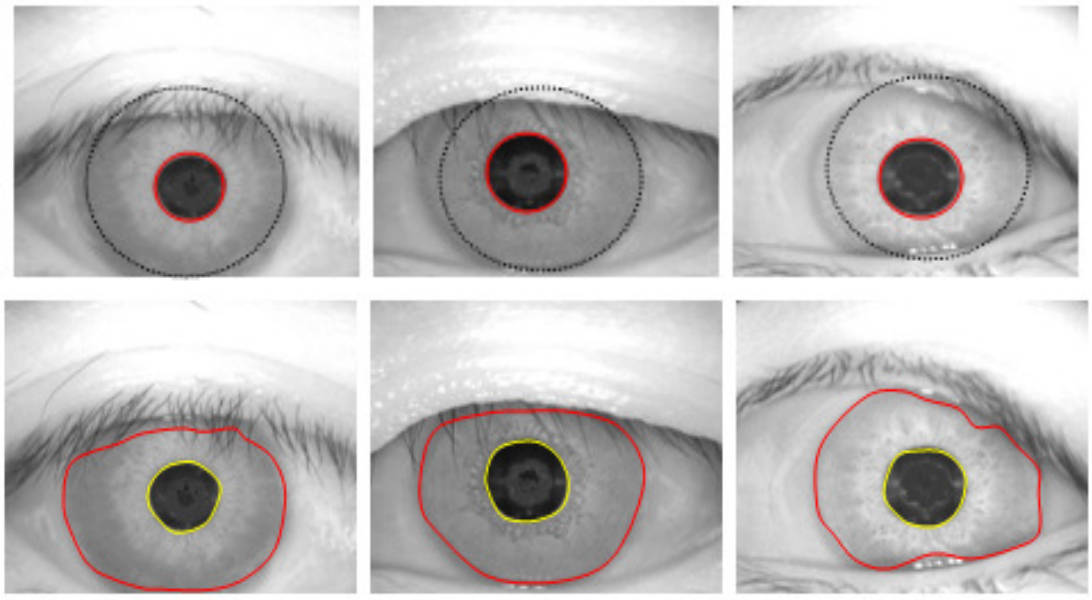

Fig. 5.16 Samples of iris images from CASIA Version 3 Interval dataset, on which the DLS elliptical fitting approach fails to detect the outer boundary accurately (Upper row). However, our proposed game-theoretic segmentation approach successfully isolates the inner and boundaries for the corresponding images (Lower row).

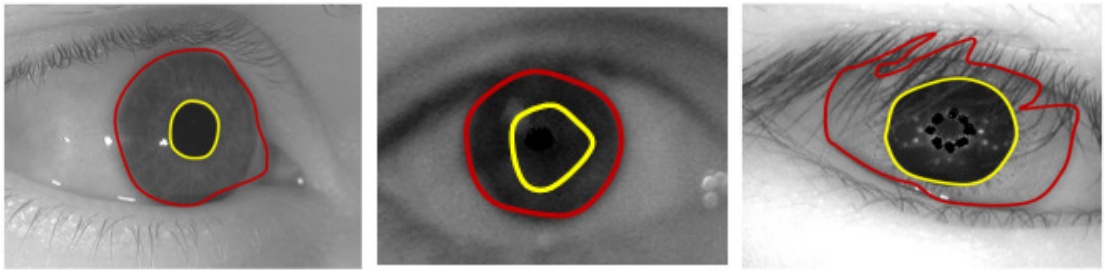

(a) (b) (c)

Fig. 5.17 Game-theoretic segmentation errors found on several images in: (a) WVU nonideal; (b) UBIRIS Version 1; and (c) CASIA Version 3 Interval datasets.

Table 5.2: Average time consumption of different parts of the proposed iris recognition system.

Algorithm	Time (ms)
Iris Segmentation	11400
Unwrapping	83
Feature Extraction	72
Matching	38
Average Execution Time	11593

the combined dataset. Fig. 5.18 exhibits the ROC curves of the proposed algorithms with the curve evolution approach based on game-theoretic fusion for the heterogeneous combined dataset. The ROC curves of the approaches demonstrated in [22, 27-29, 31] are also plotted for comparison, and this figure shows that the proposed algorithm achieves a higher GAR with a very low EER of 0.86% for the combined dataset. It means that the proposed algorithm achieves higher discriminating capabilities than the approaches proposed in [22, 27-29, 31]. Moreover, the approaches proposed in [22, 27-29, 31] were not adjusted specifically for the noncooperative situations. The proposed segmentation algorithm that is based on the noncooperative game-theoretic fusion obtains a higher GAR of 97.20% at the fixed FAR of 0.001% on the combined dataset, which contains the iris images with the irregularities due to motion blur, off angle gaze, diffusion, and other real-

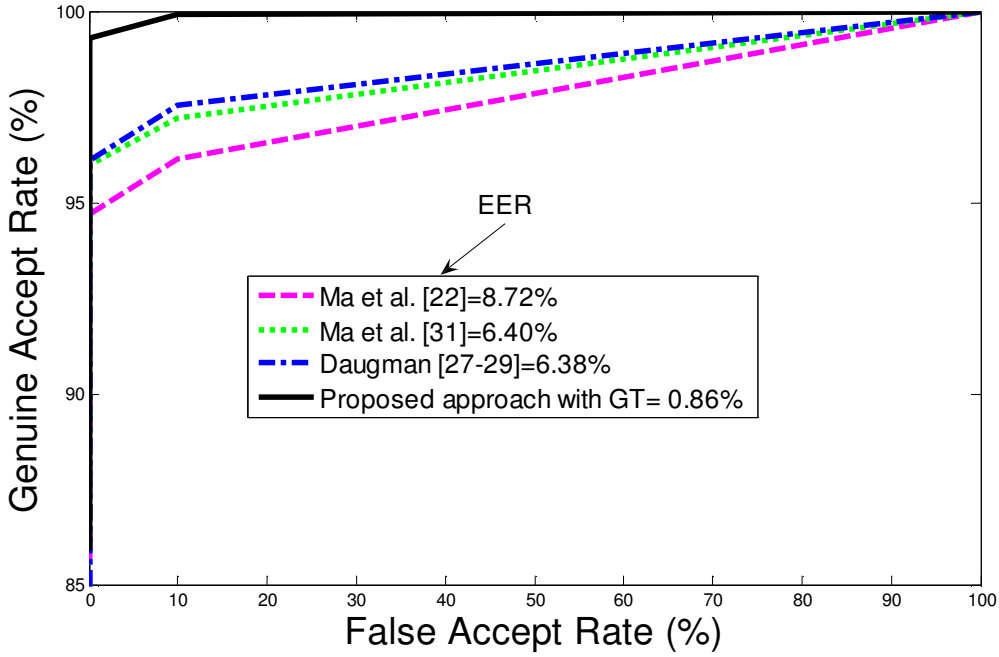

Fig. 5.18 Comparison of our method with existing iris recognition schemes on the combined dataset.

world problems. Therefore, the ROC curves in Fig. 5.18 reveal the effectiveness of the proposed scheme in a nonideal situation.

The major difficulty, which is common to any dataset, is the segmentation error. The localization approach described in Section 5.2 works well for most of the cases, even with the iris images of deviated gazes. The DLS-based elliptical fitting provides an initial estimate of the inner boundary, and the game-theoretic fusion approach localizes the iris and pupil regions accurately. In Table 5.3 (a, b), the proposed scheme exhibits the highest CRR for ICE, CASIA, WVU and UBIRIS datasets. For the combined dataset, we found a CRR of 97.30% revealing a top class performance with respect to the nonideal datasets under consideration. The EER of the proposed approach on the combined dataset was 0.86% and that was encouraging.

Table 5.3: Comparison of CRR and EER.

(a) Comparison of CRR.

Algorithm	Correct Recognition Rate (CRR) (%)				
	ICE	CASIA	UBIRIS	WVU	Combined
Daugman [27-29]	98.13	95.70	97.28	83.14	93.43
Ma *et al.* [31]	95.79	95.54	95.45	78.33	92.56
Ma *et al.* [22]	95.64	94.90	95.78	77.24	91.23
Proposed scheme using GT	**98.29**	**97.25**	**97.57**	**96.50**	**97.30**

(b) Comparison of EER

Algorithm	Equal Error Rate (EER) (%)				
	ICE	CASIA	UBIRIS	WVU	Combined
Daugman [27-29]	0.49	1.80	0.96	8.45	6.38
Ma *et al.* [31]	1.72	2.07	1.21	10.50	6.40
Ma *et al.* [22]	1.80	2.62	1.13	11.43	8.72
Proposed scheme using GT	**0.38**	**0.74**	**0.50**	**1.70**	**0.86**

5.4 Conclusion

The accurate segmentation of the iris plays an important role in iris recognition. The proposed iris segmentation algorithm has achieved four performance goals. First, the game-theoretic integration algorithm brings together the region-based and boundary-based methods and operates different probability spaces into a common information-sharing framework. Second, the accurate localization of the iris regions from degraded eye images has been achieved. Third, the proposed localization scheme based on GT avoids the over-segmentation and performs well for the blurred images of iris/sclera boundary. Fourth, the image enhancement algorithm increases the quality of the iris image and reduces the effect of noise. We validated

the proposed iris recognition scheme on the ICE 2005, the CASIA Version 3, the UBIRIS Version 1, WVU Nonideal datasets and also on the nonhomogeneous combined dataset, and the proposed scheme showed encouraging performances on all the underlying datasets.

Chapter 6

Improving Iris Recognition Performance Using Shape Guided Approach and Game Theory

---

In this chapter, we present algorithms for iris segmentation and feature ranking in order to improve the accuracy of iris recognition scheme. Section 6.1 discusses the motivation behind this research effort. In Section 6.2, we present the proposed iris segmentation algorithm based on shape guided model. In this section, we also discuss an improved unwrapping scheme that can deal with the shape irregularities contained in the localized iris regions. We describe the iris feature ranking scheme based on GT in Section 6.3. The verification and identification performance of the proposed scheme is demonstrated in Section 6.4, and finally, Section 6.5 summarizes the important findings of this investigation.

6.1 Introduction

The accuracy of iris recognition heavily depends on the segmentation routine, which should elicit the effective iris region from an iris image. A robust localization

algorithm, on the one hand, should deal with the different noise factors, i.e., specular reflections, obstructions due to eyelashes, eyelids, glasses, etc., and on the other hand, the algorithm should be defined by a reduced number of parameters [80]. In the Chapter 4, we have discussed different iris segmentation algorithms that can deal with the iris images in unconstrained situations. From the previous discussions, we found that most of the current iris segmentation methods use the gradient information or the region data to localize the iris region. The LS and VLS-based methods proposed in Chapter 4 mainly rely on the image gradients and thus, are highly sensitive to the presence of noise and poor image contrast, which can lead to inaccurate segmentation results. To overcome this drawback, we have applied the RAC model that can deal with the nonideal iris images with intensity inhomogeneity [70, 171]. The main advantage of this scheme is that it depends directly on the gray-level image and thus, it is less affected by the different noise factors. However, such a region-based scheme suffers from poor localization and over-segmentation problems [9, 160, 178]. Therefore, the region-based schemes perform better against noise and are less affected by the weak iris/sclera boundary, and the gradient-based approaches, on the contrary, show better localization performances and work well against the shape irregularities. Addressing the above problems, in Chapter 5, we have proposed a GT-based iris localization algorithm, which integrates both segmentation methods and incorporates the complementary strengths of these individual schemes [36]. However, this integrated scheme is not able to handle the eyelid occlusion problems properly and may fail to localize the blurred outer boundary in the presence of severe noise. Also, in the images where the eyes are not

properly opened, the highly occluded regions cannot be extracted using the GT-based method proposed in Chapter 5 [175, 176], and hence, the segmentation performance deteriorates. Therefore, if we integrate the shape prior information of the iris region to be segmented into the gradient and region-based methods, then the occlusion problem can be mitigated. In this chapter, we propose to apply a variational approach to segment the iris region belonging to a given shape space using the active contour method, a geometric shape prior and the Mumford-Shah functional [16, 179]. Shape Guided Approaches (SGAs) have been extensively used in the field of medical image analysis to segment various images [9, 16, 180]. They have also been used in machine vision [85]. In this research effort, their significance in the context of nonideal iris segmentation is demonstrated.

In the field of iris biometrics recognition, the real-world iris data obtained from experiments are often highly dimensional with SSS, which results in a number of computational and representational problems [17, 54, 68, 70, 171, 181]. In Chapters 3 and 4, we have applied GA-based feature selection criteria to rank and select the best iris texture features from a higher dimensional feature sequence. The feature selection scheme using GA has demonstrated an improved performance, however, this approach tends to converge early and involves a huge computational cost. To overcome this problem, we propose a feature ranking scheme in the context of GT [17]. An iterative algorithm for feature ranking, called the Contribution-Selection Algorithm (CSA) [17], is modified and used to select the optimal feature subset. This algorithm depends on the Multi-Perturbation Shapley Analysis (MSA), a framework that is based on the cooperative game theory, to estimate the usefulness of features

and rank them accordingly. The DBWT is used to elicit the textural features, and a simple HDD is used for iris template matching. Fig. 6.1 shows the block diagram of the proposed iris recognition system. In this chapter, we focus mainly on improving the performance of the iris recognition scheme by applying more accurate iris segmentation and feature ranking algorithms.

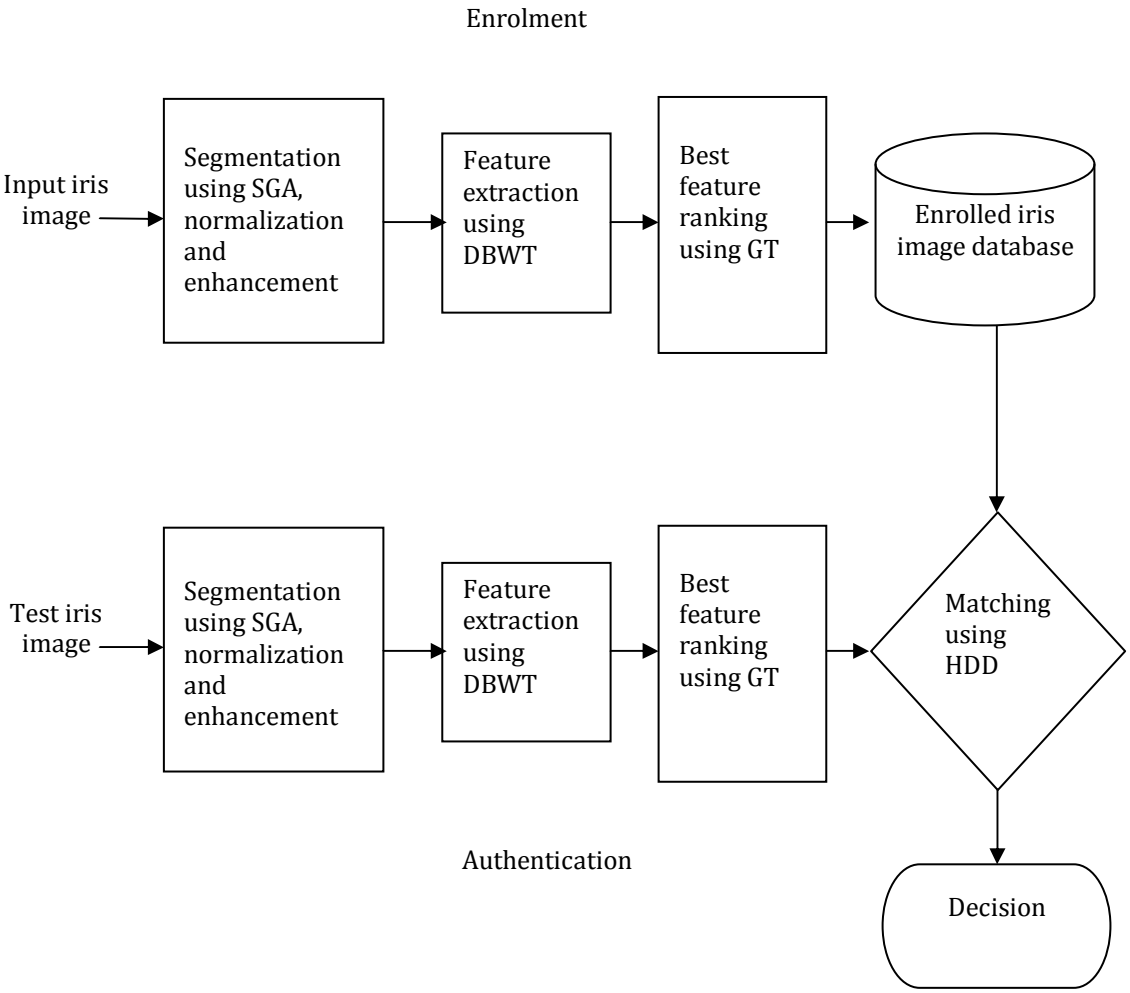

Fig. 6.1 Block diagram of the proposed iris recognition system.

Table 6.1: Comparison of the state-of-the-art nonideal iris recognition algorithms.

Iris recognition approaches	Iris segmentation	Nature of features	Matching process	Quality evaluation
Daugman [75]	Active contours and generalized coordinates, excluding eyelashes using statistical inference	Iris Code	HD	Gaze deviation has been estimated, low time complexity
Miyazawa et al. [3]	Deformable iris model with 10 parameters	2D FPC	Band Limited Phase Only Correlation (BLPOC) function	Faster feature extraction process, lower EER
Vatsa et al. [67]	Nonideal iris segmentation using modified Mumford-Shah functional	1D log-Gabor filters to extract the textural features, and Euler number for extraction of the topological features	Iris indexing algorithm	Reasonable identification rate on nonideal iris datasets, 2ν-SVM-based fusion strategy to combine match scores obtained by matching textural and topological features
Proenca and Alexandre [164]	Normalized iris is divided into six regions	2D Gabor filters	Iris classification using a fusion rule	Experiments show a decrease of the FRR in the recognition of noisy iris images
Belcher and Du [147]	--	Region-based SIFT	Euclidean distance	The proposed scheme does not require polar transformation, or affine transformation, reasonable segmentation performance on nonideal iris datasets
Schuckers et al. [74]	IDO and angular deformation model	ICA and Bi-orthogonal wavelets	HD	Improved recognition performance on nonideal datasets
Abhyankar and Schuckers [182]	Non-linear Active Shape Model (ASM)	Bi-orthogonal wavelets	HD	Reasonable segmentation performance on nonideal iris images
He et al. [166]	Pulling and pushing elastic approach	Regional ordinal measure	Advanced correlation filter	Improved performance with respect to speed and accuracy on three nonideal iris datasets

Iris recognition approaches	Iris segmentation	Nature of features	Matching process	Quality evaluation
Boddeti and Kumar [143]	Active contour method	Gabor filters	Normalized HD and correlation filter	Experimental results show that wavefront coding can increase the depth of field of an iris recognition system by a factor of four
Krichen et al. [126]	Hough transform	Global and local Gabor phase correlation schemes	Normalized cross-correlation	Effectively deals with illumination variations
Proposed approaches using LS method, VLS method, RAC model	LS, VLS and RAC methods	DBWT	AASVMs	Good recognition rate, effectively deals with degraded iris images, extra cost for feature selection
Proposed approach using GT	Game-theoretic fusion strategy that combines the complementary strengths of region-based and boundary-based methods	DBWT	HDD	Higher segmentation performance on nonideal iris datasets
Proposed approach using SGA	variational model to localize the iris region belonging to a given shape space using active contour method, a geometric shape prior and the Mumford–Shah functional	DBWT	HDD	Relatively higher recognition rate, lower EER with respect to the underlying nonideal datasets, extra cost for feature ranking

6.2 Iris Segmentation using Shape Guided Approach (SGA)

In this chapter, we propose a three stage iris segmentation scheme, in which we first detect the specular reflections, and in the second stage, we apply the elliptical fitting process to detect the pupil boundary. In the third stage, we propose to apply the SGA to segment the outer boundary based on a given shape space using the active

contour method, the geometric shape prior information and the Mumford-Shah functional [16, 178, 180]. In [182], Abhyankar and Schuckers applied a similar approach based on the Active Shape Models (ASMs) [183] to learn non-linear shape distributions for the isolation of iris information using a set of training iris images. This shape model is based on the PCA that captures the main variations of a training set while removing the irrelevant information. In [182], authors used the ASM on the parametric contours to localize the iris regions. In this research effort, we apply the PCA on the SDFs of the active contours, which are inherent and parameter-free representations [178, 183]. The application of PCA on the SDFs shows a higher tolerance than the parametric curves due to the slight misalignment occurring during the time of alignment of the training images. Also, the inherent shape representation shows an improved curve registration process with respect to robustness, correctness, and speed. In the following paragraphs, we discuss the proposed segmentation scheme.

In the first stage, we remove the specular reflection spots that are found inside the pupillary region (see Figs. 6.2(a), 6.3(a) and 6.4(a)), as discussed in the chapter 5. In the second stage, we deploy a DLS-based elliptical fitting to estimate the pupil boundary [68-70, 184]. Therefore, the inner boundary can be detected as an ellipse on the iris image for which there will be a sudden change in luminance summed around its circumference. This method, thus, provides a reasonable estimation of the pupil boundary. Figs. 6.2(f), 6.3(f) and 6.4 (f) show the detected pupils. In the third stage, we apply the following energy functional to segment the outer boundary, using a geometric shape prior with local and global information [16]:

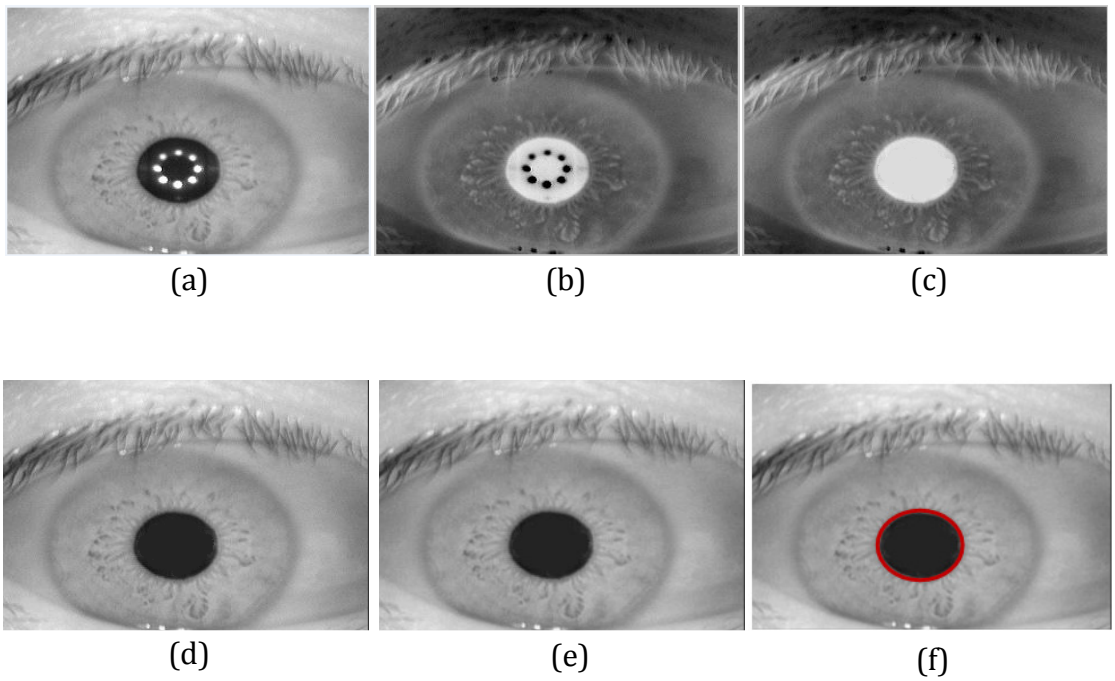

Fig. 6.2 Image preprocessing on CASIA Version 3 Interval dataset: (a) original image; (b) complement of the image (a); (c) filling the holes; (d) complement of image (c); (e) image after Gaussian smoothing; and (f) pupil segmentation.

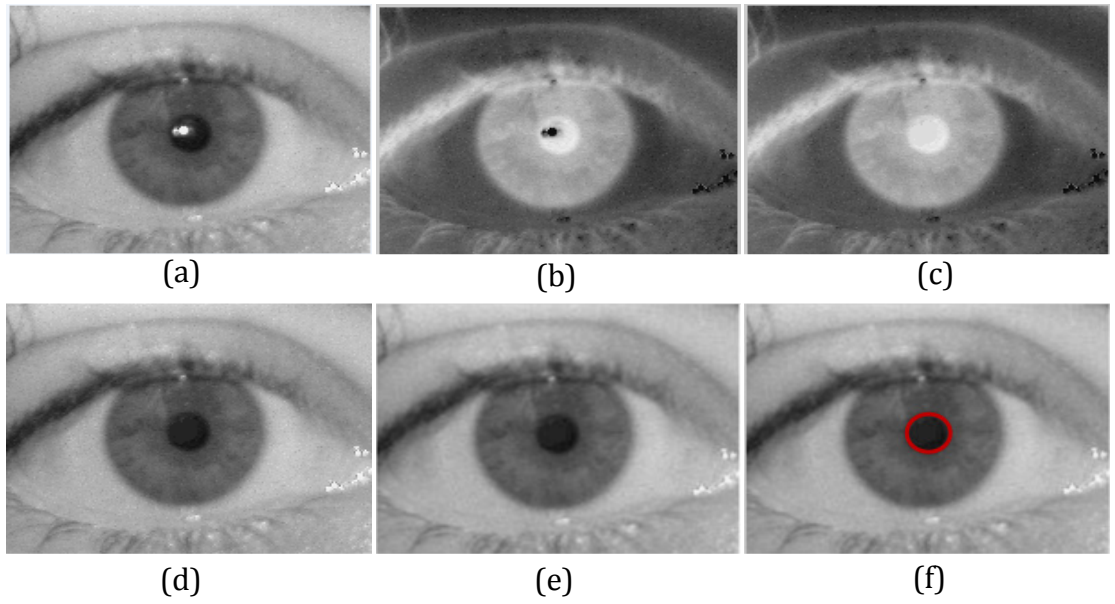

Fig. 6.3 Image preprocessing on UBIRIS Version 1 dataset: (a) original image; (b) complement of the image (a); (c) filling the holes; (d) complement of image (c); (e) image after Gaussian smoothing; and (f) pupil segmentation.

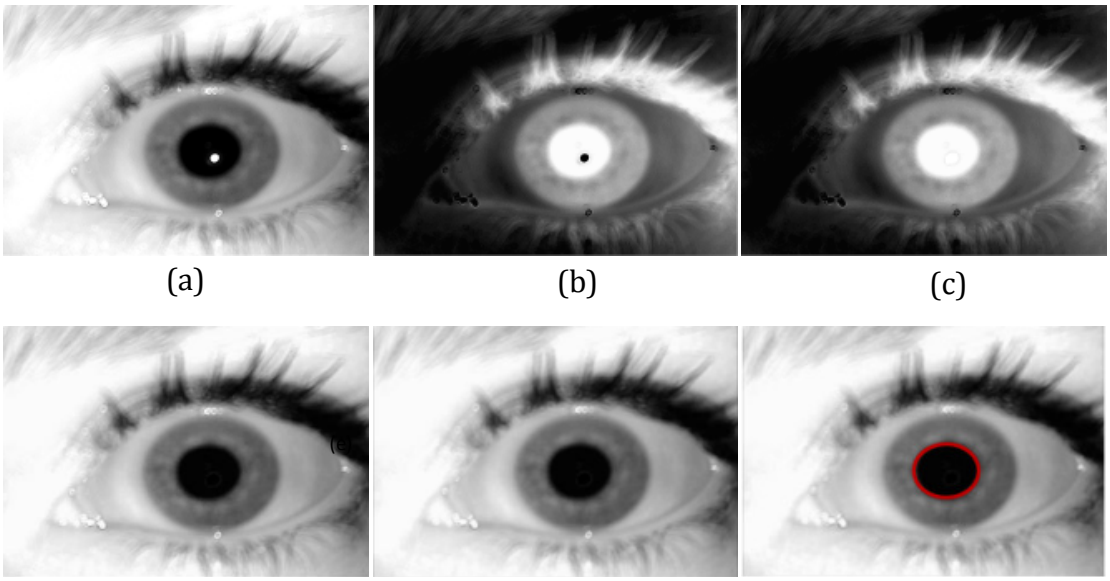

Fig. 6.4 Image preprocessing on ICE 2005 dataset: (a) original image; (b) complement of the image (a); (c) filling the holes; (d) complement of image (c); (e) image after Gaussian smoothing; and (f) pupil segmentation.

$$E = \lambda_1 E_s\left(C, \boldsymbol{y_{pca}}, \boldsymbol{y_{GT}}\right) + \lambda_2 E_b(C) + \lambda_3 E_r(\boldsymbol{y_{pca}}, \boldsymbol{y_{GT}}, c_{in}, c_{out}) \tag{6.1}$$

with

$$E_s = \oint_0^1 \varphi^2\left(\boldsymbol{y_{pca}}, e_{\boldsymbol{y_{GT}}}\left(C(z)\right)\right)|C'(z)|dz, \tag{6.2}$$

$$E_b = \oint_0^1 g(|\nabla I(C(z))|)|C'(z)|dz, \tag{6.3}$$

$$E_r = \int_{\Omega_{\text{in}}(\boldsymbol{y_{pca}}, \boldsymbol{y_{GT}})}(|I - c_{in}|^2 + \beta|\nabla c_{in}|^2)d\Omega \; +$$

$$\int_{\Omega_{\text{out}}(\boldsymbol{y_{pca}}, \boldsymbol{y_{GT}})}(|I - c_{out}|^2 + \beta|\nabla c_{out}|^2)d\Omega \tag{6.4}$$

where, E_s, $E_b$and E_r are the shape, boundary and region terms, respectively, C represents an active contour, φ denotes a shape function of the iris region provided by the PCA, $\boldsymbol{y_{pca}}$ is the vector of PCA eigencoefficients, $e_{\boldsymbol{y_{GT}}}$ is an element of a group

of geometric transformations parameterized by $\boldsymbol{y_{GT}}$ (parameter vector), g is the edge detecting function, Ω_{in} and Ω_{out} represent the inside and outside regions of the zero LS of φ, respectively, c_{in} and c_{out} are smooth approximations of the original image I in Ω_{in} and Ω_{out}, and $\lambda_1, \lambda_2 \lambda_3$ are the positive constants that reflect the relative importance among boundary, shape and region terms. The shape term, E_s depends on the active contour C, the vector $\boldsymbol{y_{pca}}$of the PCA eigencoefficients and the vector $\boldsymbol{y_{GT}}$ of the geometric transformations. This energy functional estimates the difference between the contour C and the zero LS $\hat{\varphi}$ of the shape function φ given by the PCA. The LS representation of the shape functional can be formulated as [178, 180]:

$$E_s = \int_{\Omega} \varphi^2 \left(\boldsymbol{y_{pca}}, e_{\boldsymbol{y_{GT}}}(y)\right) |\nabla\psi| \delta(\psi) d\Omega \tag{6.5}$$

where, ψ is the LS function embedding the active contour C, $\delta(.)$ is the Dirac function and $\delta(\psi)$ estimates the contour on $\{\psi = 0\}$. This energy functional forces the active contour to obtain a particular shape. The energy term E_r is used to drive the shape model towards the homogeneous intensity region with the shape of interest. The modified Mumford-Shah functional presented in [160] is applied here to segment the iris region whose shape is described by the PCA model:

$$E_r\left(\boldsymbol{y_{pca}}, \boldsymbol{y_{GT}}, c_{in}, c_{out}\right) =$$

$$\oint_{\hat{\varphi}(\boldsymbol{y_{pca}}, \boldsymbol{y_{GT}})} ds + \int_{\Omega_{\text{in}}(\boldsymbol{y_{pca}}, \boldsymbol{y_{GT}})} (|I - c_{in}|^2 + \beta|\nabla c_{in}|^2) d\Omega$$

$$+ \int_{\Omega_{\text{out}}(\boldsymbol{y_{pca}}, \boldsymbol{y_{GT}})} (|I - c_{out}|^2 + \beta|\nabla c_{out}|^2) d\Omega \tag{6.6}$$

where $\hat{\varphi}$ is the zero LS representation of the shape function φ, obtained using the

PCA. The function φ indicates an image I portioned into two regions, Ω_{in} and Ω_{out}, respectively representing the iris and sclera regions that are separated by the boundary $\hat{\varphi}$:

$$\Omega_{\text{in}}\left(\boldsymbol{y_{pca}}, \boldsymbol{y_{GT}}\right) = \{\text{y } \in \Omega | \varphi\left(y, \boldsymbol{y_{pca}}, \boldsymbol{y_{GT}}\right) > 0\},$$
$$\Omega_{\text{out}}\left(\boldsymbol{y_{pca}}, \boldsymbol{y_{GT}}\right) = \{\text{y } \in \Omega | \varphi\left(y, \boldsymbol{y_{pca}}, \boldsymbol{y_{GT}}\right) < 0\}, \quad (6.7)$$
$$\hat{\varphi}\left(\boldsymbol{y_{pca}}, \boldsymbol{y_{GT}}\right) = \{\text{y } \in \Omega | \varphi\left(y, \boldsymbol{y_{pca}}, \boldsymbol{y_{GT}}\right) = 0\}$$

After the minimization of the energy functional E_r , we obtain the shape parameters $\boldsymbol{y_{pca}}$ and the parameters $\boldsymbol{y_{GT}}$ of the rigid or affine transformation of the contour $\hat{\varphi}$. The contour $\hat{\varphi}$ captures the shape of the iris region. Since the shapes generated by the PCA are smooth enough, the smoothing term $\oint_{\hat{\varphi}(\boldsymbol{y_{pca}}, \boldsymbol{y_{GT}})} ds$ is not considered here. Therefore, the functional E_r of (6.6) can be rewritten as follows:

$$E_r\left(\boldsymbol{y_{pca}}, \boldsymbol{y_{GT}}, c_{in}, c_{out}\right) = \int_{\Omega} \Phi_{in} H(\varphi(\boldsymbol{y_{pca}}, \boldsymbol{y_{GT}}))\, d\Omega +$$
$$\int_{\Omega} \Phi_{out} H(-\varphi(\boldsymbol{y_{pca}}, \boldsymbol{y_{GT}}))\, d\Omega \quad (6.8)$$

where, $H(.)$ is the Heaviside function, with $\Phi_{in} = (|I - c_{in}|^2 + \beta|\nabla c_{in}|^2)$ and $\Phi_{out} = (|I - c_{out}|^2 + \beta|\nabla c_{out}|^2)$. The energy functional of (6.8) captures the global shape variations provided by the PCA. However, this functional cannot acquire the local edge variations. In order to capture the local variations around the global shape, we apply the classic Geodesic Active Contour (GAC) given by E_b [185]. The functional E_s provides the similarity between the active contour shape and the iris shape prior being localized. The term E_r forces the shape prior globally to move towards a homogeneous intensity region. Next, we combine these two energy functionals with the gradient-based boundary finding functional E_b, which finds the

boundary information between the iris and sclera regions. Therefore, we obtain a functional E for the localization of the limbic boundary with a shape model that uses both global and local information:

$$E = \oint_{\Omega} f\left(y, \boldsymbol{y_{pca}}, \boldsymbol{y_{GT}}\right) |\nabla\psi| \delta(\psi) d\Omega$$

$$+ \lambda_3 \int_{\Omega} \left(\Phi_{in} H\left(\varphi\left(\boldsymbol{y_{pca}}, \boldsymbol{y_{GT}}\right)\right) + \Phi_{out} H(-\varphi)\right) d\Omega \qquad (6.9)$$

where:

$$f\left(y, \boldsymbol{y_{pca}}, \boldsymbol{y_{GT}}\right) = \lambda_1 \varphi\left(\boldsymbol{y_{pca}}, e_{y_{GT}}(y)\right) + \lambda_2 g(|\nabla I(y)|) \qquad (6.10)$$

Therefore, the combined energy functional of (6.9) is robust against shape variation and noise, and is not affected by the oversegmentation. Now, to segment the iris region, we minimize E using the calculus of variations and the gradient descent method. The evolution equations that minimize E are depicted as follows. First, the evolution equation that minimizes *E w.r.t.* LS curve ψ [16] is:

$$\partial_t \psi(t, y) = \left(f_l - \langle \nabla f, \frac{\nabla\psi}{|\nabla\psi|} \rangle\right) \delta(\psi) \text{ in }]0, \infty[\times \Omega,$$

$$\psi(0, y) = \psi_0(y) \text{ in } \Omega, \qquad (6.11)$$

$$\frac{\delta(\psi)}{|\nabla(\psi)|} \partial_N \psi = 0 \text{ on } \partial\Omega$$

The evolution equation that minimizes *E w.r.t.* the vector of eigencoefficients $\boldsymbol{y_{pca}}$ is [16]:

$$d_t \boldsymbol{y_{pca}}(t) = -\int_{\Omega} \nabla_{\boldsymbol{y_{pca}}} \varphi \left(2\lambda_1 \varphi |\nabla\psi| \delta(\psi) + \lambda_2 (\Phi_{in} -\right.$$

$$\left.\Phi_{out}) \delta(\varphi)\right) d\Omega \text{ in }]0, \infty[\times \Omega_{pca}, \qquad (6.12)$$

$$\boldsymbol{y_{pca}}(t = 0) = \boldsymbol{y_{pca_0}} \text{in } \Omega_{pca}$$

The evolution equation that minimizes E *w.r.t.* the vector of geometric transformations $\boldsymbol{y_{GT}}$ is:

$$d_t \boldsymbol{y_{GT}}(t) = -\int \langle \nabla\varphi, \nabla_{\boldsymbol{y_{GT}}} e_{\boldsymbol{y_{GT}}} \rangle \ (2\lambda_1 \varphi |\nabla\psi| \delta(\psi) +$$

$$\lambda_2 (\Phi_{in} - \Phi_{out}) \delta(\varphi)) d\Omega \text{ in }]0, \infty[\times \Omega_{GT}, \tag{6.13}$$

$$\boldsymbol{y_{GT}}(t=0) = \boldsymbol{y_{GT_0}} \text{in } \Omega_{GT},$$

Next, we solve the Euler-Lagrange equations for c_{in} and c_{out}:

$$\partial_t c_{in}(t,y) = c_{in} - I - \beta \Delta c_{in} \text{ in }]0, \infty[\times \{\varphi > 0\},$$

$$c_{in}(0,y) = I \text{ in } \{\varphi > 0\}, \tag{6.14}$$

$$\partial_t c_{out}(t,y) = c_{out} - I - \beta \Delta c_{out} \text{ in }]0, \infty[\times \{\varphi < 0\},$$

$$c_{out}(0,y) = I \text{ in } \{\varphi < 0\},$$

The first stage of the PCA is to rigidly align the training curves that represent the iris shape information. This is estimated using the shape similarity measure proposed in [180]. In the second stage of PCA, SVD is performed on the SDFs of the aligned training curves to extract the n eigenvalues and eigenvectors [16, 179]. Finally, the evolution equations (6.11) to (6.14) are numerically solved iteratively until convergence is reached for the optimal estimation of the iris region. Figs. 6.5, 6.6 and 6.7 show the iris segmentation process using the shape guided model.

We deployed the eyelash detection techniques, as used in the chapter 3 [26, 186]. Fig. 6.8 shows the segmented iris images after iris/pupil localization and eyelash detection. In order to compensate for the elastic deformation in the iris texture, we

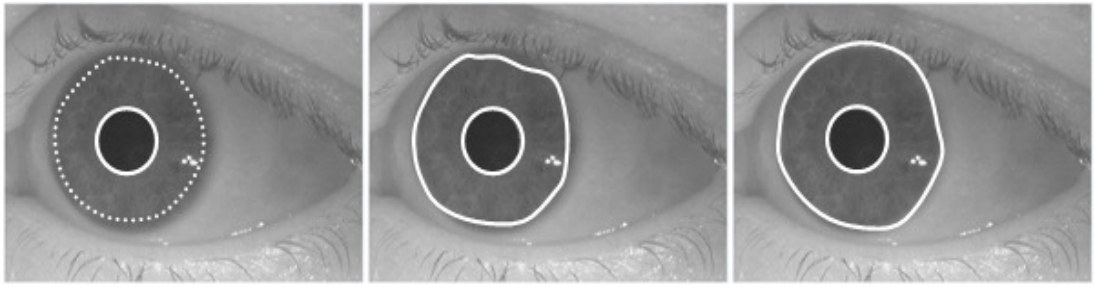

(a) (b) (c)

Fig 6.5 Iris segmentation on a sample in the WVU nonideal dataset: (a) initial contour; (b) evolution of the active contour model with shape prior; and (c) segmented iris.

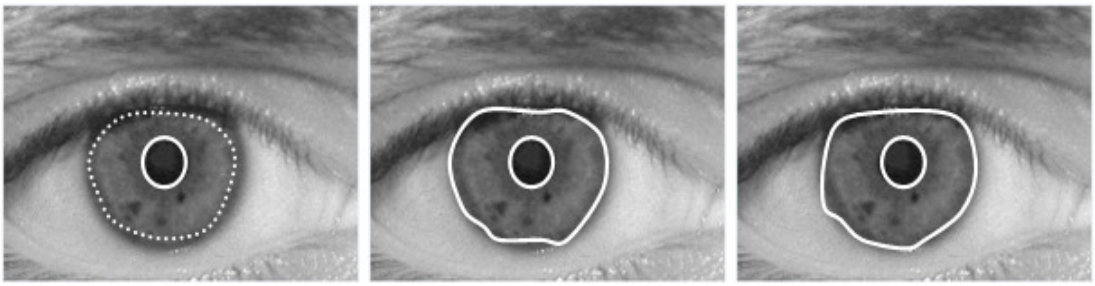

(a) (b) (c)

Fig 6.6 Iris segmentation on a sample in the UBIRIS Version 1 dataset: (a) initial contour; (b) evolution of the active contour model with shape prior; and (c) segmented iris.

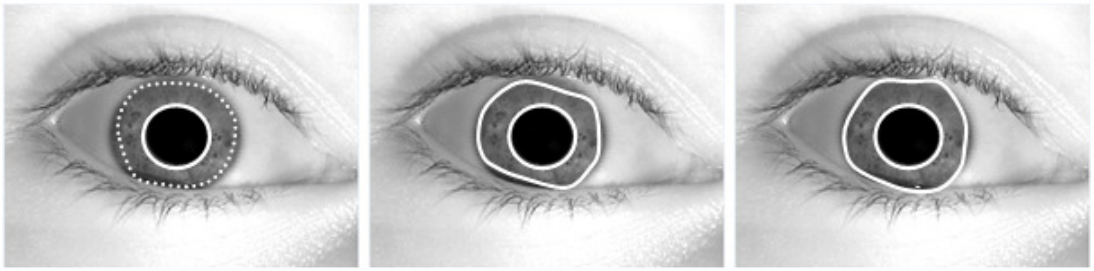

(a) (b) (c)

Fig 6.7 Iris segmentation on a sample in the ICE 2005 dataset: (a) initial contour; (b) evolution of the active contour model with shape prior; and (c) segmented iris.

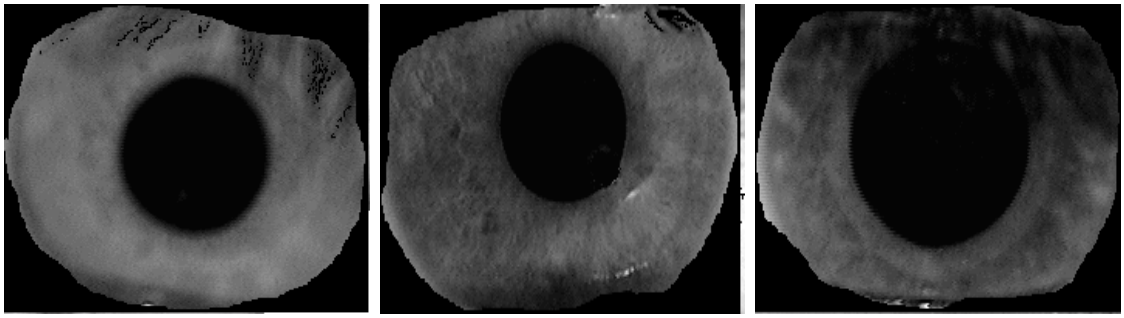

(a)

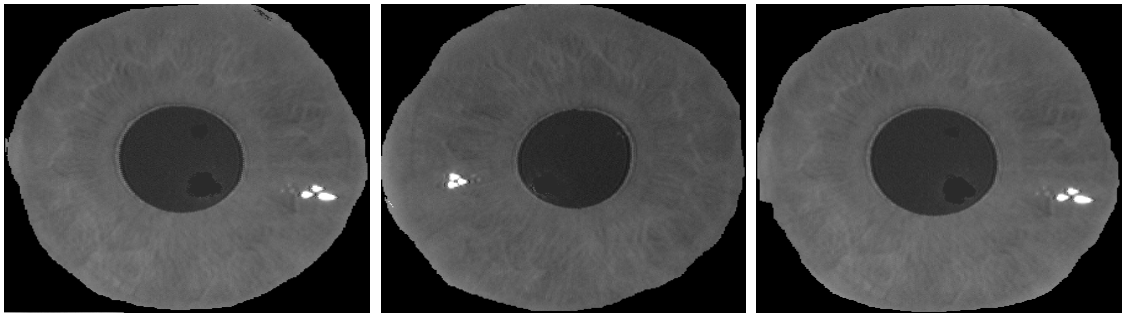

(b)

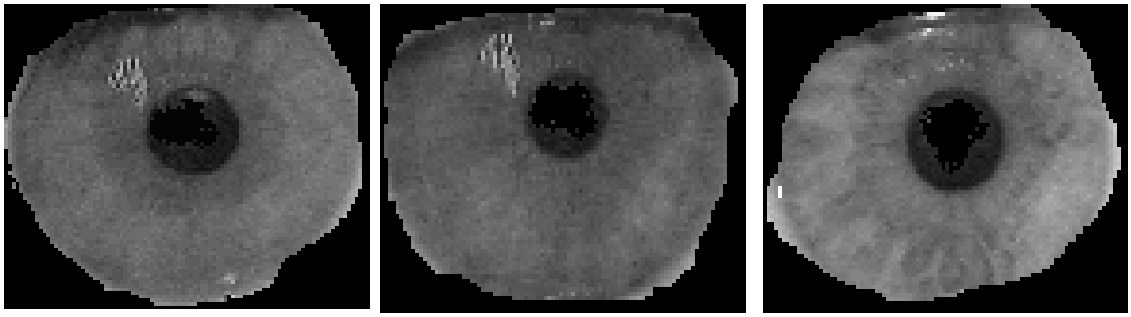

(c)

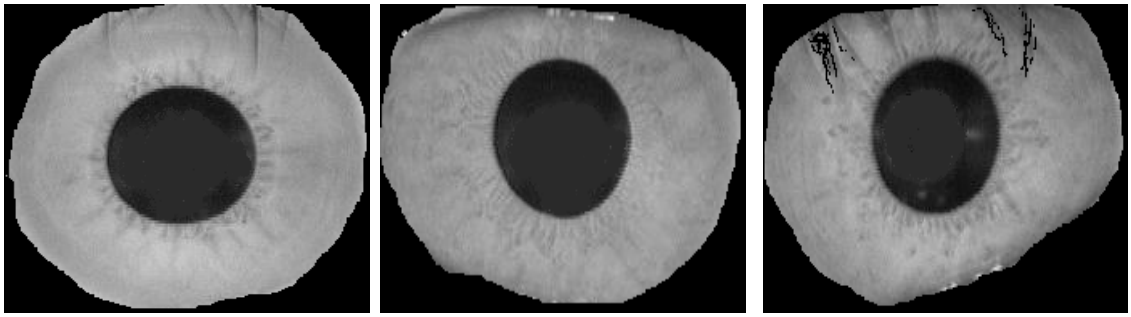

(d)

Fig 6.8 Three samples of segmented iris images after iris/pupil detection and eyelash detection from: (a) ICE 2005 dataset; (b) WVU Nonideal dataset; (c) UBIRIS Version 1 dataset; and (d) CASIA Version 3 Interval dataset.

needed to unwrap the extracted (and localized) iris region into a normalized rectangular block, by converting from the Cartesian coordinates to the polar coordinates as proposed by Daugman [27-29]. However, the extracted iris boundaries are not exactly circular and may be in the shape of any kind of curve. Therefore, to solve this size inconsistency, we first select a starting point in the inner boundary, based on the estimated centre point obtained by the DLS-based elliptical fitting [94]. Then, we connect this point to the corresponding point in the outer boundary, as shown in Fig. 6.9(a). In the next stage, an equal number of points is selected clockwise in the inner boundary, and these points are connected to the corresponding points in the outer boundary (see Fig. 6.9(b)). Finally, the selected coordinates of iris and pupil boundaries are mapped into a dimensionless polar space, using Daugman's method [27-29]. In this way, the localized iris region is unwrapped into a rectangular block with a fixed size of 64× 512, as demonstrated in Fig. 6.9(c). In order to improve the quality of the iris image, we have applied a two-step image enhancement technique, described in Section 5.2.1. In this chapter, the DBWT is applied to extract the characteristic values from the normalized

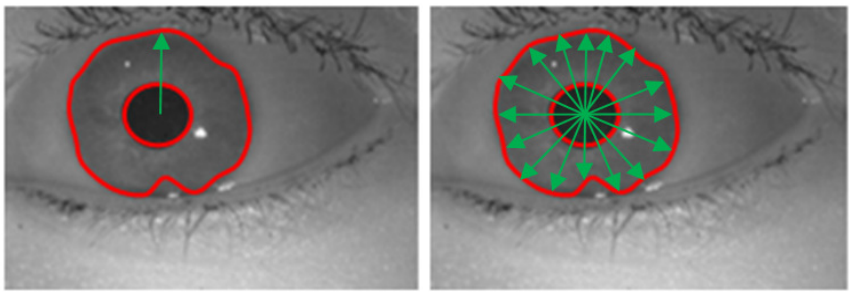

(a) (b)

(c)

Fig. 6.9 Unwrapping process: (a) selection of the starting points in the inner and outer boundaries; (b) selection of equal number of points in the inner boundary and corresponding points in the outer boundary; and (c) unwrapped image.

(and enhanced) image block of size 64 ×512 pixels, as described in Chapter 4, where the normalized image is represented by a distinctive feature set of 176 components.

6.3 Feature Ranking using Game Theory (GT)

In this section, we apply a feature ranking scheme in the context of cooperative or coalitional games, a notion from game theory [17]. The algorithm is based on the MSA, a framework which relies on game theory to estimate the effectiveness of features [17, 171, 179]. This algorithm iteratively computes the usefulness of features and selects them accordingly using either forward selection or backward elimination processes.

Let us consider the three disjoint sets, *Train*, *Valid*, and *Test*, representing the training set, validation set, and test set, respectively. These sets independently and identically contain the distributed sample instances of the form $\boldsymbol{x_j}, y_j$, where $x_j \in \boldsymbol{R^n}$ indicates the *j*-th instance and y_j is the target class value associated with it. Given an induction algorithm and a set of features such that $F \subseteq \{1, 2, \ldots\ldots, n\}$, $CSF_F(x)$ represents a classifier constructed from the training set using the induction

algorithm, after its input features have been narrowed down to the ones in *F.* Therefore, $CSF_F(x)$ labels each instance of the form $\left(x_{k_1}, \ldots\ldots, x_{k_{|F|}}\right), k_i \in F, 1 \leq i \leq |F|$ with an appropriate class value. The main objective of the feature selection scheme is to choose a subset *F* of the extracted iris feature sequence that maximizes the performance of the classifier on the test set. In [17], authors only focused on optimizing the accuracy of classifier. However, in this chapter, we focus on minimizing four performance measures: the Recognition Error (RE), FAR and FRR of the classifier, and FSS using forward selection and backward elimination approaches.

A modified iterative algorithm for the feature selection, called the Modified Contribution-Selection Algorithm (MCSA), is used to optimize the performance of the classifier on unseen data. The MCSA algorithm combines both the filter and wrapper approaches. However, unlike the filter methods, the features are ranked at each step by using the classifier as a black box. The ranking is based on the Shapley value [17], a well-known concept from game theory, to estimate the importance of each feature for the task at hand by taking into account the interactions between the features. In the coalitional game theory, a set of players is associated with a "payoff", a real function that denotes the benefit achieved by different sub-coalitions in a game. Formally, we can define the coalitional game theory by the pair *(N, u),* where $N = \{1, 2, \ldots\ldots, n\}$ is the set of all players and $u(F)$, for every $F \subseteq N$, denotes a real number associating a value with the coalition *F.* Game theory represents the contribution of each player to the game by constructing a certain value function. This function assigns a real-value to each player and the values correspond to the

contribution of the players in achieving an optimal payoff. The calculation of the contribution value is based on the Shapley value [179]. We briefly discuss the Shapley value in the following paragraph.

The marginal importance of a player *i* to a coalition *F, with* $i \notin F$ is given by:

$$\Delta_i(F) = u(F \cup \{i\}) - u(F) \tag{6.15}$$

Then, the Shapley value using the payoff is defined as follows:

$$\Phi_i(u) = {}^{1}/_{n!} \sum_{\pi \in \Pi} \Delta_i\left(F_i(\pi)\right) \tag{6.16}$$

where Π denotes the set of all permutations over N, and $F_i(\pi)$ is the set of players appearing before the *i*-th player in the permutation π. Essentially, the Shapley value of a player is a weighted mean of its marginal value, averaged over all the possible subsets of players. If we transform the concept of game theory into the arena of iris feature subset selection, in which the contribution of each feature is estimated to generate a classifier, then the players N are mapped to the features of a dataset and the payoff is denoted by a real valued function *u(F).* This function estimates the performance of four measures RE, FAR, FRR and FSS that are generated by the set of F features. The estimation of Shapley values requires the summing of all the possible subsets of the players, and thus, it is not suitable for the case of iris feature selection due to its computational load. So, in our feature selection algorithm, we use the Shapley value heuristically to estimate the contribution value of a feature. We can calculate the contribution values from the sampled permutations of the whole set of players, with *d* being the bound on the permutation-size:

$$\theta_i(u) = \frac{1}{|\Pi_d|} \sum_{\pi \in \Pi_d} \Delta_i\left(F_i(\pi)\right) \tag{6.17}$$

where, Π_d denotes the set of sampled permutations on the subsets of size *d.*

The MCSA is iterative in nature, and can either adopt a forward selection or backward elimination approach. Based on the contribution value, MCSA ranks each feature and then selects features with the lowest contribution values with forward selection, or eliminates features with the highest contribution values with backward elimination. The algorithm continues to calculate the contribution values of the remaining features, given those that have already been selected (or eliminated), and selects (or eliminates) the new features, until the contribution values of all the candidate features fall below a contribution threshold with the forward selection (or exceed a contribution threshold with the backward elimination). The algorithm can be regarded as a generalization of filter methods. However, the main idea of the algorithm is that the contribution value is calculated for each feature according to its assistance in improving the classifier's performance, which is generated using a specific induction algorithm, and in conjunction with other features. Based on the nature of our problem, we propose the following payoff function that optimizes the four performance issues mentioned above:

$$u(F) = W_1.RE + W_2.FAR + W_3.FRR + W_4.\left(\frac{FSS}{Total\ Number\ of\ Features}\right) \quad (6.18)$$

where, W_1, W_2, W_3, and W_4 are constant weighting parameters which reflect the relative importance between RE, FAR, FRR, and FSS. The MCSA algorithm in its forward selection version is depicted as follows:

$Modified\ Contribution\ Selection\ Algorithm\ (P, T_d, d, f\ )$: P is the set of input iris features, T_d denotes the contribution threshold, d is the maximal permutation size for estimating contribution values, and f is the selected feature subset size in each phase.

This algorithm calculates the contribution value of the p feature, using the payoff function, $u(F)$, described above, and selects at most f features with the lowest contribution values that fall below T_d. In the backward elimination version, the selection routine is replaced with an elimination routine which eliminates features in each phase and the halting criterion is changed accordingly.

The forward selection version of the MCSA is given as follows:

1. $SelectedFeatures := \phi$
2. $For\ each\ \ p \in P \setminus SelectedFeatures$
   i) $MCNT_p = Contributions\ (p, SelectedFeatures, d)$
3. $if\ min\ \ MCNT_p < T_d$
   i) $SelectedFeatures := SelectedFeatures\ \cup Selection\ (\{MCNT_p\}; f, T_d)$
   ii) $Goto\ Step\ 2$
   else
   iii) $return\ SelectedFeatures$

The case $SelectedFeatures := \phi$ is handled by returning the fraction of majority class instances. The maximum permutation size, *d,* plays an important role in deciding the contribution values of the different features. The *d* should be selected in a way that ensures that the different combinations of features interacting together will be inspected. Each feature is ranked according to its contribution, based on the Shapley value as discussed before, and the features with the lowest contribution values are selected with the forward selection approach, or the features with the highest contribution values are eliminated by using the backward elimination approach. The decision tree is used for the feature selection. The AASVMs, proposed in Chapter 4 [70, 136], are deployed to perform the actual

prediction on the selected features based on the performance of the classifier along with FAR and FRR.

In this chapter, we use HDD for iris template matching. The HDD is used to measure the dissimilarity between two sets of feature points, as mentioned in Chapter 5.

6.4 Results and Analysis

In this section, we report the results of a set of experiments and evaluate the performance of the proposed scheme. The extensive experiments were conducted again on four datasets: the ICE 2005 [189], the CASIA Version 3 Interval [190], the UBIRIS Version 1 [191], and the WVU Nonideal [192]. The details about the datasets are given in Appendix A. The Performance of the proposed scheme was also evaluated on the combined dataset. Our experiments will be described in two stages: first, we will describe the performance of our proposed algorithms with respect to segmentation and feature ranking, and second, we will compare the performance of our method with those of the other state-of-the-art algorithms. We have conducted the extensive experiments in two modes: the verification mode and the identification mode.

6.4.1 Performance Evaluation of the Proposed Scheme

In our experiment, 100 iris images from each iris dataset were used for training by using PCA. For the combined dataset, we applied PCA on the training set of 500 images (i. e., 125 irises from each dataset). The alignment process, which performs the registration of shapes, was conducted by genetic programming, and this

approach took around 2 minutes per training of each iris. The alignment step was not fast enough as it was based on genetic optimization. However, the alignment process was performed once for all the experiments. The decomposition into principal components, which was also performed only once for all the experiments, took a few seconds. A new shape was computed by the following equation, based on the training set $\{\varphi\}$:

$$\varphi = \bar{\varphi} + \boldsymbol{W}_p \boldsymbol{y}_{pca} \tag{6.19}$$

where, the principal components, p, are stored in the matrix $\boldsymbol{W}_p$. The spatial transformations done with the B-splines interpolation method also took a few seconds [16]. Based on the extensive experiments, we selected the values of $\lambda_1, \lambda_2, \lambda_3$, β and Δt. Here, β selected the size of the neighborhood in which the gray level information was averaged with the help of diffusion (see equation 6.14). λ_1 permitted the active contour to move around the shape prior to acquiring the local boundary information. The value of λ_2 was always kept at 1, and λ_3 allowed the shape prior to move towards the iris region to be segmented. For the iris segmentation, we applied the SGA, and the segmentation results are shown in Figs. 6.10-6.13. These figures show that our segmentation scheme gives an encouraging performance, even when the iris and the sclera regions are separated by a blurred boundary, especially in the CASIA and WVU datasets. The selected values for $\lambda_1, \lambda_2, \lambda_3$, β and Δt were set at 0.4, 1.0, 15, 100 and 0.1, respectively. In Fig. 6.14, comparisons were first made between the outputs generated using GAC, with and without shape prior information, and using the proposed SGA. The final contour output, as shown in Fig. 6.14 (c) with shape prior information, is much better than

the outputs generated by using classic GAC as shown in Fig. 6.14 (b, c), where only the boundary-based information is used for segmentation. Similarly, Fig 6.15 shows that SGA performs better than the region-based active contour model proposed in [160]. Therefore, the localization performance improves when we use the shape information. Furthermore, the proposed SGA utilizes both the gradient data and the region information to localize the iris region, and this enhances the segmentation accuracy. Our proposed segmentation scheme also performs reasonably well in noisy situations. The sudden variation in the intensity level may halt the ongoing propagation of the traditional active contour. However, in our case, the other boundary points continue to move and, hence, the curve evolution process based on the shape guided model keeps propagating towards the outer iris boundary. We can see the outputs of applying our proposed shape-guided scheme to an iris

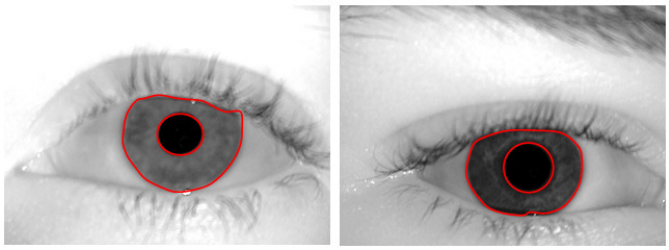

Fig. 6.10 Segmentation results for two samples on ICE 2005 dataset.

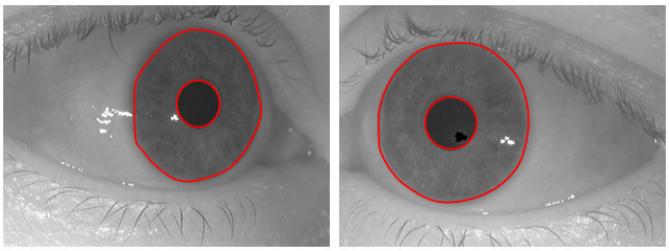

Fig. 6.11 Segmentation results for two samples on WVU Nonideal dataset.

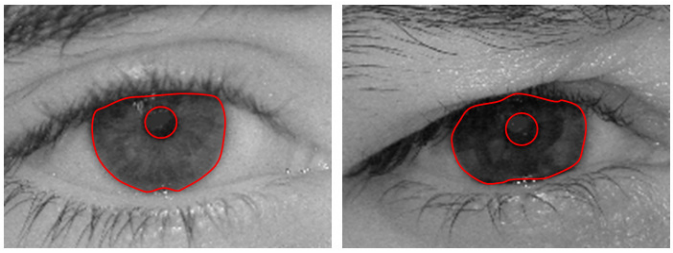

Fig. 6.12 Segmentation results for two samples on UBIRIS Version 1 dataset.

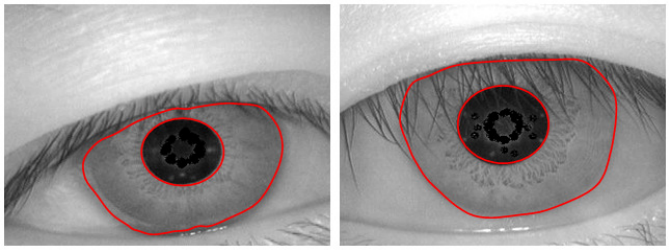

Fig. 6.13 Segmentation results for two samples on CASIA Version 3 Interval dataset.

image with Gaussian white noise in Fig. 6.16 (b, c). Fig. 6.16 (d, e, f) shows the outcomes of deploying our approach to an iris image with the Poisson noise, the salt and pepper noise, and the speckle noise, respectively. Therefore, Fig. 6.16 shows that the iris segmentation using SGA is well-suited for the iris images that are captured in an unconstrained situation. However, the proposed SGA-based segmentation algorithm fails to perform on some images of the UBIRIS dataset due to a huge occlusion, as shown in Fig. 4.20. Also, Fig. 6.17 reveals that segmentation errors may occur on several iris images due to the poor quality of the images, huge occlusions and the deviated gazes. For experimental purposes, we also applied the Masek's segmentation algorithm [53, 187], which utilizes the Hough transform to detect the outer boundary. Fig. 6.18 exhibits that Masek's segmentation scheme fails to detect the outer boundary accurately in several cases. However, the SGA-based localization process isolates the iris boundary accurately in those corresponding

cases. Therefore, our experiments demonstrate that the traditional Hough transform-based segmentation scheme cannot handle the nonideal nature of the iris images. The above experiments were conducted on a 3.00 GHz Pentium IV PC with 2.5 GB RAM in a MATLAB 7.2 environment. The average time consumption of matching an iris image was 9541ms, as exhibited in Table 6.2. Therefore, the SGA-based scheme consumed a smaller amount of time than the GT-based and LS–based segmentation approaches as discussed in previous chapters.

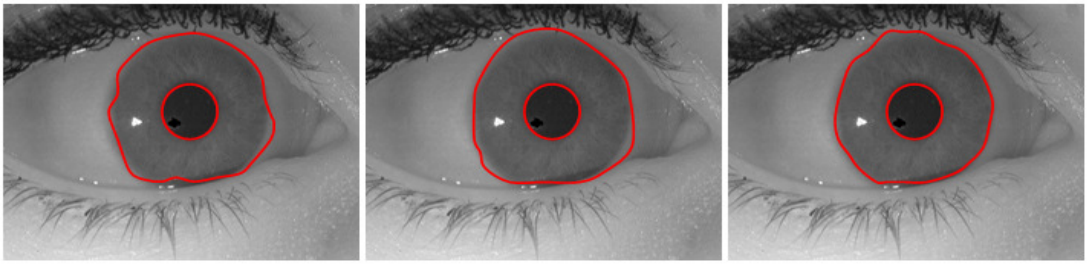

(a) (b) (c)

Fig. 6.14 Curve evolution on WVU Nonideal dataset: (a) using GAC without shape prior; (b) using GAC with shape prior; and (c) using SGA.

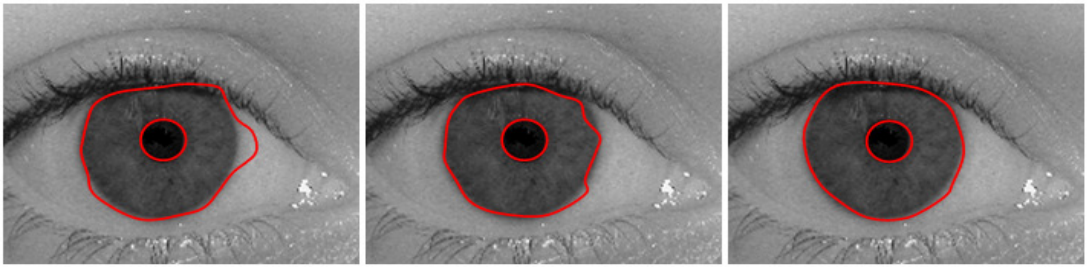

(a) (b) (c)

Fig. 6.15 Curve evolution on UBIRIS Version 1 dataset: (a) using region-based active contour of Vese and Chan [160] without shape prior; (b) using region-based active contour of Vese and Chan [160] with shape prior; and (c) using SGA.

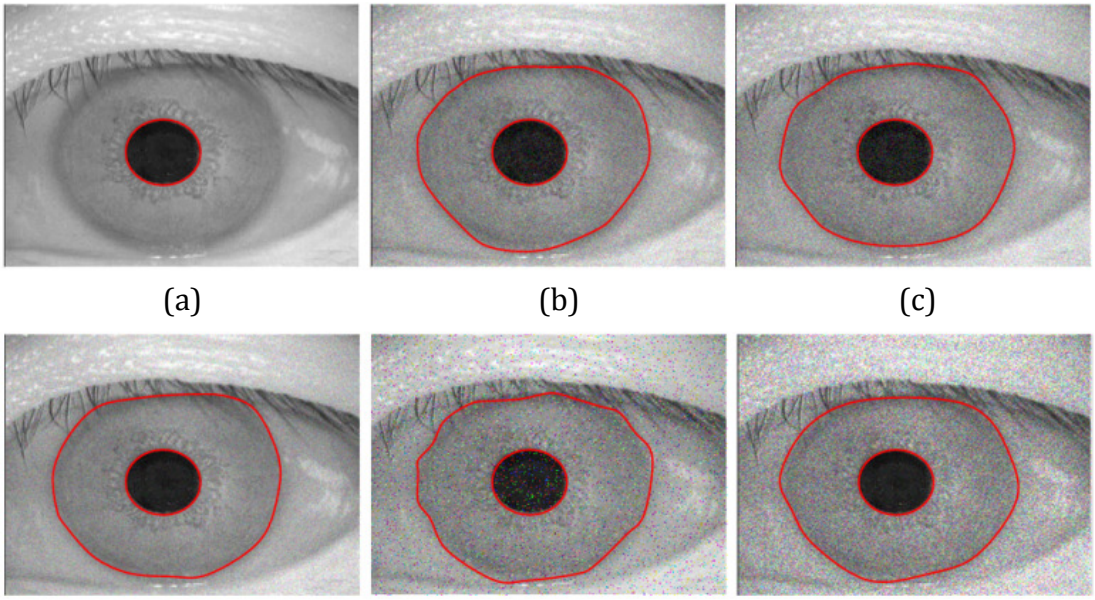

Fig. 6.16 Performance of SGA in noisy situations: (a) original image after filling the white spots from CASIA Version 3 Interval dataset; (b) image (a) with Gaussian white noise (mean=0 and variance = 0.005); (c) image (a) with Gaussian white noise (mean=0 and variance = 0.007); (d) iris image (a) with Poisson noise; (e) iris image (a) with salt and pepper noise (noise density = 0.06); and (f) iris image (a) with speckle noise which adds the multiplicative noise (mean=0 and variance = 0.07).

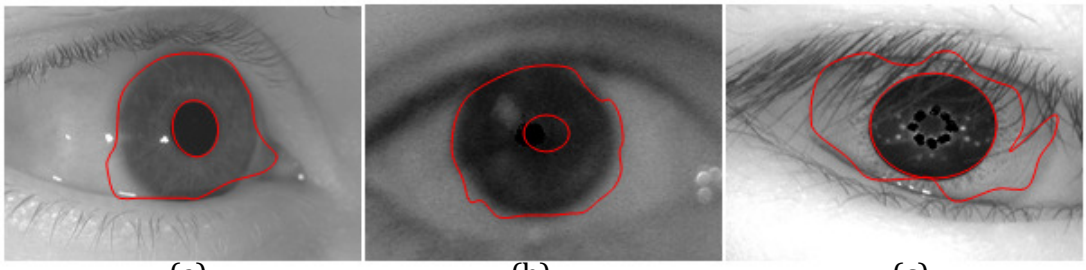

Fig. 6.17 Segmentation errors found on several images of: (a) WVU Nonideal, (b) UBIRIS Version 1, and (c) CASIA Version 3 Interval datasets, using SGA.

The proposed cooperative GT-based feature selection approach has been used to reduce the feature dimension without compromising the recognition accuracy. The MCSA is prone to overfitting on the validation set. The "curse of dimensionality"

appears, and the irrelevant features are selected if the classifier's performance is evaluated on a small validation set. Since the number of samples from most iris research is limited, we used the cross-validation procedure to evaluate the performance of a classifier. In this research effort, the LOOCV was used for the ICE and WVU datasets. For the CASIA, and UBIRIS datasets, we used a 2-fold cross

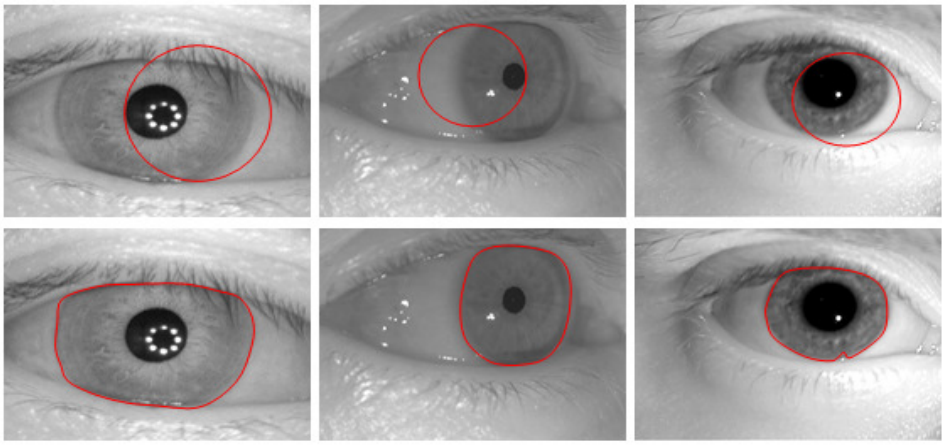

Fig. 6.18 Images in the first row show the segmentation errors found on several images using Masek's algorithm [53]. Corresponding images in the second row were correctly segmented using SGA.

validation to obtain the validation accuracy. The AASVMs [70, 136] were used to acquire the validation accuracy for the MCSA algorithm. Fig. 6.19 shows the cross-validation accuracy of the selected feature subsets for the forward selection and the backward elimination approaches on the four data sets. Fig. 6.19(a) shows that a reasonable accuracy is obtained with the forward feature selection scheme, when the number of features is selected as follows: (a) 98 in ICE; (b) 111 in CASIA; (c) 105 in UBIRIS; and (d) 101 in WVU datasets, and the 102 best features are ranked for the combined dataset when the highest accuracy is achieved. Fig. 6.19 (b) demonstrates the performance of the backward feature elimination approach. Fig. 6.19(b) shows

that a reasonable accuracy is obtained with the backward feature elimination when the number of features is eliminated as follows: (a) 71 in ICE; (b) 72 in CASIA; (c) 61 in UBIRIS; and (d) 74 in WVU datasets; and 77 features are eliminated from the combined dataset when the highest accuracy is achieved. Therefore, in Fig. 6.19, it is clear that the MCSA-based feature selection with the backward feature elimination exhibits a better performance than the feature selection scheme with the forward feature selection. The reason is that a feature that contributes in prediction merely by coincidence may be selected on account of other truly informative features due to the higher dimensionality of the feature set. The forward selection scheme is affected severely in such cases where some features are not selected among the few significant ones. However, the backward elimination always keeps the most prominent features, which truly enhances the SVM's generalization performance as these features are not removed in the noneliminated set. This elimination process results in more stable generalization behavior for the backward elimination approach on the test set through the MCSA-based feature selection. Therefore, the backward elimination process selects only 99 features, whereas the forward selection process selects 102 features for the combined dataset. Thus, for our experiments, we adopted the backward elimination for the feature selection due to its higher performance. In order to achieve a higher performance, we ran the MCSA algorithm on the combined datasets with different values of the subset-size, *d*. Fig. 6.20 implies that there are optimal values of *d* to reach the highest performance. For small values of *d,* a few interactions occur between the different features. With the increase of *d,* the performance on the dataset increases until it reaches a critical

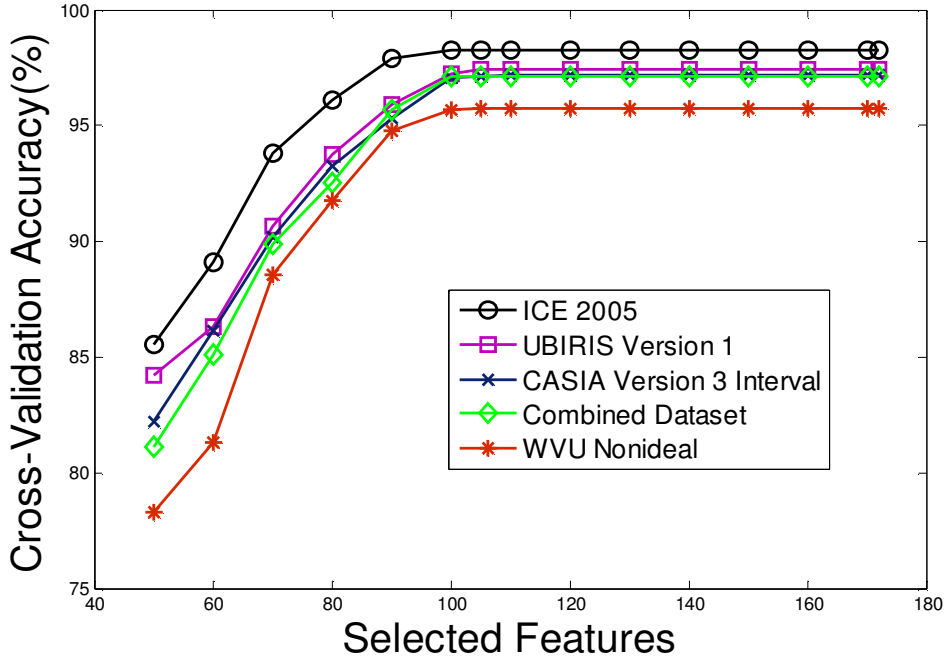

(a)

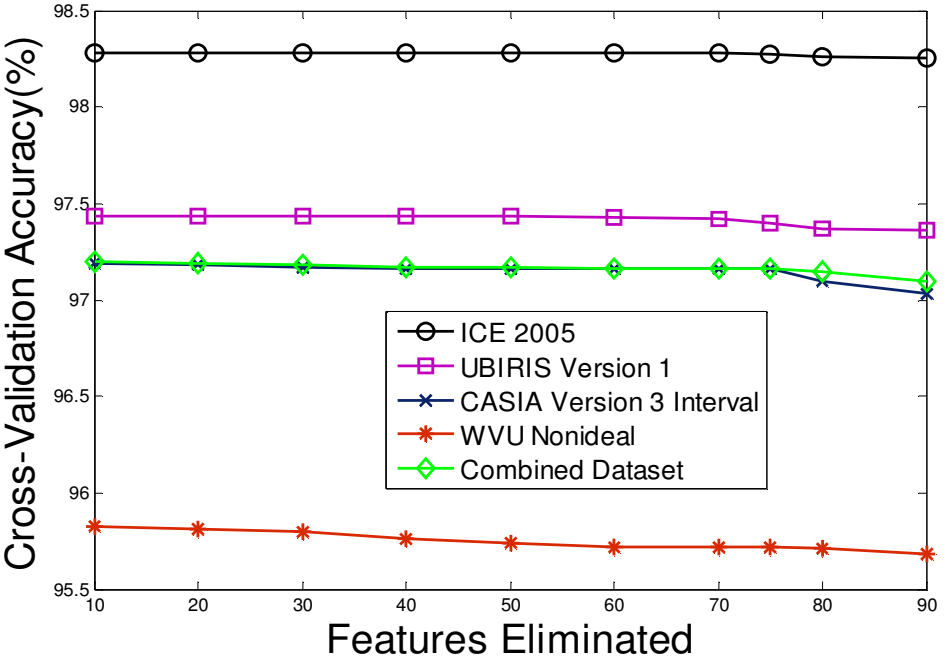

(b)

Fig. 6.19 Game-theoretic feature selection process with: (a) forward feature selection, and (b) backward feature elimination.

Table 6.2: Average time consumption of different parts of the proposed iris recognition system.

Algorithm	Time (ms)
Segmentation	9350
Unwrapping	87
Feature Extraction	71
Matching	33
Average Execution Time	9541

value. The performance remains stable around the critical value's performance as the *d* exceeds the critical value. The optimal subset size, *d* for the forward selection and backward elimination on the combined datasets are 8 and 10, respectively. After conducting several experiments, we set the values of four weighting parameters W_1, W_2 , W_3, and W_4 to 2000, 150, 10 and 1000, respectively, for the all of the datasets.

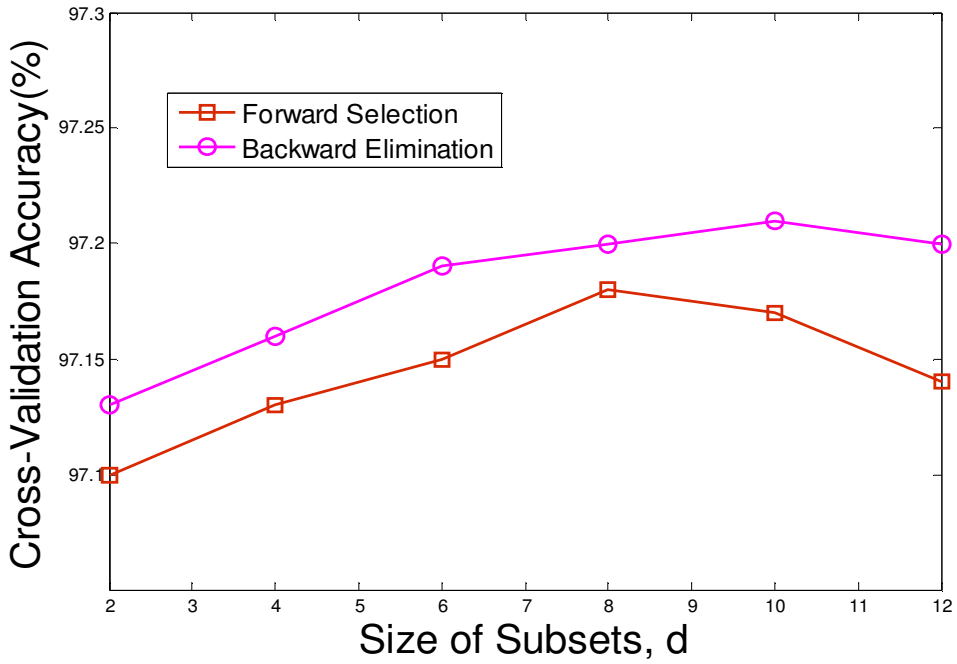

Fig. 6.20 Selection of subset size, *d,* on the combined dataset.

6.4.2 Comparison of the Proposed Method with the State-of-the-Art Algorithms

To exhibit the effectiveness of our segmentation approach, we compared our SGA with the IDO proposed by Daugman [27-29], Canny edge detection and Hough transform-based approach proposed by Masek [53, 187], the active contour-based localization approaches proposed by Vatsa et al. [67] and Shah-Ross [85, 86] and also with the ASM introduced by Cootes et al. [183, 188], for all the datasets. For comparison purposes, we only implemented the segmentation approaches proposed in [27-29, 67, 85, 86, 53, 183]. The ROC curves in Figs. 6.21-6.23 show that the matching performance improves when the combined approach, based on the shape prior information, is used for segmentation. The proposed segmentation scheme shows a better performance than the active contour-based methods, reported in

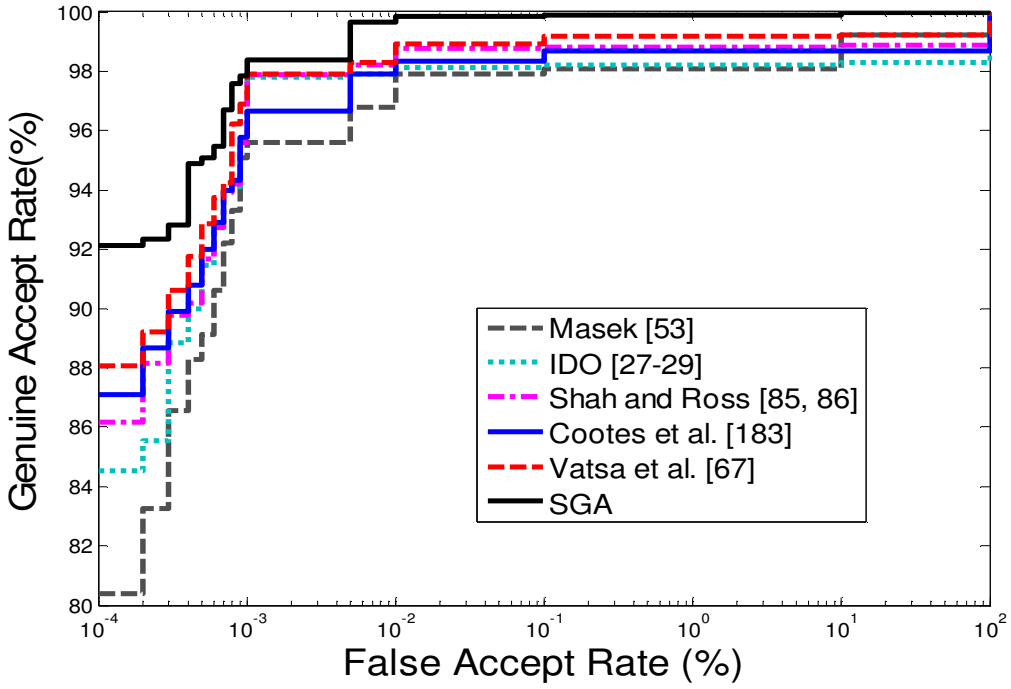

(a)

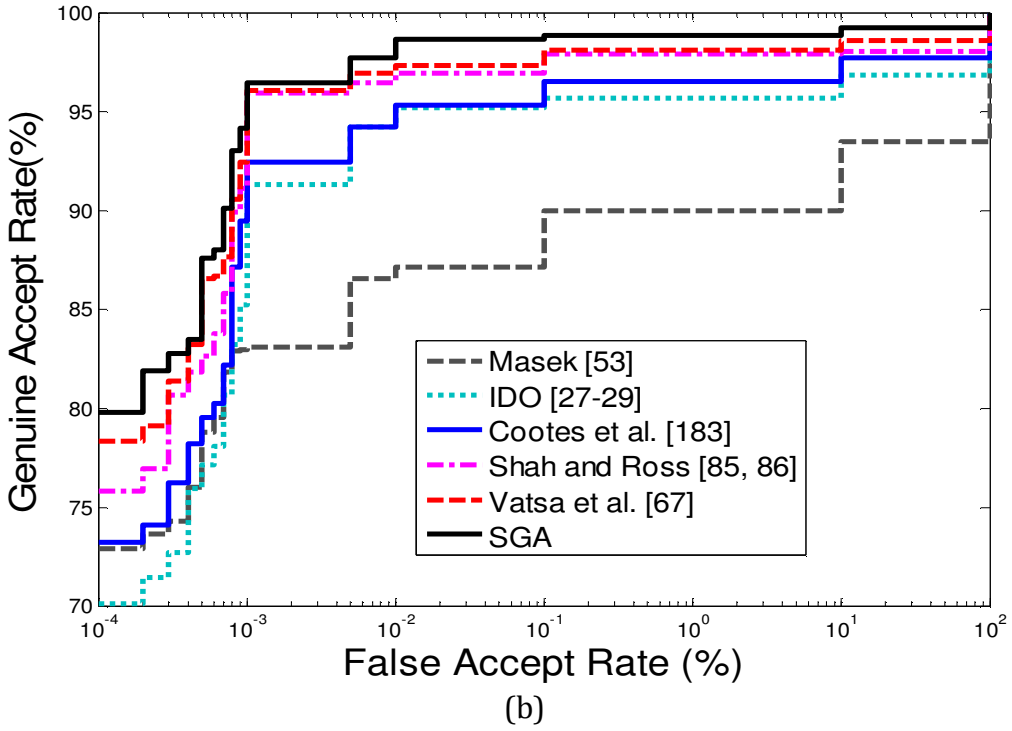

Fig. 6.21 ROC curves show the comparison of different segmentation techniques on: (a) ICE 2005, (b) WVU Nonideal datasets.

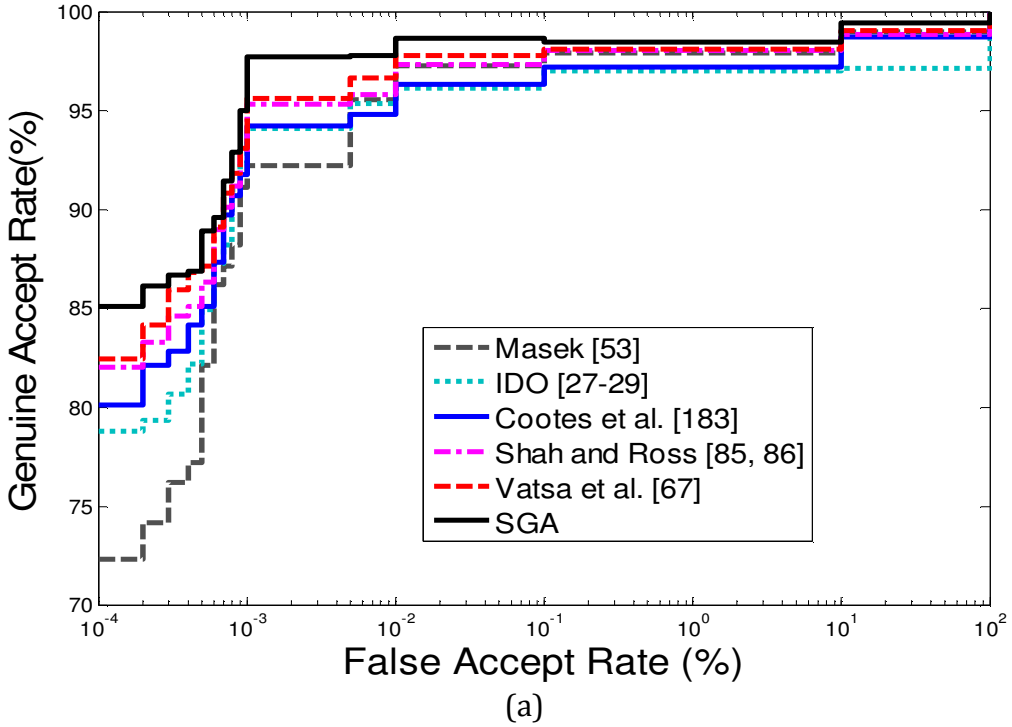

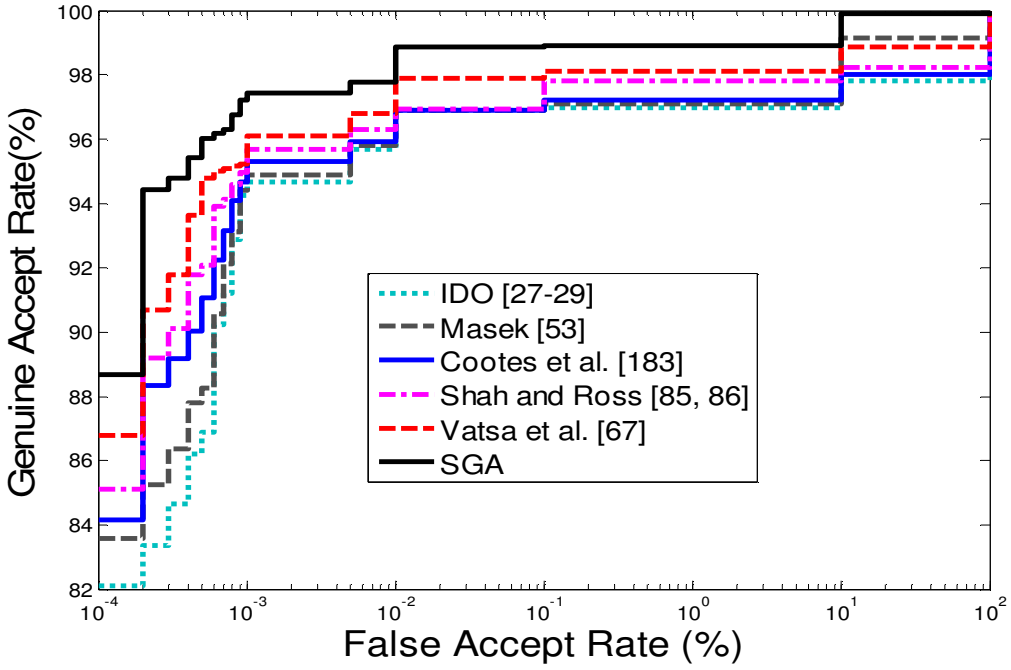

(b)

Fig. 6.22 ROC curves show the comparison of different segmentation techniques on: (a) CASIA Version 3 Interval, (b) UBIRIS Version 1 datasets.

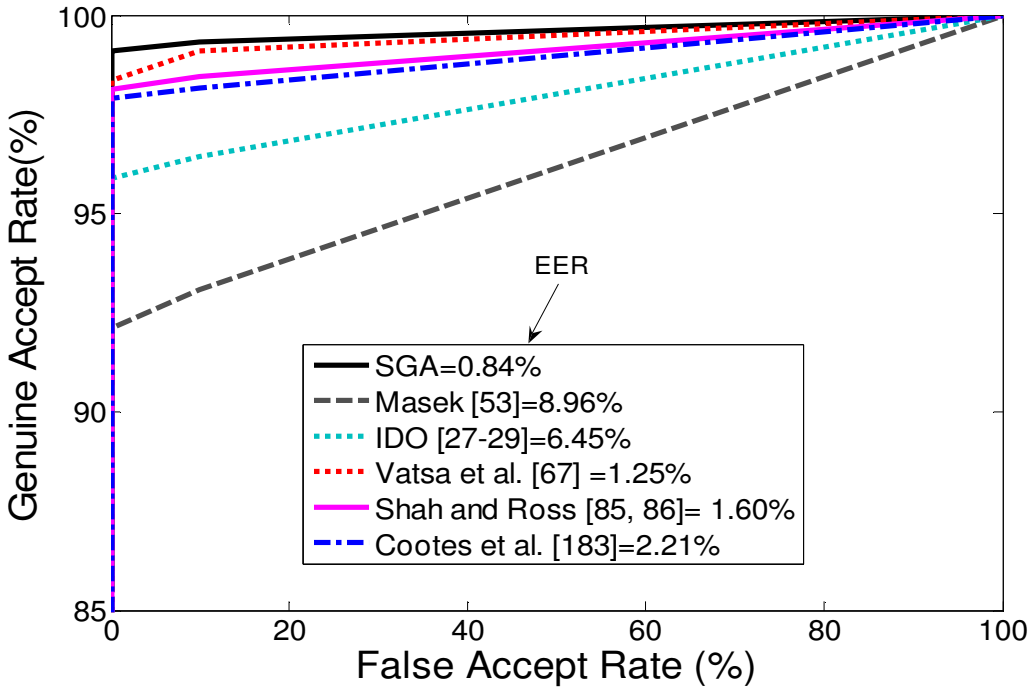

Fig. 6.23 ROC curves show the comparison of different segmentation techniques on nonhomogeneous Combined dataset.

[67, 85, 86], and the reason seems to be the utilization of both the region-based information and the gradient data along with the shape prior information. Moreover, we deployed a white spot detection technique to an input image to suppress the effect of the specular reflections. Furthermore, we proposed a new normalization technique to deal with the off angle occlusion problem. The GAR at a fixed FAR of 0.001% was: (a) 98.38% in ICE; (b) 97.66% in CASIA; (c) 97.43% in UBIRIS; and (d) 96.41% in WVU datasets. Fig. 6.23 shows that our algorithm achieved the highest GAR of 97.31% on the combined dataset at the fixed FAR of 0.001%. We also provide the EERs of each of these schemes in Fig 6.23, and our proposed segmentation scheme effectively increases the performance with the lowest EER of 0.84%. The inclusion of both the region-based and boundary-based information for segmentation along with the shape data, obtained from the trained iris images using PCA, assists in decreasing the EER. We also compared the proposed shape-guided model with five of our previous proposed methods, namely, the LS method (Section 4.2.1), the VLS method (Section 4.2.2), the RAC model (Section 4.2.3), the GT-based scheme (Section 5.2) and the CHT-based approaches (Section 3.3). The ROC curves in Fig. 6.24 clearly demonstrate that the proposed approach outperforms our previous methods with an EER of 0.81%, since the proposed curve evolution scheme takes into account the iris shape prior information. Furthermore, we compared the performance of the proposed algorithm with the methods reported in [27-29, 22, 31]. Fig. 6.25 exhibits the ROC curve of the proposed algorithm that is based on the shape guided curve evolution method on the non-homogeneous combined dataset. This figure shows that the proposed

algorithm achieves a higher GAR with a very low EER of 0.81% for the combined dataset. This result indicates that the proposed algorithm has higher distinguishing capabilities than the approaches reported in [27-29, 22, 31]. Moreover, the approaches proposed in [27-29, 22, 31] were not adjusted specifically for the degraded iris images. The proposed approach, based on the SGA, obtains a higher GAR of 97.34% at the fixed FAR of 0.001% on the Combined dataset. Therefore, the ROC curves in Fig. 6.25 reveal the effectiveness of the proposed scheme in a nonideal situation. In Figs 6.21-6.23, we did not apply the feature ranking scheme. However, in Figs. 6.24 and 6.25, we deployed the proposed feature ranking criteria based on MCSA. In Fig. 6.26, a comparison of the feature selection method using the

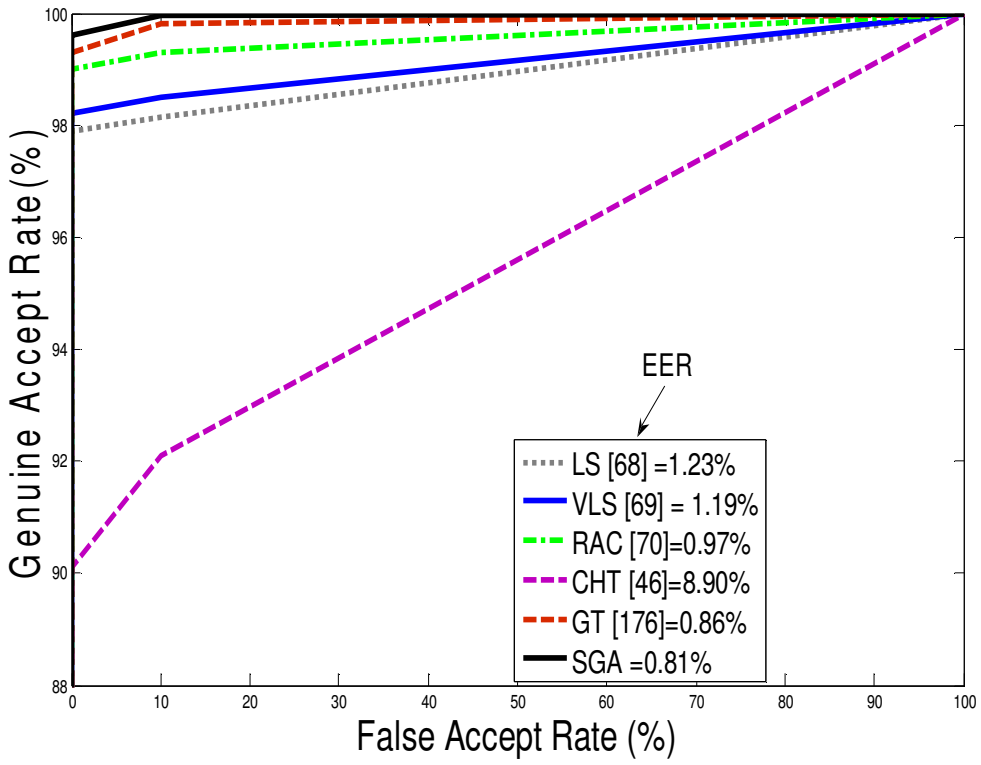

Fig. 6.24 ROC curves show the comparison of the proposed scheme with our previous techniques on the Combined dataset.

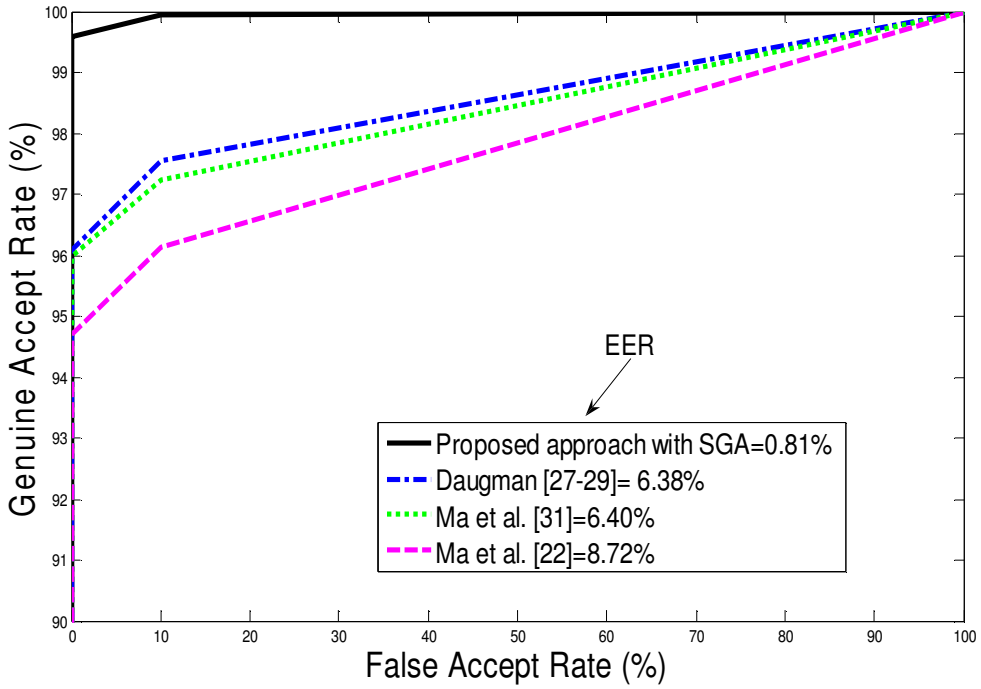

Fig. 6.25 Comparison of our method with existing iris recognition schemes on the combined dataset.

proposed GT scheme has been made with the GA-based approach, which was applied in the Chapter 4 (see Section 4.4). The ROC curves in Fig. 6.26 clearly demonstrate that the feature selection criteria using GT performs better than the GA-based approach. In Table 6.3, the proposed scheme exhibits the highest CRR for CASIA, ICE, WVU and UBIRIS datasets. For the combined dataset, we found a CRR of 97.39%, which reveals a top class performance with respect to the nonideal iris images under consideration. The EER of the proposed approach was 0.81% on the combined dataset, which was also encouraging. Moreover, the length of the feature vector was only 99, which was much less than the feature vector lengths reported in the other existing iris recognition algorithms, thereby, reducing the computational complexities without compromising the recognition rate.

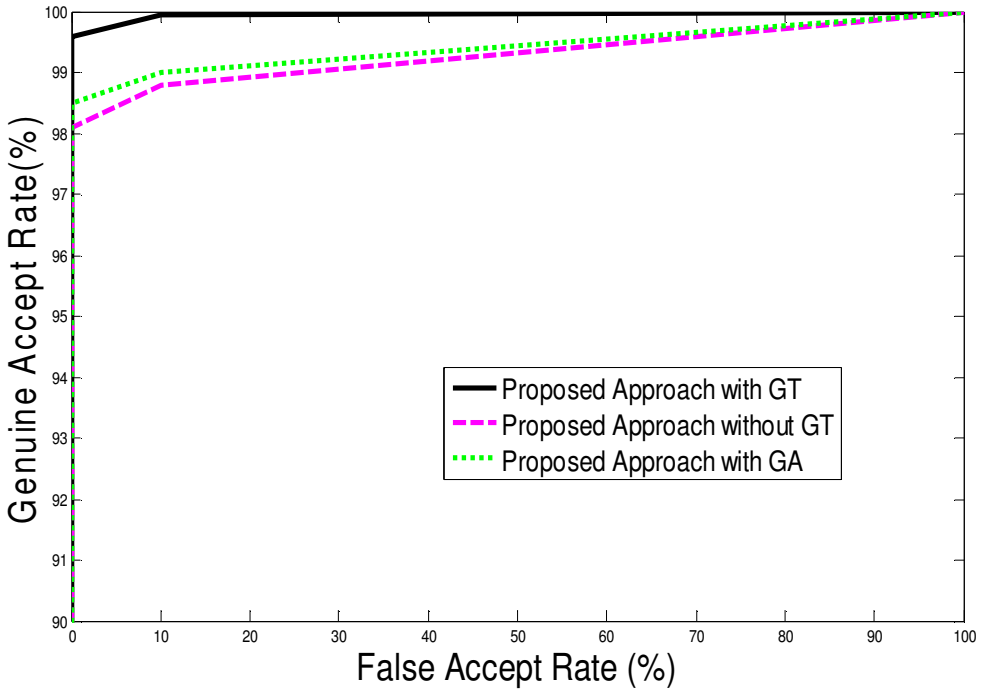

Fig. 6.26 ROC curves showing that GT-based feature selection with backward feature elimination performs better than the GA-based method on combined dataset.

Table 6.3: Comparison of CRR, EER and feature vector lengths.

(a) Comparison of CRR.

Algorithm	Correct Recognition Rate (CRR) (%)				
	ICE	CASIA	UBIRIS	WVU	Combined
Daugman [27-29]	98.13	95.70	97.28	83.14	93.43
Ma *et al.* [31]	95.79	95.54	95.45	78.33	92.56
Ma *et al.* [22]	95.64	94.90	95.78	77.24	91.23
Proposed SGA	**98.43**	**97.32**	**97.49**	**96.49**	**97.39**

(b) Comparison of EER.

Algorithm	Equal Error Rate (EER) (%)				
	ICE	CASIA	UBIRIS	WVU	Combined
Daugman [27-29]	0.49	1.80	0.96	8.45	6.38
Ma *et al.* [31]	1.72	2.07	1.21	10.50	6.40
Ma *et al.* [22]	1.80	2.62	1.13	11.43	8.72
Proposed SGA	**0.33**	**0.71**	**0.48**	**1.68**	**0.81**

(c) Comparison of feature vector lengths

Algorithm	Length of feature Vectors
Daugman [27-29]	2048 bits
Ma *et al.* [31]	160 elements
Ma *et al.* [22]	384 elements
Proposed SGA	**99 elements**

6.5 Conclusion

In this chapter, we have achieved two performance goals. First, the SGA addresses the problem of segmenting the iris region using a geometric shape prior with local and global iris image information. The proposed SGA localizes the iris regions from degraded eye. The localization scheme based on SGA avoids the over-segmentation and performs well against the blurred iris/sclera boundary. Second, the GT is used to find the subset of informative texture features, and our proposed scheme requires only 99 elements to store an iris feature template, which is much less than the amount required in most current iris recognition algorithms. We validated the proposed iris recognition scheme on the ICE 2005, the CASIA Version 3 Interval, the UBIRIS Version 1, the WVU Nonideal datasets, and also on the nonhomogeneous combined dataset with encouraging performances.

Chapter 7

Conclusions and Future Work

This chapter discusses the key contributions of our research work in Section 7.1, and suggests the ways of conducting future research in Section 7.2.

7.1 Research Findings and Conclusions

Iris recognition has been a hot research topic over the last decade due to the enhanced security requirements for sophisticated personal identification based on biometrics. The rich textural details and stability of the iris pattern make it a robust biometric modality to identify an individual accurately and reliably. Most current iris recognition algorithms exhibit high recognition accuracies in relatively cooperative environments. However, the processing and recognition of a degraded iris image still remains a challenging issue. In this thesis, we focus on the processing of nonideal iris images using active contours, GAs, the shape guided model, AASVMs and GT. In order to verify the claimed performance, the proposed methods are evaluated on several challenging iris datasets, namely, ICE 2005, WVU Nonideal, UBIRIS Version 1, CASIA Version 3 Interval, and non-homogeneous Combined. Furthermore, to show the effectiveness of the proposed algorithms, comparisons

are made with several state-of-the-art iris recognition methods. In this thesis, the proposed iris recognition method is divided into two phases: cooperative iris recognition, and noncooperative iris recognition. The proposed noncooperative iris recognition method is further divided into three approaches.

While most of the current iris recognition schemes utilize the complete iris information for recognition, in the first phase of our research, an efficient iris segmentation approach is presented, which utilizes only the pupillary information and is based on a morphological operation, the Hough transform and the Canny edge detection. The information extracted from the pupillary zone is less affected by the eyelids and eyelashes, and therefore, can lead to a higher segmentation accuracy. The GA-based feature selection method reduces the dimensionality of the extracted iris feature sequence without losing the matching accuracy. The employed asymmetrical SVMs perform well in a poorly balanced sample space and control different types of misclassification errors. We also provide experimental validation which exhibits an encouraging performance with respect to the accuracy for a relatively ideal imagery setup. Although the proposed iris recognition algorithm based on pupillary information, GAs and asymmetrical SVMs can be applied in a wide range of security-related applications, this approach may fail to demonstrate the expected level of performance in a noncooperative environment. Therefore, in the second phase, we move towards the processing and recognition of nonideal iris images that have been affected by different noise factors, to further improve the matching performance.

In the second phase of our research, we propose three different nonideal iris

recognition approaches: 1) active contour-based approaches, 2) game-theoretic approaches, and 3) shape guided method. In the first approach of the second phase, we achieve three performance goals: (a) LS methods are deployed for the exact localization of the iris/pupil regions from the degraded eye images. The active contours with the edge stopping function are applied to detect the inner boundary since the pupil is considered as the darkest part of the iris. The Mumford-Shah segmentation model with an energy minimization algorithm is employed to detect the outer boundary with the assumption that the iris/sclera region is separated by a weak boundary. One limitation of the applied LS method is that the curve evolution process has a higher time complexity. Thus, a segmentation scheme based on the VLS method, which uses a significantly larger time step to solve the evolution PDE, is used and thereby, the curve evolution process speeds up substantially. The intensity inhomogeneity is another source of noise factors, and results in inaccurate segmentation. The proposed RAC algorithm exhibits a higher performance on the challenging iris datasets where the images are affected by asymmetrical intensity levels in many cases. (b) To improve the feature selection performance, a GA-based hybrid algorithm has been developed, which incorporates four feature selection criteria, namely, the SVM-RFE, the k-NN, the T-statistics, and the entropy-based methods. The experimental results demonstrate that the proposed method selects feature subsets with a better classification accuracy and/or a smaller size when compared to each individual feature selection algorithm. (c) The proposed iris pattern classification scheme based on AASVMs involves less computational time in the testing phase than the traditional SVMs and controls different types of

misclassification losses.

Accurate segmentation is an essential task in iris recognition because the accuracy of the subsequent phases depends on the correct localization of the iris region. In the second approach, the proposed game-theoretic segmentation algorithm fuses the region-based and boundary-based methods and operates different probability spaces into a common information-sharing framework. This algorithm localizes the iris regions accurately from the degraded irises that have been affected by different nonideal factors. The proposed localization method based on GT avoids the over-segmentation and performs well against the smooth iris/sclera boundary. The proposed image enhancement technique increases the quality of the normalized iris image and reduces the effects of different noise factors.

In the final approach, we focus on improving the iris recognition performance by accurate iris detection and feature ranking. The SGA detects the iris regions from degraded eye images that have been affected by severe gaze deviations, diffusions, non-linear deformations, low image intensities, poor acquisition processes, eyelash occlusions and small openings of the eyes. This segmentation method, in particular, demonstrates a reasonable improvement in isolating the upper and lower eyelids. The proposed localization scheme also performs well against over-segmentation, shape variation and blurred iris/sclera boundary. The GT is deployed to rank the best informative texture features from the extracted feature set and most importantly, our proposed scheme requires a smaller number of elements to store an iris template than most of the current iris recognition methods.

7.2 Future Research

In this thesis, the proposed iris recognition approaches perform reasonably well. However, there are numerous issues that should be addressed and resolved. Future research could be conducted along the following directions to build a robust iris (biometrics) recognition system.

1. In this thesis, GT fuses the complementary strengths of the gradient and region-based methods to localize the iris boundary. However, a simple region-based method is used in the game-theoretic fusion. An improved iris segmentation scheme can possibly be developed if we integrate the RAC model with the VLS-based boundary finding method while using GT as a fusion scheme. We can also include the shape information along with the region and boundary data in an attempt to further improve the segmentation performance. Similarly, the accuracy of SGA can probably be increased by integrating the RAC model, which works well on the images with heterogeneous intensity levels, instead of applying the current region-based method used in the proposed SGA.
2. In order to increase the accuracy of the system, a more accurate and elaborate eyelash detection scheme can be employed.
3. Since the quality of the images affects the overall matching accuracy, an iris image quality assessment scheme can be deployed. While most of the current iris image quality assessment methods deal exclusively with the iris images that are captured in a Near Infra-Red (NIR) setup, an enhanced method can be deployed to assess the quality of iris images captured by using the Visible Wavelength

(VW) light imagery. In general, the VW imaging setup is used to acquire iris data at significantly larger distances and on moving subjects.

4. In this thesis, we only utilize the global or local features for recognition. However, the recognition performance can possibly be improved by fusing both the local and global features while using game theory and SVMs as fusion strategies.
5. Although, in this thesis, we deal with the iris images that have been captured in both the NIR and VW imagery setups, a more sophisticated iris segmentation scheme can be developed to process the VW iris images. In this respect, the whitish sclera region can be utilized for segmentation instead of the iris information.
6. In many real-world applications, the unimodal biometric system, such as iris recognition, often faces significant limitations due to noisy sensor data, restricted degrees of freedom, intra-class variability, unacceptable error rates, and other factors. Multimodal biometric systems seek to alleviate some of these problems by providing multiple pieces of evidence for the same identity. Multibiometric systems can significantly improve the recognition performance in addition to improving population coverage, providing antispoofing measures, increasing the degrees of freedom, and reducing the failure to enroll rate. Therefore, an effective fusion scheme that combines information presented by multiple domain experts, based on the score-level fusion method, can be used to address some of the limitations of the existing unimodal authentication systems.

To be more specific, the combination of iris, fingerprint, and palmprint features of an individual can be utilized for accurate and reliable identification purposes.

7. We see that the most computation intensive part involves the segmentation with Hough transform technique and active contour-based curve evolution approaches. Since we have implemented the system in Matlab, which is an interpreted language, a development in speed can be achieved if the most time consuming parts are implemented in C++ programming language environment.
8. The iris liveness detection is a major issue in the area of iris recognition, otherwise a high resolution photograph can be presented to an iris recognition camera which may result in an unauthorized match. Fake iris detection is another important factor which should be handled carefully. Contact lenses are vastly used nowadays which can change the color of an individual's iris. This may create a problem to any iris recognition system, since a fake iris pattern is printed on the surface of the lens. The system may falsely reject an enrolled user. Contrarily, the system may falsely accept a subject, if the fake iris pattern of that subject has been enrolled in the database. Therefore, further research is required to avoid these errors.

List of Accepted and Published Articles Based on Doctoral Thesis

Published and Accepted Journal Articles:

1. K. Roy, P. Bhattacharya, and C. Y. Suen, “Iris segmentation using game theory,” *Signal, Image and Video Process.*, Springer-Verlag, In press, 2010. doi 10.1007/s11760-010-0193-5.

2. K. Roy, P. Bhattacharya, and C. Y. Suen, “Iris segmentation using variational level set method,” *Optics and Lasers in Engg.*, Elsevier, In press, 2010. doi:10.1016/j.optlaseng.2010.09.011.

3. K. Roy, P. Bhattacharya, and C. Y. Suen, “Iris recognition using shape guided approach and game theory,” *Pattern Anal. and Applications*, Springer-Verlag, Accepted for Publication, 2010.

4. K. Roy, P. Bhattacharya, and C. Y. Suen, “Towards nonideal iris recognition based on level set method, genetic algorithms and adaptive asymmetrical SVMs,” *Engg. Applications of Artificial Intell.,* Elsevier, In Press, 2010. doi:10.1016/j.engappai.2010.06.014.

5. K. Roy and P. Bhattacharya, "Improvement of iris recognition performance using region-based active contours, genetic algorithms and SVMs," *Int. J. of Pattern Recog. and Artificial Intell.*, World Scientific Publishing Company, vol. 24, no. 8, pp. 1209-1236, 2010.

6. K. Roy and P. Bhattacharya, “Iris recognition using genetic algorithms and asymmetrical SVMs,” *Machine Graphics & Vision J.*, Published by Institute of Computer Science, Polish Academy of Sciences, vol. 19, no. 1, pp. 1-30, 2009.

7. K. Roy and P. Bhattacharya, “Optimal feature subset selection and classification for iris recognition,” *EURASIP J. on Image and Video Process.*, vol. 2008, Article ID 743103, 20 pages, 2008. doi:10.1155/2008/743103.

Book Chapters:

8. K. Roy and P. Bhattacharya, "Iris recognition based on genetic algorithms and multi-class Gaussian mixture model," *Int. Workshop on Combinatorial Image Anal.*, Buffalo, New York, USA, Apr. 2008. Appeared as a Chapter of the Book Titled "Image Analysis - From Theory to Applications" (ed. R. P. Barneva and V. E. Brimkov), pp. 103-112. Publisher: Research Publishing, 2008. ISBN978-981-08-0228-8.

9. K. Roy and P. Bhattacharya, "Optimal feature selection and classification for iris recognition," *Int. Workshop on Combinatorial Image Anal.*, Buffalo, New York, USA, Apr. 2008. Appeared as a Chapter of the Book Titled "Image Analysis - From Theory to Applications" (ed. R. P. Barneva and V. E. Brimkov), pp. 113-124. Publisher: Research Publishing, 2008. ISBN 978-981-08-0228-8.

Conferences and Workshops Articles:

10. K. Roy, P. Bhattacharya, and C. Y. Suen, “Recognition of unideal iris images using region-based active contour model and game theory,” *Proc. in IEEE Int. Conf. on Image Process.*, pp. 1705-1708., Hong Kong, 2010.

11. K. Roy, P. Bhattacharya, and C. Y. Suen, "Segmentation of unideal iris images using game theory," *Proc. in IAPR IEEE Int. Conf. on Pattern Recog.*, pp. 2844-2847, Istanbul, Turkey, Aug. 2010.
12. K. Roy, P. Bhattacharya, and C. Y. Suen, "Unideal iris segmentation using region-based active contour model," *Proc. in Int. Conf. on Image Anal. and Recog*., Springer Lecture Notes in Computer Science, vol. 6112, pp. 256-265, Povoa de Varzim, Portugal, Jun. 2010,.
13. K. Roy and P. Bhattacharya, "Iris recognition in nonideal situations," *Proc. in Info. Security Conf.*, Springer Lecture Notes in Computer Science, vol. 5735, pp. 143-150, Pisa, Italy, Sep. 2009.
14. K. Roy and P. Bhattacharya, "Variational level set method and game theory applied for nonideal iris recognition," *Proc. in IEEE Int. Conf. on Image Process.*, pp. 2721 – 2724, Egypt, Nov. 2009.
15. K. Roy and P. Bhattacharya, "Nonideal iris recognition using level set approach and coalitional game theory," *Proc. in Int. Conf. on Comp. Vis. Syst.*, Springer Lecture Notes in Computer Science, vol. 5815, pp. 394-402. Belgium, Oct. 2009.
16. K. Roy and P. Bhattacharya, "Level set approaches and adaptive asymmetrical SVMs applied for nonideal iris recognition," *Proc. in Int. Conf. on Image Anal. and Recog*., Springer Lecture Notes in Computer Science, vol. 5627, pp. 418–428, Halifax, Canada, Jul. 2009.
17. A. Mondal, K. Roy and P. Bhattacharya, "Home appliance control using biohashing," *Proc. in IEEE Int. Conf. on Internet Tech. and Secured Trans.*, pp. 1-7, London, UK, Nov., 2009.

18. A. Mondal, K. Roy and P. Bhattacharya, "Secure and simplified access to home appliance using iris recognition," *Proc. in IEEE Workshop on Computational Intell. in Biometrics: Theory, Algorithms, and Applications*, pp 22-29, Nashville, Tennessee, USA, Mar. 2009.
19. K. Roy and P. Bhattacharya, "Adaptive asymmetrical SVM and genetic algorithms based iris recognition," *Proc. in IEEE IAPR Int. Conf. on Pattern Recog.*, pp. 1-4, Tampa, Florida, USA, Dec 2008.
20. K. Roy and P. Bhattacharya, "Improving feature subset selection using genetic algorithms for iris recognitionn," *Proc. in IAPR Int. Workshop on Artificial Neural Networks in Pattern Recog.*, Springer Lecture Notes in Artificial Intell., vol. 5064, pp. 292-304, Pierre & Marie Curie University, Paris, France, Jul. 2008.
21. K. Roy and P. Bhattacharya, "Optimal feature subset selection using genetic algorithms for iris recognition," *Proc. in Int. Conf. on Image Anal. and Recog.*, Springer Lecture Notes in Computer Science, vol. 5112, pp.894-904, Povoa de Varzim, Portugal, Jun. 2008.
22. K. Roy and P. Bhattacharya, "Multi-class SVM based iris recognition," *Proc. in IEEE Int. Conf. on Comp. and Info. Tech.*, pp. 1-6, Dhaka, Bangladesh, Dec. 2007.
23. K. Roy, D. Hudgin and P. Bhattacharya, "Iris recognition: a java-based implementation," *Proc. in IEEE Int. Conf. on Comp. and Info. Tech.*, pp. 1-6, Dhaka, Bangladesh, Dec. 2007.
24. K. Roy and P. Bhattacharya, "Application of multi-objective genetic algorithm and asymmetrical SVM to improve the reliability of an iris recognition system," *Proc. in*

IEEE Conf. on Syst., Man, and Cybernetics, vol. 4, pp. 1952-1957, Montreal, Canada, Oct. 2007.

25. K. Roy and P. Bhattacharya, "Iris recognition based on zigzag collarette region and asymmetrical support vector machines," *Proc. in Int. Conf. on Image Anal. and Recog.*, Springer Lecture Notes in Computer Science, vol. 4633, pp. 854-865, Montreal, Canada, Aug. 2007.
26. K. Roy and P. Bhattacharya, "Collarette area localization and asymmetrical support vector machines for efficient iris recognition," *Proc. in IEEE Int. Conf. on Image Anal. and Process.*, pp. 3-8, Modena, Italy, Sep. 2007.

Bibliography

[1] H. Proença and L. A. Alexandre, "Toward non-cooperative iris recognition: a classification approach using multiple signatures," *IEEE Trans. Pattern Anal. Machine Intell.*, vol. 29, no. 4, pp. 607-612, Apr. 2007.

[2] Z. Sun and T. Tan, "Ordinal measures for iris recognition," *IEEE Trans. Pattern Anal. Machine Intell.*, vol. 31, no. 12, pp. 2211 - 2226, Dec. 2009.

[3] K. Miyazawa, K. Ito, T. Aoki, K. Kobayashi, and H. Nakajima, "An effective approach for iris recognition using phase-based image matching," *IEEE Trans. Pattern Anal. Machine Intell.*, vol. 30, no. 10, pp. 1741-1756, Oct. 2008.

[4] R. Bolle, J. H. Connell, S. Pankanti, N. K. Ratha, and A. W. Senior, *Guide to biometrics,* 1st ed., New York, Springer-Verlag, 2004.

[5] A.K. Jain, A. Ross, and S. Prabhakar, "An introduction to biometric recognition," *IEEE Trans. Circuits and Syst. for Video Tech.*, vol. 14, no.1, pp. 4–20, Jan. 2004.

[6] S. Prabhakar, S. Pankanti, and A.K. Jain, "Biometric recognition: security and privacy concerns," *Security & Privacy,* IEEE Comp. Society, vol. 1, no. 2, pp.33-42, Mar. 2003.

[7] P. Ding, Z. Chen, Y. Liu, and B. Xu, "Asymmetrical support vector machines and application in speech processing," *in Proc. IEEE Int. Conf. on Acousts.,*

Speech, and Signal Process., vol. 1, pp. I73-I76, Minneapolis, MN, USA, Apr. 1993.

[8] Michael Wasilewski, "Active contours using level sets for medical image segmentation," *Medical Imaging: Segmentation*.

[9] T. Chan and L. Vese, "Active contours without edges," *IEEE Trans. Image Process.,* vol. 10, no. 2, pp. 266-277, Feb. 2001.

[10] D. Mumford and J. Shah, "Optimal approximation by piecewise smooth functions and associated variational problems," *Commu. Pure Appl. Math*, vol. 42, no. 5, pp. 577-685, Jul. 1989.

[11] C. Li, C. Xu, C. Gui, and M. D. Fox, "Level set evolution without re-initialization: a new variational formulation," *Proc. in IEEE Int. Conf. on Comp. Vis. and Pattern Recog.,* vol. 1, pp. 430-436, San Diego, CA, USA, Jun. 2005.

[12] C. Li, C. Y. Kao, J. C. Gore, and Z. Ding, "Implicit active contours driven by local binary fitting energy," *Proc. in IEEE Int. Conf. on Comp. Vis. and Pattern Recog.*, pp. 1-7, Minneapolis, USA, Jun. 2007.

[13] Q. Li, L. Jiao, and Y. Hao, "Adaptive simplification of solution for support vector machine," *Pattern Recog,* vol. 40, no. 3, pp. 972-980, Mar. 2007.

[14] A. Chakraborty and J. S. Duncan, "Game-theoretic integration for image segmentation," *IEEE Trans. Pattern Anal. and Machine Intell.*, vol. 21, no. 1, pp. 12-30, Jan. 1999.

[15] A. Chakraborty, L. H. Staib, and J. S. Duncan, "Deformable boundary finding in medical images by integrating gradient and region information," *IEEE Trans. Pattern Anal. Machine Intell.*, vol. 15, no. 6, pp. 859-870, Dec. 1996.

[16] X. Bresson, P. Vandergheynst, and J. P. Thiran, "Variational model for object segmentation using boundary information and shape prior driven by the Mumford-Shah functional," *Int. J. Comp. Vis.*, vol. 68, no. 2, pp. 145 – 162, 2006.

[17] S. Cohen, D. Dror, and E. Ruppin, "Feature selection via coalitional game theory," *Neural Comput.*, MIT Press, vol. 19, no. 7, pp. 1939-1961, Jul. 2007.

[18] A. K. Jain, P. Flynn, A. A. Ross (Eds.), *Handbook of biometrics*, New York, Springer-Verlag, 2008.

[19] S. Makthal, "Analysis and synthesis of iris images," *Master's Dissertation*, Dept. of Electrical Engineering, West Virginia University, USA, 2005.

[20] K. Roy, "Iris recognition using support vector machines," *Master's Dissertation*, Dept. of Computer Science and Software Engineering, Concordia University, Canada, Aug. 2006.

[21] M. Tistarelli, S. Li, and R. Chellappa (Eds.), *Handbook of remote biometrics: for surveillance and security*, London, Springer-Verlag, 2009.

[22] L. Ma, T. Tan, Y. Wang, and D. Zhang, "Personal identification based on iris texture analysis," *IEEE Trans. on Pattern Anal. Machine Intell.*, vol. 25, no. 12, pp. 1519-1533, Dec. 2003.

[23] UTHSCSA Teacher Enrichment Initiatives. Positively aging® & M.O.R.E. curricular programs, anatomy of the human eye, 2001. Available Online: http://teachhealthk-12.uthscsa.edu/curriculum/vision-hearing/vision01-anatomy.htm.

[24] H. P. M. C. Proenca, “Towards non-cooperative biometric iris recognition,” *Ph.D. Dissertation*, Dept. of Computer Science, University of Beira Interior, Portugal, Oct. 2006.

[25] John Daugman’s homepage. Available Online: http://www.cl.cam.ac.uk/~jgd1000/.

[26] W. Kong and D. Zhang, “Accurate iris segmentation based on novel reflection and eyelash detection model,” *Proc. in Int. IEEE Sympos. on Intelligent Multimedia, Video and Speech Process.*, pp. 263–266, Hong Kong, 2001.

[27] J. Daugman, “High confidence visual recognition of persons by a test of statistical independence,” *IEEE Trans. on Pattern Anal. Machine Intell.,* vol. 15, no. 11, pp. 1148-1161, Nov. 1993.

[28] J. Daugman, “How iris recognition works,” *IEEE Trans. Circuits and Syst. for Video Tech.*, vol. 14, no. 1, pp. 21–30, Jan. 2004.

[29] J. Daugman, "The importance of being random: statistical principles of iris recognition," *Pattern Recog.*, vol. 36, no. 2, pp 279-291, Feb. 2003.

[30] J. Daugman, “Statistical richness of visual phase information: update on recognizing persons by iris patterns,” *Int. J. Comp. Vis.*, vol. 45, no. 1, pp. 25-38, Oct. 2001.

[31] L. Ma, T. Tan, Y. Wang, and D. Zhang, “Efficient iris recognition by characterizing key local variations,” *IEEE Trans. Image Process.*, vol. 13, no. 6, pp. 739-750, Jun. 2004.

[32] W. Boles and B. Boashash, "A human identification technique using images of the iris and wavelet transform," *IEEE Trans. Signal Process.*, vol. 46, no. 4, pp. 1185-1188, Apr. 1998.

[33] R. Wildes, "Iris recognition: an emerging biometric technology," *Proc. in IEEE*, vol. 85, no. 9, pp. 1348-1363, Sep. 1997.

[34] L. Ma, Y. Wang, and T. Tan, "Iris recognition based on multichannel Gabor filtering," *Proc. in Asian Conf. on Comp. Vis.*, vol. 1, pp. 279-283, Melbourne, Australia, Jan. 2002.

[35] L. Ma, Y. Wang, and T. Tan, "Iris recognition using circular symmetric filters," *Proc. in IEEE Int. Conf. on Pattern Recog.*, vol. 2, pp. 414-417, Quebec City, Canada, Aug. 2002.

[36] K. W. Bowyer, K. Hollingsworth, and P. J. Flynn, "Image understanding for iris biometrics: a survey," *Comp. Vis. Image Understanding*, vol. 110, no. 2, pp. 281-307, May 2008.

[37] D M. Monro, S. Rakshit, and D. Zhang, "DCT-based iris recognition," *IEEE Trans. on Pattern Anal. Machine Intell.,* vol. 29, no. 4, pp. 586 - 595, Apr. 2007.

[38] N. Sudha, N.B. Puhan, H. Xia, and X. Jiang, "Iris recognition on edge maps," *IET Comp. Vis.*, vol. 3, no. 1, pp. 1-7, Mar. 2009.

[39] C. Sanchez-Avila and R. Sanchez-Reillo, "Two different approaches for iris recognition using Gabor filters and multiscale zero-crossing representation," *Pattern recog.,* vol. 38, no. 2, pp. 231-240, Feb. 2005.

[40] X. Feng, X. Ding, Y. WU, and P. Wang, "Classifier combination and its application in iris recognition," *Int. J. of Pattern Recog. and Artificial Intell.*, vol. 22, no. 3, pp. 617-638, 2008.

[41] X. He and P. Shi, "An efficient iris segmentation method for recognition," *Proc. in Int. Conf. on Adv. Pattern Recog*, Springer Lecture Notes in Computer Science, vol. 3687, pp. 120-126, Bath, UK, Aug. 2005.

[42] H. Sung, J. Lim, J. Park, and Y. Lee, "Iris recognition using collarette boundary localization," *Proc. in IEEE Int. Conf. on Pattern Recog*., vol. 4, pp. 857-860, Cambridge, UK, Aug. 2004.

[43] M. B. Pereira and A. C. P. Veiga, "Application of genetic algorithms to improve the reliability of an iris recognition system," *Proc. in IEEE Workshop on Machine Learning for Signal Process.*, pp. 159-164, Nov. 2005.

[44] A. Azizi and H. R. Pourreza, "Efficient iris recognition through improvement of feature extraction and subset selection," *Int. J. Comp. Vis. and Pattern Recog.*, vol. 2, no. 1, 10 pages, Jun. 2009.

[45] K. Roy and P. Bhattacharya, "Optimal feature subset selection and classification for iris Recognition," *EURASIP J. Image and Video Process.*, vol. 2008, Article ID 743103, 20 pages, doi:10.1155/2008/743103.

[46] K. Roy and P. Bhattacharya, "Iris recognition using genetic algorithms and asymmetrical SVMs," *Machine Graphics & Vis.*, vol. 19, no. 1, pp. 33-62, 2010.

[47] S. Bandyopadhyay, S. K. Pal, and B. Aruna, "Multiobjective GAs, quantitative indices, and pattern classification," *IEEE Trans. Syst, Man and Cyber. B*, vol. 34, no. 5, pp. 2088-2099, Oct. 2004.

[48] K. Deb, *Multi-objective optimization using evolutionary algorithms*, J. Wiley & Sons, West Sussex, UK, 2004.

[49] V. N. Vapnik, *Statistical learning theory*, J. Wiley & Sons, New York, USA, 1998.

[50] X. Wang, B. S. Wong, and C. Tan, "Recognition of welding defects in radiographic images by using support vector machine classifier," *Research J. of Applied Sciences, Engg. and Tech.*, vol. 2, no. 3, pp. 295-301, May 2010.

[51] X. Liu, K. W. Bowyer, and P. J. Flynn, "Experiments with an improved iris segmentation algorithm," *Proc. in IEEE Workshop on Automatic Identification Advanced Tech.*, pp. 118–123, Buffalo, NY, USA, Oct. 2005.

[52] X. Liu, K. W. Bowyer, and P. J. Flynn, "Experimental evaluation of iris recognition," *Proc. in IEEE Int. Conf. on Comp. Vis. and Pattern Recog.* , vol. 3, pp. 158–165, San Diego, CA, USA, Jun. 2005.

[53] L. Masek, "Biometric identification systems based on iris patterns," *B.Sc. Dissertation*, School of Computer Science and Software Engineering, University of Western Australia, Australia, 2003.

[54] H. Gu, Z. Gao, and F. Wu, "Selection of optimal features for iris recognition," *Proc. in Int. Sympos. on Advances in Neural Net.*, Springer Lecture Notes in Computer Science, vol. 3497, pp. 81-86, Chongqing, China, May 2005.

[55] B. Son, H. Won, G. Kee, and Y. Lee, "Discriminant iris feature and support vector machines for iris recognition," *Proc. in IEEE Int. Conf. on Image Process*., vol. 2, pp. 865-868, Singapore, Oct. 2004.

[56] K. Roy and P. Bhattacharya, "Iris recognition with support vector machine," *Proc. in Int. Conf. on Advances in Biometrics*, Springer Lecture Notes in Computer Science, vol. 3882, pp. 486-492, Hong Kong, China, Jan. 2006.

[57] Y. Chen, S. C. Dass, and A. K. Jain, "Localized iris image quality using 2D wavelets," *Proc. in Int. Conf. on Advances in Biometrics*, Springer Lecture Notes in Computer Science, vol. 3832, pp. 373-381, Hong Kong, China, Jan. 2006.

[58] H. Tan and Y. Zhang, "Detecting eye blink states by tracking iris and eyelids," *Pattern Recog. Lett.*, vol. 27, no. 6, pp. 667-675, 2006.

[59] T. Tangsukson and J. P. Havlicek, "AM-FM image segmentation," *Proc. in IEEE Int. Conf. on Image Process.*, vol. 2, pp. 104–107, Vancouver, BC, Canada, Sep. 2000.

[60] J. P. Havlicek, D. S. Harding, and A.C. Bovik, "The multi-component AM-FM image representation," *IEEE Trans. Image Process.*, vol. 5, no. 6, pp. 1094-1100, Jun. 1996.

[61] L. S. Oliveira, R. Sabourin, F. Bortolozzi, and C.Y. Suen, "Feature selection using multi-objective genetic algorithms for handwritten digit recognition," *Proc. in IEEE Int. Conf. on Pattern Recog.*, vol. 1, pp. 568-571, Quebec City, Canada, Aug. 2002.

[62] D. E. Goldberg, *Genetic algorithms in search, optimization and machine learning*, Addison-Wesley Reading, MA, 1989.

[63] Z. Sun, Y. Wang, T. Tan, and J. Cui, “Improving iris recognition accuracy via cascaded classifiers,” *IEEE Trans. Syst, Man and Cyber. C*, vol. 35, no. 3, pp. 435-441, Aug. 2005.

[64] S. Y. Kung, M.W. Mak, and S.H. Lin, *Biometric authentication: a machine learning approach*, Prentice Hall, USA, 2005.

[65] J. Dong, A. Krzyzak, and C. Y. Suen, “An improved handwritten Chinese character recognition system using support vector machines,” *Pattern Recog. Lett.*, vol. 26, no. 12, pp. 1849-1856, Sep, 2005.

[66] R.O. Duda, P.E. Hart, and D.G. Stork, *Pattern classification*, 2nd. Ed., John Wiley & Sons, NY, USA, 2001.

[67] M. Vatsa, R. Singh, and A. Noore, “Improving iris recognition performance using segmentation, quality enhancement, match score fusion, and indexing,” *IEEE Trans. Syst. Man and Cyber. B*, vol. 38, no. 4, pp. 1021-1035, Aug. 2008.

[68] K. Roy, P. Bhattacharya, and C. Y. Suen, “Towards nonideal iris recognition based on level set method, genetic algorithms and adaptive asymmetrical SVMs,” *Engg. Applications of Artificial Intell.,* 2010, In Press, DOI:10.1016/j.engappai.2010.06.014.

[69] K. Roy, P. Bhattacharya, and C. Y. Suen, “Iris segmentation using variational level set method,” *Optics and Lasers in Engg.,* 2010 In Press, DOI:10.1016/j.optlaseng.2010.09.011.

[70] K. Roy and P. Bhattacharya, "Improvement of iris recognition performance using region-based active contour model," *Int. J. Pattern Recog. and Artificial Intell.*, vol. 24, no. 8, pp. 1209-1236, 2010.

[71] R. P. Wildes, J. C. Asmuth, G. L. Green, S. C. Hsu, R. J. Kolczynski, J. R. Matey, and S. E. McBride, "A machine-vision system for iris recognition," *Machine Vis. Applications*, vol. 9, no. 1, pp.1-8, 1996.

[72] S. Rakshit and D. M. Monro, "An evaluation of image sampling and compression for human iris recognition," *IEEE Trans. Info. Forensics and Security*, vol. 2, no. 3, pp. 605-612, Sep. 2007.

[73] J. Zuo, N. A. Schmid, and X. Chen, "On generation and analysis of synthetic iris images," *IEEE Trans. on Info. Forensics and Security,* vol. 2, no. 1, pp. 77-90, Mar. 2007.

[74] S. A. C. Schuckers, N. A. Schmid, A. Abhyankar, V. Dorairaj, C. K. Boyce, and L. A. Hornak, "On techniques for angle compensation in nonideal iris recognition," *IEEE Trans. Syst, Man and Cyber. B*, vol. 37, no. 5, pp. 1176-1190, Oct. 2007.

[75] J. G. Daugman, "New methods in iris recognition," *IEEE Trans. Syst. Man and Cyber. B*, vol. 37, no. 5, pp. 1167-1175, Oct. 2007.

[76] H. Proença, "Iris recognition: on the segmentation of degraded images acquired in the visible wavelength," *IEEE Trans. on Pattern Anal. Machine Intell.*, vol. 32, no. 8, pp. 1502-1516, Aug. 2010.

[77] W. Zhang, B. Li, X. Ye, Z. Zhuang, and K. Q. Wang, "A robust iris localization algorithm via radial symmetry for nonideal capturing condition," *Int. J. Pattern Recog. and Artificial Intell.*, vol. 23, no. 1, pp. 45-57, 2009.

[78] S. Pundlik, D. Woodard, and S. Birchfield, "Iris segmentation in non-ideal images using graph cuts," *Image and Vis. Comput.*, vol. 28, no. 12, pp. 1671-1681, Dec. 2010.

[79] A. Abhyankar and S. Schuckers, "Iris quality assessment and bi-orthogonal wavelet based encoding for recognition," *Pattern Recog.*, vol. 42, no. 9, pp. 1878–1894, Sep. 2009.

[80] M. A. Luengo-Oroz, E. Faure, and J. Angulo, "Robust iris segmentation on uncalibrated noisy images using mathematical morphology," *Image and Vis. Comput.*, vol. 28, no. 2, pp. 278-284, Feb. 2010.

[81] E. Al-Daoud, "A new iris localization method based on the competitive chords," *Signal, Image and Video Process.*, pp. 1-9, Sep. 2010. DOI: 10.1007/s11760-010-0183-7.

[82] D. S. Jeong, J. W. Hwang, B. J. Kang, K. R. Park, C. S. Won, D. K. Park, and J. Kim, "A new iris segmentation method for non-ideal iris images," *Image and Vis. Comput.*, vol. 28, no. 2, pp. 254-260, Feb. 2010.

[83] H. Proença and L. A. Alexandre, "Iris recognition: analysis of the error rates regarding the accuracy of the segmentation stage," *Image and Vis. Comput.*, vol. 28, no. 1, pp. 202-206, Jan. 2010.

[84] J. Koh, V. Govindaraju, and V. Chaudhary, "A robust iris localization method using an active contour model and Hough transform," *Proc. in IEEE Int. Conf. on Pattern Recog.*, pp. 2852-2856, Istanbul, Turkey, Aug. 2010.

[85] S. Shah and A. Ross, "Iris segmentation using geodesic active contours," *IEEE Trans. Info. Forensics and Security*, vol. 4, no. 4, pp. 824-836, Dec. 2009.

[86] A. Ross and S. Shah, "Segmenting non-ideal irises using geodesic active contours," *Proc. in Biometric Consortium Conf.*, *Biometrics Sympos.,* pp. 1-6, Baltimore, MD, USA, Sep. 2006.

[87] K. R. Park, H. A. Park, B. J. Kang, E. C. Lee, and D. S. Jeong, "A study on iris localization and recognition on mobile phones," *EURASIP J. Advances in Signal Process.*, vol. 2008, Article ID 281943, 12 pages doi:10.1155/2008/281943.

[88] A. Poursaberi and B. N. Araabi, "Iris recognition for partially occluded images: methodology and sensitivity analysis," *EURASIP J. Advances in Signal Process.*, vol. 2007, Article ID 36751, 12 pages doi:10.1155/2007/36751.

[89] B. J. Kang and K. R. Park, "A robust eyelash detection based on iris focus assessment," *Pattern Recog. Lett.*, vol. 28, no. 13, pp. 1630-1639, Oct. 2007.

[90] Y. K. Jang, B. J. Kang, and K. R. Park, "A study on eyelid localization considering image focus for iris recognition," *Pattern Recog. Lett.*, vol. 29, no. 11, pp. 1698-1704, Aug. 2008.

[91] E. Sung, X. Chen, J. Zhu, and J. Yang, "Towards non-cooperative iris recognition systems," *Proc. in IEEE Int. Conf. on Control, Automation, Robotics and Vis.*, vol. 2, pp. 990-995, Singapore, Dec. 2002.

[92] X. Li, "Modeling intra-class variation for nonideal iris recognition," *Proc. in Int. Conf. on Advances in Biometrics*, Springer Lecture Notes in Computer Science, vol. 3882, pp. 419-427, Hong Kong, China, Jan. 2006.

[93] X. Ming, T. Xu, and Z. Wang, "Using multi-matching system based on a simplified deformable model of the human iris for iris recognition," *Proc. in*

Int. Conf. on Biometric Authentication, Springer Lecture Notes in Computer Science, vol. 3072, pp. 434-441, Hong Kong, China, Jul. 2004.

[94] N. Barzegar and M. S. Moin, "A new approach for iris localization in iris recognition systems," *Proc. in IEEE/ACS Int. Conf. on Comp. Syst. and Applications*, pp. 516-523, Doha, Qatar, Mar. 2008.

[95] P. Li and X. Liu, "An incremental method for accurate iris segmentation," *Proc. in IEEE Int. Conf. on Pattern Recog*., pp. 1-4, Tampa, Florida, USA, Dec. 2008.

[96] A. A. Jarjes, W. Kuanquan, and G. J. Mohammed, "Iris localization: detecting accurate pupil contour and localizing limbus boundary," *Proc. of IEEE Int. Asia Conf. on Informatics in Control, Automation and Robotics,* pp. 349-352, Wuhan, China, Mar. 2010.

[97] T. H. Min and R. H. Park, "Comparison of eyelid and eyelash detection algorithms for performance improvement of iris recognition," *Proc. in IEEE Int. Conf. on Image Process.,* pp. 257-260, San Diego, California, U.S.A., Oct. 2008.

[98] T. H. Min and R. H. Park, "Eyelid and eyelash detection method in the normalized iris image using the parabolic Hough model and Otsu's thresholding method," *Pattern Recogn. Lett.*, vol. 30, no. 12, pp. 1138-1143, Sep. 2009.

[99] R. Youmaran, L. P. Xie, and A. Adler, "Improved identification of iris and eyelash features," *Proc. in Biennial Sympos. on Commu.*, pp. 387-390, Kingston, Ontario, Canada, Jun. 2008.

[100] N. Tajbakhsh, K. Misaghian, and N. M. Bandari, "A Region-based iris feature extraction method based on 2D-wavelet transform," *Proc. in joint COST 2101 and 2102 int. conf. on Biometric ID management and multimodal commu.*, Springer Lecture Notes in Computer Science, vol. 5707, pp. 301-307, Madrid, Spain, Sep. 2009.

[101] A. Abhyankar and S. Schuckers, "A novel biorthogonal wavelet network system for off-angle iris recognition," *Pattern Recog.*, vol. 43, no. 3, pp. 987-1007, Mar. 2010.

[102] A. Abhyankar, L. Hornak, and S. Schuckers, "Off-angle iris recognition using bi-orthogonal wavelet network system," *Proc. in IEEE Workshop on Automatic Identification Advanced Tech.*, pp. 239-244, Buffalo, NY, USA, Oct. 2005.

[103] V. Dorairaj, N. A. Schmid, and G. Fahmy, "Performance evaluation of non-ideal iris based recognition system implementing global ICA encoding," *Proc. in IEEE Int. Conf. on Image Process.*, pp. 285-288, Genoa, Italy, Sep. 2005.

[104] M. Nabti and A. Bouridane, "An improved iris recognition system using feature extraction based on wavelet maxima moment invariants," *Proc. of Int. Conf. on Advances in Biometrics*, Springer Lecture Notes in Computer Science, vol. 4642, pp. 988-996, Seoul, Korea, Aug. 2007.

[105] J. Zuo and N. A. Schmid, "On a local ordinal binary extension to Gabor wavelet-based encoding for improved iris recognition," *Biometrics Sympos.*, pp. 1-6, Baltimore, MD, USA, Sep. 2007.

[106] P. Yao, J. Li, X. Ye, Z. Zhuang, and B. Li , "Iris recognition algorithm using modified log-Gabor filters," *Proc. in IEEE Int. Conf. on Pattern Recog.*, vol. 4, pp. 461-464, Hong Kong, China, Aug. 2006.

[107] D. Cai, Q. Tan, Y. Yan, G. Jin, and Q. He, "Using optical wavelet packet transform to improve the performance of an optoelectronic iris recognition system," *Proc. in SPIE Int. Society for Optical Engg.*, *Info. Optics and Photonics Tech.,* vol. 5642, pp. 497-506, 2005.

[108] W. S. Chen, C. A. Chuan, S. W. Shih, and S. H. Chang, "Iris recognition using 2D-LDA+2D-PCA," *Proc. in IEEE Int. Conf. on Acoustics, Speech and Signal Process.,* pp. 869–872, Taipei, Taiwan, Apr. 2009.

[109] M. Han, W. Sun, and M. Li, "Iris recognition based on a novel normalization method and contourlet transform," *Proc. in IEEE Int. Congress on Image and Signal Process.,* pp. 1-3, Tianjin, China, Oct. 2009.

[110] Y. Zhou and A. Kumar, "Personal identification from iris images using localized Radon transform," *Proc. in IEEE Int. Conf. on Pattern Recog.*, pp. 2840-2843, Istanbul, Turkey, Aug. 2010.

[111] B.V.K. Vijaya Kumar, C. Xie, and J. Thornton, "Iris verification using correlation filters," *Proc. in Int. Conf. on Audio- and Video-Based Biometric Person Authentication,* Springer Lecture Notes in Computer Science, vol. 2688, Guildford, UK, pp. 697-705, 2003.

[112] V. Velisavljevic, "Low-complexity iris coding and recognition based on directionlets," *IEEE Trans. Info. Forensics and Security*, vol. 4, no. 3, pp. 410-417, Sep. 2009.

[113] H. A. Park and K. R. Park, "Iris recognition based on score level fusion by using SVM," *Pattern Recog. Lett.*, vol. 28, no. 15, pp. 2019-2028, Nov. 2007.

[114] K. Hollingsworth , T. Peters, K. W. Bowyer, and P. J. Flynn, "Iris recognition using signal-level fusion of frames from video," *IEEE Trans. Info. Forensics and Security*, vol. 4, no. 4, pp. 837-848, Dec. 2009.

[115] N. Tajbakhsh, B. N. Araabi, and H. Soltanianzadeh, "Feature fusion as a practical solution toward noncooperative iris recognition," *Proc. in IEEE Int. Conf. on Info. Fusion*, pp. 1-7, Cologne, Germany, Jun. 2008.

[116] J. Zuo, and N. A. Schmid, "Global and local quality measures for NIR iris video," *Proc. in IEEE Comp. Vis. and Pattern Recog. Workshops,* pp. 120-125, Miami, FL, USA, Jun. 2009.

[117] C.C. Tsai, J. Taur, and C. W. Tao, "Iris recognition based on relative variation analysis with feature selection," *Optical Engg.*, vol. 47, no. 9, pp. 097202, Sep. 2008.

[118] K. R. Chen, C. T. Chou, S. W. Shih, W. S. Chen, and D. Y. Chen, "Feature selection for iris recognition with AdaBoost," *Proc. in Int. Conf. on Intelligent Info. Hiding and Multimedia Signal Process.*, pp. 411-414, Kaohsiung, Taiwan, Nov. 2007.

[119] Y. Du, C. Belcher, Z. Zhou, and R.W. Ives, "Feature correlation evaluation approach for iris image quality measure," *Signal Process.*, vol. 90, no. 4, pp. 1176-1187, Apr. 2010.

[120] C. Belcher and Y. Du, "A selective feature information approach for iris image quality measure," *IEEE Trans. Info. Forensics and Security*, vol. 3, no. 3, pp. 572-577, Sep. 2008.

[121] H. Proença and L. A. Alexandre, "Iris recognition: measuring feature's quality for the feature selection in unconstrained image capture environments," *Proc. in IEEE Int. Conf. on Computational Intell. for Homeland Security and Personal Safety*, vol. 1, pp. 35-40, Alexandria, VA, USA, Oct. 2006.

[122] K. P. Hollingsworth, K. W. Bowyer, and P. J. Flynn, "Using fragile bit coincidence to improve iris recognition," *Proc. in IEEE Int. Conf. on Biometrics: Theory, Applications, and Syst.,* pp. 1-6, Washington, DC, USA, Sep. 2009.

[123] K. P. Hollingsworth , K. W. Bowyer, and P. J. Flynn, "The best bits in an iris code," *IEEE Trans. Pattern Anal. and Machine Intell.*, vol. 31, no. 6, pp. 964-973, Jun. 2009.

[124] A. W. K. Kong, D. Zhang, and M. S. Kamel, "An analysis of iriscode," *IEEE Trans. Image Process.*, vol. 19, no. 2, pp. 522-532, Feb. 2010.

[125] N. Sudha and Y. H. K. Wong, "Hausdorff distance for iris recognition," *Proc. in IEEE Int. Sympos. on Intelligent Control,* pp. 614 – 619, Singapore, Oct. *2007.*

[126] E. Krichen, S. Garcia-Salicetti, and B. Dorizzi, "A New phase-correlation-based iris matching for degraded images," *IEEE Trans. Syst. Man and Cyber. B,* vol. 39, no. 4, pp. 924-934, Aug. 2009.

[127] Y. Du, R. W. Ives, D. M. Etter, and T. B. Welch, "Use of one-dimensional iris signatures to rank iris pattern similarities," *Optical Engg.*, vol. 45, no. 3, pp. 037201, Mar. 2006.

[128] J. Thornton, M. Savvides, and B.V.K. Vijaya Kumar, "A Bayesian approach to deformed pattern matching of iris images," *IEEE Trans. Pattern Anal. and Machine Intell.*, vol. 29, no. 4, pp. 596-606, Apr. 2007.

[129] S. Ziauddin and M. N. Dailey, "Iris recognition performance enhancement using weighted majority voting," *Proc. in IEEE Int. Conf. on Image Process.*, pp. 277-280, San Diego, CA, USA, Oct. 2008.

[130] A. Kumar and A. Passi, "Comparison and combination of iris matchers for reliable personal authentication," *Pattern Recog.*, vol. 43, no. 3, pp. 1016-1026, Mar. 2010.

[131] K. W. Bowyer, S. E. Baker, A. Hentz, and K. P. Hollingsworth, T. Peters, and P. J. Flynn, "Factors that degrade the match distribution in iris biometrics," *Identity in the Info. Society*, vol. 2, no. 3, pp. 327-343, 2010.

[132] S. E. Baker, K. W. Bowyer, and P. J. Flynn, "Empirical evidence for correct iris match score degradation with increased time-lapse between gallery and probe matches," *Proc. in Int. Conf. on Advances in Biometrics*, Springer Lecture Notes in Computer Science, vol. 5558, pp. 1170-1179, Alghero, Italy, Jun. 2009.

[133] B. Son, G. Kee, and Y. Lee, "Iris recognition system using wavelet packet and support vector machines," *Proc. in Int. Conf. Info. Security Applications*,

Springer Lecture Notes in Computer Science, vol. 2908, pp. 1915-1932, Jeju Island, Korea, Aug. 2003.

[134] A. Ross, "Iris recognition: The path forward," *Computer*, vol. 43, no. 2, pp. 30-35, Feb. 2010.

[135] K. Roy and P. Bhattacharya, "Iris recognition based on collarette region and asymmetrical support vector machines," *Proc. in Int. Conf. on Image Anal. and Recog*., Springer Lecture Notes in Computer Science, vol. 4633, pp. 854-865, Montreal, Canada, Aug. 2007.

[136] K. Roy and P. Bhattacharya, "Adaptive asymmetrical SVM and genetic algorithms based iris recognition," *Proc. in IEEE Int. Conf. on Pattern Recog.*, pp. 1-4, Tampa, FL, USA, Dec. 2008.

[137] H. Proença and L. A. Alexandre, "A method for the identification of inaccuracies in the pupil segmentation," *Proc. in IEEE Int. Conf. on Availability, Reliability and Security,* pp. 224-228, Vienna, Austria, Apr. 2006.

[138] T. Tan, Z. He, and Z. Sun, "Efficient and robust segmentation of noisy iris images for non-cooperative iris recognition," *Image and Vis. Computing*, vol. 28, no. 2, pp. 223-230, Feb. 2010.

[139] N. A. Schmid, M. V. Ketkar, H. Singh, and B. Cukic, "Performance analysis of iris-based identification system at the matching score level," *IEEE Trans. Info. Forensics and Security,* vol. 1, no. 2, pp. 154-168, Jun. 2006.

[140] Z. Zhou, Y. Du, and C. Belcher, "Transforming traditional iris recognition systems to work on non-ideal situations," *IEEE Trans. Industrial Electronics*, vol. 56, no. 8, pp. 3203-3213, Aug. 2009.

[141] N. B. Puhan, N. Sudha, and A. S. Kaushalram, "Efficient segmentation technique for noisy frontal view iris images using Fourier spectral density," *Signal, Image and Video Process.*, Nov. 2009, DOI: 10.1007/s11760-009-0146-z.

[142] Y. Du, E. Arslanturk, Z. Zhou, and C. Belcher, "Video-based non-cooperative iris image segmentation," *IEEE Trans. Syst. Man and Cyber. B*, vol. 41, no. 1, pp. 64-74, Feb. 2011.

[143] V. N. Boddeti and B. V. K. V. Kumar, "Extended-depth-of-field iris recognition using unrestored wavefront-coded imagery," *IEEE Trans. Syst. Man and Cyber. A*, vol. 40, no. 3, pp. 495-508, May 2010.

[144] K. Hollingsworth, K. W. Bowyer, and P. J. Flynn, "Pupil dilation degrades iris biometric performance," *Comp. Vis. and Image Understanding*, vol. 113, no. 1, pp. 150-157, Jan. 2009.

[145] N. Tajbakhsh, B. N. Araabi, and H. Soltanian-zadeh, "Noisy iris verification: a modified version of local intensity variation method," *Proc. in Int. Conf. On Advances in Biometrics,* Springer Lecture Notes in Computer Science, vol. 5558, pp. 1150-1159, Alghero, Italy, Jun. 2009.

[146] J. Zuo and N. A. Schmid, "On a methodology for robust segmentation of nonideal iris images," *IEEE Trans. Syst. Man and Cyber. B*, vol. 40, no. 3, pp. 703-718, Jun. 2010.

[147] C. Belcher and Y. Du, "Region-based sift approach to iris recognition," *Optics and Lasers in Engg.*, vol. 47, no. 1, pp. 139-147, Jan. 2009.

[148] N.B. Puhan, N. Sudha, and J. Xudong, “Robust eyeball segmentation in noisy iris images using Fourier spectral density,” *Proc. in IEEE Int. Conf. on Info., Commu. and Signal Process.,* pp. 1-5, Singapore, Dec. 2007.

[149] H. Proenca and L. A. Alexandre, “Iris segmentation methodology for non-cooperative recognition,” *Proc. in IEE Vis., Image and Signal Process.*, vol. 153, no. 2, pp. 199-205, Apr. 2006.

[150] K. Roy and P. Bhattacharya, “Iris recognition in nonideal situations,” *Proc. in Int. Conf. on Info. Security*, Springer Lecture Notes in Computer Science, vol. 5735, pp. 143-150, Pisa, Italy, Sep. 2009.

[151] Y. Du, C. Belcher, and Z. Zhou, "Non-cooperative iris recognition," *EURASIP J. on Advances in Signal Process.*, 2010. To appear.

[152] N. Sudha and N.B. Puhan, “Comparing noisy irises using a modified partial Hausdorff distance,” *Int. J. of Automated Identification Tech.*, vol. 1, no. 1, pp. 23-30, Jun. 2008.

[153] R. Ives, D. Bishop, Y. Du, and C. Belcher, “Iris Recognition: the consequences of image compression,” *EURASIP J. on Advances in Signal Process.*, 2010. To appear.

[154] F. Tan, X. Fu, Y. Zhang, and A. G. Bourgeois, “Improving feature subset selection using a genetic algorithm for microarray gene expression data,” *Proc. in IEEE Congress on Evolutionary Comput.*, pp. 2529-2534, Vancouver, BC, Canada, Jul. 2006.

[155] X. Zhang, Z. Zhu, J. XU, and S. Ren, "The classification algorithm of defects in weld image based on asymmetrical SVMs," *Proc. in IEEE Int. Conf. on Control and Automation*, vol. 2, pp. 1215-1219, Budapest, Hungary, Jun. 2005.

[156] R. Malladi, J. A. Sethian, and B. C. Vemuri, "Shape modeling with front propagation: a level set approach," *IEEE Trans. Pattern Anal. and Machine Intell.*, vol. 17, no. 2, pp. 158–175, Feb. 1995.

[157] J. A. Sethian and J. Strain, "Crystal growth and dendritic solidication," *J. of Computational Physics*, vol. 98, no. 2, pp. 231-253, Feb. 1992.

[158] A. Tsai, A. Yezzi Jr., and A. S. Willsky, "Curve evolution implementation of the Mumford–Shah functional for image segmentation, denoising, interpolation, and magnification," *IEEE Trans. Image Process.*, vol. 10, no. 8, pp. 1169–1186, Aug. 2001.

[159] S. Osher and J. A. Sethian, "Fronts propagating with curvature dependent speed: algorithms based on Hamilton-Jacobi formulation," *J. of Computational Physics*, vol. 79, no. 1, pp. 12-49, Nov. 1988.

[160] L. A. Vese and T. F. Chan, "A multiphase level set framework for image segmentation using the Mumford and Shah model," *Int. J. Comp. Vis.*, vol. 50, no. 3, pp. 271–293, Dec. 2002.

[161] Z. He, Z. Sun, T. Tan, X. Qiu, C. Zhong, and W. Dong, "Boosting ordinal features for accurate and fast iris recognition," *Proc. in IEEE Int. Conf. on Comp. Vis. and Pattern Recog.*, pp. 1-8, Alaska, USA, Jun. 2008.

[162] A. Jensen and A. la Cour-Harbo, *Ripples in mathematics: the discrete wavelet transform,* Springer-Verlag, Berlin, Heidelberg, New York, 2001.

[163] J. Shen and G. Strang, “Asymptotics of Daubechies filters, scaling functions, and wavelets,” *Applied and Computational Harmonic Anal.*, vol. 5, no. 3, pp. 312-331, Jul. 1988.

[164] H. Proenca and L. A. Alexandre, “Toward noncooperative iris recognition: a classification approach using multiple signatures,” *IEEE Trans. Pattern Anal. Machine Intell.*, vol. 29, no. 4, pp. 607–612, Apr. 2007.

[165] L. Yu, D. Zhang, and K. Wang, “The relative distance of key point based iris recognition,” *Pattern Recog.*, vol. 40, no. 2, pp. 423–430, Feb. 2007.

[166] Z. He, T. Tan, Z. Sun, and X. Qiu, “Toward accurate and fast iris segmentation for iris biometrics,” *IEEE Trans. Pattern Anal. Machine Intell.*, vol. 31, no. 9, pp. 1670–1684, Sep. 2009.

[167] C. Yu and M. Adjouadi, “A New noise tolerant segmentation approach to nonideal iris image with optimized computational speed,” *Proc. in Int. Conf. on Image Process., Comp. Vis., & Pattern Recog,* pp. 547-553, Las Vegas, Nevada, USA, Jul. 2009.

[168] S. J. Pundlik, D. L. Woodard, and S. T. Birchfield, “Non-ideal iris segmentation using graph cuts,” *Intl. Conf. On Comp. Vis. and Pattern Recog.,* pp. 1-6, 2008.

[169] K. Roy and P. Bhattacharya, “Nonideal iris recognition using level set approach and coalitional game theory,” *Proc. in Int. Conf. on Comp. Vis. Syst.*, Springer Lecture Notes in Computer Science, vol. 5815, pp. 394-402, Belgium, Oct. 2009.

[170] K. Roy, P. Bhattacharya, and C. Y. Suen, "Unideal iris segmentation using region-based active contour model," *Proc. in Int. Conf. on Image Anal. and*

Recog., Springer Lecture Notes in Computer Science, vol. 6112, pp. 256-265, Povoa de Varzim, Portugal, Jun. 2010.

[171] K. Roy, P. Bhattacharya, and C. Y. Suen, "Recognition of unideal iris images using region-based active contour model and game theory," *Proc. in IEEE Int. Conf. on Image Process.*, pp. 1705-1708, Hong Kong, China, Sep. 2010.

[172] P. K. Dutta, *Strategies and games: theory and practice*, MIT Press, MA, USA, 1999.

[173] Available online: http://en.wikipedia.org/wiki/Game_Theory_in_Communication_Networks.

[174] R. C. Gonzalez and R. E. Woods, *Digital image processing,* 3rd ed., Prentice Hall, NJ, USA, 2007.

[175] K. Roy, P. Bhattacharya, and C. Y. Suen, "Segmentation of unideal iris images using game theory," *Proc. in IEEE Int. Conf. on Pattern Recog.*, pp. 2844-2847, Istanbul, Turkey, Aug. 2010.

[176] K. Roy, P. Bhattacharya, and C. Y. Suen, "Iris segmentation using game theory," *Signal, Image and Video Process.*, DOI: 10.1007/s11760-010-0193-5.

[177] S. Mallat, and W. L. Hwang, "Singularity detection and processing with wavelets," *IEEE Trans. Info. Theory,* vol. 38, no. 2, pp. 617-643, Mar. 1992.

[178] M. E. Leventon, W. E. L. Grimson, and O. Faugeras, "Statistical shape influence in geodesic active contours," *Proc. in IEEE Int. Conf. of Comp. Vis. and Pattern Recog.*, vol. 1, pp. 316–323, Hilton Head, SC, USA, Jun. 2000.

[179] K. Roy, P. Bhattacharya, and C. Y. Suen, "Iris recognition using shape guided approach and game theory," *Pattern Anal. and Applications*, 2010. To appear.

[180] Y. Chen, H. D. Tagare, S. Thiruvenkadam, F. Huang, D. Wilson, K. S. Gopinath, R. W. Brigg, and E. A. Geiser, "Using prior shapes in geometric active contours in a variational framework," *Int. J. of Comp. Vis.*, vol. 50, no. 3, pp. 315–328, Dec. 2002.

[181] K. Roy and P. Bhattacharya, "Variational level set method and game theory applied for nonideal iris recognition," *Proc. in IEEE Int. Conf. on Image Process.,* pp. 2721-2724, Egypt, Nov. 2009.

[182] A. Abhyankar and S. Schuckers, "Active shape models for effective iris segmentation," *Proc. in SPIE Conf. Biometric Tech. Human Identification III*, vol. 6202, pp. 62020H, Orlando, FL, Apr. 2006.

[183] T. F. Cootes, C. J. Taylor, D. H. Cooper, and J. Graham, "Active shape models-their training and application," *Comp. Vis. and Image Understanding*, vol. 61, no. 1, pp. 38-59, Jan. 1995.

[184] A. Fitzgibbon, M. Pilu, and R. B. Fisher, "Direct least square fitting of ellipses," *IEEE Trans. Pattern Anal. Machine Intell.*, vol 21, no. 5, pp. 476-480, May 1999.

[185] V. Caselles, R. Kimmel, and G. Sapiro, "Geodesic active contours," *Int. J. of Comp. Vis.*, vol. 22, no. 1, pp. 61–79, Mar. 1997.

[186] W. Kong and D. Zhang, "Detecting eyelash and reflections for accurate iris segmentation," *Int. J. on Pattern Recog. and Artificial Intell.*, vol 17, no. 6, pp. 1025-1034, 2003.

[187] L. Masek and P. Kovesi, "Biometric identification systems based on iris patterns," *MATLAB source code*, School of Computer Science and Software

Engineering, University of Western Australia, Australia, 2003. Available online: http://www.csse.uwa.edu.au/~pk/studentprojects/libor/sourcecode.html

[188] Active shape model Matlab code. Available online: http://www.mathworks.com/matlabcentral/fileexchange/26706-active-shape-model-asm-and-active-appearance-model-aam.

[189] Iris Challenge Evaluation (ICE) 2005 dataset. Available online: http://iris.nist.gov/ICE/.

[190] CASIA-Iris Version 3 interval dataset. Available online: http://www.cbsr.ia.ac.cn/IrisDatabase.htm.

[191] UBIRIS Version 1 dataset obtained from Dept. of Computer Sci., University of Beira Interior, Portugal. Available online: http://iris.di.ubi.pt/.

[192] WVU Nonideal iris dataset obtained from West Virginia University. Available online: http://citer.wvu.edu/biometric_dataset_collections.

[193] C. T. Chou, S. W. Shih, W. S. Chen, V. W. Cheng, and D. Y. Chen, "Non-orthogonal view iris recognition system," *IEEE Trans. Circuits and Syst. for Video Tech.,* vol. 20, no. 3, pp. 417–430, Mar. 2010.

[194] H. Proença, E. Y. Du, and J. Scharcanski (Eds.), "Unconstrained biometrics: advances and trends," *Signal, Image and Video Process.*, Special Issue, vol. 5, no. 3, Sep. 2011.

Appendix A

Datasets Used

The extensive experiments were conducted on four datasets, namely, the ICE 2005 [189], the CASIA Version 3 [190], the UBIRIS Version 2 [191], and WVU Nonideal [192], plus non-homogeneous combined dataset. We have selected the afore-mentioned datasets for the performance evaluation since these datasets contain nonideal iris images including off angle, occluded, blurred and noisy images that are acquired with different devices under varying conditions to facilitate a comprehensive performance evaluation in a real word application level scenario. These datasets also represent different ethnicities. A brief description of each of these datasets is given below:

- The Iris Challenge Evaluation (ICE) 2005 [189] dataset contains 2953 images corresponding to 244 classes. The ICE dataset consists of left and right iris images for experimentation (1528 left iris images from 120 classes and 1425 right iris images from 124 classes). This dataset is divided into two categories: the ‘‘gallery’’ images, which are considered as good quality images, and the ‘‘probe’’ images, which represent iris images of varying quality. The iris images are intensity images with a resolution of 640×480. The average diameter of an iris is 228 pixels.

- The CASIA Version 3 Interval [190] iris dataset includes 2655 iris images from 249 different persons, with 396 iris classes. Most of the images are captured in two sessions with at least one month interval. The iris images are 8-bit gray level images with a resolution of 320×280.
- The UBIRIS Version 1 [191] dataset contains 2410 iris images from 241 classes. The iris images are captured in two sessions. The iris images captured in the first session represent the good quality images whereas the images in the second session have the irregularities with respect to focus, intensity, and reflection.
- The West Virginia University (WVU) Nonideal [192] iris dataset contains 800 images corresponding to 200 classes. Each class is represented by four images collected at three angles on the order of 0°, 15°, 30° and again 0°. The iris images are intensity images with a resolution of 640×480.
- The combined non-homogeneous dataset -- In order to perform an extensive experimentation and to validate our proposed approach, we generate a heterogeneous dataset by combining the above four datasets, and this dataset consists of 8818 images corresponding to 1081 classes.